Development of Composites of Silica Aerogels with Hydroxy-terminated Poly(dimethylsiloxane)

by

Deniz Şanlı

A Thesis Submitted to the
Graduate School of Sicences and Engineering
in Partial Fulfillment of the Requirements for
the Degree of

Doctor of Philosophy
in
Chemical and Biological Engineering

Koc University

September 2014

Koc University

Graduate School of Sciences and Engineering

This is to certify that I have examined this copy of a Ph.D. thesis by

Deniz Şanlı

and have found that it is complete and satisfactory in all respects, and that any and all revisions required by the final examining committee have been made.

Committee Members:

_____

Can Erkey, Ph. D. (Advisor)

_____

Yaman Arkun, Ph. D.

_____

Levent Demirel, Ph. D.

_____

Seda Kızılel, Ph. D.

_____

Alexandr Jonas, Ph. D.

Date: _____

ABSTRACT

Vacuum insulation panels (VIPs) with typical thermal conductivity values of 3 to 5 mW/mK are emerging as excellent systems nowadays for effective thermal insulation in buildings and household applications. The achievement of such low thermal conductivities in VIPs relies on the suppression of the gaseous convection by applying vacuum. A VIP structure is composed of a core insulation material and an envelope film covering the core material. Among different materials, fumed silica and glass fiber are the most commonly utilized core materials owing to their appreciably low thermal conductivity values, especially under vacuum conditions. However, these materials are not transparent and thus cannot be used in the development of transparent vacuum insulation panels. The idea of transparent VIPs has been recently established in order to replace the conventional window glazing. Since then, research about transparent core materials and barrier films that can be utilized in the development of transparent vacuum insulation panels has been gaining increasing interest. Silica aerogels appear as the most promising nanostructured materials to be implemented as filler materials in transparent vacuum insulation panels due to their transparency in addition to extremely low thermal conductivity. One drawback of silica aerogels is their poor mechanical properties which makes their utilization as monolithic and crack-free materials challenging. This problem can be solved by reinforcing aerogels with polymers which results in improved resilience that would allow for practical utilization.

In this study, monolithic composites of silica aerogels with hydroxyl-terminated poly(dimethylsiloxane) (PDMS(OH)) were developed. The first route that was followed for the synthesis of the composites was the modification of the conventional two-step sol-gel process. The incorporation of the polymer in the synthesis was performed at different stages of the sol-gel process. Additionally, different co-solvents such as THF and toluene were used. The effects of several processing parameters such as polymer amount, type of

co-solvent and the polymer addition step, on the properties of the composites were investigated. The composites synthesized with this route were obtained as opaque materials since PDMS(OH) was not soluble in the sol mixture. Utilization of THF and toluene as the co-solvents avoided the solubility problem, however the mechanical durability of the aerogel composites was very low which resulted in very high volumetric shrinkage during the supercritical drying.

Reactive supercritical deposition technique was employed as the second route and the composites of silica aerogels with PDMS(OH) were developed by the deposition of the polymer from supercritical CO_2. The technique is composed of two stages; the first stage includes the dissolution of PDMS(OH) in supercritical CO_2 that results in a single phase binary mixture of PDMS(OH)-CO_2 and the second stage is the exposure of the silica aerogel samples to the single phase binary mixture. Initially, the demixing pressures of PDMS(OH)-CO_2 binary mixtures at various compositions were measured up to 24 MPa to determine the single phase region of the binary mixture. The demixing pressures were observed to decrease with increasing polymer content of the binary mixture. Subsequently, deposition experiments were performed and monolithic aerogel composites were obtained. The deposited samples were characterized by ATR-FTIR and BET analysis. It was revealed that during the course of the deposition, the polymer molecules react with the surface –OH groups of the aerogel. The effects of various parameters such as polymer concentration, deposition temperature, deposition time and polymer molecular weight on the properties of composites were investigated. The polymer uptake of the deposited aerogels increased with increasing PDMS(OH) concentration, deposition time and deposition temperature. It was found that the transparency of the aerogels can be controlled by the amount of the polymer loaded to the samples. It was also demonstrated that the deposition resulted in the coating of silica aerogel surface with a thin layer (~1-2 nm) of polymer molecules. According to the thermal conductivity model simulations, such a thin coating layer did not cause a

noticeable increase in the thermal conductivity of the composites. Moreover, compression tests revealed a threefold improvement in the mechanical strength of the composites when compared to native silica aerogels. Hereby, this work presents silica aerogel-PDMS(OH) composite materials as novel candidates to be used as core insulation materials in transparent VIPs.

ÖZET

Tipik olarak 3 ila 5 mW/mK ısı iletim katsayısına sahip olan vakum izolasyon panelleri (VİP) günümüzde bina ve beyaz eşya uygulamalarında mükemmel ısı yalıtımı sağlayan sistemler olarak ortaya çıkar. Vakum izolasyon panellerinde düşük ısı iletimi katsayısı, gaz faz iletiminin vakum koşulları altında yüksek oranda azalmasıyla sağlanır. Vakum izolasyon panelleri, bir çekirdek izolasyon malzemesi ve onu çevreleyen zarf film tarafından oluşturulur. Özellikle vakum koşulları altındaki düşük ısı iletim katsayılarından dolayı, vakum izolasyon panellerinde çekirdek malzeme olarak en çok silica ya da cam yünü kullanılır. Fakat saydam olmadıklarından dolayı bu malzemeler, saydam vakum izolasyon panellerinde kullanım için uygun değildir. Saydam vakum izolasyon panelleri binalarda kullanılan pencerelerin görevini yapabilmek üzere geliştirilmeye çalışılmaktadır. Saydam vakum izolasyon panelleri fikri ilk ortaya atıldığından itibaren, saydam çekirdek yalıtım malzemesi ve zarf filmlerin geliştirilmesi günden güne artak bir ilgi uyandırmıştır. Silika aerojeller, düşük ısı iletim katsayıları ve saydamlıklarından dolayı, saydam vakum izolasyon panellerinde çekirdek yalıtım malzemesi olarak kullanılabilecek en yüksek potansiyele sahip malzemelerdir. Fakat silika aerojeller zayıf mekanik özelliklere sahiptir ve bu sebeple monolit ve kırıksız olarak üretimleri çok zordur. Silika aerojellerin zayıf mekanik özellikleri, polimerler ile kompozitlerinin geliştirilmesi ile iyileştirilebilir.

Bu çalışmada, silika aerojellerin hidroksil-son gruplu-poli(dimetilsilokzan) (PDMS(OH)) ile monolit komozitleri geliştirilmiştir. Kompozitler, ilk olarak sol-jel metodunun farklı aşamalarında polimerin eklenmesiyle elde edilmiştir. Ayrıca sentez aşamasında tetrahirofuran (THF) ve toluene gibi farklı ikincil çözücüler de kullanımıştır. Polimer miktarı, çözücü cinsi ve polimerin eklenme aşaması gibi farklı parametrelerin, kompozitlerin özellikleri üzerindeki etkileri incelenmiştir. Bu yöntemle sentezlenen kompozitler, PDMS(OH) suda çözünmediğinden dolayı opak olarak elde edilmiştir. THF

ve toluenin ikincil çözücü olarak kullanılması çözünürlük problemini ortadan kaldırmış ancak kompozitlerin mekanik özelliklerini olumsuz yönden etkilemiştir.

Kompozitlerin üretiminde ikinci yol olarak, reaktif süperkritik depozisyon yöntemi kullanımış ve polimerin süperkritik karbon dioksitten silika aerojellere depozisyonu gerçekleştirilmiştir. Bu yöntem iki aşamadan oluşur. Birinci aşamada polimer süpercritik karbon dioksitte çözülür ve tek fazda ikili karışım (PDMS(OH)-CO_2) oluşturulur. İkinci aşamada ise silika aerojel, tek fazdaki bu karışıma maruz bırakılır ve polimerin depozisyonu gerçekleştirilir. Depozisyon deneylerinde tek faz PDMS(OH)-CO_2 karışımları kullanıldığından dolayı, öncelikle bu karışımların faz ayrım basınçları, geniş bir bileşim aralığında ve 24 MPa basınç değerlerine kadar ölçülmüştür. Bu ölçümler neticesinde, faz ayrım basıncının karışımdaki polimer konsantrasyonunun artmasıyla azaldığı görülmüştür. Faz ayrım deneylerinin ardından, polimerin depozisyonu gerçekleştirilmiş ve monolit kompozitler elde edilmiştir. Elde edilen kompozitler ATR-FTIR ve BET yöntemleriyle analiz edilmiş ve özellikleri belirlenmiştir. Depozisyon sırasında polimerin, silika aerojelin yüzeyinde bulunan hidroksil gruplarıyla reaksiyona girdiği ortaya çıkarılmıştır. Polimer konsantrsayonu, depozisyon sıcaklığı, depozisyon süresi ve polimer molekül ağırlığı gibi birçok parametrenin, kompozitlerin özellikleri üzerindeki etkileri incelenmiştir. Kompozitlerdeki polimer miktarı, artan polimer konsantrasyonu, depozisyon süresi ve depozisyon sıcaklığı ile artmıştır. Kompozitlerin saydamlığının, depozisyon yapılan polimer miktarıyla kontrol edilebildiği görülmüştür. Ayrıca polimerin silika aerojel yüzeyini yaklaşık 1 nm kalınlığında bir tabaka halinde kapladığı ortaya çıkarılmıştır. Yapılan ısı iletim katsayısı simülasyonlarıyla, bu miktardaki polimer tabakasının silika aerojelin ısı iletim katsayısını etkilemediği gözlemlenmiştir. Ayrıca yapılan mekanik testlerle, kompozitlerin mekanik özelliklerinin silika aerojelin mekanik özelliklerinden 3 kat daha iyi olduğu görülmüştür. Sonuç olarak, bu çalışmada üretilen silika aerojel-PDMS(OH) kompozit malzemelerinin, saydam vakum izolasyon panellerinde çekirdek

yalıtım malzemesi olarak kullanılmak üzere çok uygun malzemeler olduğu ortaya çıkarılmıştır.

ACKNOWLEDGEMENTS

This thesis has been submitted in partial fulfillment of the requirements for the degree of Ph.D. Entire of the presented work was conducted at Department of Chemical and Biological Engineering at Koç University.

I would like express my gratitude to the following great people who contributed to this work:

First and foremost, I am amply grateful to my supervisor Can Erkey for the opportunity of working with him in the friendly and productive environment he created in Energy Technologies and Supercritical Fluids Research Group. I would like to thank him for his guidance, invaluable support and trust on me during the course of my Ph.D. studies. He has always been patient and kind, sometimes like a father, sometimes like a supervisor, sometimes like a friend. His brilliant mind and pure logic always enlightened my way through fundamental as well as practical research. I'm grateful for his invaluable time that he spent for me.

I am thankful to my colleagues in our research group, Selmi Erim Bozbağ, Zeynep Ülker, Yaprak Özbakır, Metin Karayılan, Gamze Eriş and İbrahim Şahin, for always being fun, helpful and encouraging. Special thanks to Selmi Erim Bozbağ and Zeynep Ülker for the fruitful discussions.

I also would like to thank all of my friends that I met at Koç University during the past seven years, İhsan Ozan Yıldırım, Ayşe Dilan Çelebi, Selma Bulut and Volkan Balcı. We shared so many together, some of which were unique, life time experiences (June 2013).

Finally, I am grateful to and owe everything to my family for their never-ending support and encouraging me to always follow my own path. I am sincerely thankful to İzzet Yıldız for just being there for me.

This work was funded by the European Union Seventh Framework Program (FP7/2007 – 2013) under grant agreement no. NMP4-SL-2010-260086. I also acknowledge the financial support of the Scientific and Technological Research Council of Turkey (TÜBİTAK) during my Ph.D. studies.

TABLE OF CONTENTS

List of Tables **xi**

List of Figures **xiii**

Chapter 1: Introduction **1**

Chapter 2: Silica Aerogels **5**

Chapter 3: PDMS(OH)–Silica Aerogel Composites by Modification of the Sol–Gel Process **39**

Chapter 4: Phase Behavior & Modeling **67**

Chapter 5: PDMS(OH)–Silica Aerogel Composites by Reactive Supercritical Deposition (RSCD) **103**

Chapter 6: Conclusion **144**

Bibliography **146**

Appendix **155**

LIST OF TABLES

Table 1 Properties of silica aerogels. 14
Table 2 Thermal conductivities of some porous insulation materials at room temperature. ... 16
Table 3 Synthesis conditions for PDMS(OH)–silica aerogel composites derived with the standard sol–gel procedure. 41
Table 4 Synthesis conditions for PDMS–bis(alkylOH)–silica aerogel composites derived with the standard sol–gel procedure. 41
Table 5 PDMS(OH)–silica aerogel composites synthesized with THF as the co–solvent. 42
Table 6 PDMS(OH)–silica aerogel composites synthesized with THF as co–solvent (overnight gelation). 43
Table 7 PDMS(OH)–silica aerogel composites synthesized with THF as co–solvent (gelation at 323.2 K, without aging). 44
Table 8 PDMS(OH)–silica aerogel composites synthesized with toluene as the co–solvent. . 44
Table 9 PDMS(OH)–silica aerogel composites synthesized with THF and toluene as the co–solvents. 45
Table 10 Properties of native silica aerogels synthesized by standard two–step sol–gel process. 46
Table 11 Bulk density, porosity, BET surface area and average pore widths of PDMS(OH)–silica aerogel composites synthesized with the standard sol–gel procedure. 52
Table 12 Properties of PDMS–bis(alkyl–OH)–silica aerogel composites synthesized with the standard sol–gel procedure. 57
Table 13 Density, porosity and volumetric shrinkage of the PDMS(OH)–silica aerogel composites synthesized with THF as the co–solvent. 59
Table 14 TEOS/PDMS–OH composite aerogels synthesized with THF as the co–solvent (overnight gelation). 59
Table 15 Properties of PDMS(OH)–silica aerogel composites synthesized with THF as the co–solvent (gelation at 323.2 K, without aging). 60
Table 16 Properties of PDMS(OH)–silica aerogel composites synthesized with toluene as the co–solvent. 61
Table 17 PDMS(OH)–silica aerogel composites synthesized with THF and toluene as the co–solvents. 62
Table 18 Experimental bubble point pressures for HMDS-CO_2 binary mixture at various mole fractions of CO_2 and temperatures. 81
Table 19 Thermodynamic parameters of HMDS and CO_2 together with the optimized κ1 values. The average absolute errors (AAE %) were computed from the experimental and calculated vapor pressure data. 82
Table 20 Computed binary interaction parameters. AAE (%) values were calculated from the experimental and computed pressures. 82
Table 21 Computed liquid and vapor phase mole fractions for HMDS-CO2 binary mixture at 1 atm. 88
Table 22 Experimental P-T data and calculated excess volumes (V^{Excess}) of HMDS-CO_2 binary mixture at various mixture densities and CO_2 mole fractions 90
Table 23 Pure component characteristic parameters. 98

Table 24 Regressed binary interaction parameters for the polymer mixtures together with the predicted compositions and AE (%) [101]. 99
Table 25 Deposition results with and without $scCO_2$ extraction..... 106
Table 26 N_2 adsorption–desorption analysis results for the deposited aerogel sample compared to the native silica aerogel. 107
Table 27 Mass uptakes of the silica aerogel samples after the PDMS(OH) deposition..... 110
Table 28 N_2 adsorption–desorption analysis results of the silica aerogel samples before and after PDMS(OH) deposition..... 110
Table 29 Densities and pore characteristics of the deposited aerogels. 119
Table 30 Summary of N_2 adsorption–desorption analyses results. 131
Table 31 NLDFT results from N_2 adsorption–desorption analyses. 133
Table 32 The thermal conductivities and densities of 6.5x6.5 cm^2 silica aerogel samples.... 136

LIST OF FIGURES

Figure 1 Composites of silica aerogels with a) poly(hexamethylene diisocyanade) [4] b) di-isocyanades [5] c) cellulose [6] 2
Figure 2 Chemical structure of PDMS and PDMS(OH), respectively. 3
Figure 3 Molecular structures of TEOS and TMOS, respectively. 5
Figure 4 Two step acid–base catalysis of silica aerogels. 6
Figure 5 Hydrolysis reaction scheme for TEOS. 7
Figure 6 pH dependencies of hydrolysis and condensation reaction rates [4]. 7
Figure 7 Alcohol and water producing condensation reactions. 8
Figure 8 Gel structures for acid and base catalyzed reactions [5]. 10
Figure 9 Evolution of viscosity and Si–O–Si as a function of time. 10
Figure 10 Syneresis during aging. 11
Figure 11 Coarsening and ripening during aging. 12
Figure 12 Capillary pressure formed in the small pores during ambient drying. 12
Figure 13 Structure of silica aerogels at nanometer scale 14
Figure 14 (a) SEM and (b) TEM images showing the pore characteristics of silica aerogels. 14
Figure 15 Heat transfer mechanisms in a porous media. 17
Figure 16 Variation of total thermal conductivity, λ_t (■), calculated radiative thermal conductivity, λ_r (——), gaseous conductivity, λ_g (●), and solid conductivity, λ_s (▲) of Risolcinol Formaldehyde (RF) aerogels with density [38]. 22
Figure 17 Reactivity of silylating agents containing different functional groups [55] 28
Figure 18 Effectiveness of silylation agents on inorganic materials [60] 29
Figure 19 Fundamental steps of silylation of porous materials with $scCO_2$ 31
Figure 20 Micromeritics ASAP 2020 N2 adsorption-desorption analysis system; (A) analysis dewar; (B) sample tube; (C) analysis port; (D) degas dewar; (E) heating jacket; (F) degas ports. 33
Figure 21 Thermo Scientific Nicolet Avatar ATR system 34
Figure 22 (1) Shimadzu UV-VIS Spectrophotometer with (2) $BaSO_4$ powder and (3)integrating sphere system 35
Figure 23 Components of integrating sphere apparatus. 36
Figure 24 Methodology for transparency measurements; (A) baseline correction; (B) total transmittance measurement; and (C) diffuse transmittance measurement. 36
Figure 25 Thermal Analysis (TA) Instruments Dynamic Mechanical Analyzer (DMA) Q800 instrument. 37
Figure 26 Molecular structures of (a) PDMS(OH) and (b) PDMS–bis(alkyl–OH). 40
Figure 27 Top view of a cylindrical aerogel sample after supercritical drying. 46
Figure 28 ATR–FTIR spectrum of native silica aerogel. 47
Figure 29 TGA results of native silica aerogel. 48
Figure 30 Pore size distribution and N2 adsorption/desorption isotherm of native silica aerogel. 49
Figure 31 Total and diffuse transmittance of native silica aerogel obtained by UV–VIS measurements. 50

Figure 32 Stress–strain curve of native silica aerogel sample obtained with DMA compression test. 50
Figure 33 Top view of cylindrical aerogel samples; native silica aerogel (left) and PDMS(OH)–silica aerogel composite (right). 52
Figure 34 Pore size distribution of composites synthesized with different amounts of polymer together with native silica aerogel. 53
Figure 35 TGA analysis of PDMS(OH)–silica aerogel composite with TEOS:PDMS(OH) mass ratio of 1:0.1. 54
Figure 36 TGA analysis of PDMS(OH)–silica aerogel composite with TEOS:PDMS(OH) mass ratio of 1:0.5. 54
Figure 37 ATR–FTIR spectra of PDMS(OH)–silica aerogel composites synthesized with the standard sol–gel procedure. 55
Figure 38 Pore size distribution of composites synthesized with different TEOS/polymer ratios together with native silica aerogel. 57
Figure 39 ATR–FTIR spectra of PDMS–bis(alkyl–OH)–silica aerogel composites synthesized with the standard sol–gel procedure. 58
Figure 40 ATR–FTIR spectra of different PDMS(OH)–silica aerogel composites synthesized with THF as the co–solvent. 60
Figure 41 Pore size distribution of composites synthesized with THF and/or toluene as co–solvents together with native silica aerogel. 63
Figure 42 Top views of cylindrical–shaped native silica aerogel (left), PDMS(OH)–silica aerogel composite (right) that is produced by aging in polymer 64
Figure 43 ATR–FTIR spectra of native silica aerogel and aerogel composite derived by aging in PDMS(OH) 64
Figure 44 Experimental setup for the phase behavior measurements [101]. 69
Figure 45 Algorithm for calculating the bubble point pressure. 74
Figure 46 Comparison with literature values of bubble point pressures of C_2H_5OH-CO_2 binary mixture at (a) 298.2 K; (b) 313.2 K; (c) 333.2 K. The deviations in pressure for the data of the present work were represented as error bars. 79
Figure 47 Reproducibility of bubble point pressure measurements of HMDS-CO_2 binary mixture at five temperatures (298.2 K, 308.2 K, 313.2 K, 323.2 K, 333.2 K) with CO_2 mass fraction of 0.83. The deviations in pressure were given as the error bars. 80
Figure 48 Bubble point and dew point pressures of HMDS-CO_2 binary mixture at different temperatures. The color filled symbols represents the dew points for the respective temperatures. The dashed lines represent the PRSVEoS model predictions for respective temperatures. 81
Figure 49 Variation of k_{ij} with temperature. 83
Figure 50 P-T projection of HMDS-CO_2 binary mixture computed for each k_{ij} value. 84
Figure 51 Demixing pressures of HMDS-CO_2, PDMS-CO_2 and Selexol-CO_2 binary mixtures at (a) 298.2 K and (b) 313.2 K. 87
Figure 52 Variation of temperature with pressure for pure CO_2 with densities of 809 kg/m^3, 868 kg/m^3, and 910 kg/m^3. 89

Figure 53 Variation of temperature with pressure for HMDS-CO_2 binary mixture at; (a) fixed ρmix=803 kg/m^3 and at two different CO_2 mole fractions; (b) fixed x_{CO2}=0.95 and at two different mixture densities. 91
Figure 54 Excess volumes of HMDS-CO_2 binary mixtures at various temperatures and CO_2 mole fractions. 93
Figure 55 Demixing pressures of PDMS(OH) (Mn=2750 g/mol) – CO_2 binary mixture at 313.2 K, 323.2 K and 333.2 K [101]. 95
Figure 56 Demixing pressures of PDMS(OH) (Mn=18000 g/mol) – CO_2 binary mixture at 313.2 K, 323.2 K and 333.2 K [101]. 96
Figure 57 The effect of molecular weight on the demixing pressures of PDMS(OH) – CO_2 binary mixtures at 323.2 K. 97
Figure 58 The effect of molecular weight on the demixing pressures of PDMS(OH) – CO_2 and PDMS(CH3) – CO_2 binary mixtures at 323.2 K for 5 wt.% of polymer composition. 97
Figure 59 Temperature dependency of the regressed binary interaction parameters for low and high polymer molecular weight mixtures [101]. 100
Figure 60 SLEoS model predictions of bubble point data for PDMS(CH3) (Mw=308000)–CO_2 binary mixture [79]. 101
Figure 61 The experimental setup for the reactive supercritical deposition. 104
Figure 62 Silica aerogel after the deposition and scCO_2 extraction. 106
Figure 63 ATR–FTIR spectra of the deposited aerogel sample obtained with scCO_2 extraction and native silica aerogel. 107
Figure 64 Images of A) hydrophilic and B) superhydrophobic aerogel samples after the deposition. 109
Figure 65 Pore size distribution of the aerogel samples. 111
Figure 66 ATR–FTIR spectra of the silica aerogel samples. 112
Figure 67 The mass uptakes for different initial PDMS(OH) compositions. 114
Figure 68 ATR–FTIR spectra showing the evolution of Si–C, C–H and Si–O–Si peaks upon deposition. 115
Figure 69 Mass uptake values for various deposition times. 116
Figure 70 Images of aerogel samples with A) 15.8 wt.%; B) 20.9 wt.% and C) 36.6 wt.% mass uptakes. 118
Figure 71 ATR–FTIR spectra of the samples from the center and outer surface of the monoliths deposited for 72 hours. 119
Figure 72 Pore size distribution and N_2 adsorption–desorption isotherms of the deposited samples (m.u.: mass uptake). 120
Figure 73 Correlation between volume of PDMS(OH) in the pores and pore volume reduction obtained from BJH analysis (red dotted line is the linear fit). 121
Figure 74 The thickness of the polymer layers for different pore sizes of the deposited samples. 122
Figure 75 The surface areas of the samples obtained from BJH analysis and calculated from deposited layer thicknesses. 123
Figure 76 Mass uptakes of the aerogel samples at different temperatures. 124
Figure 77 Grafting densities of PDMS(OH) on the deposited aerogel samples at different temperatures. 125

Figure 78 ATR–FTIR spectra of native silica aerogel sample and silica aerogel–PDMS(OH) nanocomposite. 126
Figure 79 ATR–FTIR spectra of aerogel sample deposited with PDMS(OH) of molecular weight 2750 g/mol. 128
Figure 80 ATR–FTIR spectra of aerogel sample deposited with PDMS(OH) of molecular weight 18000 g/mol. 128
Figure 81 Images of native silica aerogel (left) and aerogel deposited with PDMS(OH) at 313.2 K (right). 129
Figure 82 Pore size distributions and isotherms of native silica aerogel and aerogels deposited with PDMS(OH) of molecular weight 18000 g/mol. 131
Figure 83 Cumulative surface areas of the aerogel samples for different pore widths obtained from NLDFT analyses. 132
Figure 84 Differential pore volumes of the aerogel samples for different pore widths obtained from NLDFT analyses. 133
Figure 85 Differential pore volumes of the aerogel samples for different pore widths obtained from NLDFT analyses. 134
Figure 86 The water droplets on the deposited aerogels with 36.6 wt.% (left) and 75.4 wt.% (right) PDMS(OH). 135
Figure 87 6.5x6.5 cm^2 silica aerogel samples with densities; 0.183 g/cm3 (left) and 0.272 g/cm3 (right). 136
Figure 88 Contributions of different mechanisms on total thermal conductivity. 137
Figure 89 Effects of pore size on total thermal conductivity. 137
Figure 90 Effects of polymer deposition on total thermal conductivity. 138
Figure 91 Effects of different mass uptakes on density and total thermal conductivity. 139
Figure 92 Strain–stress curves for native silica aerogel and deposited silica aergel sample obtained from compression tests. 141
Figure 93 CO_2 uptakes of the native silica aerogel and deposited aerogel samples (m.u.=mass uptake). 142

CHAPTER 1

INTRODUCTION

High population growth rates combined with increasing energy consumption per capita in developing countries are causing a steady increase in the worldwide energy demand. The increase in energy production to meet this demand is resulting in higher energy prices, increased emissions of greenhouse gases and a deterioration of the environment due to increased usage of fossil fuels. These problems can be overcome by either usage of renewable energy sources or reduction of the energy consumption or both. The biggest contribution to total energy consumption originates from the amount of energy consumed in the buildings. Moreover, 70 % of this amount is solely consumed for heating and cooling applications for both residential and commercial buildings. Under these circumstances, thermal insulation has been receiving increased attention and is considered as one of the most effective ways to reduce energy consumption. The efforts in development of more effective thermal insulation systems have concentrated on the improvement of existing materials as well as the development of novel materials with enhanced thermal insulation properties.

Vacuum insulation panels (VIPs) with typical thermal conductivity values of 3 to 5 mW/mK are emerging as excellent systems nowadays for effective thermal insulation in buildings and household applications since with VIPs one can achieve high insulation properties with low thicknesses [1-3]. The achievement of such low thermal conductivities in VIPs relies on the suppression of the gaseous convection by applying vacuum. A VIP structure is composed of a core insulation material and an envelope film covering the core material. The idea of transparent VIPs has been recently established in order to replace the conventional window glazing. Since then, research about transparent core materials and barrier films that can be utilized in the development of transparent vacuum insulation panels has been gaining increasing interest. Silica aerogels appear as the most promising nanostructured materials to be implemented as filler materials in transparent vacuum insulation panels due to their transparency in addition to extremely low thermal conductivity.

Silica aerogels have many extraordinary properties such as low density, transparency, narrow pore size distribution, high surface area, high porosity and very low thermal conductivity. One

drawback of silica aerogels is that they are highly fragile and brittle materials due to their poor mechanical properties which make their utilization and handling highly challenging. However, this problem can be solved by reinforcing aerogels with polymers which results in improved resilience that would allow for practical utilization. There have been many attempts to produce flexible silica aerogel composites using various compounds and polymers. However, it is apparent from Figure 1 that all of these composites had opaque appearances and hence they are not suitable to be used in transparent VIPs. Under these circumstances one critical question emerges: how can the mechanical properties of silica aerogels be improved without losing the transparency? The answer of this question is that a transparent polymer can be incorporated into the solid silica skeleton of the aerogel in such a way that the transparency can be retained or the silica aerogel surface can be coated with a transparent polymer. In the former case, the polymer addition should be performed during the synthesis so that the polymer molecules are included in the solid network. On the other hand, the later case can be achieved with a post-synthesis treatment employing techniques such as reactive supercritical deposition.

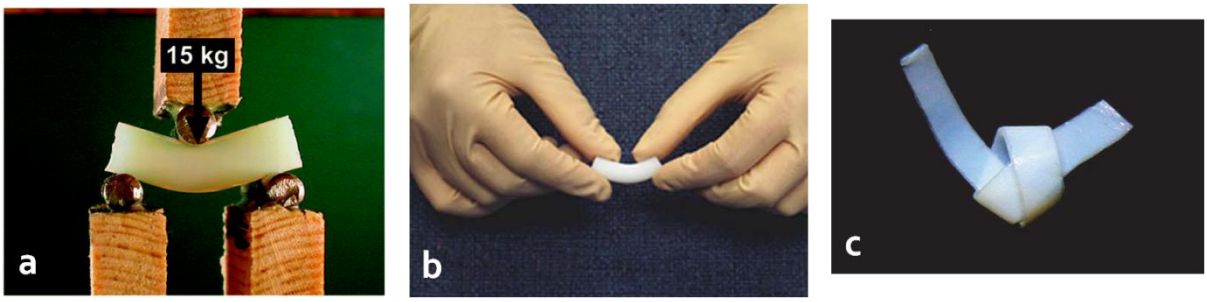

Figure 1 Composites of silica aerogels with a) poly(hexamethylene diisocyanade) [4] b) di-isocyanades [5] c) cellulose [6]

Regarding the above considerations, composites of silica aerogels with hydroxyl-terminated poly(dimethylsiloxane) (PDMS(OH)) were developed within the scope of NanoInsulate project (FP7/2007 – 2013) in order to obtain monolithic, crack-free, transparent and mechanically strong materials to be used as core insulation materials in transparent VIPs. Among various polymers PDMS(OH) which is a functionalized form of poly(dimethylsiloxane) (PDMS) with terminal –OH groups was chosen as the polymer component for several reasons. PDMS is a rubbery polymer that belongs to a group of polymeric organosilicon compounds, and is well known for its unusual rheological properties. PDMS molecules have quite flexible polymer backbones due to the siloxane linkages. It has high level of viscoelasticity owing to these flexible chains and a shear modulus varying

between 100 kPa and 3 MPa which can improve the mechanical properties of silica aerogels [22]. It is extensively produced and consumed as silicon oil, and thus it is cheap. PDMS is a clear liquid polymer at room temperature with a low refractive index of 1.4 which is advantageous in terms of transparency of the composites. PDMS has a high chemical and thermal stability and it provides hydrophobicity which is a key aspect for the long term utilization of the composites. PDMS has relatively low thermal conductivity (0.17 W/mK) compared to most of the polymers and it has substantial solubility in supercritical CO_2 ($scCO_2$). The chemical structures of PDMS and PDMS(OH) are displayed in Figure 2.

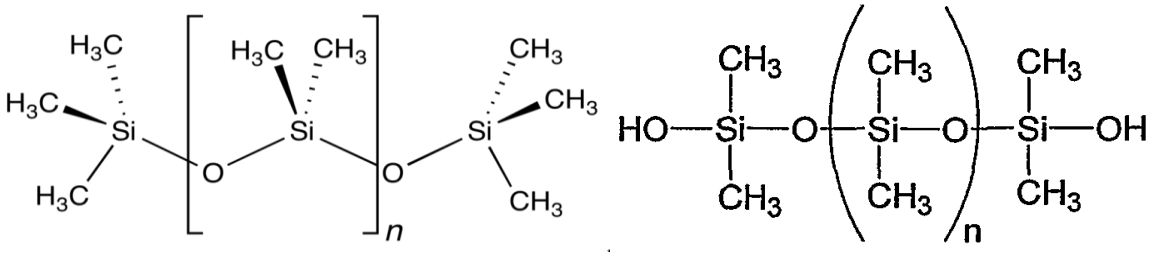

Figure 2 Chemical structure of PDMS and PDMS(OH), respectively.

Several techniques were adopted in the synthesis of the composites to achieve the goals of the NanoInsulate project and the procedures that were followed as well as the properties of the developed composites are described in detail in the following chapters.

Chapter 2 involves with some fundamental information about the synthesis, structure and properties of silica aerogels as well as production of composites of silica aerogels. Silylation is briefly defined as a novel route for the development of silica aerogel composites which is one of the most frequently utilized surface modification techniques. Furthermore, the fundamentals of the heat transfer mechanisms in silica aerogels are explained. In addition, the analytical techniques that were employed to characterize the derived composite materials are also explained.

In chapter 3, the development of PDMS(OH)-silica aerogel composites by the modification of the standard sol-gel process is defined. Different synthesis procedures are defined and several material properties of the developed composites are demonstrated.

In chapter 4, the phase behavior studies of PDMS(OH)-CO_2 binary mixtures are explained. The experimental technique to study the phase behavior is explained in detail. The experimental demixing pressure data as well as different phase separation characteristics of PDMS(OH)-CO_2 binary mixtures are demonstrated. Moreover, modeling of the bubble point pressure data with Sanchez-Lacombe equation of state is also defined.

In chapter 5, the development of PDMS(OH)-silica aerogel composites by reactive supercritical deposition is explained. The effects of different parameters such as polymer concentration, temperature, deposition time and polymer molecular weight on the properties of the composites are demonstrated. The properties of the developed composite materials such as pore structure, hydrophobicity, mechanical durability and transparency are given in detail.

Finally, in chapter 6, summary and conclusion of the overall study is given.

CHAPTER 2

SILICA AEROGELS

2.1 Synthesis of Silica Aerogels

Silica aerogels are nanostructured materials that have been attracting considerable attention due to their unique and intriguing properties such as low density, transparency, high surface area, high porosity and low thermal conductivity. Silica aerogels are produced as a result of a *two-step sol-gel process* which is a complex chemical synthesis procedure. The sol–gel process is generally used to describe any chemical process capable of producing ceramic oxides from solution. In the two-step sol–gel process, there are five basic steps leading to silica aerogel synthesis which are hydrolysis of the precursor compound, condensation of the hydrolysis products, gelation, aging and supercritical drying [7].

Precursor compounds are the starting points of aerogel synthesis and thus have determinant roles in the structure and properties of the final products. In the sol–gel process metal alkoxide precursors are used which can vary in type depending on the metal and side groups named as ligands. The general form of a metal precursor is $M(OR)_x$ where M can be a silicon, titanium, aluminum or a transition metal, R is an alkyl group, and x is the number of alkoxide groups that the metal can have which determines the functionality and molecular conformation of the precursor [1–2]. The most common alkyl groups are methyl and ethyl groups, attached to the tetra–functional silicon atom. Thus, tetraethoxysilane (TEOS) and tetramethoxysilane (TMOS) are the most well known silica aerogel precursor compounds having the molecular formulas of $Si(OC_2H_5)_4$ and $Si(OCH_3)_4$, respectively. Figure 3 displays the molecular structures of TEOS and TMOS precursors.

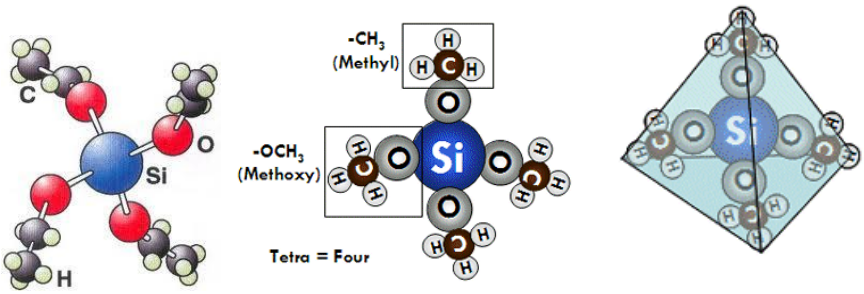

Figure 3 Molecular structures of TEOS and TMOS, respectively.

The silicon atom has four alkoxide groups tetrahedrally attached to it, making it tetra–functional. The four alkoxide groups are evenly spaced in three dimensions, resulting in a cancellation of dipole moments, thus resulting in a non–polar structure and immiscibility with water. Therefore, in order for hydrolysis reactions to take place, a need for a co–solvent arises with which both the precursor and water are miscible. The commonly used co–solvents are the alcohols of the alkyl groups attached to the silicon, thus ethanol and methanol for TEOS and TMOS, respectively. The co–solvents provide good miscibility and homogenous mixing of the precursor and water for hydrolysis reaction [1–2,9]. Furthermore, acid or base catalysts are widely used in order to accelerate the hydrolysis and condensation reactions. Figure 4 displays a typical sol–gel route for silica aerogel production with two step acid–base catalysis. Understanding the underlying chemistry of the sol–gel process is necessary for the development of the aerogel hybrid materials. The following subsections provide such detailed information about each step of the sol–gel process.

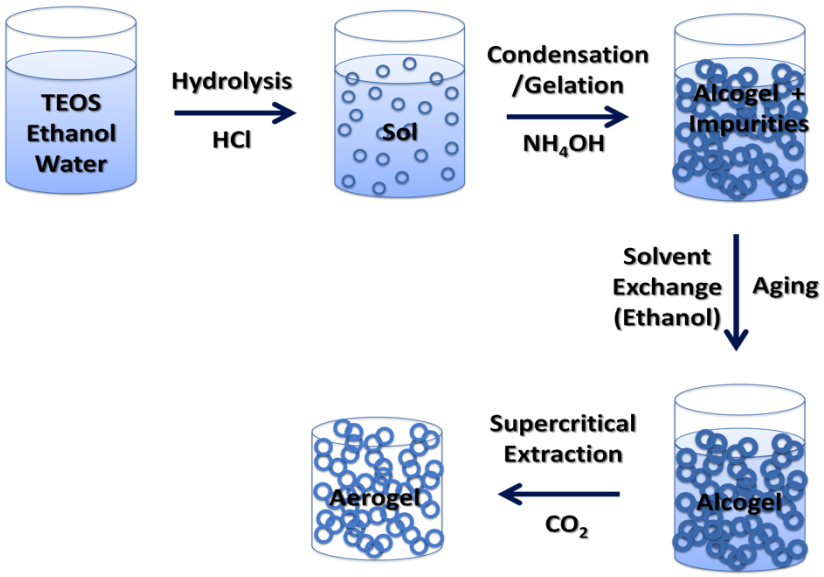

Figure 4 Two step acid–base catalysis of silica aerogels.

2.1.1. Hydrolysis

Hydrolysis is the initial step of the sol–gel process which involves basically the hydrolysis of the metal precursor, replacing the alkoxide groups (OR) with hydroxyl groups (OH). As mentioned above, the addition of the co–solvent enables the formation of a homogenous mixture of the precursor and water thus facilitates the hydrolysis reaction of the precursor

molecule [1]. A general hydrolysis reaction scheme for a tetra–functional silica precursor is displayed in Figure 5.

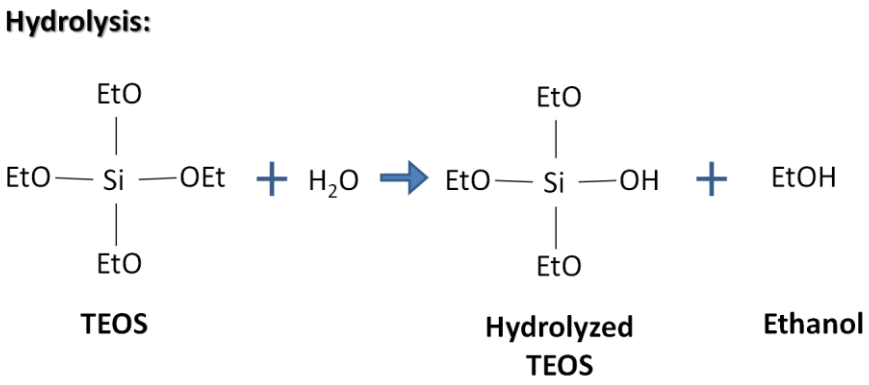

Figure 5 Hydrolysis reaction scheme for TEOS.

The hydrolysis reaction occurs by nucleophilic attack of the oxygen contained in water on the silicon atom. This nucleophilic attack includes bimolecular nucleophilic displacement reactions involving penta–coordinate intermediates or transition states [1]. The rate of the hydrolysis reaction as well as the condensation reaction is intensively pH dependent which can be observed from Figure 6 given below [4]. Strong pH dependency of the hydrolysis reaction evokes utilization of catalysts in order to achieve rapid and complete reaction. Depending on the catalysts used, the hydrolysis reactions can be attained in two different ways; acid and base catalyzed hydrolysis.

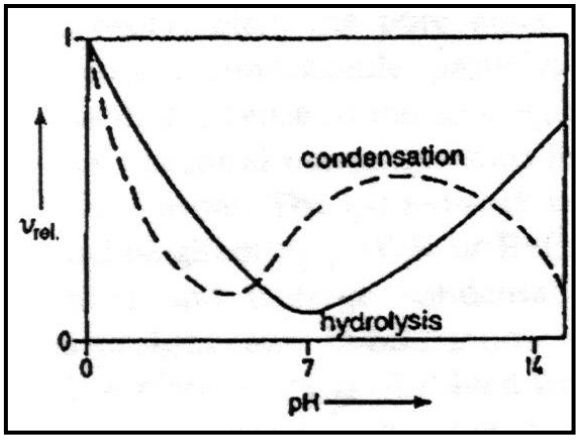

Figure 6 pH dependencies of hydrolysis and condensation reaction rates [4].

The rate and extent of the hydrolysis reaction is mostly influenced by the strength and the concentration of the acid or base catalyst utilized. It was reported that the mineral acids are more effective catalysts than equivalent concentrations of base catalysts [1].

Besides pH and type of catalyst, the hydrolysis reaction is also influenced by steric and inductive effects, water to silicon ratio, and solvent effects. Steric factors exert the greatest effect on the hydrolytic stability of the precursor. The hydrolysis rate is mostly lowered by bulky, branched alkoxide groups, which explains the retarded hydrolysis of TEOS compared to TMOS. Moreover, although the increased water to silicon ratio seems to promote hydrolysis, this increase reduces the condensation reaction rate thus causing an increase in the gelation time since water is also the by–product of the condensation reaction. On the other hand, the type and physicochemical properties of the solvent used such as polarity, dipole moment, and viscosity are important as the solvent control the concentrations of silicate and water that influence the gelation kinetics [1,9].

2.1.2. Condensation

Condensation is basically a polymerization reaction of hydrolyzed/unhydrolyzed silica precursor species to form siloxane bonds. This polymerization reaction can occur in two different ways, depending on the type of the product. In alcohol producing condensation reaction an unhydrolyzed precursor molecule reacts with a hydrolyzed molecule, leading to a leaving alcohol group. On the other hand, water producing condensation reaction occurs by the reaction of two hydrolyzed precursor molecules [1–2]. The reaction schemes of these two different condensation reactions are given in Figure 7.

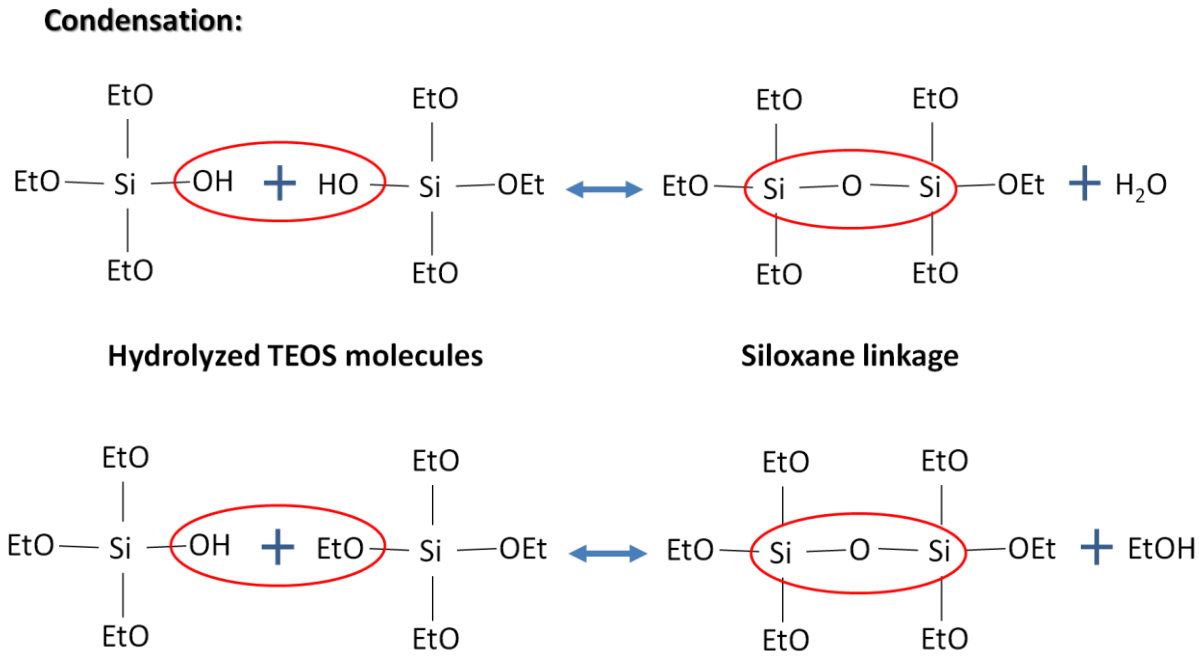

Figure 7 Alcohol and water producing condensation reactions.

Condensation step is the most complicated step of the sol–gel process as all the reactions are reversible and occur simultaneously. Condensation is initiated during hydrolysis thus, generally the siloxane bond formation starts before the hydrolysis reactions are completed, which makes it even more complicated [1]. Similar to hydrolysis, condensation reactions also have a strong pH dependency which can also be observed from Figure 6. According to Figure 6, there are two types of condensation reactions; acid and base catalyzed, although condensation of silanols can proceed thermally without involving catalysts. The overall condensation rate is minimized at about pH 1.5 and maximized at intermediate pH values [1,4].

Condensation preferentially occurs between more highly condensed species and those less highly condensed and somewhat neutral. This suggests that the rate of dimerization is low, however, once dimers form, they react preferentially with monomers to form trimers, which in turn react with monomers to form tetrameters. Further growth occurs by addition of lower molecular weight species to more highly condensed species and aggregation of the condensed species to form chains and networks [1].

The condensation reaction kinetics is influenced both by steric and inductive factors. Reduced steric crowding in the transition state or on intermediate molecules enhances the condensation kinetics, whereas the bulky groups attached to silicon retard the process. Furthermore, the type of the solvent used is also effective in condensation kinetics similar to hydrolysis [1].

The type of the catalyst used during hydrolysis and condensation reactions has a great influence on the microstructure of the solid network. For acid catalyzed reactions an open network structure results initially, followed by further hydrolysis and co–condensation reactions. On the other hand, in base catalyzed reactions highly cross–linked large sol particles are initially obtained which eventually link to form gels with large pores formed between the interconnected network particles [1,4–5]. Gel structures for acid and base catalyzed reactions are displayed in Figure 8.

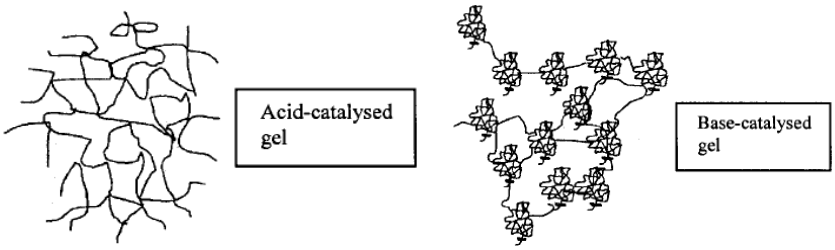

Figure 8 Gel structures for acid and base catalyzed reactions [5].

The reverse reactions of alcohol and water condensation of siloxane bonds (alcoholysis and hydrolysis) provide bond breakage and re-formation allowing continual restructuring of the growing polymers. These reverse reactions also have pH dependency similar to condensation reactions and they have determinant role in re-distribution of siloxane bonds and structuring of the solid network [1].

2.1.3. Gelation

Gelation occurs when links form between colloidal sol particles that are produced as a result of hydrolysis and condensation reactions. These links occur to such an extent that a giant spanning cluster reaches across the containing vessel. At this point, although the mixture has a high viscosity and it does not pour when the vessel is tipped, many sol particles are still present as entrapped and entangled species in the spanning cluster. This initial gel has a high viscosity but a low elasticity. There is no endotherm or exotherm, nor any discrete chemical charge at the gel point, only the sudden increase in viscosity can be observed which is illustrated in Figure 9 [1].

Following gelation, further cross–linking and chemical inclusion of isolated sol particles into the spanning cluster continues, leading to an increase in the elasticity. The gelation time is basically used as a measure of the overall condensation kinetics as it is inversely proportional to the average condensation rate [1].

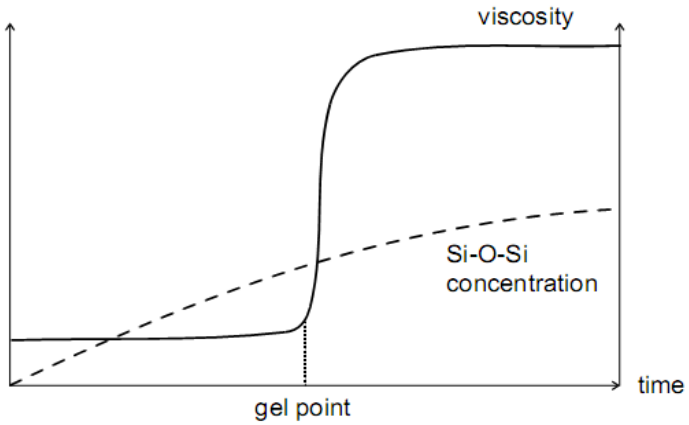

Figure 9 Evolution of viscosity and Si–O–Si as a function of time.

2.1.4. Aging

After gelation occurs, the gelled samples, so called alcogels or wet gels, are aged in appropriate solutions. Since the cross–linking of the network and structure evolution continues after the gel point, aging is also a critical step of the sol–gel process. Aging process can be controlled by varying the pH, temperature, pressure, and composition of the liquid aging medium, and may thus be optimized. During aging, the structure and properties of the alcogels are chemically and physically improved via evolutionary processes such as cross–linking, syneresis, coarsening, ripening, and phase transformations [1,4–5].

During aging, a continuing gradual increase in the number of Q^3 and Q^4 species (silicon attached via four oxygen links to three and four other silicon atoms) was observed with NMR studies, due to cross–linking via condensation reactions of surface hydroxyl groups in the pores. The net effects of these processes are stiffening and shrinkage of the alcogel. Shrinkage occurs because new bonds are formed instead of weak interactions between the surface hydroxyl and/or alkoxide groups. This shrinkage leads to expulsion of the liquid from the pores of the gel, which is termed as syneresis [1]. However, syneresis can occur only in small pores with diameter in the order of two hydroxyl or alkoxide molecular diameters. For larger pores, these surface groups wouldn't be at an appropriate distance to interact with each other. Figure 10 illustrates syneresis during aging step of the sol–gel process.

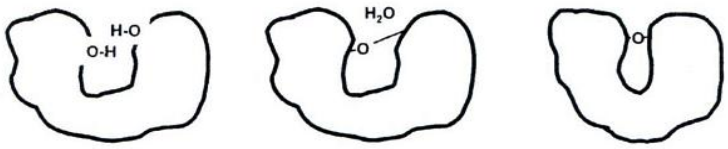

Figure 10 Syneresis during aging.

In coarsening and ripening, material dissolves from the surface of large particles and deposits on the initially narrow "necks" which join particles to each other. These processes strengthen the solid as well as leading to some evolution in pore sizes and shapes [1]. A schematic representing the coarsening and ripening processes is illustrated in Figure 11.

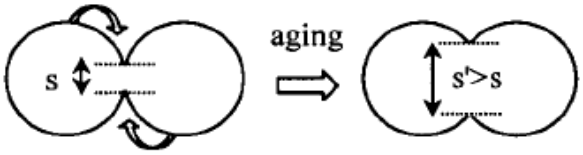

Figure 11 Coarsening and ripening during aging.

The final aging effect may be in the form of phase transformation. When gelation occurs very quickly or several precursors of different miscibility with water are used, the porous alcogel may contain isolated regions of unreacted precursor. On prolonged soaking in aging medium, this material may react either completely or partially giving inclusions of material of different structure and composition [1].

2.1.5. Drying

Drying is basically the removal of the liquid from the pores by replacing it with air and is one of the most important steps of the sol-gel process. Due to the nanoporous structure of the gels produced, drying is usually problematic since the removal of the filler liquid disrupts the pore structure leading to modified material properties. The destruction of the pore structure during drying occurs because of the capillary stresses produced in the pores due to the liquid-gas phase boundary. This can lead to changes in pore size and shape, collapse of the pores, even cracks in the macroscopic gel structure. This corruption is more significant in smaller pores since the resulting capillary stresses are inversely proportional to the pore size [1,4–5]. Thus ambient drying of the alcogels which is basically the evaporation of the liquid from the pores causes remarkable shrinkage and enormous change in gel structure. The capillary pressure effect which occurs during ambient drying is illustrated in Figure 12.

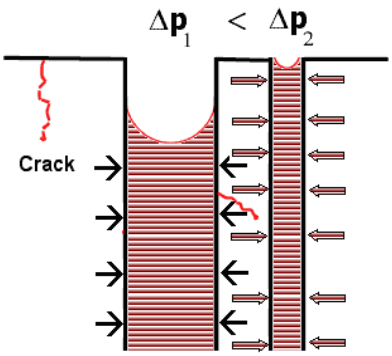

Figure 12 Capillary pressure formed in the small pores during ambient drying.

In addition to ambient drying, freeze drying can also be used which is a more efficient technique than the ambient drying since the liquid-gas phase boundary is avoided in freeze drying. In freeze drying, the crystallization of the pore liquid is accomplished by rapid cooling and the liquid crystals are drained from the pores via vacuum. However, one disadvantage of freeze drying is that it requires long aging periods. Supercritical drying is the most efficient

and harmless technique eliminating the phase boundary in the pores, and thus capillary stresses. The wet gel having - most commonly - alcohol inside the pores, is contacted with the solvent in the supercritical state. Upon this contact the pore fluid is dissolved in the supercritical fluid forming a single phase binary mixture. The pore fluid is drained from the pores by continuous flow of fresh supercritical fluid. Finally, the system is depressurized resulting in a gaseous phase inside the pores. Since no phase boundary is experienced throughout the process, the removal of the pore fluid is accomplished without damaging the aerogel structure [4–5]. Being relatively nontoxic and cheap, CO_2 is the most widely utilized solvent in supercritical drying processes, due to its good solvation power for alcohols, since the pore liquid is usually an alcohol in the sol-gel process. Additionally, CO_2 has mild critical conditions with a critical temperature of 304 K and a critical pressure of 74 bar which can easily be attained.

2.2. Structure and Properties of Silica Aerogels

Silica aerogels are highly porous materials, consisting of up to more than 99% air and less than 1% silicon dioxide. Aerogels were first created by Samuel Stephens Kistler in 1931 from a gel by replacing the liquid part with gas [1–2]. Among various organic and inorganic aerogels, silica aerogels are the most widely studied and utilized type of aerogels. They are amorphous materials having a disordered molecular structure with tortuous paths through their solid network [1]. Silica aerogels are mesoporous materials having pores in 2 - 50 nm size range. The solid skeleton of silica aerogels are composed of so-called secondary silica particles with sizes 5-10 nm that are arranged like random beads on a string. These secondary particles are built up from primary silica particles which are formed from non-porous, dense silica. The air-filled voids between the secondary particles are the so-called pores having widths at nanometer scale. Figure 13 and Figure 14 display the structure of silica aerogels in nano-scale. Silica aerogels possess unique properties that are listed in Table 1, most of which arises because of their highly porous structure [3–7]. For instance, due to their high porosity they have extremely high specific surface areas and low densities such that they are one of the lightest solid materials derived so far. Furthermore, they have a monolithic structure meaning that they can be produced in any shape and size. Another important property of silica aerogels is their transparency. The light scattering property of aerogels varies basically with the solid network and pore structures which can be tuned during synthesis with the type of precursors, composition of the components, and processing conditions such as temperature. Hence, transparent, translucent or opaque aerogels can be obtained for specific applications by

changing the aforementioned variables [2]. Aerogels are materials that have the lowest thermal conductivity values of any solid known so far. They have thermal conductivities even lower than still air. Typical thermal conductivity values of silica aerogels vary in the range of 0.010–0.020 W/mK at ambient conditions [3–7]. Due to this unusual thermal property, silica aerogels gained tremendous interest in thermal insulation applications. The fundamental reasons for the low thermal conductivity of silica aerogels are described in the following section.

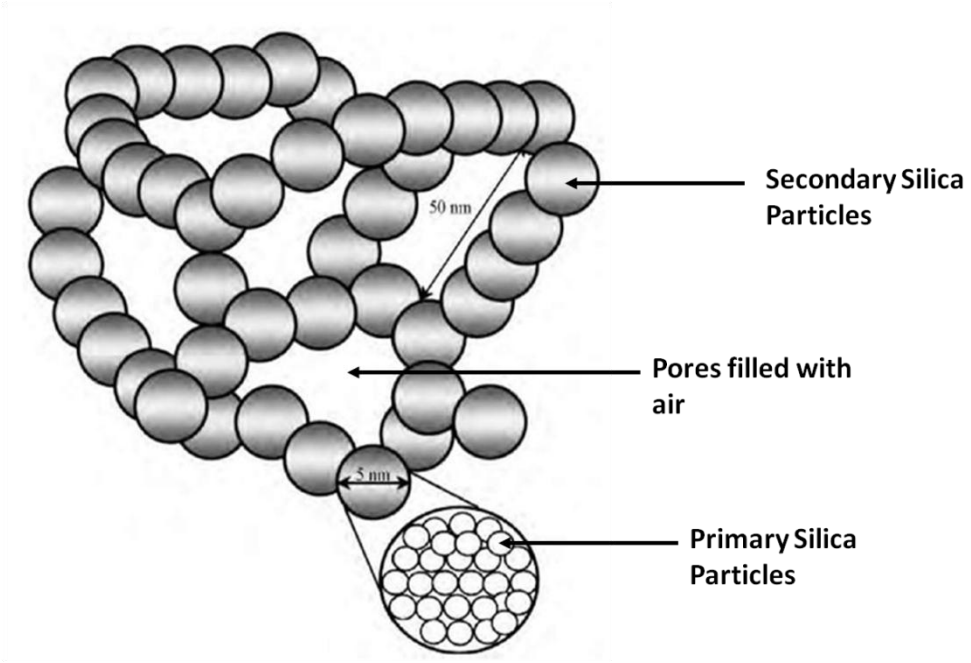

Figure 13 Structure of silica aerogels at nanometer scale

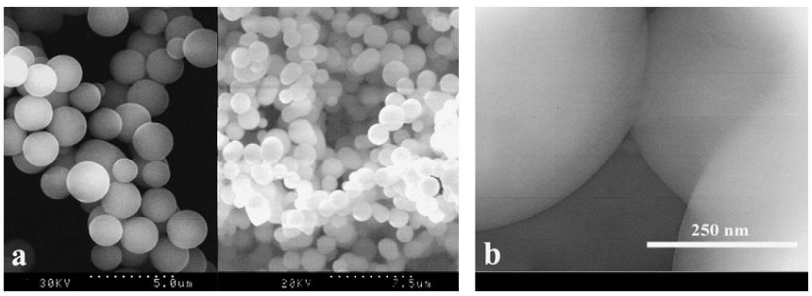

Figure 14 (a) SEM and (b) TEM images showing the pore characteristics of silica aerogels.

Table 1 Properties of silica aerogels.

Property	Value	Comment
Density	~0.003g/cm^3	One of the lowest density solids [8]

Porosity	80–99.8%	High porosity [8-9]
Surface Area	500–1200 m^2/g	Determined by Nitrogen Adsorption/Desorption (BET) [8-9]
Mean Pore Diameter	20–150 nm	Mostly in mesoporous range [8]
Thermal Conductivity	0.017–0.021 W/m.K	High thermal insulation property[8-9]
Thermal Tolerance	Up to 500 ^oC	Shrinkage starts at 500^oC and increases with temperature. Melting point is 1200 ^oC [10]
Dielectric Constant	1.0–2.0	Low for a solid material [8]
Sound Velocity	100 m/s	One of the lowest velocities for a solids[8]
Poisson's Ratio	0.2	Independent of density, similar to the dense silica [10]
Young's Modulus	0.002–100 MPa	Very small compared to dense silica (10^4MPa) [9]
Index of refraction	~1.05	Low for a solid material [8]
Optical Property	> 90%	Transmittance Measurement at 630 nm [10]

One of the most important features of silica aerogels is that their properties can be tailored for specific applications and thus silica aerogels have enormous number of application areas expanding day by day such as acoustic insulation, catalyst support, optical applications, low dielectric constant materials, batteries, etc [8]. Despite having numerous fascinating properties, silica aerogels have one inadequate characteristic: they are highly brittle materials unable to endure mechanical loads, which cause difficulties in processing and handling, and thus limit their widespread use in various application fields. Due to the weak interactions between the components of the solid silica network, aerogels are very fragile materials inadequate to bear even small amount of mechanical loading. Therefore, even small cracks in the microstructure damages the whole structure and makes production of monolithic and crack–free silica aerogels highly challenging. However, these problems can be overcome by reinforcing silica aerogels with polymers in such a way that monolithic, crack-free silica aerogels with improved mechanical properties can be obtained. Some of the notable studies that attempted to develop silica aerogel composites with polymers are explained in Section 2.4.

2.2.1. Heat Transfer in Aerogels

As stated previously, aerogels have gained special attention in the insulation applications due to their superior insulating properties compared to conventional insulation materials.

Therefore, the heat transfer phenomenon through aerogels has become a crucial topic for most of the scientific studies as well as industrial applications. Some porous materials with appreciably low thermal conductivities are listed in Table 2. Unlike continuous and single phase materials, heat transfer is more complicated in aerogels, since the means of energy transportation is altered according to the highly porous structure, and thus the classical heat transfer theory is generally insufficient to be applicable. Understanding the fundamentals of the transfer of heat in aerogels necessitates a detailed knowledge about the structure of the material as well as how the porous structure affects the heat transfer mechanisms. In this section, different mechanisms of heat transfer in aerogels will be reviewed and the effects of structural parameters on these mechanisms will be briefly discussed.

Table 2 Thermal conductivities of some porous insulation materials at room temperature.

Material	Thermal Conductivity (W/mK)
Molded Polystyrene	0.034 [11](ρ = 19 kg/m^3)
Extruded Polystyrene	0.032 (ρ = 28 kg/m^3)
Injected Polystyrene	0.034 (ρ = 20 kg/m^3)
Polyurethane board	0.023 (ρ = 28 kg/m^3)
Glass fiber	0.035 (ρ = 30 kg/m^3)
Rock wool	0.042 (ρ = 50 kg/m^3)
Lightweight concrete	0.120 [11](ρ = 551 kg/m^3)
Silica Aerogel	0.016 (ρ = 100–130 kg/m^3)
Resorcinol Formaldehyde Aerogel	0.012 (ρ = 157 kg/m^3)
Polyurea Aerogel	0.019 (ρ = 118 kg/m^3)

2.2.1.1. Mechanisms of Heat Transfer in Aerogels

The thermal insulation performance of a material is evaluated by its effective thermal conductivity. Therefore it is crucial to be able to determine the total or effective thermal conductivity of aerogels [12]. Thermal conductivity of a material is extracted by solving the energy equation throughout the material however there have been various correlations developed so far to obtain the thermal conductivity value in a more simplistic way.

The three major mechanisms by which heat can be transferred are conduction, convection and radiation. However, for porous materials such as aerogels some of the components that

contribute to each of these mechanisms differ from that of homogenous media. For instance, the flow of the gas molecules within the pores is suppressed due to the fine pore sizes (2–50 nm) of aerogels. Therefore, at ambient pressure, the contribution from convection approaches to negligible values for the structures composed of pore sizes smaller than 1 mm [13]. As a result, convection is not pronounced for aerogels. For the case of conduction, the transfer of heat is achieved by phonon conduction of the solid matrix and the gas phase conduction that emerges due to the collisions between the gas molecules and the pore walls. Heat transfer by radiation is mainly attained by the scattering from the interfaces and the grain boundaries. Figure 15 displays the schematic representation of different mechanisms of heat transfer in a porous material which is built up of interconnected pores. All of these mechanisms are considered to apply simultaneously that can be realized as parallel resistances in a circuit; therefore the total thermal conductivity in aerogels is given as the sum of the aforementioned terms:

$$\lambda_{total} = \lambda_{solid\ conduction} + \lambda_{gaseous\ conduction} + \lambda_{radiation} \quad (2.1)$$

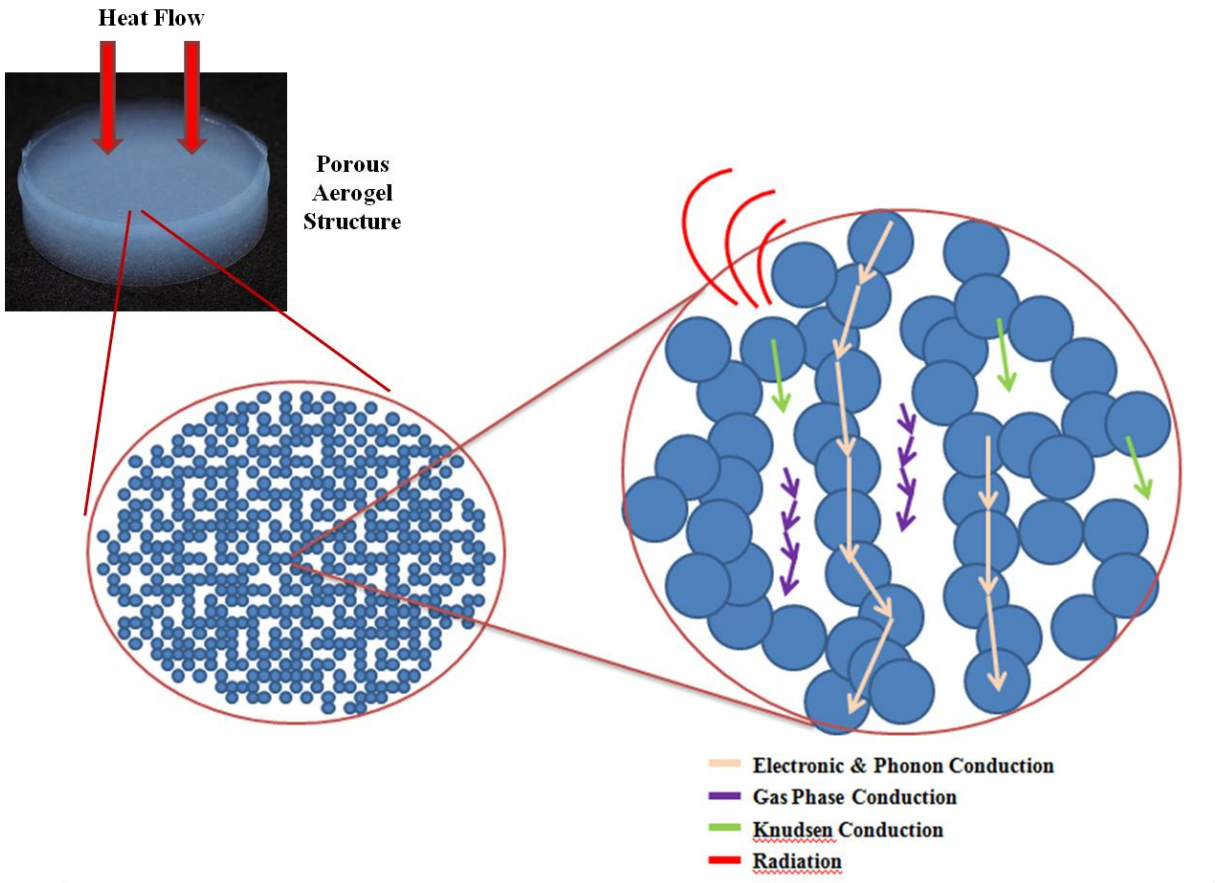

Figure 15 Heat transfer mechanisms in a porous media.

2.2.1.2. Solid Conduction

One of the terms that contribute to heat transfer by conduction is the solid conduction which strongly depends on the structural parameters of the material such as density, porosity and the intrinsic conductivity of the material that build up the solid network. The solid conductivity term for a porous material can be given with a simple model by [14]:

$$\lambda_s = \frac{1}{3}\lambda_{s^o}\left(\frac{\rho}{\rho_0}\right) \tag{2.2}$$

where λ_s is the solid conductivity, λ_{s^o} is the intrinsic conductivity of the nonporous network material, ρ and ρ_0 are densities of porous and nonporous forms of the material, respectively. Fricke et.al. [15] and Hrubesh et.al. [16] derived a similar formula from kinetic theory to be implemented for aerogels:

$$\lambda_s = \lambda_{s^o}\left(\frac{\rho_{aerogel}}{\rho_{SiO2}}\right)\left(\frac{v_{aerogel}}{v_{SiO2}}\right) \tag{2.3}$$

where, $\rho_{aerogel}$ and ρ_{SiO2} are the density of aerogel and silica, $v_{aerogel}$ and v_{SiO2} are the longitudinal sound velocities in aerogel and bulk silica medium, respectively.

2.2.1.3. Gaseous Conduction

Another parameter that contributes to the conductive term of thermal conductivity is gaseous conductivity which is governed by the Knudsen equation [14-15, 17-19].

$$\lambda_g = \frac{\lambda_{g^o} V_g}{(1+\beta K_n)} \tag{2.4}$$

with, λ_{g^o} is the thermal conductivity of free air, β is a gas parameter that considers the energy transfer between the gas molecules and the solid matrix during the collisions (~2), V_g is the volume fraction of voids or porosity, and K_n is the Knudsen number. Knudsen number is a characteristic parameter for the transfer of heat in porous media which describes the flow of gas molecules. For $K_n \gg 1$, the gas molecules are considered to obey the Knudsen flow in which they collide mainly with the pore walls rather than each other. On the other hand, for $K_n \ll 1$, gas molecules behave like liquid, and thus they frequently collide with each other [13]. Knudsen number is a function of the mean free path of the gas molecules, l_g, and the pore diameter, ϕ, with the following equation [14-15, 17-19].

$$K_n = \frac{l_g}{\phi} \tag{2.5}$$

The mean free path term depends on the temperature and pressure, and at ambient conditions it has a value of 60–70 nm for air. The highly porous structure of aerogels confines the gas molecules within the pores since the average pore size is in a comparable range with the mean free path of the gas molecules (2 to 50 nm). With this confinement, the collisions between the gas molecules are restrained due to their restricted motion which results in a reduced K_n. Therefore, the gaseous thermal conductivity is greatly reduced with fine pore sizes and solely comprises the gas molecule–solid collisions, which is known as the Knudsen effect [13, 15, 17-19].

2.2.1.4. Radiation

For most materials, the heat transfer by radiation is generally ignored and its contribution to the total thermal conductivity is neglected in the models. However, radiation term becomes dominant at high temperatures. The contribution of radiation is also significant for porous materials since it is affected by the scale of the pore structure and scattering by the interfaces and the grain boundaries [20]. For optically thick materials, the heat transfer by radiation is considered to be a local phenomenon and can be regarded as a diffusion process through a homogenous medium. Under these circumstances, the radiative conductivity is governed by the following formulation based on the Rosseland approximation [14, 19, 21-22].

$$\lambda_r = \frac{16}{3}\frac{\sigma n^2 T^3}{\rho e(T)} \tag{2.6}$$

where, σ is the Stephan–Boltzmann constant, n is the refractive index, T is the absolute temperature, ρ is the density of the material and $e(T)$ is the mass–specific extinction coefficient which is obtained from the IR–optical measurements of spectral mass specific extinction coefficient.

2.2.1.5. Parameters Controlling the Thermal Conductivity

There are some important structural parameters that influence the thermal conductivities of aerogels according to the above equations. Among these parameters, porosity and density are the two prominent factors that are inversely related and can be converted to one another by using the formula given in Eqn. 2.9. Solid conductivity is directly related to the density and porosity in Eqn. 2.2. With this relation, it can be realized that with increasing porosity and

thus decreasing density, the amount of solid material is reduced, so is the solid conductivity of the material.

A more direct relationship between the density and solid thermal conductivity was established by Lu et.al. who proposed that the solid thermal conductivity scales with the density of the material with the following relation [15, 23];

$$\lambda_s = C\rho^{\alpha} \tag{2.7}$$

where the pre–factor C is expected to depend on the interconnectivity of the solid network and the scaling exponent, α, was found to be approximately 1.5 for both silica and carbon aerogels [15, 18, 21, 23-24].

From Eqn. 2.4. and 2.5. it can be realized that for average pore sizes of $\phi \gg 140\ nm$ the gaseous conductivity becomes solely a function of the porosity, since the second term in denominator of Eqn. 2.4. becomes negligible, and decreases when the porosity is decreased. However, for values $\phi \ll 140\ nm$ the second term in the denominator of Eqn. 2.4. cannot be neglected. Indeed, it becomes dominant as the pore size decreases. Therefore, the gaseous conductivity depends on both the porosity and the average pore size for that pore size range. In that case, the reduction of gaseous thermal conductivity can be accomplished by reducing both the porosity and the pore size [17]. The important point is that porosity can be decreased by increasing the solid network content which in turn raises the solid thermal conductivity contribution. On the other hand, decreasing the pore size does not have such an adverse effect, hence the most effective way to reduce the thermal conductivity is considered to be the synthesis of aerogels with very fine pore sizes [17]. It is obvious from these considerations that the material density strongly affects the gaseous thermal conductivity term owing to its direct relation to the porosity. In order to elucidate this effect, in 1992 Hümmer et.al. conducted thermal conductivity experiments with aerogels having definite densities, and proposed the below correlation [15, 24-25].

$$\lambda_g = K\rho^{-0.6} \tag{2.8}$$

with parameter K considering the material properties.

It is clear with Eqn. 2.7. and 2.8. that, the solid and gaseous thermal conductivities have different dependencies on the material density. Hence the total thermal conductivity is

affected by material density according to a combinatorial effect of solid and gaseous thermal conductivities which is shown in Figure 16.

Besides the structural parameters, temperature and pressure also have influence on the thermal conductivity. Temperature dependency of the total thermal conductivity majorly arises from the radiative contribution, especially for the materials where the heat transfer by radiation plays a significant role. This dominant dependency can be realized from the third power of the temperature term in Eqn. 2.6. [26]. The mass–specific extinction coefficient in the denominator of Eqn. 2.6. also has a temperature dependency, which becomes negligible when compared to the temperature term in the numerator. Moreover, temperature affects the mean free path of the gas molecules that is employed for the calculation of the Knudsen number in Eqn. 2.5. The relation between the mean free path and temperature in fact originates from the kinetic theory of gases and the formulation can be found elsewhere. Combination of all of these effects results in a complex temperature dependency of the total thermal conductivity [27]. For optically thick materials such as carbon aerogels, the effect of the temperature increase on total thermal conductivity is insignificant due to the small contribution of the radiative term. However, for silica aerogels the contribution of the radiative term becomes significant and thus the temperature dependency of the total thermal conductivity.

Pressure is another determinant parameter for the total thermal conductivity, as the contribution of gaseous conduction is also influenced by pressure, since the mean free path of the gas molecules depends on pressure, as well, from the kinetic theory of gases.

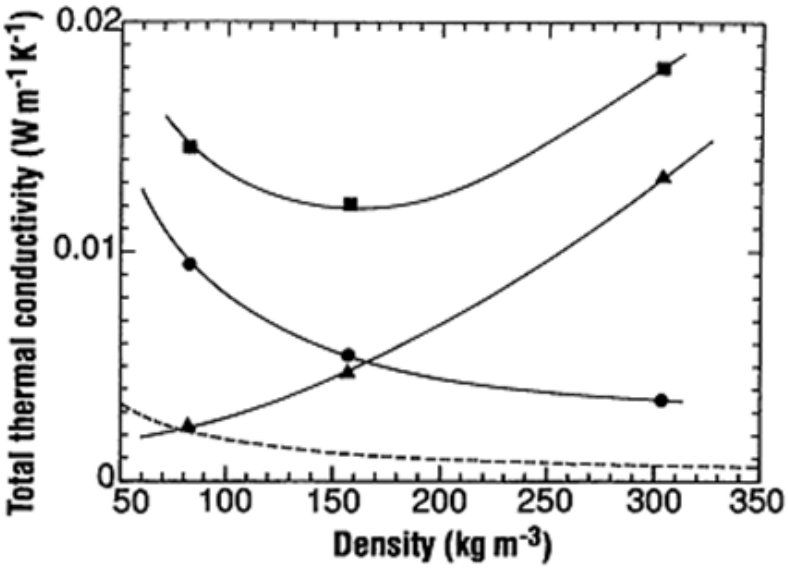

Figure 16 Variation of total thermal conductivity, λ_t (■), calculated radiative thermal conductivity, λ_r (——), gaseous conductivity, λ_g (●), and solid conductivity, λ_s (▲) of Risolcinol Formaldehyde (RF) aerogels with density [38].

With the above considerations, it can be realized that the density of the aerogel is the major parameter that controls the total or effective thermal conductivity. It has a determinant role for the amount of gas molecules inside the pores and thus the gaseous conductivity due to the direct relation with the porosity of the aerogel. Different mechanisms of heat transfer that contribute to the total thermal conductivity exhibit different dependencies on density. The solid conduction term increases with increasing density, since increasing density implies additional solid content. On the other hand, increasing density causes a reduction of gaseous conduction term owing to the decreasing porosity. Entire of these coupling effects yield in a complex behavior of total thermal conductivity which is depicted in Figure 16.

2.3. Composites of Silica Aerogels

One way to improve the mechanical properties of silica aerogels is the development of composites with polymers which can be achieved by somehow incorporating an organic or inorganic polymer into the silica framework. Some of the recent studies on polymer-silica aerogel composites reported so far, utilized trialkoxysiyly terminated polyoxyethylene (POE) [12–13], poly(vinylalcohol) (PVA) [14–15], poly(hexamethylene di–isocyanate) (di–ISO) [16–17], polymethylcyano acrylate, polyvinylacetate (PVAc) [15], polymethylmetacrylate (PMMA) [15], polypropylene oxide (PPO) [15], polyethylene–polyethylene glycol (PEPEG) [18], polydimethysiloxane (PDMS) [12, 19–21], and polymethylhydrosiloxane (PMHS) [22] as the polymer phase. In the synthesis of silica aerogel-polymer hybrid materials there are several critical factors such as polymer-to-precursor ratio, chemical structure of the polymer, chain length of the polymer, the stage that the polymer is incorporated into the silica aerogel, duration of treatment, temperature and pressure which affects the final product characteristics.

There are different routes that can be followed for the incorporation of a polymer into the aerogel structure. One way is to add the polymer to the sol mixture before the gelation occurs, i.e. during the hydrolysis or condensation steps of the sol-gel process. Composites of silica aerogels with poly(2-vinylpyridine) [28], syndiotactic polystyrene (sPS) [29] and polyethylene glycol (PEG) [30] constitute some examples to this technique where the gelation of the precursor molecules occur in the presence of the polymers chains. By this way, the polymer chains are distributed between the silica particles which make-up the network resulting in a composite material with a silica phase and a polymer phase.

An alternative route involves the reaction of the polymer molecules with the surface groups of the silica aerogel which is carried out after the formation of the solid gel network. The hydroxyl groups of the native silica aerogel surface can in principle participate in such reactions. A more commonly used method is to functionalize the aerogel surface with specific chemical groups. The surface functionalization procedure can be performed during the synthesis by adding the appropriate agents into the reactant mixture, or can be carried out as a post-gelation treatment by utilizing surface –OH groups of the already formed silica network. Once attached, the functional surface groups constitute active sites for further reactions and are used for the attachment of the polymers. Thus far, there have been many studies on the modification of the silica aerogel surface with various silane based compounds having different functionalities. For instance, amine groups have been introduced to the silica aerogel surface by co-condensation of TEOS or TMOS with bis(trimethoxysilylpropyl)amine (BTMSPA) [31], and 3-aminopropyltriethoxysilane (APTES) [32-34]. These amine groups have further been employed for the reactions with isocyanates to yield a coating of polyurea on the aerogel surface. As an alternative method for the coating of the silica network with polyurea, the surface –OH groups have been directly employed after the gelation step for the binding of di- or tri- isocyanates [35-36]. Additionally, amine functionalized silica gel surfaces have also been reacted with different epoxy compounds to yield epoxy reinforced materials [32-33, 37]. In all these cases, the polymers coat the surface of the silica particles which make up the silica aerogel network. Such conformal coatings were also achieved with polycyanoacrylates [38-40], polystyrene [34, 41-43], polymethylmethacrylate [44] and polyvinyl alcohol [45] by utilizing native or functionalized gel surfaces.

As a third alternative, polymers can be added to the reactant mixture during the synthesis and can directly participate in the co-condensation reactions with the hydrolyzed precursor molecules. This method requires specific polymers that can undergo co-condensation reactions with –OH groups of the hydrolyzed silane precursors. PDMS with hydroxyl end groups (PDMS(OH)) is one of the rare polymers that can participate in such reactions. Kramer *et.al.* synthesized a composite of PDMS(OH) with silica aerogel for the first time by reacting the polymer with the hydrolyzed TEOS molecules [46]. After the supercritical extraction of ethanol from the pores, an aerogel composite also termed as “aeromosil” was obtained. The aeromosil had a polymer content up to 20 wt% with improved mechanical properties, however had an opaque appearance. Being a water-insoluble polymer, PDMS is quite incompatible with the conventional sol mixture (ethanol, water and TEOS) for synthesis of

silica aerogels and the addition of the polymer into this mixture causes immiscibility. The immiscibility between the polymer molecules and the sol mixture results in composites with two different phases; silica gel network and polymer aggregates. The clusters of polymer molecules form additional scattering centers in the aerogel and thus lead to opaque materials. Eventually non-homogenous composites are formed with poor optical properties [47-48]. This incompatibility can be overcome somewhat by eliminating the water from the reactant mixture. Following a similar route, Jespersen *et.al.* produced aeromosils having up to 75% PDMS(OH) content by direct synthesis in $scCO_2$ without any water [49].

So far, PDMS(OH) as well as epoxy–PDMS have been extensively studied in sol–gel process. Most of these studies correspond to incorporation of PDMS into the xerogels which are sol–gel products obtained with ambient drying. There are only few studies associated with the PDMS–incorporated silica aerogels. In the study of de la Rosa–Fox *et al.,* PDMS(OH)/TEOS aerogels were derived via high–power–ultrasound–assisted reactions and the mechanical behavior and modifications made to the microstructure were investigated. Their results revealed phase separation between the tough silica matrix and the elastic polymer chains. They also observed micro cracks in the pores of the synthesized composites [19]. The phase separation probably originated from the lack of co–solvent usage in their synthesis procedure. The effect of co–solvent is dramatic in sol–gel synthesis since it enables homogenous mixing of the precursor, water and PDMS, and thus prevents phase separation. In another study, Luis Esquivias *et al.* synthesized OH–PDMS/TEOS aerogels to study the bioactivity of these hybrids. They used ultrasound mixing in order to ensure homogenous mixing of the solution, avoid cyclidation of chains and increase its cross linking. However, they also observed heterogeneities in their structures and low branched network [20]. Similar to the previous study, these heterogeneities were probably caused by the lack of co–solvent during the synthesis. Moreover, the composites they synthesized had a molar ratio of TEOS/DMS=1.05 which corresponds to a very high polymer content. It was reported in xerogel studies that when the polymer content is increased above the molar ratio of TEOS/DMS=2.5, achieving a homogenous mixture of precursor and polymer becomes harder, and thus the phase separation is inevitable. In all the aforementioned studies ethanol was used as the supercritical drying medium.

A significant contribution in this area was carried out by ASPEN aerogels. They synthesized OH–PDMS as well as epoxy–PDMS–based aerogels and investigated the transparency, shrinkage, thermal conductivity and mechanical properties of the derived composites. They

utilized a partially hydrolyzed silica source as a precursor and HF as acid catalyst. They performed two different synthesis procedures; one was carried out at room temperature and the other was at 70 ^{o}C. They examined the effects of processing routes, aging solution, PDMS ratio, and PDMS molecular weight on the aforementioned properties of the derived composites. Higher density aerogel hybrids made with OH–PDMS and epoxy–PDMS showed higher maximum flexural strengths and strains than pure silica aerogels due to the effects resulting from bonding between PDMS and the silica precursor. However, for composites with higher molecular weight PDMS, they observed a decrease in flexural strain due to phase separation between PDMS and the silica precursor, caused by the lower solubility of PDMS. Additionally, with increasing molecular weight of PDMS, the transparency of the hybrids decreased, although the thermal conductivity value didn't have a remarkable alteration compared to the pure silica aerogel [12].

A novel route that can be followed for the processing of composites of silica aerogels is the *Reactive Supercritical Deposition Technique (RSCD)* with $scCO_2$. One requirement for this technique is that, the polymer that is used in the development of composites should be soluble in $scCO_2$. Among others, silane-based compounds are known to have appreciable solubilities in $scCO_2$ [50-54]. In fact, thus far many silane-based agents dissolved in $scCO_2$ have been extensively employed in surface modification applications, the name of the technique being *Silylation from* $scCO_2$. In addition to silane-based compounds, substantial solubilities of silane-based polymers in $scCO_2$ allow for exploitation of silylation to develop composites of silica aerogels.

2.4. Silylation from Supercritical CO_2

Surface modification is frequently used in many fields to bring new physical, chemical and/or biological characteristics to the surfaces. Different methods can be employed for the modification of surfaces to alter a wide range of functional properties such as roughness, hydrophilicity, surface charge, surface energy, electronic, magnetic, mechanical properties, corrosion resistant properties, biological functionality and reactivity. One prominent requirement for the surface modification applications is the uniformity of the introduced characteristics throughout the surfaces or at a desired region in the case of graded surfaces, which can be accomplished merely by a controlled process. However, achieving homogenous surface characteristics after the modification is the biggest challenge for the conventional techniques. $scCO_2$ based techniques come into play when the control over the process is of

interest. It is well known that deposition or impregnation processes that were carried out using $scCO_2$ provides uniform distribution as well as easy control since the final material properties can be fine-tuned by simply adjusting the processing parameters such as pressure and/or temperature when $scCO_2$ processes are employed. More importantly, high solubilities of silane-based compounds in $scCO_2$ pave the way for silane-$scCO_2$ mixtures to be easily employed in surface modification. Thus far, such systems have been frequently utilized in several studies related to diverse research areas.

Being one of the most frequently employed surface modification techniques silylation is exploited to bring novel functionalities to the materials. Silylation agents are extensively utilized in paints and adhesives to improve transparency and adhesion to inorganic substrates, and to reduce viscosity [55]. They are also essential for semiconductor encapsulants and flat-panel displays in electrical applications. In the automotive sector, silylation is utilized for the development of silica reinforced tires, high molecular weight rubbers, highly weatherable paints and new types of materials. In addition, silylation agents are frequently used in energy applications to manufacture encapsulating resins for solar panels and hybrid materials for use in wind power systems. Recently, the utilization of silane reagents in construction sector gained increased attention. Silylation reagents were started to be used in paints and plasters to impose water repellant property and to improve the durability of exterior walls and infrastructure of buildings [55]. The diversity of the research and application areas as well as the properties that can be introduced to the materials demonstrates the role and importance of the silylation process nowadays.

Silylation is carried out by contacting a surface with a silane based reagent containing reactive groups that have the ability to form stable bonds with the organic and inorganic materials. During the contact, silane agents react with the surface groups which results in the attachment of silicon containing functional groups to the surface. There are conventionally two different routes that are followed for silylating a surface. First route is to expose the surface to the vapor of silane reagent at high temperatures [56]. One requirement for this technique is that the silylation agent should have a high vapor pressure at the working temperatures. Hence, the vapor phase treatment is limited to volatile organosilanes. The second route is the modification from the liquid phase which is performed by contacting the surface with a liquid solution of the silylation agent. This technique is usually employed at low temperatures which can be advantageous in terms of energy savings. However, at these low temperatures there is usually no direct reaction between the silylation agent and the surface groups [57-58]. During

the indirect route self-polymerization can occur between the organosilanol molecules before reaching and reacting with the surface groups which reduces the effectiveness of the technique and gives rise to non-uniform surfaces. The competition between the surface reaction and self-polymerization is dictated by various factors including type of solvent and organosilane, working temperature and the amount of water adsorbed on the surface which results in poor control of the modification process and makes it even more complicated.

Regardless of the technique employed, the underlying mechanism for silylating a surface is the same. Silanes, especially organosilanes of the form R_nSiX_{4-n} is generally employed as reagents, where R is the non-hydrolysable organic group that possess the functionality and X is a hydrolysable group i.e. halogen, alkoxy, acyloxy or amine [59-60]. In the case of X group being a halogen or an amine, the silane reagent can readily react with the surface hydroxyl groups of the substrates whereas a priori hydrolysis reaction is required for alkoxy and acyloxy groups. Water, either adsorbed on the surface or present at trace amounts in the silane solution, can be used to convert the alkoxy or acyloxy organosilane to reactive organosilanol which then reacts with the appropriate surface groups of the material to be modified. As a result of these reactions covalent attachment of the organosilane to the surface is achieved where the organic group, R, extends from the surface and imparts the desired functionality to the surface [56, 59-60]. The type of the R group determines the final physical and chemical properties of the surface, and thus silylation agent should be selected considering the desired material properties.

It was mentioned previously that the main advantages of silylation from $scCO_2$ over conventional techniques is the high and fast penetration provided by the low viscosity and high diffusion coefficients which result in enhanced mass transfer rates. The viscosity and diffusion coefficient is closely related to the solubility of the silylation reagent in $scCO_2$ at a specific temperature and pressure. With increasing solubility, the amount of silane dissolved in a certain amount of $scCO_2$ at a specific temperature and pressure increases which raises the density and viscosity of the mixture resulting in decreased diffusion coefficient. Moreover, increasing the molecular weight of the silane also affects the mass transfer rate by influencing the diffusion coefficient. In addition, temperature also affects the mass transfer rates by altering the diffusion coefficient and viscosity. Increasing temperature decreases the viscosity while increasing the diffusion coefficient. The temperature dependency of the diffusion coefficient can be simply explained by Stokes-Einstein equation. Besides, pressure of the system also has a significant effect on mass transfer, such that increasing pressure decreases

the mass transfer rates by increasing the density. Regarding these effects, it is apparent that temperature, pressure, the solubility of silane reagents in $scCO_2$ as well as their molecular weights influences the mass transfer rates by affecting the diffusion coefficients.

When the surface reaction rates are considered, the most important parameters become the reactivity of the silane against the surface, temperature, solubility and concentration of the silane in $scCO_2$. The reactive groups of the silanes are of prominent importance and the reactivity of silylating reagents varies depending on the functional groups they possess. Hydroxyl groups are the most reactive moieties followed by phenol, carboxyl, amino and mercapto groups as shown in Figure 17 [55]. Moreover, the chemistry of the substrate surface is also crucial for the effectiveness of the silylation of the surfaces. The effectiveness of silylation reagents on different substrates are summarized in Figure 18 [60]. In addition, the concentration of the silane in $scCO_2$ also affects the rate of surface reaction. From the kinetic point of view, a rate of a reaction depends on the concentration of the reactants and the effect of concentration on reaction rate is determined by the order of reaction on reactants. However in a simplistic view, one can say that with increasing concentration, the probability of the silane molecules coming across the surface groups to react increases. Moreover, it is well known that the reaction rate constant has an Arrhenius type dependency on temperature, that is, with increasing temperature the rate constant increases exponentially. However, the effect of temperature also depends on the energetic characteristics of the surface reaction. Therefore it should be taken into consideration whether the surface reaction is endothermic or exothermic.

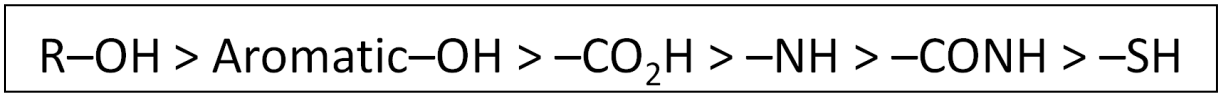

Figure 17 Reactivity of silylating agents containing different functional groups [55]

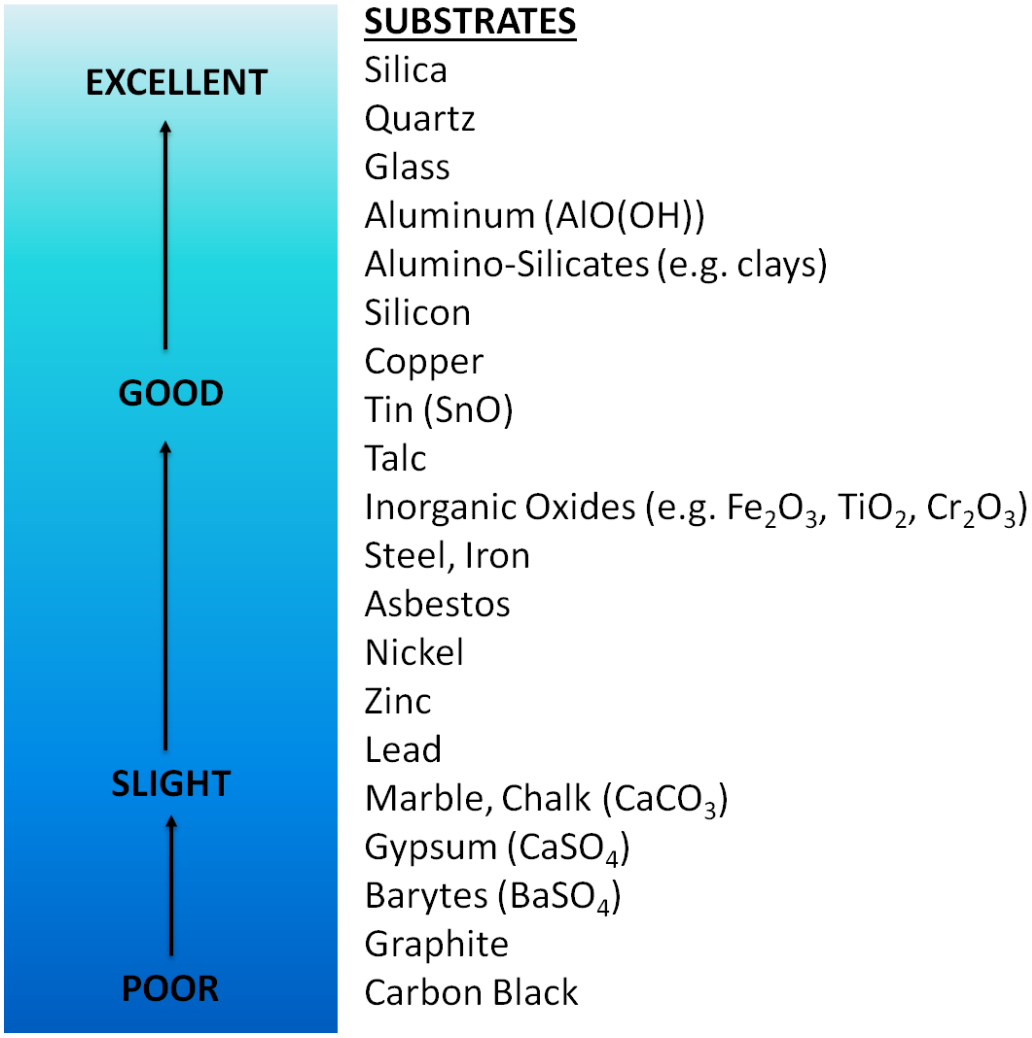

Figure 18 Effectiveness of silylation agents on inorganic materials [60]

Modification of the surface chemistry of porous materials has always been challenging when conventional vapor or liquid phase treatments are employed. The diffusion and homogenous distribution of the molecules on the surfaces is precluded due to the fine pore sizes which forms the major limitations of the conventional processes. Deposition of the modifying agents from $scCO_2$ is considered as an alternative route which eliminates such drawbacks of the conventional techniques. More importantly, for some porous materials such as aerogels, utilization of $scCO_2$ based surface modification eliminates the possible damages in the porous structure that originate from the surface tension occurring at the vapor-liquid phase boundary, therefore the original porous structure can be retained after the surface modification.

During the silylation of surfaces of porous materials, such as aerogels, there are few basic steps that are followed; the silane molecules first dissolve in $scCO_2$, the binary mixture of silane-CO_2 then diffuses through the pores and reaches to the reaction site on the surface, and

finally the silane reacts with surface groups of the material. These steps can be generalized as the dissolution, mass transfer and surface reaction and are represented schematically in Figure 19. In the case of nonporous materials, the diffusion step is eliminated since there is no tortuous path for the molecules to diffuse through and as a result the mass transfer step reduces to only external mass transfer which is the transfer from bulk fluid to the surface. Elimination of the diffusion simplifies the overall process steps for nonporous materials. Although the mechanism of silylation is not fully understood, it is well known that the mass transfer and reaction rates govern the overall surface modification process. The overall rate of the silylation process is determined by the slowest step, namely, rate limiting step which can be either diffusion or surface reaction. The time needed to achieve a desired level of silylation thereof can be identified considering the rate limiting step. There are several factors that affect the mass transfer and reaction rates to some extent, the most important ones being solubility of the silane in $scCO_2$, molecular weight and the functional groups of the silane, concentration, temperature and pressure.

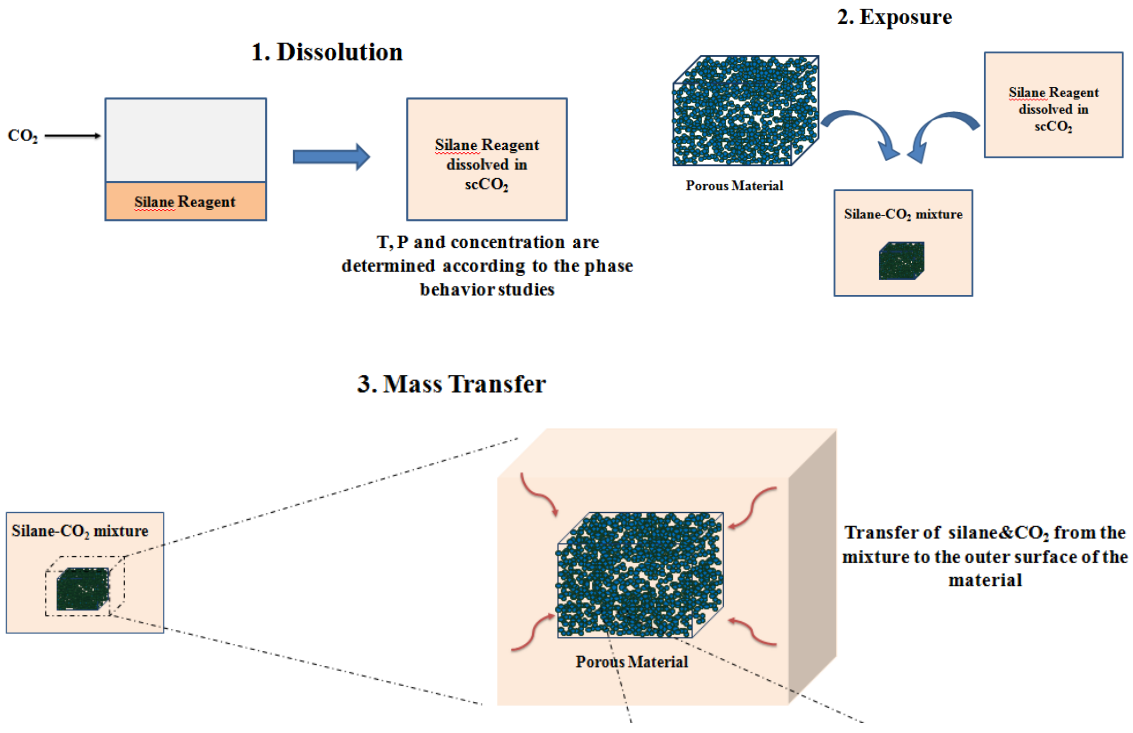

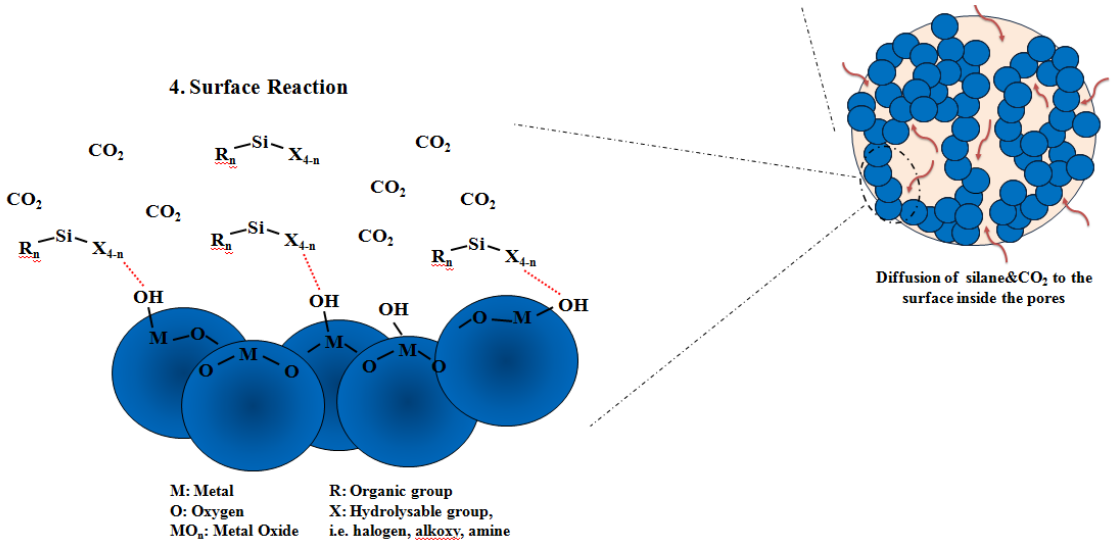

Figure 19 Fundamental steps of silylation of porous materials with $scCO_2$

Silica aerogels consist of interlinked tetrahedral SiO_4 groups and at the pore surface, the structure can terminate in either Si–O–Si groups with the oxygen link pointing to the surface, or in several types of Si–OH groups. The polarity and reactivity of aerogels largely depends on the ability of these groups to interact with each other by the formation of hydrogen bonds. Due to the presence of these surface hydroxyl groups, aerogels are inherently produced as hydrophilic materials. However, their hydrophilic nature is generally considered as a drawback since to the adsorption of water vapor on the surface destroys the porous structure and limits the life time. Modification of silica aerogel surface with suitable silane-based agents can be achieved rendering them hydrophobic. Moreover, the surface of aerogels can also be silylated in such a way that appropriate chemical groups for specific applications such as catalysis can be attached to the surface [1–2].

There have been few studies aiming to adjust the surface chemistry of silica aerogels to render them hydrophobic. In 2010, Kartal and Erkey demonstrated that hydrophobic silica aerogels can be obtained by the reactive deposition of hexamethyldisilizane (HMDS) from $scCO_2$ [61]. The modification of surface chemistry was achieved by the reaction of surface –OH groups of silica aerogel with trimethylsilyl ($Si(CH_3)_3$) groups of HMDS which resulted in 130^o contact angels. A similar surface modification study was carried out by the deposition of trimethylethoxysilane (TMES), octyltriethoxysilane (OTES) and chlorotrimethylsilane (CTMS) from $scCO_2$ [62]. It was revealed by the authors that with varying the silylation agent and deposition conditions such as pressure, it is possible to control degree of functionalization which allows for gradual variation of hydrophobicity.

Considering substantial solubilities of silane-based polymers in $scCO_2$, high reactivity of –OH groups of silane agents and effective silylation of silica surfaces, RSCD technique emerges as a very promising technique also for the development of composites of silica aerogels with silicon-based polymers.

2.5. Characterization Techniques

The mass uptakes of all the aerogel composites that were produced by RSCD technique were determined gravimetrically by weighing the samples before and after the deposition. For calculations to be precise each weighing was performed five times and the average of the five values was taken into account.

2.5.1. Bulk Density, Porosity and Volumetric Shrinkage

The bulk densities of the composites were calculated by simply dividing the mass of the aerogel by its volume.

The dimensions of the samples in the alcogel or aerogel conditions are measured with the help of a caliper for most accurate results.

The porosity of the aerogels was calculated based on the following equation where ρ_{SiO2} was the density of pure silica (2.19 g/cm^3) and $\rho_{aerogel}$ was the bulk density of the aerogel.

$$Porosity\ (\%) = \frac{\rho_{SiO2} - \rho_{aerogel}}{\rho_{SiO2}} * 100 \qquad (2.9)$$

The volume shrinkage of the composites was calculated by comparing the volumes before (labeled as alcogel) and the after the supercritical drying (labeled as aerogel). The volume shrinkage can be obtained as follows:

$$\Delta V(\%) = \frac{(V_{alcogel} - V_{aerogel})}{V_{alcogel}} * 100 \qquad (2.10)$$

2.5.2. Pore Structure Characteristics with N_2 Adsorption/Desorption

The pore properties of the samples were determined by N_2 adsorption–desorption measurements by using Micromeritics ASAP 2020 instrument (Figure 20). Prior to the analysis the samples were degassed at 353 K under vacuum for the removal of the impurities from the surface. During the analysis N_2 was adsorbed on the surface of the samples at 77 K by increasing the N_2 dosing at each step up to 1 relative pressure (P/P^o). Following the adsorption, the desorption of N_2 was performed by decreasing the N_2 dosage and as a result

adsorption-desorption isotherms of the aerogel samples were obtained. The surface areas of the samples were determined with Brunauer–Emmett–Teller (BET) method which is an extended form of Langmuir's kinetic theory to multilayer adsorption [63]. The pore volumes and pore size distributions were determined with Barrett–Joyner–Halenda (BJH) method from the N_2 adsorption–desorption isotherms.

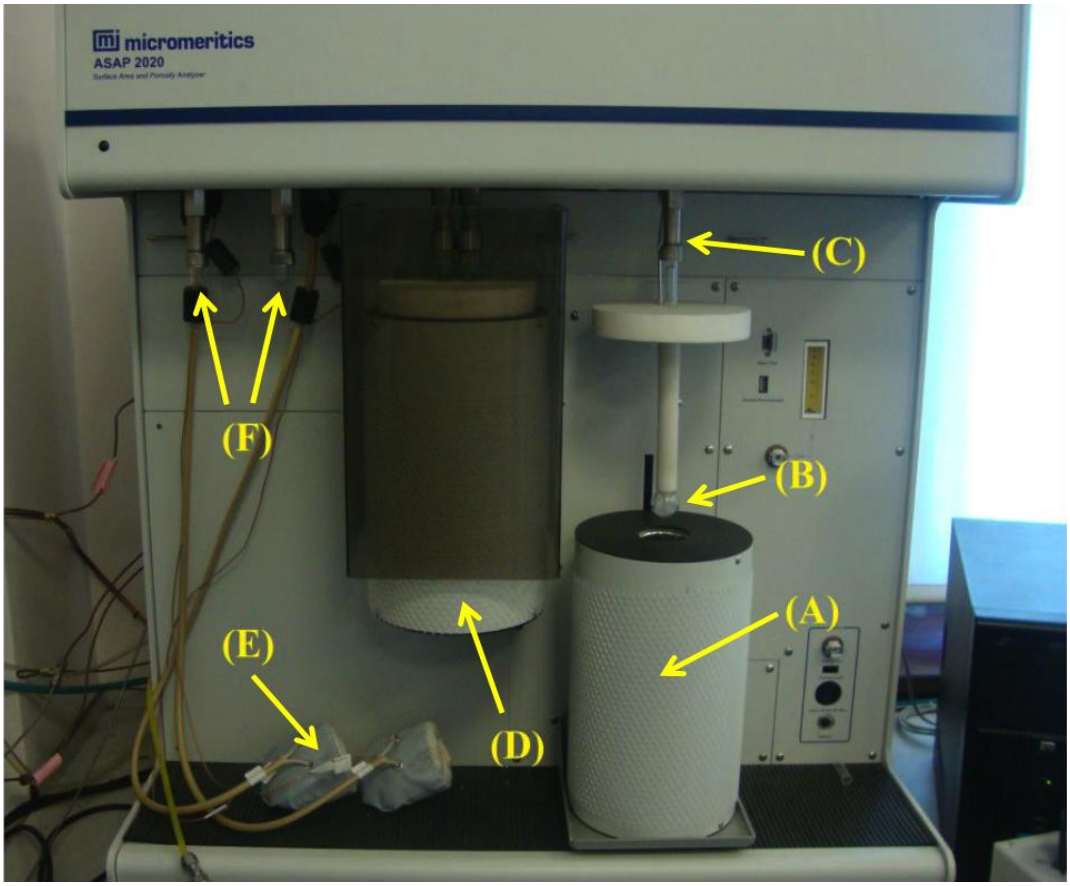

Figure 20 Micromeritics ASAP 2020 N2 adsorption-desorption analysis system; (A) analysis dewar; (B) sample tube; (C) analysis port; (D) degas dewar; (E) heating jacket; (F) degas ports.

2.5.3. Chemical Composition with ATR–FTIR

Thermo Scientific Nicolet Avatar 360 E.S.P. FTIR spectrophotometer with Horizontal Attenuated Total Internal Reflectance (ATR) Accessory (Figure 21) was employed to investigate the chemical composition of the samples. Infrared Radiation spectroscopy is used to identify the chemical structure and composition of a sample by measuring the light absorbed by different types of vibrations in molecules.

A small piece of sample is placed between a crystal of high refractive index and a clamp constructed of a metal tip. The infrared radiation is sent through the crystal towards the

sample at a specified angle for total reflection. The radiation beam can only penetrate into the sample a few wavelengths of light such as between 0.5 to 2.0 microns. During this penetration, the chemical bonds of the sample absorb some of the beam. The attenuated reflected beam is directed towards the detector that would result in the IR spectra of the sample.

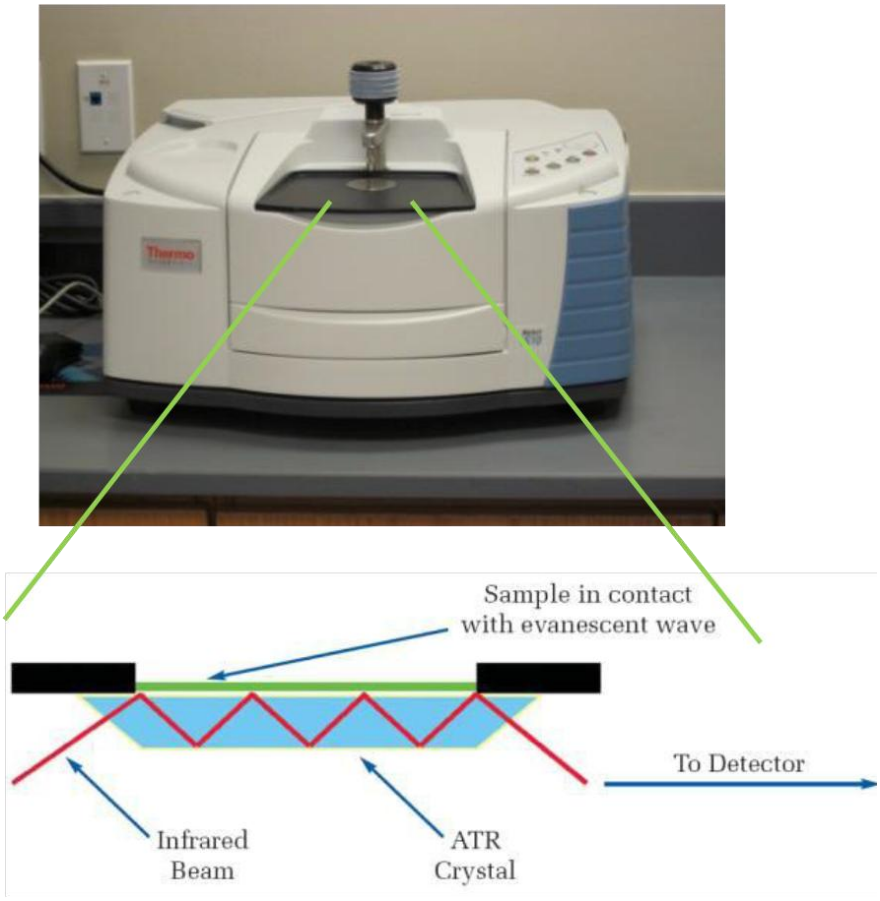

Figure 21 Thermo Scientific Nicolet Avatar ATR system

2.5.5. Transparency with UV–VIS

UV-VIS Spectrophotometer with integrating sphere apparatus that is displayed in Figure 22 was used for the analysis of transparency of the aerogels. The Integrating sphere system is composed of UV-VIS-NIR light source, sample holder, detector at the center of the system, two BaSO4 powder to reflect the incoming light and reference beam (Figure 23). Analysis range was 200 nm-900 nm. Scan speed was arranged as medium. Sampling interval (nm) was set as 1.0 and auto mode is selected for sampling mode. Measuring mode was always transmittance and slit width was selected as 20 nm. External 2 detector (Not direct) was selected for detector unit.

In order to determine haze value or transparency ratio of a sample, both total and diffuse transmittances should be analyzed by following three consecutive steps. First measurement was performed without sample for baseline correction (Figure 24(A)). After baseline correction, sample was placed inside the integrating sphere and total transmittance was measured (Figure 24(B)). For diffuse transmittance, BaSO4 I was removed from the integrating sphere and only forward scattered light was measured (Figure 24(C)). Ratio of diffuse to total transmittance gives haze value for the measured aerogel samples (Eqn. 2.11).

$$Haze = \frac{Diffuse\ Transmittance}{Total\ Transmittance} \times 100 \qquad (2.11)$$

$$Transparency\ Ratio = 1 - Haze = \frac{Total\ Transmittance - Diffuse\ Transmittance}{Total\ Transmittance} \times 100 \qquad (2.12)$$

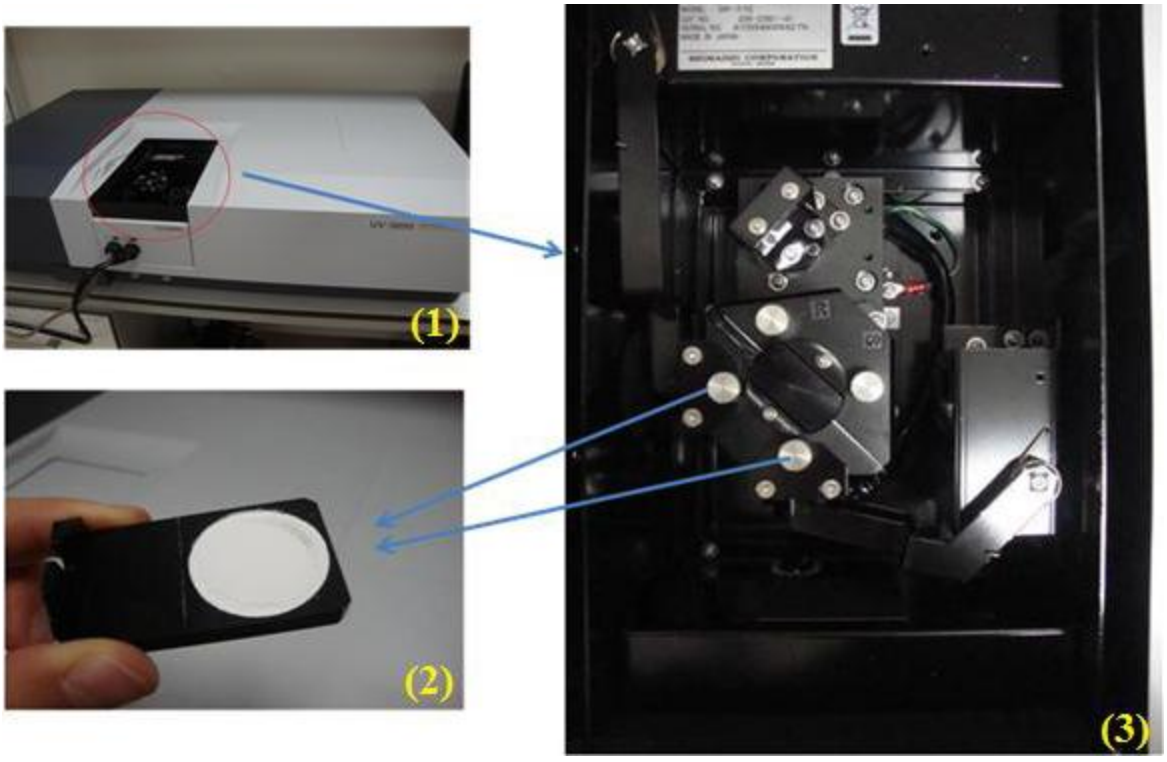

Figure 22 (1) Shimadzu UV-VIS Spectrophotometer with (2) $BaSO_4$ powder and (3)integrating sphere system

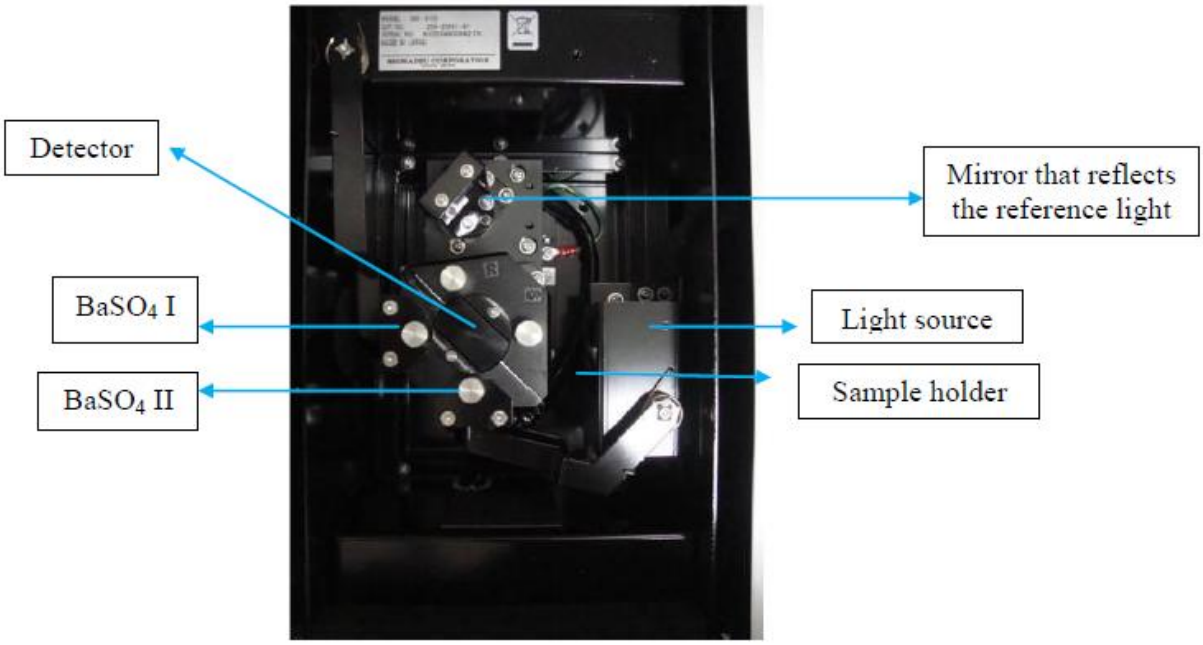

Figure 23 Components of integrating sphere apparatus.

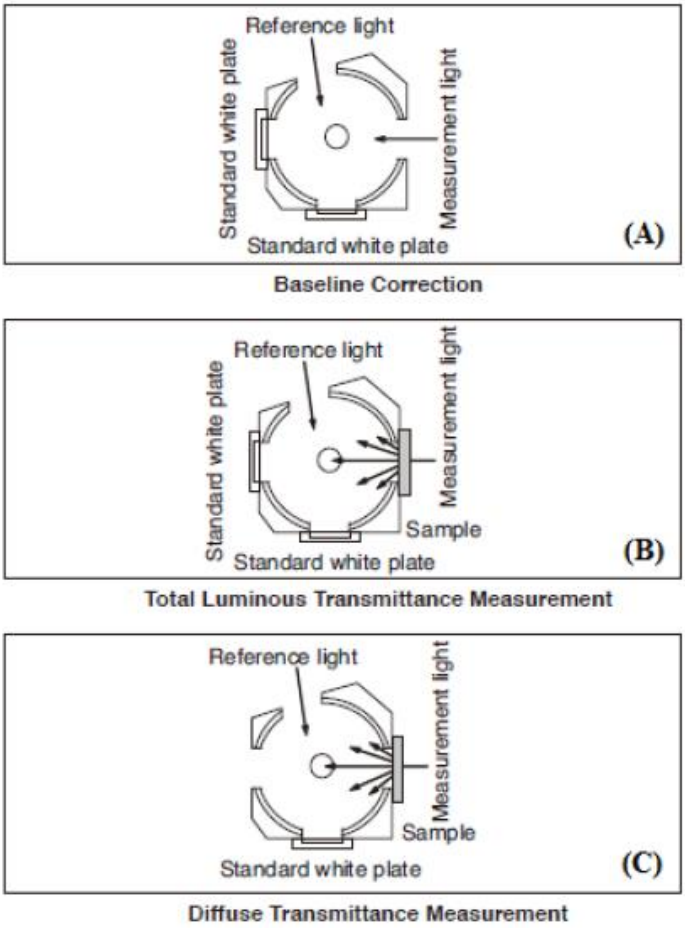

Figure 24 Methodology for transparency measurements; (A) baseline correction; (B) total transmittance measurement; and (C) diffuse transmittance measurement.

2.5.6. Mechanical Properties with Dynamic Mechanical Analyzer (DMA)

Mechanical properties of the aerogels were determined with Thermal Analysis (TA) Instruments Dynamic Mechanical Analyzer (DMA) Q800 instrument (Figure 25) which is a highly sophisticated equipment with several measuring modes such as 3-point bending, tension, shear and compression. Due to the size limitations of the samples compression mode of DMA was employed and compression tests of the aerogel samples were carried out. The small cylindrical samples of 1 cm diameter and 0.8 cm height were used in the tests. The samples were compressed with a rate of 1N/min up to 18 N of maximum load. During the compression, parameters such as displacement, static force, stress, strain, stiffness and relaxation modulus were recorded. Stress-strain curves of the samples were obtained and the compression modulus of each sample was calculated. At strains below 10%, the compression modulus can be obtained from the slope of plots of τ versus $(\lambda - \lambda^{-2})$ [64].

$$\tau = G(\lambda - \lambda^{-2}) \tag{2.13}$$

where τ is the applied stress and λ is the ratio of the deformed length over undeformed length.

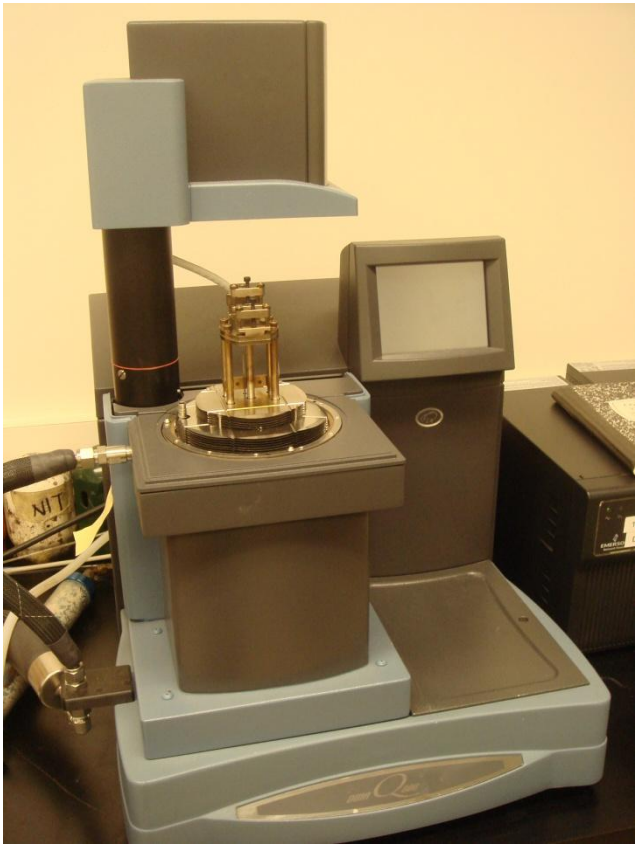

Figure 25 Thermal Analysis (TA) Instruments Dynamic Mechanical Analyzer (DMA) Q800 instrument.

2.5.7. Hydrophobicity

The contact angle measurements of the deposited samples were performed with Krüss contact angle measuring system (Krüss G10) by placing a droplet of triple distilled de–ionized water on the samples. The images of water droplets on aerogel samples were recorded and from those images the contact angles were determined by using MB-Ruler software.

CHAPTER 3

PDMS(OH)–SILICA AEROGEL COMPOSITES BY MODIFICATION OF THE SOL–GEL PROCESS

3.1. Introduction

Composites of silica aerogels were developed with the purpose of obtaining monolithic, crack-free, transparent and mechanically durable nanostructured materials to be used as core insulation materials in transparent VIPs. The first route that was followed for the development of composites of silica aerogels was the modification of the conventional two-step sol-gel process. Two different polymers were used; hydroxyl terminated poly(dimethylsiloxane) (PDMS(OH)) and bis(hydroxyalkyl) terminated poly(dimethylsiloxane) (PDMS–bis(alkylOH)), and the composites of silica aerogels with these polymers were derived. The polymers were incorporated at different stages of the sol-gel process that is displayed in Figure 4. The effects of parameters such as polymer-to-precursor ratio, aging conditions and type of co-solvent on the monolithic form, transparency, homogeneity, mechanical strength and pore structure of the aerogels were investigated.

3.2. Experimental Methodology

3.2.1. Synthesis of Native Silica Aerogels

Native silica aerogels were synthesized with the standard two–step sol–gel process by using tetraethylorthosilicate (TEOS) as the silica source, ethanol (EtOH) as the co–solvent, hydrochloric acid (HCl) as the acid catalyst and ammonium hydroxide (NH_4OH) as the base catalyst. The processing steps are displayed in Figure 4 in Chapter 2. The mass ratios of TEOS:H_2O:EtOH utilized in the synthesis was 1:0.34:1. During the hydrolysis step, the precursor – TEOS – was hydrolyzed with water in the presence of ethanol as the co–solvent. 0.2 ml of 2M HCl solution was added as the acid catalyst in order to increase the rate of hydrolysis reaction. After the addition of the acid catalyst, the sol mixture was stirred for 40 minutes for the completion of the hydrolysis reactions of the precursor molecules. Following the hydrolysis step, 0.5 ml of 5% NH_4OH in ethanol solution was added to the sol mixture as the base catalyst to accelerate the condensation reactions. Following the addition of base catalyst, the sol mixture was poured into the cylindrical syringe molds and sealed.

Subsequently, gelation occurred in the molds at room temperature, within 5–10 minutes. Following the gelation, aging of the wet gels was performed in order to replace the pore liquid with pure ethanol before the supercritical drying. The aging of the gels was carried out by immersion in equi–volume ethanol–water solution at 323.2 K for 24 h and then, in pure ethanol at room temperature for 72 h. After the aging, the wet gels (alcogels) were dried with supercritical CO_2 ($scCO_2$) at 313.2 K and 88 bar.

3.2.2. PDMS(OH)–Silica Aerogel Composites with Standard Synthesis Procedure

PDMS does not have any solubility in water. However, it has partial solubility in ethanol. Based on this information, initially, the composites of silica aerogels were developed by following the standard sol–gel processing routes. Two different functionalized forms of poly(dimethylsiloxane) (PDMS) were employed as the polymer phase: hydroxy–terminated PDMS (PDMS(OH)) with 65 cSt viscosity (M_n = 2750 g/mol) and bis(hydroxyalkyl)–terminated PDMS (PDMS–bis(alkylOH)) with 100 cP viscosity (M_n = 5600 g/mol). Figure 26 displays the chemical structures of these two polymers used in the synthesis.

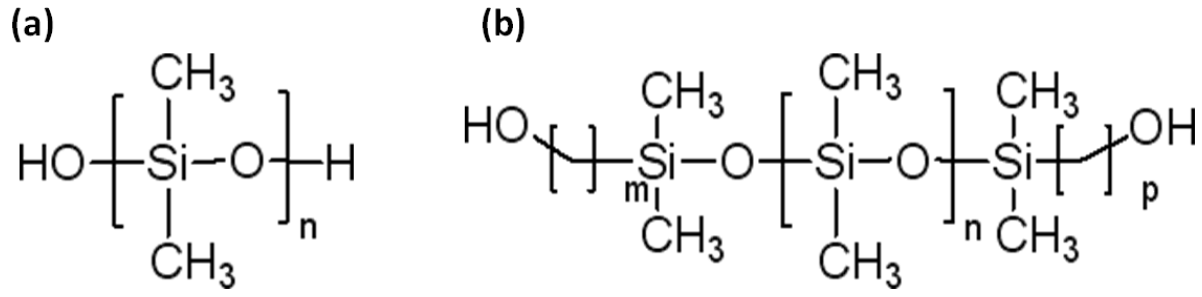

Figure 26 Molecular structures of (a) PDMS(OH) and (b) PDMS–bis(alkyl–OH).

Polymers were added to the sol mixture at two different stages during the synthesis: before and after the hydrolysis of the precursor. The amount of polymer was varied from 0.1 g to 1 g. For all of the samples, the gelation was observed to occur within 10 minutes after the base catalyst addition and the wet gels were observed to be translucent before aging. The gels were aged in the equi–volume solutions of ethanol and water at 323.2 K for 24 h. Subsequently, washing with pure ethanol was carried out for 72 h. Following the aging step, the gels were dried with $scCO_2$ at 313.2 K and 88 bar. Table 3 and Table 4 summarize the synthesis conditions for the PDMS(OH)–silica aerogel and PDMS–bisalkyl(OH)–silica aerogel composites, respectively.

The opaque appearance of the aerogel composites was attributed to the insolubility of the polymers in the sol mixture. It was stated previously that PDMS is not soluble in water although, partially soluble in ethanol. Ethanol present in the sol mixture probably dissolved a certain amount of polymer, however it was not enough to form a miscible mixture of PDMS with water, which is non–solvent of the polymer.

Table 3 Synthesis conditions for PDMS(OH)–silica aerogel composites derived with the standard sol–gel procedure.

Sample ID	TEOS /PDMS(OH) (g/g)	Appearance after drying	Addition of the polymer
D1410–1–1	1/0.1	O–PS(nH)	Before hydrolysis
D1410–2–1	1/0.1	O–H	After hydrolysis
D2010–1–1	1/0.5	O–H	After hydrolysis
D2010–2–1	1/1	O–H	After hydrolysis

O: opaque, H: homogenous, PS: phase separated, nH: non–homogenous

Table 4 Synthesis conditions for PDMS–bis(alkylOH)–silica aerogel composites derived with the standard sol–gel procedure.

Sample ID	TEOS /PDMS–bis(alkyl–OH) (g/g)	Appearance after drying	Addition of the polymer
D2210–1–1	1/0.1	O–H	Before hydrolysis
D2210–2–1	1/0.1	O–H	After hydrolysis
D2210–3–1	1/0.5	O–H	Before hydrolysis
D2510–1–1	1/1	O–PS(nH)	Before hydrolysis

O: opaque, H: homogenous, PS: phase separated, nH: non–homogenous

3.2.3. PDMS(OH)–Silica Aerogel Composites with THF as Co–solvent

Since using mixtures of ethanol and water were observed to lead to opaque aerogel composites due to the insufficient solubility of polymer, the need for a good solvent of the polymer emerged. Tetrahydrofuran (THF) is known to be a good solvent of PDMS and its derivatives. Therefore, composites of silica aerogels with PDMS(OH) were developed by employing THF as the co–solvent. Standard synthesis procedure was followed and PDMS(OH) was included in the synthesis at two different stages: before and after the

hydrolysis. Two different polymer amounts were used: 0.1 and 0.2 g. The amount of THF added to the sol mixture was determined by drop–by–drop addition until a clear mixture was obtained. The amount of THF needed to completely dissolve PDMS(OH) was observed to increase with PDMS(OH) amount and decrease with ethanol amount. However, even for very small polymer amounts, the amount of THF needed was significantly high. Additionally, the presence of water and TEOS in the sol mixture was observed to decrease the solvent power of THF for PDMS(OH). Due to these solubility reasons, the resulting sol mixtures had excess amount of co–solvent which caused dilution effects. Table 5 summarizes the amounts of the solvent, co–solvent, precursor and polymer together with the aging solution composition and conditions.

The gelation of the solutions was observed to occur within 2 h at room temperature after the addition of the base catalyst. The wet gels were observed to be transparent after the gelling in the molds. However, the gels were very soft and weak for release from the molds. The weakness of the wet gels was attributed to the dilution effect occurred due to the excess amount of co–solvent. In addition, most of the composites were broken after the supercritical drying. As a result, the strength of the gels was determined to be insufficient to retain the monolithic structure.

Table 5 PDMS(OH)–silica aerogel composites synthesized with THF as the co–solvent.

Sample ID	TEOS/PDMS(OH) (g/g)	H_2O/EtOH/THF (g/g/g)	Aging sol'n (v%/v%)	Appearance after drying	Addition of polymer
D1501–1–1	1/0.1	0.37/1.01/2.21	(E/W): 50/50, 50 ^oC	O–H, Broken	Before hydrolysis
D1501–1–2	1/0.1	0.37/1.01/2.21	(T/W): 50/50, RT	O–H, Broken	Before hydrolysis
D1501–2–1	1/0.1	0.34/1.0/2.5	(E/T): 50/50, RT	O–H	Before hydrolysis
D1501–2–2	1/0.1	0.34/1.0/2.5	(E/T/W): 33/33/33, RT	O–H, Broken	Before hydrolysis
D1501–3–1	1/0.1	0.37/1.03/2.01	(E/W): 50/50, 50 ^oC	O–H, Broken	After hydrolysis
D1501–3–2	1/0.1	0.37/1.03/2.01	(E/T/W): 33/33/33, RT	O–H, Broken	After hydrolysis
D1601–1–1	1/0.2	0.36/1.0/2.5	(E/T/W): 44/44/13, RT	O–H, Broken	Before hydrolysis
D1601–1–2	1/0.2	0.36/1.0/2.5	(E/T): 67/33, RT	O–H	Before hydrolysis

D1601–1–3	1/0.2	0.36/1.0/2.5	(E/T): 33/67, RT	O–H, Broken	Before hydrolysis
D1601–2–1	1/0.2	0.39/1.01/2.5	(E/T/W): 40/40/20, RT	O–H, Broken	After hydrolysis
D1601–2–2	1/0.2	0.39/1.01/2.5	(E/T): 67/33, RT	O–H	After hydrolysis
D1601–2–3	1/0.2	0.39/1.01/2.5	(E/T): 33/67, RT	O–H, Broken	After hydrolysis
D1601–2–4	1/0.2	0.39/1.01/2.5	(E/W): 80/20, 50 ^{o}C	O–H, Broken	After hydrolysis

O: opaque, H: homogenous, E: ethanol, W: water, T: THF, RT: room temperature

For completion of the restructuring of the pores and strengthening of the wet gels, the gels were kept in the molds overnight at room temperature after the gelation occurred. Table 6 lists the synthesis conditions for the PDMS(OH)–silica aerogel composites obtained with overnight gelation.

Furthermore, it was found that increasing the temperature of the gels enhanced the co–condensation reactions ongoing in the pores and as a result strengthened the gels. Therefore, additional experiments were performed at 323.2 K in autoclaves. Sol mixtures were poured into the glass molds after the addition of the base catalyst and gels were kept at 323.2 K for 72 h. The wet gels were directly dried with $scCO_2$ without any aging step. Table 7 lists the synthesis conditions for these aerogel composites.

Table 6 PDMS(OH)–silica aerogel composites synthesized with THF as co–solvent (overnight gelation).

Sample ID	TEOS/PDMS–OH (g/g)	H_2O/EtOH/THF (g/g/g)	Aging sol'n (v%/v%)	Appearance after drying	Addition of polymer
D2001–1–1	1.03/0.21	0.37/1.01/2.52	(E/T): 50/50, RT	O–H	Before hydrolysis
D2001–1–2	1.03/0.21	0.37/1.01/2.52	(E/T): 80/20, RT	O–H	Before hydrolysis
D2001–1–3	1.03/0.21	0.37/1.01/2.52	(E): 100, 50 ^{o}C	O–H	Before hydrolysis
D2001–2–1	1.05/0.21	0.34/1.0/2.52	(E/T): 50/50, RT	O–H	After hydrolysis
D2001–2–2	1.05/0.21	0.34/1.0/2.52	(E/T): 80/20, RT	O–H	After hydrolysis
D2001–2–3	1.05/0.21	0.34/1.0/2.52	(E): 100, 50 ^{o}C	O–H	After hydrolysis
D2001–2–4	1.05/0.21	0.34/1.0/2.52	(T): 100, RT	O–H, Broken	After hydrolysis
D2701–2–1	1.03/0.05	0.35/0.9/1.1	(Tln): 100, RT	Cracks	Before hydrolysis

O: opaque, H: homogenous, E: ethanol, T: THF, Tln: toluene, RT: room temperature

Table 7 PDMS(OH)–silica aerogel composites synthesized with THF as co–solvent (gelation at 323.2 K, without aging).

Sample ID	TEOS/PDMS(OH) (g/g)	H_2O/EtOH/THF (g/g/g)	Appearance after drying	Addition of polymer
D2101–1	1.01/0.1	0.33/1.03/2.12	Broken	Before hydrolysis
D2101–2	1.05/0.12	0.36/0.52/2.55	O–H, Broken	Before hydrolysis
D0102–1	0.51/0.1	0.16/0.5/0.75	O–H, Broken	Before hydrolysis
D0102–2	1.0/0.05	0.2/0.29/0.71	Tl–H	Before hydrolysis
D0102–3	1.0/0.1	0.19/0.3/0.8	Broken	Before hydrolysis

O: opaque, Tl: translucent, H: homogenous

3.2.4. PDMS(OH)–Silica Aerogel Composites with Toluene as Co–solvent

Toluene is another good solvent for PDMS and its derivatives. Therefore, toluene was also included in the synthesis procedure as the co–solvent. Aerogel composites with TEOS:PDMS(OH) weight ratio of 1:0.15 were synthesized. Toluene was added into the sol mixture drop–by–drop until a clear solution was obtained. The necessary amount of toluene to dissolve the polymer completely was observed to be less than the amount of THF, which indicated that toluene has stronger solvent power against PDMS(OH) than THF. Table 8 displays the compositions used in the synthesis as well as appearance of the composites after drying.

The gelation was observed to occur within 30 min at room temperature after the addition of the base catalyst. The wet gels had transparent appearances before the supercritical drying.

Table 8 PDMS(OH)–silica aerogel composites synthesized with toluene as the co–solvent.

Sample ID	TEOS/PDMS(OH) (g/g)	H_2O/EtOH/Tln (g/g/g)	Appearance after drying	Addition of the polymer
D2701–1–1	1.0/0.15	0.35/1.0/1.0	Tl–H, Broken	After hydrolysis
D2701–1–2	1.0/0.15	0.35/1.0/1.0	Tl–H	After hydrolysis

Tl: translucent, H: homogenous, E: ethanol, T: THF, Tln: toluene, RT: room temperature

3.2.5. PDMS(OH)–Silica Aerogel Composites with THF and Toluene as Co–solvents

The composites of aerogels with PDMS(OH) were additionally derived by utilizing both THF and toluene as the co–solvents. The polymer was added into the sol mixture before the hydrolysis of the precursor, at a TEOS:PDMS(OH) mass ratio of around 1:0.1. Table 9 lists the compositions used during the synthesis.

For the entire set of experiments, the gelation occurred within 1 h at room temperature. However, the gels were left in the molds overnight in order to facilitate the completion of the condensation reactions and strengthening the wet gels. The wet gels had cloudy appearances before the supercritical drying.

Table 9 PDMS(OH)–silica aerogel composites synthesized with THF and toluene as the co–solvents.

Sample ID	TEOS/PDMS(OH) (g/g)	H_2O/EtOH/THF/Tln (g/g/g/g)	Aging sol'n (v%)	Appearance after drying	Addition of the polymer
D0102–4–1	0.99/0.11	0.33/0.8/0.8/0.7	(E): 100, RT	Tl/O–H, Broken	Before hydrolysis
D0102–4–2	0.99/0.11	0.33/0.8/0.8/0.7	(T): 100, RT	Tl/O–H	Before hydrolysis
D0102–4–3	0.99/0.11	0.33/0.8/0.8/0.7	(Tln): 100, RT	O–H	Before hydrolysis
D0102–5–1	1.0/0.1	0.38/1.63/0.7/ 0.1	(E): 100, RT	Tl–H, Cracks	Before hydrolysis
D0102–5–2	1.0/0.1	0.38/1.63/0.7/ 0.1	(T): 100, RT	Tl–H, Broken	Before hydrolysis
D0102–5–3	1.0/0.1	0.38/1.63/0.7/ 0.1	(Tln): 100, RT	Tl–H	Before hydrolysis

O: opaque, Tl: translucent, H: homogenous, E: ethanol, T: THF, Tln: toluene, RT: room temperature

3.2.6. PDMS(OH)–Silica Aerogel Composites by Aging in PDMS(OH)

PDMS(OH)–silica aerogel composites were also derived by contacting the gels with PDMS(OH). Since PDMS(OH) is a liquid polymer with low viscosity, the aging was performed in pure PDMS(OH). After the gelation step, the wet gels were removed from the molds and submerged in PDMS(OH). The aging was performed in an autoclave at 393 K for 1 week to facilitate the reaction between the polymer and silica gel surface.

3.3. Results and Discussions

3.3.1. Native Silica Aerogels

All of the native silica aerogel samples synthesized by the standard two–step sol–gel procedure were monolithic and crack–free. Figure 27 displays the images of two different native silica aerogel samples. The sample on the left had a cylindrical shape with 1.1 cm diameter and 0.8 cm height, while the sample on the right was a square prism with 5x5x1 cm^3 dimensions. The image on the left shows the top view of the cylindrical aerogel sample. The high transparency of the native silica aerogels can clearly be understood from both images. Additionally, some of the measured properties of the native silica aerogel samples are listed in Table 10.

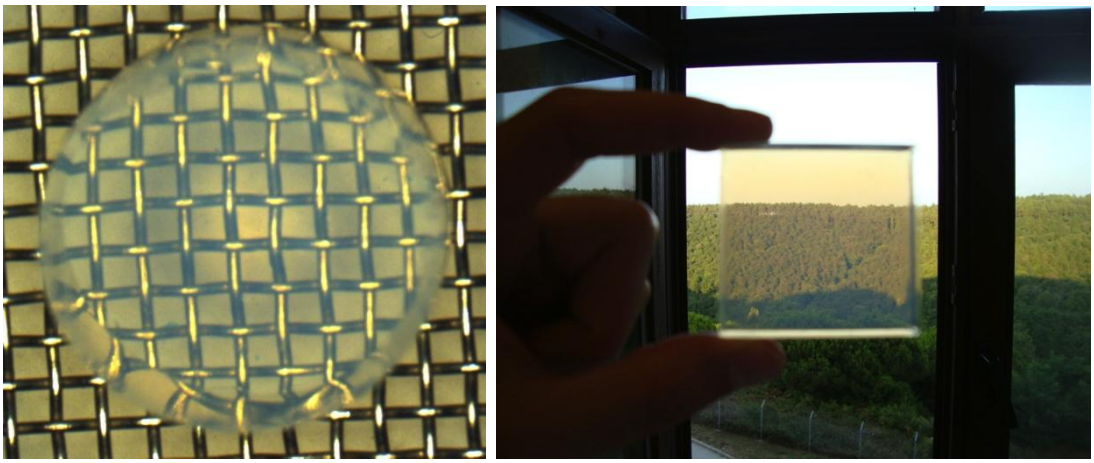

Figure 27 Top view of a cylindrical aerogel sample after supercritical drying.

Table 10 Properties of native silica aerogels synthesized by standard two–step sol–gel process.

Density (g/cm3)	0.13
Porosity (%)	94
Volumetric shrinkage ($\Delta \boldsymbol{V}(\%)$)	5
BET Surface Area (m^2/g)	1047
Pore volume (cm^3/g)	4.76
Average pore radius (nm)	9.1
Thermal Conductivity (mW/mK)	16
Haze (@ 600 nm)	18.2
Light Transmittance (%)(@ 600 nm)	81.8

Figure 28 displays the ATR–FTIR spectrum of the native silica aerogel sample. There are two intense peaks that are specific to the chemical structure of silica. These peaks occur at 800 cm^{-1} and 1061 cm^{-1} and are characteristic to Si–O–Si network bending and network stretching vibrations, respectively [65]. The broad band which appears at 3150 to 3560 cm^{-1} originates from hydrogen bonded Si–OH with the adsorbed molecular water. Furthermore, the peak at 960 cm^{-1} can be attributed to stretching of Si–OH groups of the aerogel [65-66] and the peak at 3745 cm^{-1} originates due to isolated or geminal Si–OH groups. The spectra given in the figure is quite typical for the silica aerogels.

Additionally, the graph in Figure 29 shows the TGA analysis results of the native silica aerogel sample. A 6% weight loss was observed up to 100 ^{o}C which occurred due to the removal of the molecular water that was physically adsorbed on the aerogel surface. In addition, after 300 ^{o}C, a weight loss of approximately 5% was observed up to 700 ^{o}C which was attributed to the condensation of the germinal or isolated surface –OH groups.

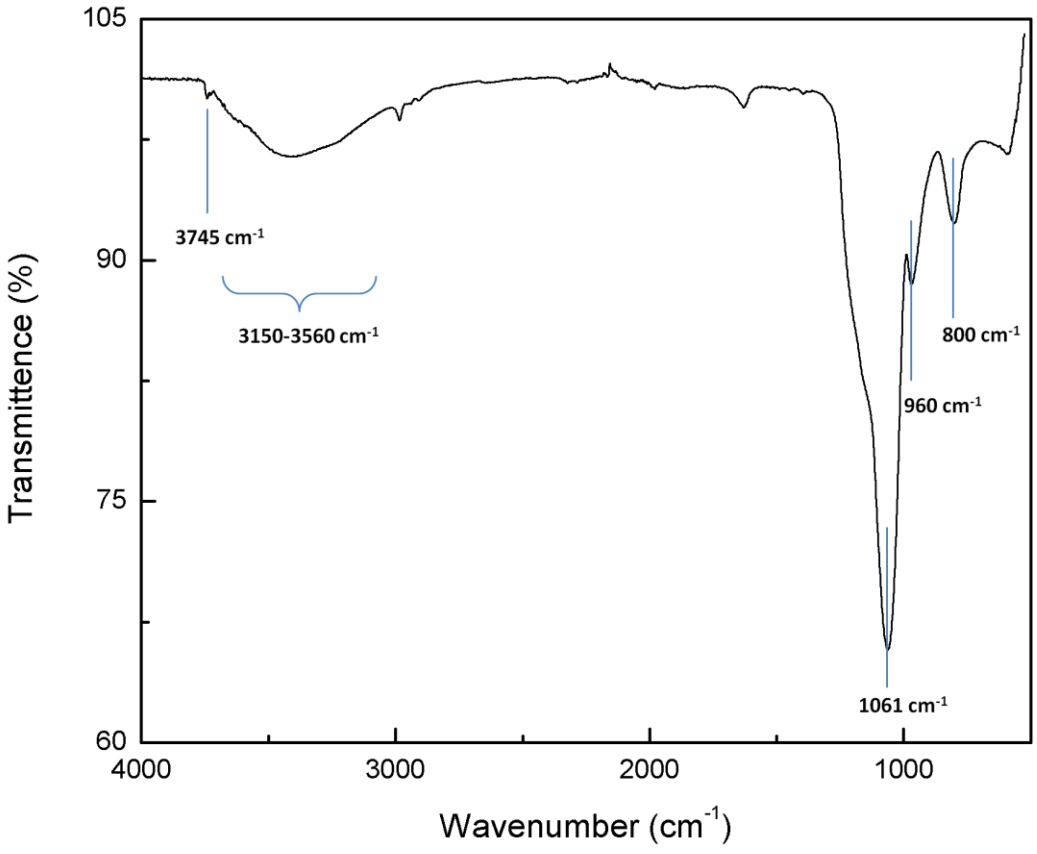

Figure 28 ATR–FTIR spectrum of native silica aerogel.

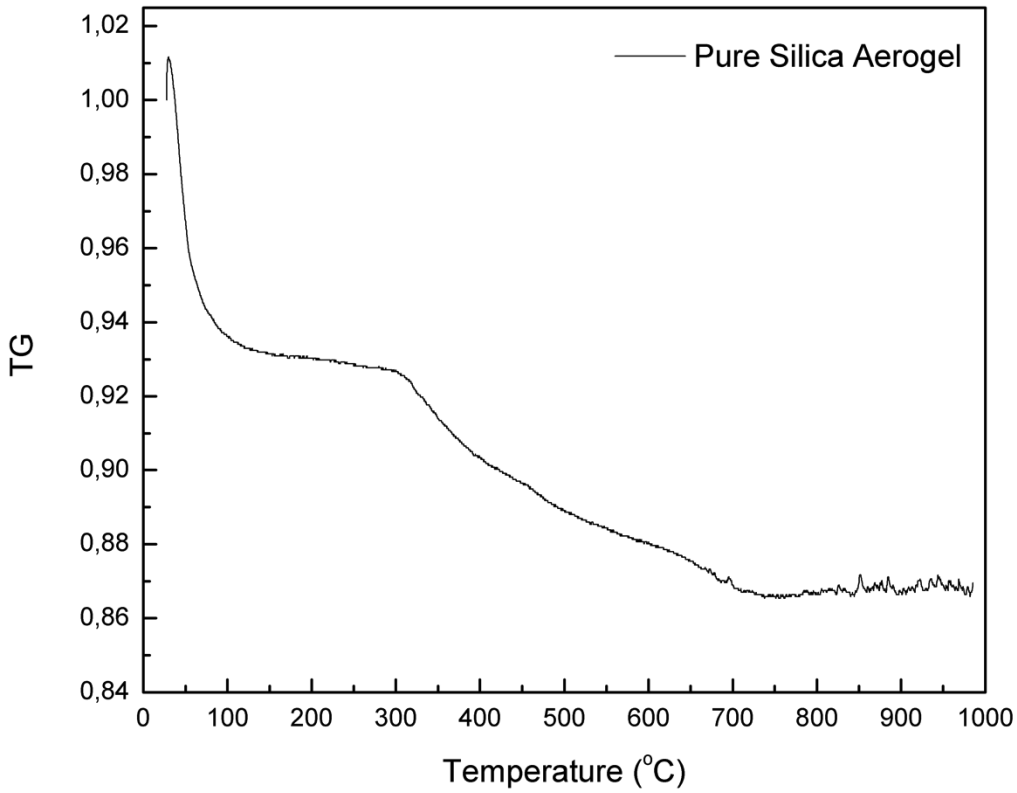

Figure 29 TGA results of native silica aerogel.

Furthermore, pore size distribution of the native aerogel sample is given in Figure 30 together with the N_2 adsorption/desorption isotherm of the sample. It is clearly observed from the isotherm that the aerogel samples have Type IV isotherm with H1 type hysteresis loop which is typically observed for mesoporous materials with narrow pore size distributions such as silica aerogels. Moreover, the existence of H1 type hysteresis loop (parallel adsorption and desorption branches of the isotherm indicates that the evaporation of the pore liquid occurs at thermodynamic equilibrium and there is no pore blocking, cavitation and percolation effects that contribute to hysteresis. The pore size distribution was obtained from the desorption branch of the isotherm by employing BJH method. Although both branches (adsorption and desorption) can be used for pore size calculations, from both a thermodynamic and historical point of view, the desorption branch is often favored for pore size assessment since the desorption process is more stable than the adsorption. It has been suggested that the adsorption of N_2 on the surface can cause contractions and can alter the structure of aerogels. Thus, the information extracted from desorption branch is more reliable. The pore size distribution given in Figure 30 reveals a narrow pore size distribution for the native silica aerogel sample.

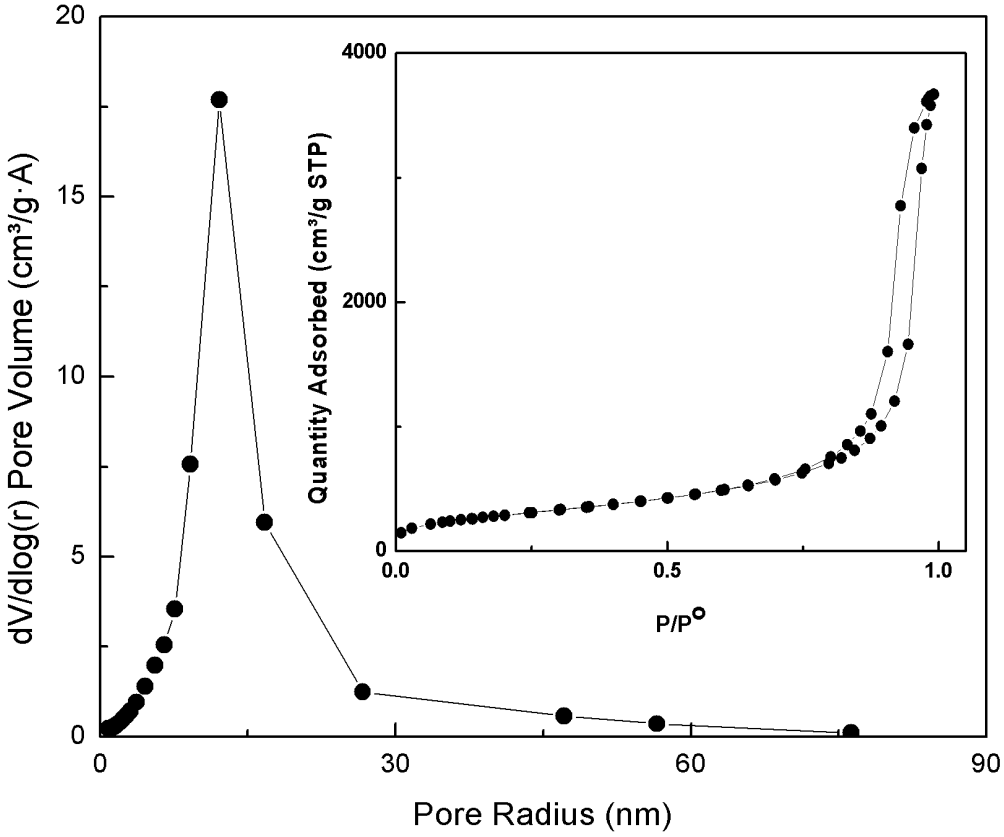

Figure 30 Pore size distribution and N2 adsorption/desorption isotherm of native silica aerogel.

Moreover, total and diffuse transmittance of the aerogel samples were measured in the UV and visible range by UV–VIS measurements. The spectrum is displayed in Figure 31. The haze of the silica aerogel was calculated from the ratio of the diffuse transmittance to total transmittance. Haze of a material is a measure of cloudiness and is usually used to quantify the transparency. Hence, the spectra obtained with UV–VIS measurements were employed for the calculation of haze and thus quantification of the transparency of the samples.

Compression test was also performed with DMA to quantify the mechanical properties of silica aerogels. The maximum load in the compression tests were 18 N and the rate of the loading was set as 1N/min. The small cylindrical samples of 1 cm diameter and 0.8 cm height were used in the tests. According to the results given in Figure 32, no yield was observed for the material. Compressive strength is defined as the capacity of a material to withstand the compressive forces and the maximum compressive strength of the native silica aerogel sample was observed to be 0.1 MPa. Additionally, the specific compression modulus was calculated as 0.113 MPa. There is no data available in the literature about the maximum compressive strength or the specific compression modulus of native silica aerogels.

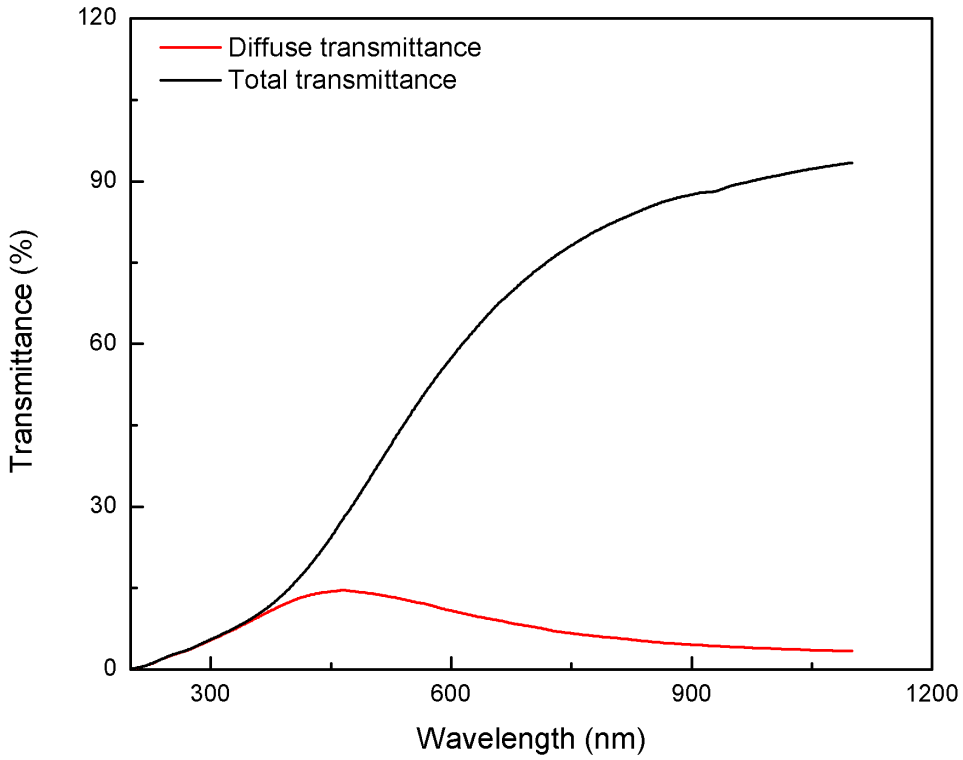

Figure 31 Total and diffuse transmittance of native silica aerogel obtained by UV–VIS measurements.

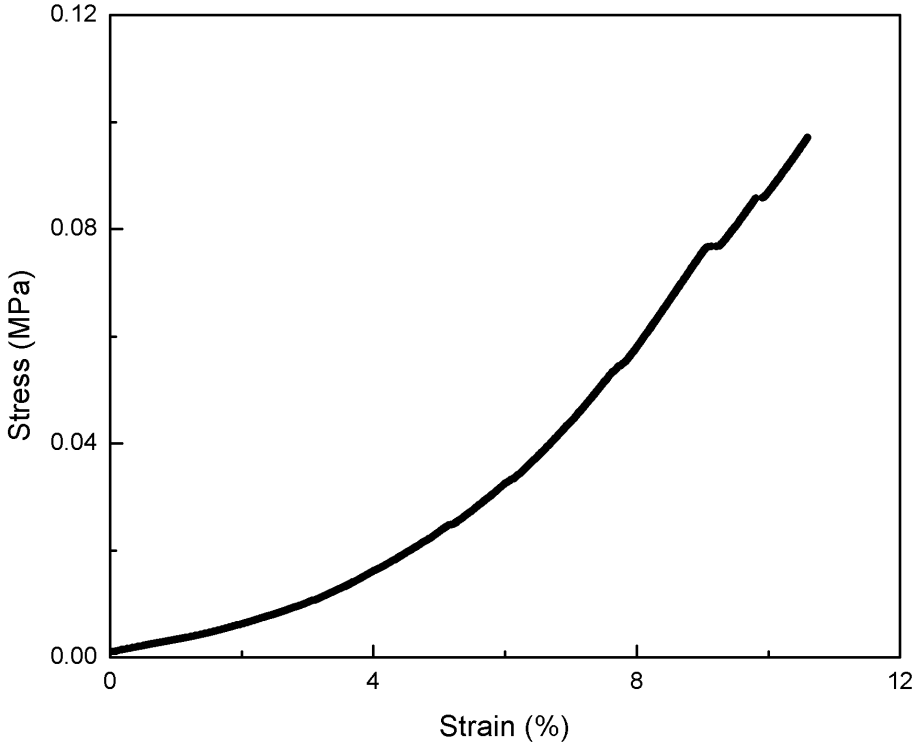

Figure 32 Stress–strain curve of native silica aerogel sample obtained with DMA compression test.

3.3.2. PDMS(OH)–Silica Aerogel Composites with Standard Synthesis Procedure

As given in Table 3, PDMS(OH)–silica aerogel composites that were synthesized by following the standard procedure described in Section 3.2.1. were monolithic, homogenous and opaque. In Figure 33 the images of a native silica aerogel and a PDMS(OH)–silica aerogel composite synthesized by the standard procedure are displayed to give an idea about how dramatically the transparency of the composites is lost. All of the composites had the same appearance. The samples were opaque because PDMS(OH) was not dissolved in the sol mixture. Upon this *"mis-dissolution"* the polymer molecules form liquid suspension in the sol mixture, resulting in a two-phase system; liquid aggregates of polymer dispersed in the sol mixture. While solid silica network was forming during the condensation and gelation steps, the aggregates of polymer molecules were probably entrapped between the network particles. Thus, PDMS(OH) was concluded to entangle inside the pores or between the silica particles of the silica network, forming additional scattering centers and thus causing opaque appearance of the composites. Table 11 summarizes some calculated and measured values of the PDMS(OH)–silica aerogel composites obtained with the standard sol–gel procedure.

It can be identified from Table 11 that, addition of the polymer after hydrolysis resulted in lower density and higher surface area. With increasing polymer amount, the density and the average pore width of the composites increased whereas the porosity and the surface area decreased. The decrease observed in BET surface area was attributed to the filling up of the pores with the polymer phase. This outcome can additionally be observed in Figure 34 which gives the pore size distributions of the composites together with the native silica aerogel. It can be clearly seen that the peak point of the pore size distribution curve decreased to smaller values with increasing amount of polymer used in the synthesis, indicating that the polymer phase that is present within the pores has an effect of filling of the pores when compared to native silica aerogel.

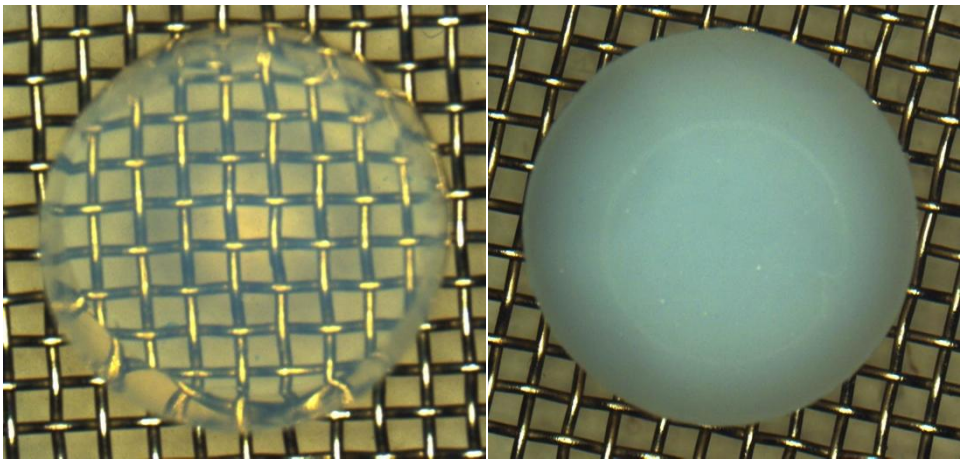

Figure 33 Top view of cylindrical aerogel samples; native silica aerogel (left) and PDMS(OH)–silica aerogel composite (right).

Table 11 Bulk density, porosity, BET surface area and average pore widths of PDMS(OH)–silica aerogel composites synthesized with the standard sol–gel procedure.

Sample ID	TEOS /PDMS(OH) (w/w)	Bulk density (g/cm^3)	Porosity (%)	BET Surface Area (m^2/g)	Average pore width (nm)
D1410–1–1	1/0.1	0.16	93	814.5	17.9
D1410–2–1	1/0.1	0.15	93	840.2	17.7
D2010–1–1	1/0.5	0.21	90	677.8	21.3
D2010–2–1	1/1	0.17	92	452.3	22.6

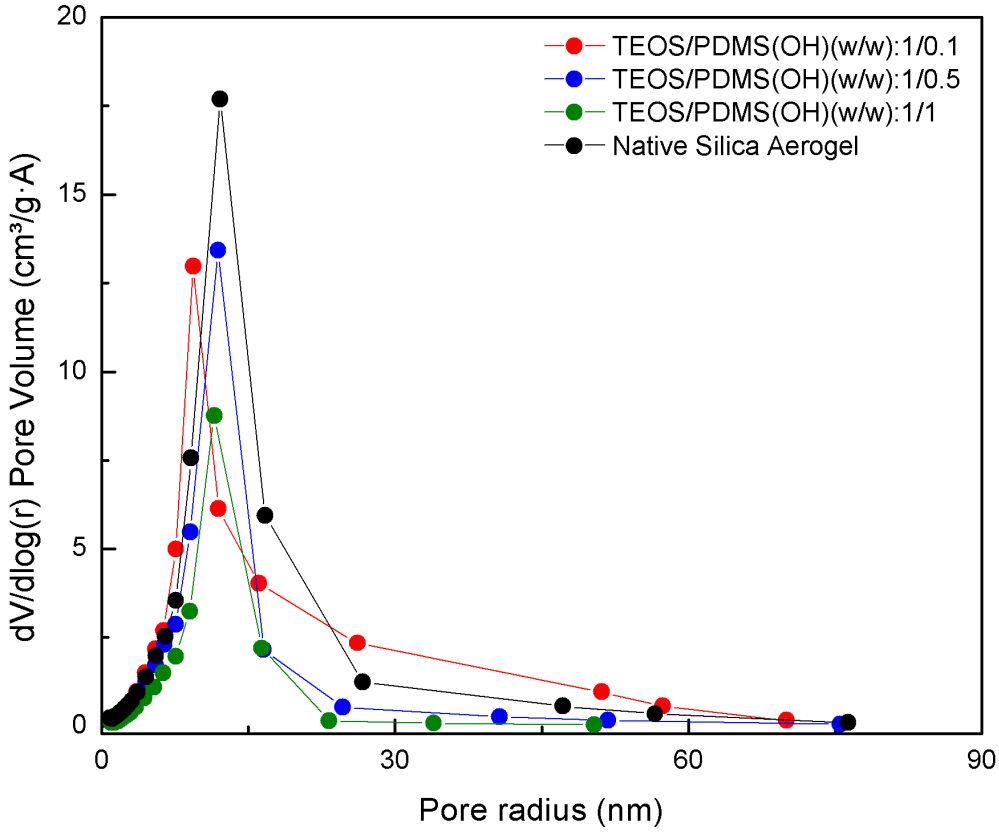

Figure 34 Pore size distribution of composites synthesized with different amounts of polymer together with native silica aerogel.

Figure 35 and Figure 36 display the TGA analysis results of PDMS(OH)–silica aerogel composites with TEOS:PDMS(OH) mass ratios of 1:0.1 and 1:0.5, respectively. The weight decrease in pure silica aerogel due to the adsorbed water was previously given as 6% in Figure 29. For the PDMS(OH)–silica aerogel composites the weight decrease due to the adsorbed water was measured as 2.1% and 2.5%, respectively, for TEOS:PDMS(OH) mass ratios of 1:0.1 and 1:0.5. PDMS(OH) is a hydrophobic polymer by nature owing to the methyl side groups attached to the backbone silicon. Thus, decrease in the amount of adsorbed water was expected since with increasing polymer in the composites the hydrophobicity increased.

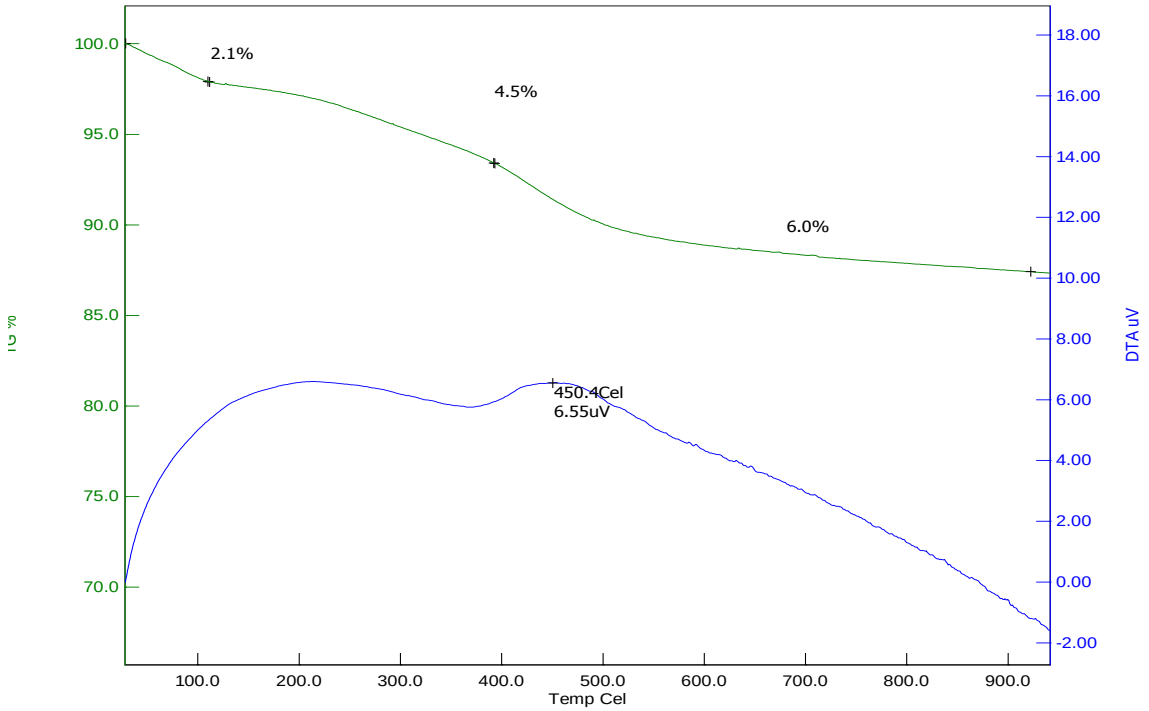

Figure 35 TGA analysis of PDMS(OH)–silica aerogel composite with TEOS:PDMS(OH) mass ratio of 1:0.1.

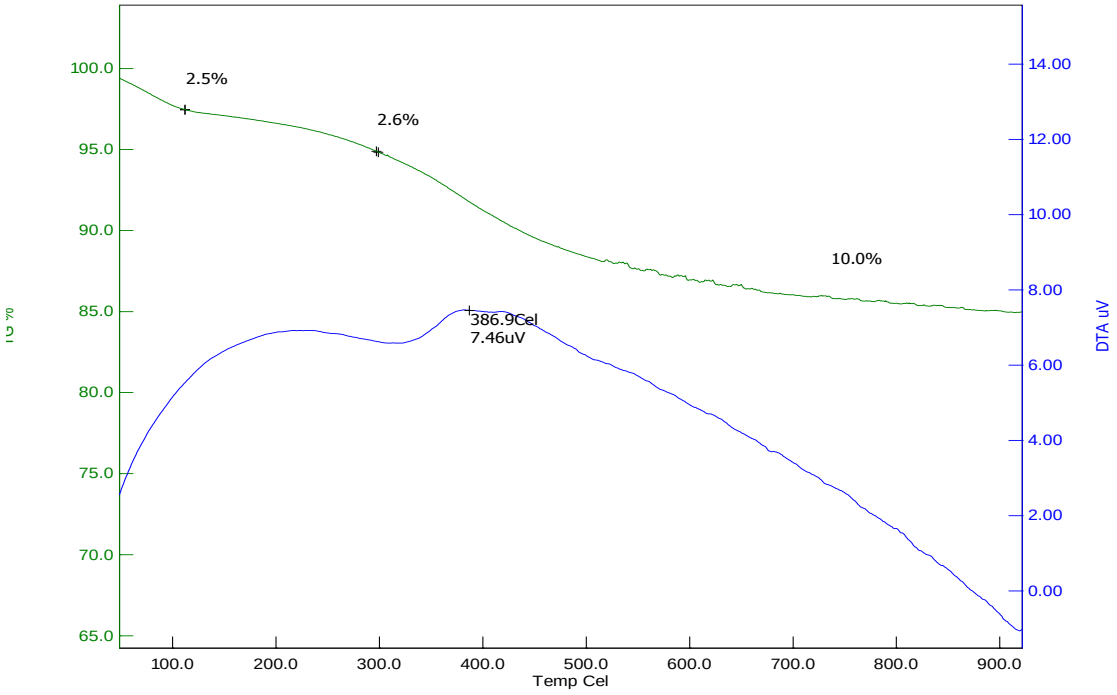

Figure 36 TGA analysis of PDMS(OH)–silica aerogel composite with TEOS:PDMS(OH) mass ratio of 1:0.5.

The ATR–FTIR analyses of the samples were performed to investigate the chemical composition and the spectra of the composites are given along with the native silica aerogel

sample in Figure 37. There are three peaks indicative of the presence of the polymer in the composites. The peak at 2963 cm^{-1} represents the C–H stretching vibrations originating from the methyl side groups of PDMS(OH). The peak at 1267 cm^{-1} is due to the Si–C stretching vibrations that originate from methyl side groups attached to the polymer backbone. The peak appearing at 850 cm^{-1} for the composite samples was attributed to ≡Si–O–Si$(CH_3)_2$–R bond that were formed due to the condensation reactions between the ≡Si–OH groups of the aerogel and OH–Si$(CH_3)_2$–R end groups of PDMS(OH) [65]. The intensities of the C–H and Si–C stretching vibration peaks as well as the Si–O–Si peak that signifies newly formed silica network increased accordingly with the increasing polymer amount in the composites.

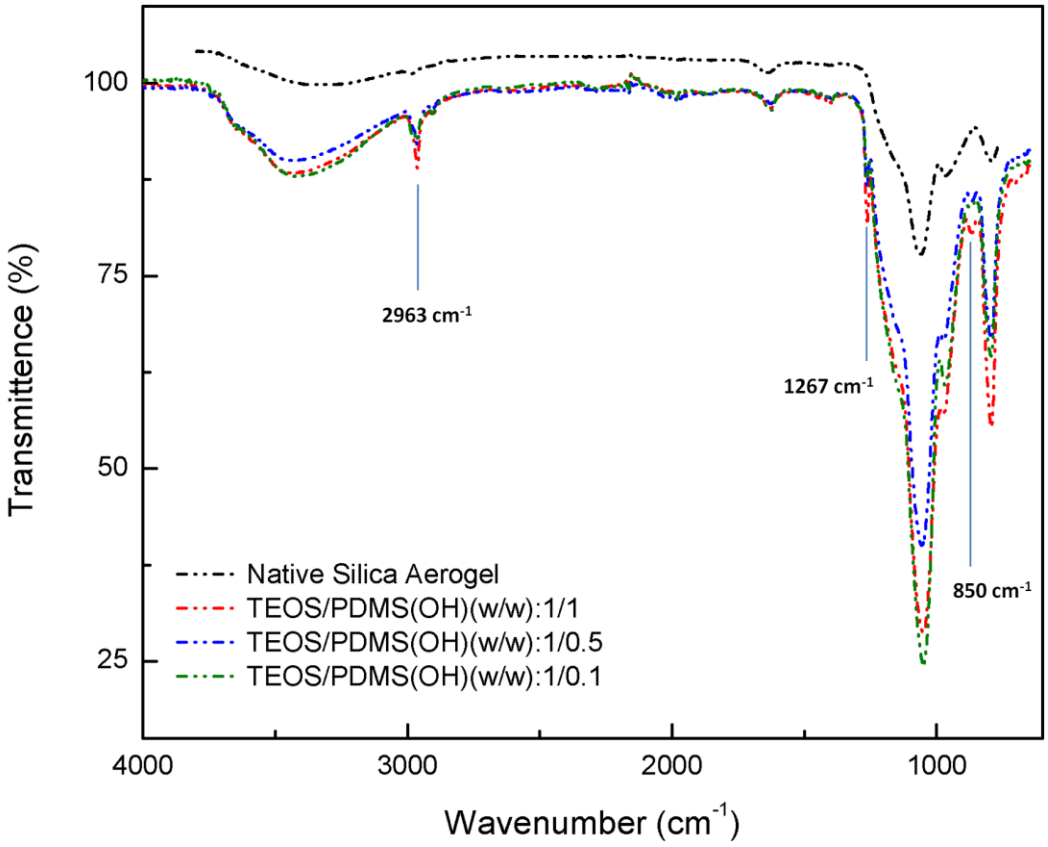

Figure 37 ATR–FTIR spectra of PDMS(OH)–silica aerogel composites synthesized with the standard sol–gel procedure.

PDMS–bis(alkyl–OH)–silica aerogel composites were additionally synthesized by following the standard two–step sol–gel procedure as described previously in Section 3.2.1. As listed in Table 4, all of the samples were obtained as opaque and the opacity was similarly attributed to the insufficient solubility of the polymer in the sol mixture. Table 12 displays some of the computed and measured properties the composites.

It is clear from Table 12 that there is not a significant correlation between the polymer amount and the surface area and pore width. However, it is interesting to note that with increasing polymer amount the bulk densities of the composites decreased while the porosities increased. This outcome can be explained by the formation of new pores within the polymer phase. It was previously explained that during the condensation and gelation steps, the hydrolyzed precursor molecules form the silica network and during this network formation the polymer molecules form a separate phase that entangled between the silica particles or small pores. It is possible that additional pores are formed within this entangled polymer phase which can explain the increasing porosity and decreasing density with increasing polymer amount. The pore size distributions of composites are compared to that of native silica aerogel in Figure 38. The peak positions of the pore size distribution curves shifted to smaller values accordingly with the increasing amount of polymer used in the synthesis which indicates filling of the pores of silica aerogel with the polymer phase.

Furthermore, ATR–FTIR analysis were performed with the PDMS–bis(alkyl–OH)–silica aerogel composites and the spectra that is displayed in Figure 39, demonstrated the same C–H (2963 cm^{-1}), Si–C (1267 cm^{-1}) and Si–O–Si (850 cm^{-1}) peaks that confirm the presence of the polymer in the composites. There is not any correlation between the intensities of these peaks and the polymer amount added during the synthesis. However, it is obvious that the intensities are much more higher compared to the PDMS(OH)–silica aerogel composites given in Figure 39. Another important finding is that, there is a significant increase in the intensity of Si–O–Si network bending vibration peak that is observed at 800 cm^{-1}. Such an increase can merely be explained by the formation of additional Si–O–Si network by the polymer molecules. In fact, such a formation additionally supports the decreasing density and increasing porosity issues discussed above, since additional pores are probably formed between the newly formed Si–O–Si network of the polymer phase.

Table 12 Properties of PDMS–bis(alkyl–OH)–silica aerogel composites synthesized with the standard sol–gel procedure.

Sample ID	TEOS /PDMS–bis(alkyl–OH) (w/w)	Bulk Density (g/cm^3)	Porosity (%)	BET Surface Area (m^2/g)	Average pore width (nm)
D2210–1–2	1/0.1	0.21	90	573.8	24.1
D2210–2–2	1/0.1	0.23	90	488.9	21.7
D2210–3–2	1/0.5	0.17	92	517.2	24.1
D2510–1–2	1/1	0.15	93	517.5	21.1

O: opaque, H: homogenous, PS: phase separated, nH: non–homogenous, E: ethanol, W: water

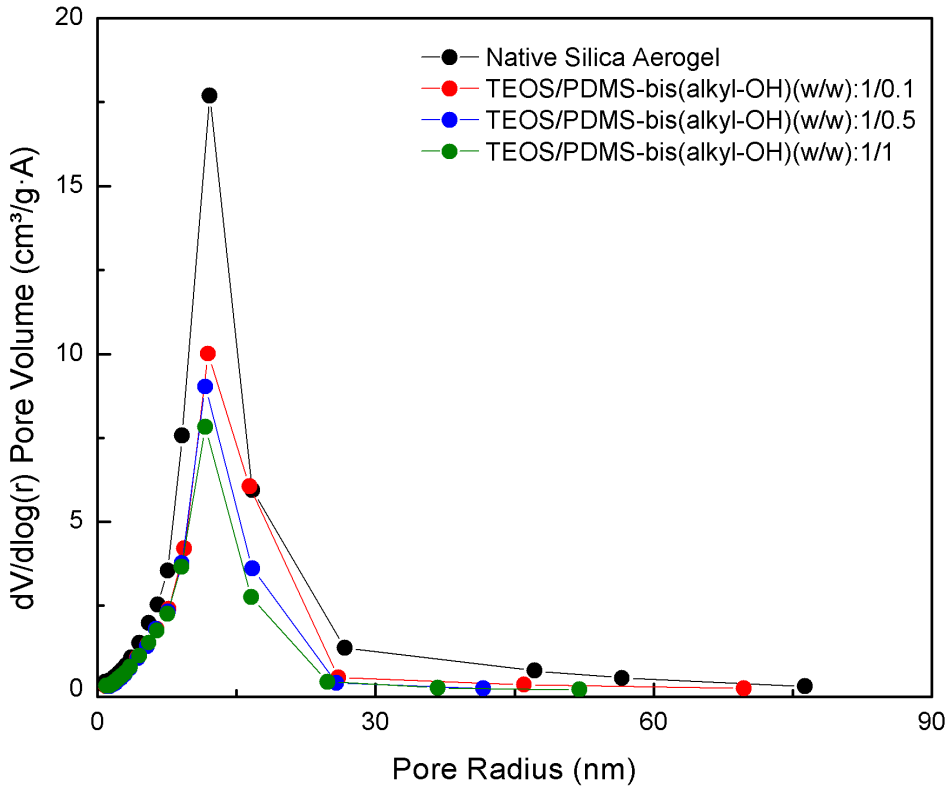

Figure 38 Pore size distribution of composites synthesized with different TEOS/polymer ratios together with native silica aerogel.

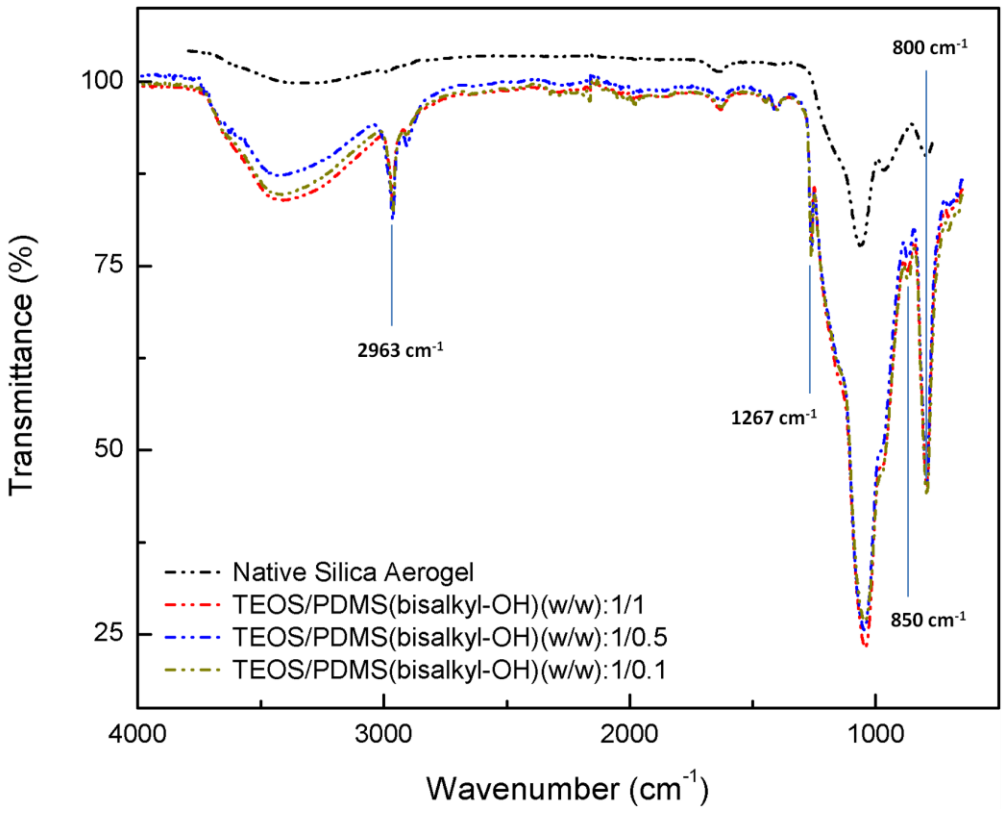

Figure 39 ATR–FTIR spectra of PDMS–bis(alkyl–OH)–silica aerogel composites synthesized with the standard sol–gel procedure.

3.3.3. PDMS(OH)–Silica Aerogel Composites with THF as Co–solvent

Being a good solvent for PDMS(OH), THF was used in the synthesis procedure as a co–solvent. Small amounts of THF is generally enough to dissolve pure PDMS(OH). However, it was observed that the presence as well as amount of water and TEOS in the sol mixture decreases the solvent power of THF for PDMS(OH). On the other hand, ethanol was found to enhance the dissolution of PDMS(OH) in THF. The amount THF that is required to obtain a clear solution of polymer was around 44 wt.% of the sol mixture which is a very large value and causes dilution effects due to the excess amount of solvent in the mixture. This led to retardation in the gelation times. Additionally, after gelation, the wet gels were very weak and soft and not intact enough to remove from the molds. The aging stage also did not improve the strength of the wet gels. As a result, most of the gels were cracked and broken during the supercritical drying and the volumetric shrinkages of the monoliths were dramatically high as displayed in Table 13. The opaque appearances of the composites were attributed to the very large shrinkage values rather than the physical entanglement of the polymer inside the pores. Moreover, due to the very high shrinkage, the bulk densities increased, whereas porosity values decreased, as given in Table 13.

Table 13 Density, porosity and volumetric shrinkage of the PDMS(OH)–silica aerogel composites synthesized with THF as the co–solvent.

Sample ID	TEOS/PDMS(OH) (w/w)	Aging sol'n (v%/v%)	Bulk Density (g/cm^3)	Porosity (%)	Volumetric shrinkage (%)
D1501–1–1	1/0.1	(E/W): 50/50, 323.2 K	0.43	80	63
D1601–2–2	1/0.2	(E/T): 67/33, RT	0.30	86	83
D1601–2–3	1/0.2	(E/T): 33/67, RT	0.28	87	79

E: ethanol, T: THF, W: water, RT: room temperature

Since the wet gels were observed to be very weak and soft right after the gelation, the gels were left overnight in the molds to increase the mechanical strength of the gels. This procedure seemed to enhance the strength and retain the monolithic structure of the wet gels, however high volumetric shrinkage was observed during overnight waiting period. Additional shrinkage during the supercritical drying step resulted in very high volumetric shrinkages similar to the previous results. However, the bulk density, porosity, surface area and pore widths that are listed in Table 14 were similar to those of native silica aerogels. It is important to note that the wet gels aged in pure THF or THF solution were observed to swell and become soft and weak. It is speculated that the hetero cyclic structure of THF may have played a role in the swelling behavior of the wet gels. The swelled gels were broken during the supercritical drying.

Table 14 TEOS/PDMS–OH composite aerogels synthesized with THF as the co–solvent (overnight gelation).

Sample ID	TEOS/PDMS(OH) (w/w)	Bulk Density (g/cm^3)	Porosity (%)	Volumetric shrinkage (%)	BET Surface Area (m^2/g)	Average pore width (nm)
D2001–1–2	1.03/0.21	0.15	93	69	941.4	12.1

Furthermore, the solutions were allowed to gel at 323.2 K instead of room temperature since higher temperatures facilitate condensation reactions and as a result enhance the strength of the gel network. The aging step was omitted to avoid additional shrinkage. The synthesized composites were observed to be stronger despite the absence of the aging step which a crucial stage for the strengthening of the solid network. However, most of the gels were broken after the supercritical drying. Table 15 displays some of the properties measured for these composites. The bulk density, porosity, BET surface area and average pore widths were obtained to be similar to those of native silica aerogels. In addition, doubling the polymer amount in the composites decreased the density while increasing the porosity and surface area.

This outcome points out the formation of new pore within the polymer phase, similar to the PDMS–bis(alkyl–OH) case.

Table 15 Properties of PDMS(OH)–silica aerogel composites synthesized with THF as the co–solvent (gelation at 323.2 K, without aging).

Sample ID	TEOS/PDMS(OH) (w/w)	Bulk Density (g/cm^3)	Porosity (%)	BET Surface Area (m^2/g)	Average pore width (nm)
D2101–2	1.05/0.12	0.17	92	933.4	10.9
D0102–2	1.0/0.05	0.23	89	849.6	13.4

ATR–FTIR analyses were also carried out and the spectra of the composites having the same amount of polymer are displayed in Figure 40. The same C–H (2963 cm^{-1}), Si–C (1267 cm^{-1}) and Si–O–Si (850 cm^{-1}) peaks that confirm the presence of the polymer were observed, expectedly. There is additional increase in the intensity of Si–O–Si network bending and stretching vibration peaks that are observed at 800 cm^{-1} and 1061 cm^{-1}. This observation indicates the formation of additional Si–O–Si network by the polymer molecules.

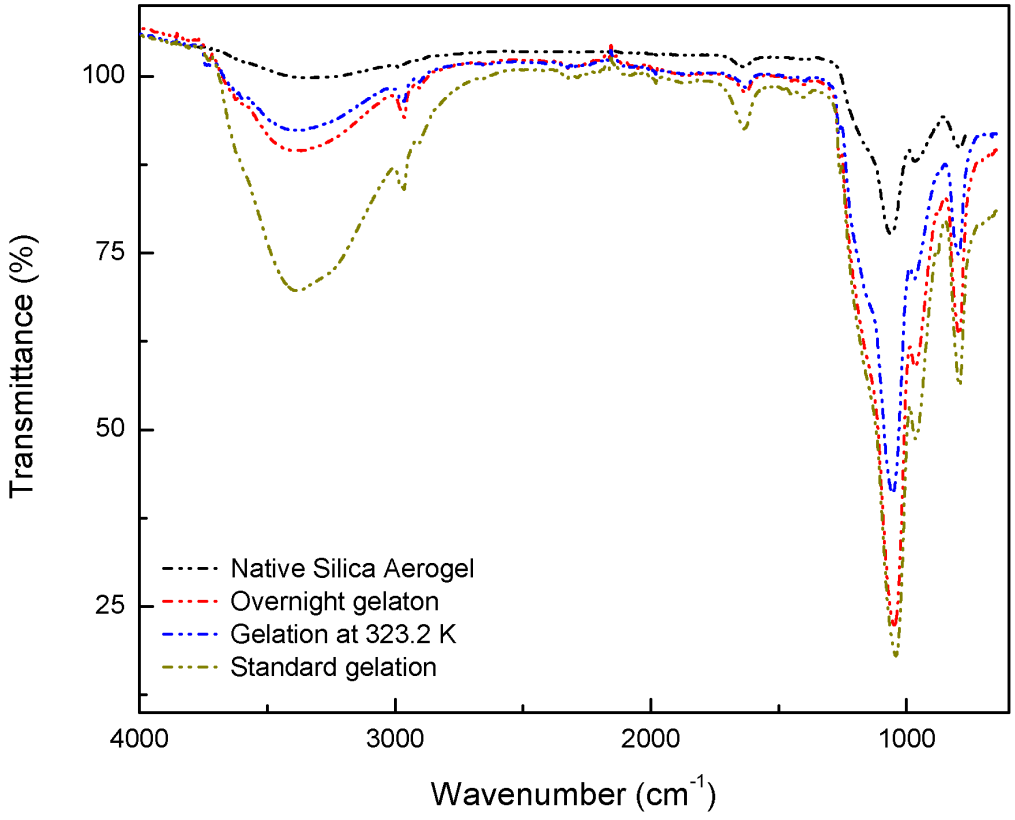

Figure 40 ATR–FTIR spectra of different PDMS(OH)–silica aerogel composites synthesized with THF as the co–solvent.

3.3.4. PDMS(OH)–Silica Aerogel Composites with Toluene as Co–solvent

Being another good solvent for PDMS(OH), toluene was also utilized in the synthesis procedures as the co–solvent. The amount of toluene that is needed to obtain a clear polymer–sol mixture was smaller than that of THF, which indicates the greater solvent power of toluene against PDMS(OH), compared to THF. The amount of toluene of 29 wt.% of the sol mixture was enough to achieve clear and homogenous mixtures whereas the minimum amount of THF needed was 44 wt.% of the sol mixture. The aerogels obtained with toluene as the co–solvent had translucent appearance unlike the ones produced with THF which were opaque. Table 16 shows the properties of a composite developed with toluene as the co–solvent. Considering the smaller amount of toluene used in the synthesis than THF, the dilution effect due to the excess solvent was expected to be diminished. However, high volumetric shrinkage was obtained similar to THF case which pointed out the weak silica network structure. The bulk density was higher than that of native silica aerogel, which was expected considering the very large volumetric shrinkage. However, the BET surface area and average pore volume was close to the values that of native silica aerogel.

ATR–FTIR analysis of the PDMS(OH)–silica aerogel composite produced with both THF and toluene revealed the same peaks that are specific to the polymer and observed for the previous composites.

Table 16 Properties of PDMS(OH)–silica aerogel composites synthesized with toluene as the co–solvent.

Sample ID	TEOS/PDMS(OH) (w/w)	Bulk Density (g/cm^3)	Porosity (%)	Volumetric shrinkage (%)	BET Surface Area (m^2/g)	Average pore width (nm)
D2701–1–2	1.0/0.15	0.234	88.90	63.5	825.5225	11.56135

3.3.5. PDMS(OH)–Silica Aerogel Composites with THF and Toluene as Co–solvents

PMDS(OH)–silica aerogel composites were further developed by utilizing both THF and toluene as the co–solvents, since the combined effect of the solvent powers of THF and toluene may be stronger. It was observed that addition of toluene as the second co–solvent greatly enhances the solvent power of THF and reduces the amount of THF that is required to obtain a clear polymer–sol mixture. Table 17 summarizes some measured properties of an aerogel composite. The reduction in the required total amount of solvent also resulted in reduced volumetric shrinkage compared to the previous composites. The aerogel composites

derived with both THF and toluene had translucent appearance which is probably associated with the reduced volumetric shrinkage. The density, porosity and average pore width of the composite is close to that of a native silica aerogel. Furthermore, BET surface area is slightly higher than native silica aerogel.

Pore size distributions of composites that were synthesized with THF and/or toluene are compared to that of native silica aerogel in Figure 41. It is clearly seen that the pore volume reached by the peak point of the pore size distribution curve decreased in all composites compared to the native silica aerogel. Additionally, when both THF and toluene are used as co–solvents the narrow distribution of the pores can be retained. However, when THF or toluene is used alone as co–solvent, there occurs to be significant changes in the distribution curves. For instance, when toluene is used as the co–solvent, the pores larger than 15 nm are diminished and the distribution curve is narrow. However, when THF is used as the co–solvent, the peak of the distribution curve is shifted to larger pore radius with a broader distribution.

Table 17 PDMS(OH)–silica aerogel composites synthesized with THF and toluene as the co–solvents.

Sample ID	TEOS/PDMS(OH) (w/w)	Bulk Density (g/cm^3)	Porosity (%)	Volumetric shrinkage (%)	BET Surface Area (m^2/g)	Average pore width (nm)
D0102–5–3	1.0/0.1	0.143	93.47	15.5	1080.9344	13.13017

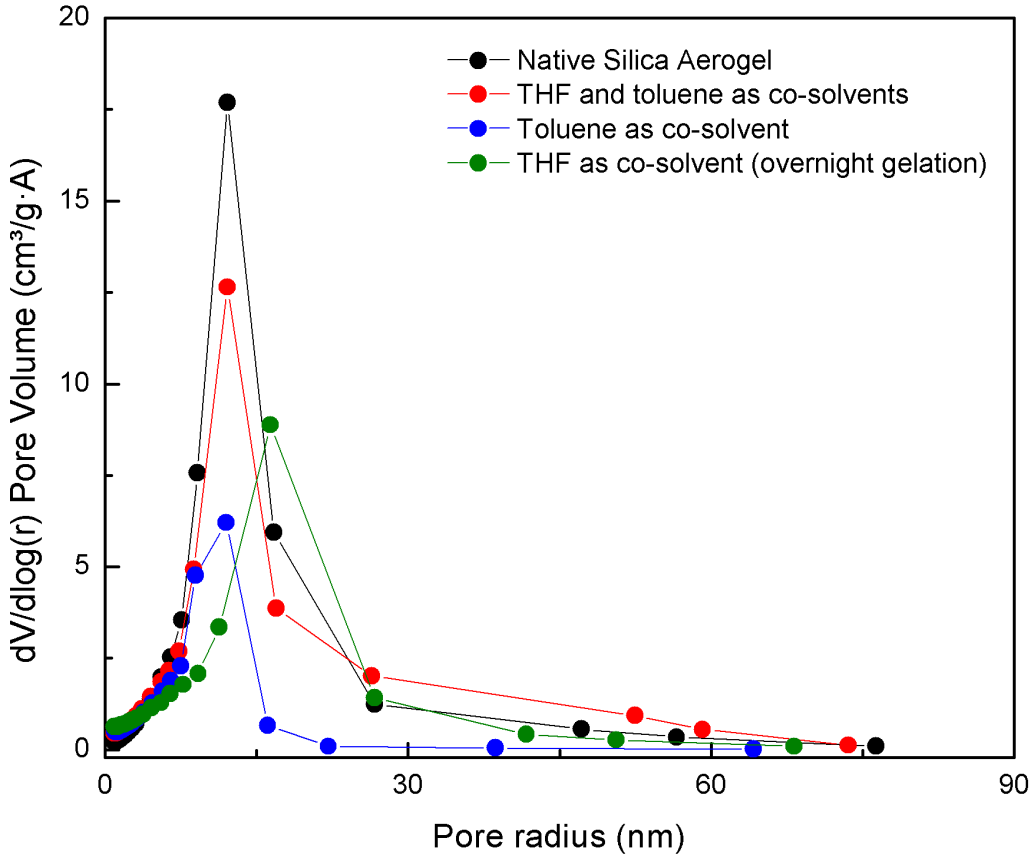

Figure 41 Pore size distribution of composites synthesized with THF and/or toluene as co–solvents together with native silica aerogel.

ATR–FTIR analysis of the PDMS(OH)–silica aerogel composite produced with both THF and toluene revealed the same peaks that are specific to the polymer and observed for the previous composites.

3.3.6. PDMS(OH)–Silica Aerogel Composites by Aging in PDMS(OH)

The PDMS(OH)–silica aerogel composite that was synthesized by placing the silica gel in PDMS(OH) was transparent after the supercritical drying. In Figure 42 the images of the composite and native silica aerogel are given. It is apparent that there is only a slight decrease in the transparency of the composite when compared to the native silica aerogel. In addition, in Figure 43 the ATR–FTIR spectra of native silica aerogel and the composite are compared. Only one of the typical polymer peaks was observed in the composite: C–H vibration peak that appears at 2963 cm^{-1} wavenumber. No experiments were carried out to investigate the homogenous distribution of the polymer molecules throughout the sample, however, no non-homogeneity was visually noticed in the appearance of the aerogel sample.

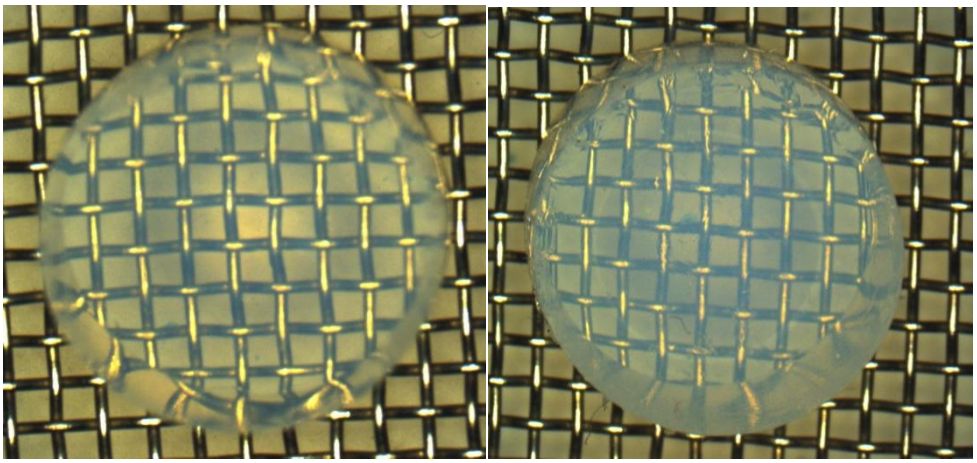

Figure 42 Top views of cylindrical–shaped native silica aerogel (left), PDMS(OH)–silica aerogel composite (right) that is produced by aging in polymer .

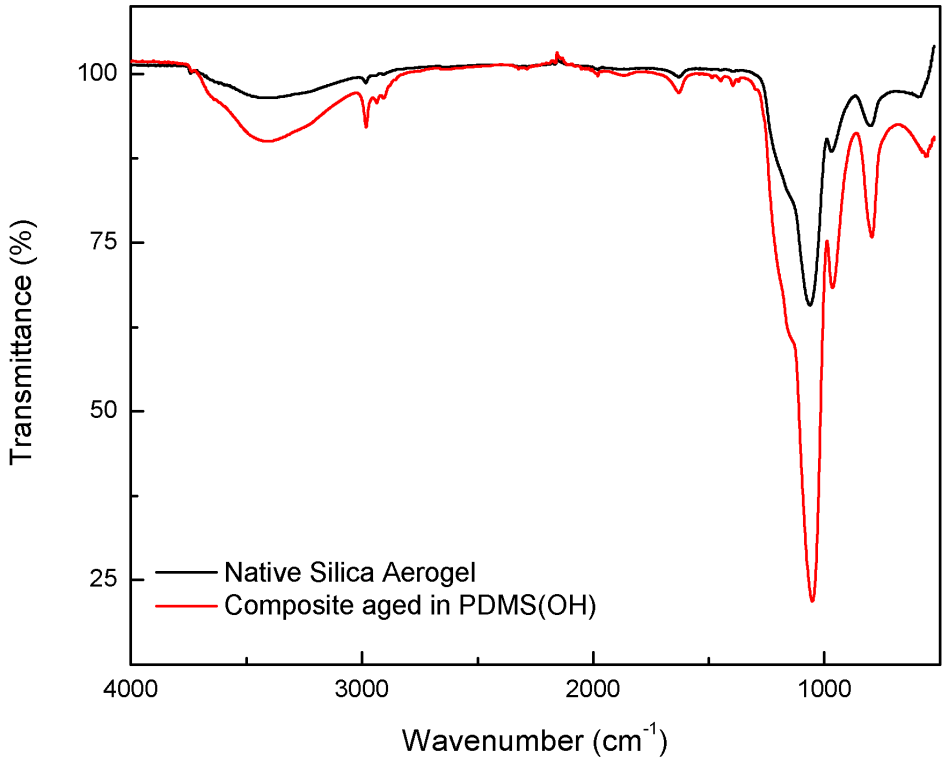

Figure 43 ATR–FTIR spectra of native silica aerogel and aerogel composite derived by aging in PDMS(OH) .

3.4. Summary and Conclusion

Composites of silica aerogels with PDMS(OH) and PDMS–bis(alkylOH) were developed by adjusting the two–step sol–gel process. The incorporation of the polymers to the synthesis procedure was performed at three different stages: before the hydrolysis, after the hydrolysis and during aging. Besides the addition step, the effects of several processing parameters, such

as aging solution, aging temperature, sol mixture composition, type and amount of co–solvent on the final composite properties were investigated.

Initially, standard sol–gel procedure was followed for the synthesis of the composites. The main drawback throughout the entire experimentation was that the polymers were not compatible with the sol–gel process since it is not possible to form single phase mixtures. Therefore the incompatibility resulted in non–homogenous aerogel composites in which the silica network and polymer were present as separate phases, regardless of different addition stages of the polymers. All of the composites could be obtained as crack–free monoliths and had improved mechanical toughness. The presence of the polymer was confirmed by ATR–FTIR analysis. However, the transparency was completely lost which was attributed to the formation of additional scattering centers by polymer phase. In addition, the porosity and surface area of the composites were reduced indicating the filling of the pores with the polymer.

Since the transparency is lost because of the immiscibility of the polymer with the sol mixture, two good solvents for PDMS, namely THF and toluene, were utilized in the synthesis to be able to form single phase mixtures and thus improve the transparency of the composites. Different amounts of THF and/or toluene were used in the synthesis as co–solvents. For the entire set of experiments, the presence of the polymer in the composites was confirmed with the ATR–FTIR analyses. When only THF was used as the co–solvent, the main problem was that the required amount of co–solvent to achieve the miscibility was very high (~44 wt.% of the sol mixture) which resulted in dilution of the sol mixture due to the excess amount of co–solvent. The dilution led to long gelation times, and soft and mechanically weak gels. As a result, the gels were either broken during the supercritical drying or had very high volumetric shrinkage, up to ~90%. When only toluene was used as the co–solvent, the drawbacks of dilution were similarly observed, although a smaller amount of toluene (~29 wt.% of the sol mixture) was sufficient to achieve miscible polymer–sol mixtures. The gels were broken after the supercritical drying or had ~64% volumetric shrinkage. However, when both THF and toluene are utilized as co–solvents, it was demonstrated that the high volumetric shrinkage due to the dilution can be decreased to ~16%. Moreover, the composite obtained with this route had a translucent appearance, very high surface area and low density. The pore size distribution was similar to the native silica aerogel.

Furthermore, composites of silica aerogels were also produced by placing the gels in neat PDMS(OH). It was observed that the transparency can be more or less retained when the polymer is incorporated after the solid silica network is formed.

One problem for the entire of the aforementioned processing techniques was that the exact amount of the polymer that was present in the composites could not be controlled properly. Since PDMS and its derivatives are highly soluble in $scCO_2$, most of the polymer that was added during the synthesis was probably extracted by $scCO_2$ during the drying step. In addition, TGA and ATR–FTIR analyses were insufficient for the determination of the amount of polymer in the composites since the composites were not homogenous and had different phases throughout the sample.

Nevertheless, it was demonstrated that opaque and translucent composites of silica aerogels with PDMS(OH) can be synthesized by properly modifying the conventional two–step sol–gel process. Moreover, it was revealed that the low density and small pore size of silica aerogels which is necessary for low thermal conductivity can be retained in the composites. Regarding these results, the composites developed by the modification of the conventional sol-gel process are suitable materials for use in opaque VIPs.

CHAPTER 4

PHASE BEHAVIOR & MODELING

4.1. Introduction

Over the past few decades, the modification of the surface chemistry of materials by reacting the surface groups with appropriate reagents has been an important research area with applications in many diverse fields. Silylation is one of the most frequently utilized surface modification techniques where a silane–based compound is employed as the modifying agent to introduce various functionalities to the surface. A surface is conventionally silylated by contacting it with a silylation reagent either from a gas phase or liquid phase. However, in recent years, a novel technique, namely supercritical reactive deposition has become especially attractive for the silylation of surfaces of porous nanostructured materials having high surface areas and various surface chemistries [67]. Performing the surface modification from the supercritical phase has significant advantages compared to conventional techniques such as enhanced mass transfer rates, uniform surface characteristics, and more importantly, control over the process, which allows for the fine–tuning of the desired properties by simply changing the temperature and/or pressure. The substantially high solubility of silane–based compounds in supercritical carbon dioxide ($scCO_2$) has spurred the developments in this area. Thus far, silylation from $scCO_2$ has been utilized for the modification of SiO_2 microparticles [68], TiO_2 nanoparticles [69-74], silica gels [75-76], silica aerogels [77], silicon wafers [78-85], nanoporous silica [81, 86], and methylsilsesquioxane films [87-91] by using several silane–based reagents including octadecyltrimethoxysilane (ODTMS), octadecyldimethylchlorosilane (ODMCS), hexamethyldisilizane (HMDS), octadecyltrichlorosilane (OTS), (dimethylamino)octadecyldimethylsilane, tetramethyldisilazane (TMDS), trimethylchlorosilane (TMCS), poly(dimethylsiloxane) (PDMS), diethyldichlorosilane (DEDCS), dibutyldichlorosilane (DBDCS), dimethyldichlorosilane (DMDCS), methyltrichlorosilane (MTCS).

Surface modification from a supercritical phase is especially attractive for silica aerogels since they are highly fragile structures which make the conventional liquid phase treatments almost impossible. In 2010, Kartal and Erkey converted the inherently hydrophilic surface of

silica aerogels to a hydrophobic surface by using HMDS dissolved in $scCO_2$ [92]. In a recent study of Sanz–Moral *et.al.*, hydrophobic silica aerogels were similarly produced by surface modification from $scCO_2$ utilizing trimethylethoxysilane, octyltrimethoxysilane and chlorotrimethylsilane [62]. Recently, we demonstrated that the surface of silica aerogels can be modified by employing a hydroxy–terminated form of PDMS (PDMS(OH)) from $scCO_2$ [93]. For the development of efficient supercritical CO_2 based processes, the knowledge of phase behavior of mixtures of silane–based modifying reagents with CO_2 is necessary. Thus far, very few studies involving the phase behavior data were reported which include the mixtures of CO_2 with chlorosilanes [94], octlytriethoxysilane [95], HMDS [92], PDMS [50, 96-100] and some other CO_2–philic oligomers [50, 53].

For synthesizing the composites of silica aerogels with PDMS(OH), the phase behavior information of PDMS(OH)-CO_2 binary mixtures is necessary since the process involves contacting silica aerogels with the single phase PDMS(OH)-CO_2 binary mixtures. Hence, prior to deriving composites, phase behavior measurements were carried out.

Initially, hexamethyldisiloxane (HMDS) was utilized in the measurements. HMDS is the smallest building block of PDMS with zero repeating unit while the chemical formula of PDMS is $(CH_3)_3Si\text{-}[O\text{-}Si(CH_3)_2]_n\text{-}O\text{-}Si(CH_3)_3$, n being the number of siloxane repeating units. The bubble and dew point pressures and densities of HMDS-CO_2 binary mixtures were determined. The measurements were performed at a wide temperature and composition range by using a constant volume view cell that is displayed in Figure 44. The bubble point pressure data were correlated using the Peng-Robinson Stryjek–Vera equation of state (PRSVEoS) and the binary interaction parameters for each temperature were regressed from experimental data. Furthermore, P-T data of the binary mixture at constant mixture densities were also obtained and excess volumes were calculated.

Following that study, the demixing pressures of binary mixtures of CO_2 with PDMS(OH) with different polymer molecular weights were determined using the same experimental setup. The demixing pressures of the binary mixtures were determined for an extensive fraction of the composition range, namely, up to 71.8 wt.% of PDMS(OH), and at three different temperatures (313.2 K, 323.2 K, 333.2 K). The bubble point data were correlated using the Sanchez–Lacombe equation of state (SLEoS) by regressing the binary interaction parameters at the studied temperatures. PDMS(OH)-CO_2 phase behavior data were further employed in deposition experiments.

4.2. Apparatus and Procedure for the Measurements

4.2.1. Experimental Setup for the Measurements

The demixing pressures of the binary mixtures were determined by visual observation in a constant volume high pressure view cell equipped with two sapphire windows of 3.2 cm diameter at each side, poly(ether ether ketone) O–rings and a rupture disk. The experimental setup that was employed for the measurements is depicted in Figure 44. A syringe pump (Teledyne ISCO model: 260D) was used for the transfer of CO_2 into the high pressure vessel. The accuracy of the syringe pump pressure transducer was ±0.1 MPa. Another pressure transducer (Omega PX4100) and a thermocouple (Omega GTMQSS–062G–6) were employed to record the temperature and pressure inside the vessel with a ± 0.1 K and ±0.1 MPa accuracy, respectively. The temperature of the vessel was controlled by circulating water through the machined internal channels of the vessel using a circulating heater (Cole–Parmer model: 12108–15). The temperature of the syringe pump was controlled at 298 K with a circulating heater (Cole–Parmer model: 12108–15) by circulating water through the jacket around the cylinder housing of the pump. A magnetic stirrer was used to mix the contents of the vessel.

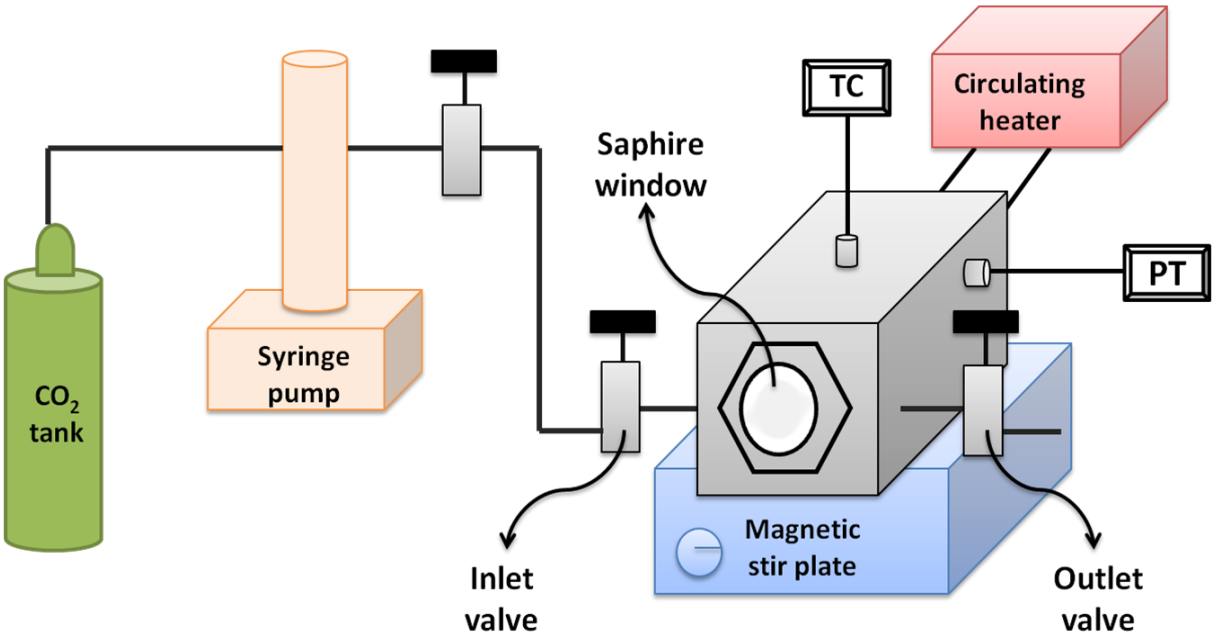

Figure 44 Experimental setup for the phase behavior measurements [101].

4.2.2. Measurement of Bubble Point Pressures and P-T-ρ Data of HMDS-CO_2 Binary Mixtures

For the bubble point and P-T-ρ measurements, the ranges for the mass of HMDS and CO_2 that were charged into the vessel were 2.51-35.21 g and 8.28-43.16 g, respectively. Initially, a certain amount of HMDS was weighed and placed inside the vessel. After sealing, the vessel was connected to the syringe pump. Prior to the liquid CO_2 charging, the lines and the vessel were flushed with CO_2 gas in order to eliminate the residual air. Keeping the inlet valve of the vessel closed, syringe pump was started. The exit valve of the syringe pump was opened and the pressure inside the syringe pump and the pressure in the line from the syringe pump to the inlet valve were brought to the desired pressure. The inlet valve of the vessel was then opened and liquid CO_2 was charged into the vessel until the pressure in the vessel reached the pressure in the line before the inlet valve of the vessel was opened. Subsequently, the inlet valve was closed and a single phase system was obtained inside the vessel. During the addition of CO_2 to the vessel, the volume change of CO_2 in the pump cylinder was recorded. The amount of CO_2 that was transferred into the system was determined using the density of CO_2 at the pump conditions and the volume change of CO_2 in the pump cylinder. The density of CO_2 at specific temperature and pressure was obtained from NIST database [102]. Consequently, the composition of the binary system was calculated from the amounts of HMDS and CO_2 added to the vessel. Following the addition of CO_2 at room temperature, the temperature of the vessel was brought to the experimental conditions using the circulating heater.

After a homogenous, single-phase mixture of HMDS and CO_2 was attained inside the high pressure vessel, the outlet valve of the vessel was slightly opened and adjusted to have a slow rate of depressurization at constant temperature. The homogeneity of the mixture in the vessel was accomplished with the slow rate of depressurization and rigorous mixing. The compositions of the outlet stream and the mixture inside the vessel do not change during the depressurization as long as the mixture is homogenous and single-phase. During the depressurization of the vessel, the appearance of the single phase system was continuously observed from the sapphire windows. At the phase separation point, a single bubble was detected to appear at the top of the cylindrically-shaped vessel. The outlet valve was instantly closed as soon as the formation of the bubble was noticed and the pressure at that point was recorded as the bubble point pressure of the binary mixture at that composition and temperature. Instead of the bubble point, dew point was also recognized at very low HMDS

contents where the single phase system was observed to transform into a mixture with a white cloudy appearance.

It is also possible to make successive measurements at the same composition and at different temperatures with the assumption that the formation of the small bubble does not alter the composition of the liquid phase as long as the outlet flow is immediately stopped as soon as the bubble point pressure is reached. Subsequent to the closure of the outlet valve, the vessel was heated to a higher temperature, during which the bubble or cloudy appearance disappeared. The binary mixture was observed to reach again a homogenous, single-phase state owing to the LCST behavior. The procedure explained above was repeated for various temperatures and bubble point pressures were recorded for the respective temperatures at the same composition. The measurements were repeated for various compositions by loading different amounts of HMDS and CO_2 to the vessel.

The same experimental set-up was also used to make P-T measurements at constant density. The vessel was filled with a certain amount of HMDS and CO_2 as described above. With the inlet and outlet valves closed, the density of the single phase mixture inside the vessel was calculated from the total amount of mass added to the vessel and the volume of the vessel chamber. The single phase mixture was then heated successively to higher temperatures and the pressure in the vessel at each temperature was recorded. From the recorded values, P-T-ρ behavior of the binary system was deducted. The volume of the vessel chamber which was needed for calculation of the mixture density was determined by filling the vessel with pure CO_2 at room temperature and various pressures (10.3 MPa, 14.4 MPa and 20.7 MPa) and by determining the volume change of CO_2 in the cylinder of the syringe pump. The experiment was repeated for four times at each pressure value and the volume of the vessel chamber was determined as 57.64 ± 0.13 mL by computing the average of the recorded values.

4.2.3. Measurement of Demixing Pressures of PDMS(OH)-CO_2 Binary Mixtures

The demixing pressure measurements of PDMS(OH)-CO_2 binary mixtures were carried out in a similar manner. Initially, a certain amount of polymer was weighed and placed inside the vessel. After it was sealed, the vessel was connected to the syringe pump and was flushed with CO_2 at atmospheric pressure in order to remove the air inside the vessel. While keeping the inlet valve of the vessel closed, the syringe pump was started and the desired pressure was attained in the line between the syringe pump and the vessel. The inlet valve of the vessel was then opened and liquid CO_2 was charged into the vessel until the set pressure was attained in

the vessel. Subsequently, the inlet valve was closed and a single phase mixture was obtained in the vessel which had a clear, homogenous appearance. During the addition of CO_2, the volume change in the pump cylinder was recorded. The mass of CO_2 that was transferred into the vessel was determined using the density of CO_2 at the pump conditions and the volume change of CO_2 in the pump cylinder. The density of CO_2 at the conditions of the pump was obtained from NIST database [103]. Consequently, the composition of the binary mixture was calculated from the masses of PDMS(OH) and CO_2 added to the vessel. Following the addition of CO_2 at room temperature, the temperature of the vessel was brought to the experimental conditions using the circulating heater. During the charging of CO_2 and demixing pressure measurements, the mixture in the vessel was continuously mixed with the stir bar to provide the homogeneity. The high molecular weight of the polymer did not cause any complication for the mixing of the solutions since the presence of the CO_2 lowered the viscosity of the polymer.

After a homogenous, single–phase mixture of PDMS(OH) and CO_2 was obtained inside the high pressure vessel, the outlet valve of the vessel was slightly opened and adjusted to have a slow rate of depressurization (~0.007 MPa/sec) at constant temperature. During the depressurization, the single phase mixture in the vessel was continuously observed from the sapphire windows. As the pressure was lowered, three different types of behavior were observed depending on the composition; cloud point, bubble point, or a color change. Such measurements of the phase behavior of HMDS–CO_2 and POSS–CO_2 binary mixtures were previously carried out with the same technique in a similar manner [92, 104].

It is important to note that the compositions of the outlet stream and the mixture inside the vessel do not change during depressurization as long as the mixture is homogenous and single–phase. Therefore, it was also possible to make successive measurements at the same composition and at different temperatures as long as the outlet flow was immediately stopped right after the detection of the changes. After the outlet valve was closed, the vessel was heated to a higher temperature, during which the binary mixture in the vessel again turned to a clear, homogenous and single–phase state due to the LCST type behavior. After the desired temperature was reached, the depressurization procedure explained above was repeated at that higher temperature and the demixing pressures were recorded at the same composition. The demixing pressures were determined at three temperatures with this procedure by consecutive heating of the binary mixtures. The measurements were repeated for various compositions which were obtained by charging the vessel with different amounts of PDMS(OH) and CO_2.

The measurements were performed with two different number averaged molecular weight PDMS(OH) (M_n=2750 and 18000). The demixing pressures were determined for various compositions and at three different temperatures, namely 313.2 K, 323.2 K and 333.2 K, for PDMS(OH)(M_n=2750)–CO_2 binary mixture, and at five different temperatures (313.2 K, 318.2 K, 323.2 K, 328.2 K and 333.2 K) for PDMS(OH)(M_n=18000)–CO_2 binary mixture.

4.3. Modeling of Phase Behavior

4.3.1. HMDS-CO_2 Binary Mixtures

The modeling of HMDS-CO_2 binary mixture was performed by employing Peng-Robinson Stryjek–Vera equation of state (PRSVEoS) together with Van der Waals one fluid mixing rules [105] using the software provided by Orbey and Sandler [106]. PRSVEoS is the modified form of Peng-Robinson Equation of State (PREoS) in the sense that the formulation for κ_i term is adjusted to depend not only on the acentric factor, ω_i, but also the reduced temperature, T_{r_i}. With this modification the vapor pressures of nonpolar, polar and associating compounds can be predicted with accuracy comparable to the Antoine equation [105]. The utilized equation of state is as follows.

$$P = \left(\frac{RT}{v-b}\right) - \left(\frac{a(T)}{v(v+b)+b(v-b)}\right) \tag{4.1}$$

with van der Waals mixing rules,

$$a = \sum_i \sum_j x_i x_j a_{ij} \tag{4.2}$$

$$b = \sum_i x_i b_i \tag{4.3}$$

$$a_{ij} = \sqrt{a_i a_j}\left(1 - k_{ij}\right) \tag{4.4}$$

In the above equations, subscripts i and j indicate HMDS and CO_2 and k_{ij} is the binary interaction parameter which depends on the nature of the molecular interaction between the species in the system which is determined by fitting the experimental data to the model. The parameters a and b for the pure components are given as follows:

$$a_i = 0.457235\left(\frac{\alpha\left(T_{r_i}\right)R^2T_{c_i}^2}{P_{c_i}}\right) \tag{4.5}$$

$$b_i = 0.077796\left(\frac{RT_{c_i}}{P_{c_i}}\right) \tag{4.6}$$

where

$$\alpha(T_{r_i}) = \left[1 + \kappa_i\left(1 - \sqrt{T_{r_i}}\right)\right]^2 \tag{4.7}$$

$$\kappa_i = \kappa_{0i} + \kappa_{1i}\left(1 + \sqrt{T_{r_i}}\right)\left(0.7 - T_{r_i}\right) \tag{4.8}$$

$$\kappa_{0i} = 0.378893 + 1.4397153\omega_i - 0.17131848{\omega_i}^2 + 0.0196554{\omega_i}^3 \tag{4.9}$$

In the above equations, T_r is the reduced temperature which is expressed as $T_r = T/T_c$, T and T_c being the system and critical temperature, respectively. P_c and ω are the critical pressure and acentric factor of each component, respectively. κ_{1i} is a component-specific parameter and it is calculated by fitting the vapor pressure data for each component.

The basic algorithm for the computation of the bubble and dew point pressures involves an iterative method since both the vapor phase composition and pressure are not known for the system. The binary interaction parameters that result in the minimum deviation at pressure were regressed from the experimental data for each temperature value. The basic steps of the algorithm that was followed in the computations are given in Figure 45.

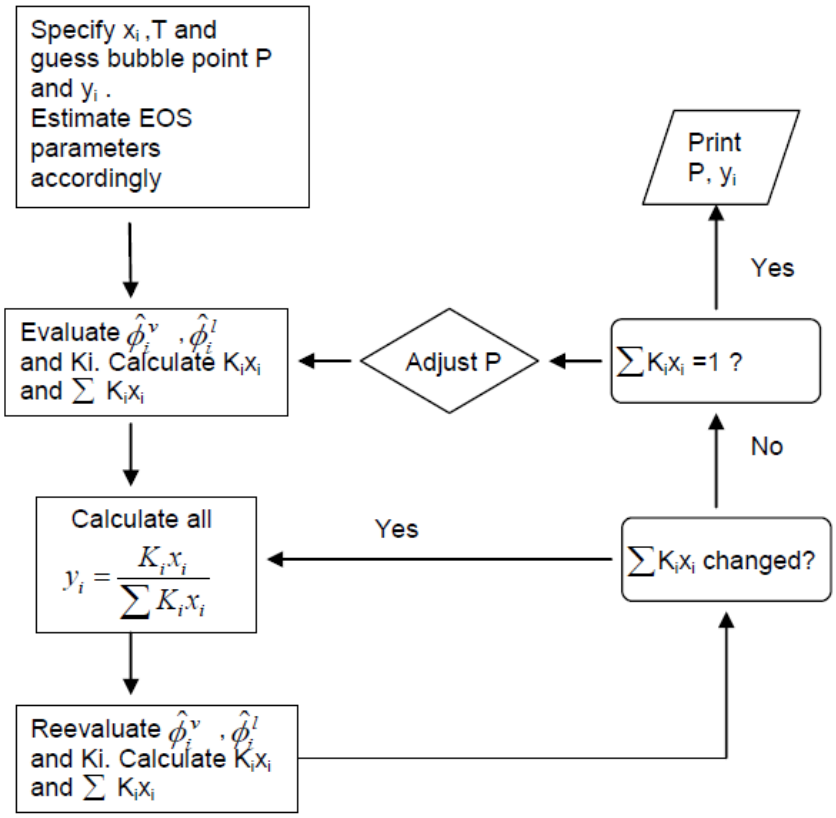

Figure 45 Algorithm for calculating the bubble point pressure.

4.3.2. PDMS(OH)-CO_2 Binary Mixtures

For the modeling of the bubble point pressure data of PDMS(OH)–CO_2 binary mixtures, Sanchez–Lacombe Equation of State (SLEoS) was employed which is known to be a well established model for the correlation of the thermodynamic properties of polymer blends as well as polymers in supercritical solutions [107]. SLEoS is applicable to polymers which are non–crystalline, not cross–linked or only slightly cross–linked, and that are above their melting temperatures [108]. By introducing the free volume (empty lattice sites) to account for the compressibility of the systems, SLEoS is derived from Ising (lattice) fluid model which is originally based on Flory–Huggins theory [97, 107, 109]. The SLEoS for a pure component is given by:

$$\tilde{\rho}^2 + \tilde{P} + \tilde{T}[ln(1-\tilde{\rho}) + (1-1/r)\tilde{\rho}] = 0 \tag{4.10}$$

where $\tilde{\rho}$, $\tilde{P}$ and $\tilde{T}$ are the reduced density, reduced pressure and reduced temperature, respectively, and r is the number of lattice sites occupied by a molecule of molecular weight M. The reduced parameters for pure components are defined as:

$$\tilde{T} = T/T^* \tag{4.11}$$

$$\tilde{P} = P/P^* \tag{4.12}$$

$$\tilde{\rho} = \rho/\rho^* \tag{4.13}$$

where T^*, P^* and ρ^* are the component characteristic temperature, pressure and density, respectively. For predicting the thermodynamic properties of mixtures, the mixing rules are employed to obtain the mixture characteristic parameters where an additional parameter, namely binary interaction parameter, δ_{ij} is introduced [108, 110]. Mixture characteristic pressure for the mixture is given by:

$$P^* = \sum_j \sum_i \emptyset_i \emptyset_j P^*_{ij} \tag{4.14}$$

where $\emptyset_i$ and $\emptyset_j$ are the close–packed volume fractions of components i and j and can be obtained by the following equation:

$$\emptyset_i = \frac{m_i/\rho_i^*}{\sum_j m_j/\rho_j^*} \tag{4.15}$$

The term P_{ij}^* is defined as:

$$P_{ij}^* = (P_i^* P_j^*)^{1/2}\left(1 - \delta_{ij}\right) \tag{4.16}$$

Where δ_{ij} is the only adjustable parameter in the model which is required to calculate the mixture characteristic parameters from the pure component characteristic parameters and it is obtained by regressing the experimental data. The characteristic temperature of a mixture can be obtained from:

$$\frac{T}{T^*} = \frac{\frac{\emptyset_i}{\widetilde{T_i}} + \eta\frac{\emptyset_j}{\widetilde{T_j}}}{\emptyset_i + \eta\emptyset_j} - \emptyset_i\emptyset_j\frac{\left(P_i^* + P_j^* - 2P_{ij}^*\right)v^*}{RT} \tag{4.17}$$

where,

$$\eta = v_i^*/v_j^* \tag{4.18}$$

The mixing rule for the characteristic volume is based on the assumption of conservation of the close–packed volume of each component and is given by:

$$v^* = \emptyset_i{}^0 v_i^* + \emptyset_j{}^0 v_j^* \tag{4.19}$$

where,

$$\emptyset_i{}^0 = \frac{m_i/(\rho_i^* v_i^*)}{\sum_j m_j/(\rho_j^* v_j^*)} \tag{4.20}$$

$$v_i^* = RT_i^*/P_i^* \tag{4.21}$$

At equilibrium, the criterion to be satisfied is the equality of the chemical potentials of a component at different phases.

$$\mu_1^I(T, P, \emptyset_i^C) = \mu_1^{II}(T, P, \emptyset_i^F) \tag{4.22}$$

where superscripts *I* and *II* represents different phases, and subscript 1 stands for CO_2. The chemical potential of CO_2 in phase *I* is given by [108]:

$$\mu_1^I(T, P, \emptyset_i^I) = RT\left\{ln\emptyset_1 + \left(1 - \frac{r_1}{r_2}\right)\emptyset_2 + r_1^0\tilde{\rho}\chi_1\emptyset_2^2\right\} + r_1^0 RT\left\{-\frac{\tilde{\rho}}{\widetilde{T_1}} + \frac{\widetilde{P_1}\tilde{v}}{\widetilde{T_1}} + \tilde{v}\left[(1-\tilde{\rho})\ln(1 - \tilde{\rho}) + \frac{\tilde{\rho}}{r_1^0} ln\tilde{\rho}\right]\right\} \tag{4.23}$$

The chemical potential of CO_2 in phase *II* and the chemical potential of polymer in phases *I* and *II* can be obtained in a similar manner by simply changing the subscripts and superscripts.

In the modeling, only the bubble point pressure data were employed. At the bubble point, the chemical potentials of the fluid phase with the known composition and the bubble phase (gas phase) which was taken as pure CO_2 were equated. The binary interaction parameters were regressed for each temperature and polymer mixture. The regression algorithm was based on the minimization of the objective function which was defined as:

$$f(\delta_{ij}) = \sum \left(w_{PDMS(OH)}^{experimental} - w_{PDMS(OH)}^{SLEoS} \right)^2 \tag{4.24}$$

Levenberg–Marquardt method was employed in the nonlinear regression procedures.

The input parameters for the model are the three pure component characteristic parameters for each component that are defined with Eqn. (4.11), (4.12) and (4.13). The characteristic parameters are generally obtained by fitting the pure component PVT data with the model equations (Eqn. 4.10). In the case of polymers, the liquid density data can be utilized to obtain the characteristic parameters [110]. The pure component characteristic parameters for CO_2 [108] and PDMS(CH_3) [98, 110] were taken from the literature considering the studied temperature and pressure ranges. The detailed description of the SLEoS model can be found elsewhere [110-111].

4.4. Results and Discussion

4.4.1. HMDS-CO_2 Binary Mixtures

4.4.1.1. Bubble and Dew Point Pressures

In order to investigate the accuracy of the measurement technique, the bubble point pressure measurements for the frequently investigated ethanol-carbon dioxide (C_2H_5OH-CO_2) binary mixture were carried out. The bubble point pressures of C_2H_5OH-CO_2 binary mixture at different compositions were determined and compared with the literature values. The measurements for each data points were repeated three times and the deviations were given as the error bars in Figure 46(a) to (c). The standard deviations are very low indicating that the data are very reproducible. The reported data for the bubble point pressures at 298.2 K for this binary mixture exhibit significant variations, especially for CO_2 mole fractions between 0.1 and 0.8 as displayed in Figure 46(a) [112-116]. Nevertheless, it can be also observed that the

values determined in this study agree very well with the values published by Chin *et. al.* and Mehl *et. al.* and also follow the same trend with the data of Gui *et. al.* [113-114, 117]. Moreover, according to Figure 46(b) and Figure 46(c), the bubble point pressures measured with the proposed technique at 313.2 K and 333.2 K were in very good agreement with the literature values [113-114, 118-128].

Before conducting further measurements with HMDS-CO_2 binary mixture, the bubble point pressures at the same composition (w_{CO2}=0.83) and at five temperatures were determined with four successive experiments in order to verify the reproducibility of the measurements for this binary mixture, as well. Figure 47 displays the results with standard deviations as error bars for each temperature. The highest standard deviation was ±0.15 MPa (2.6%) at 298.2 K and the lowest standard deviation was ±0.06 MPa (0.6%) at 333.2 K indicating that the data are reproducible.

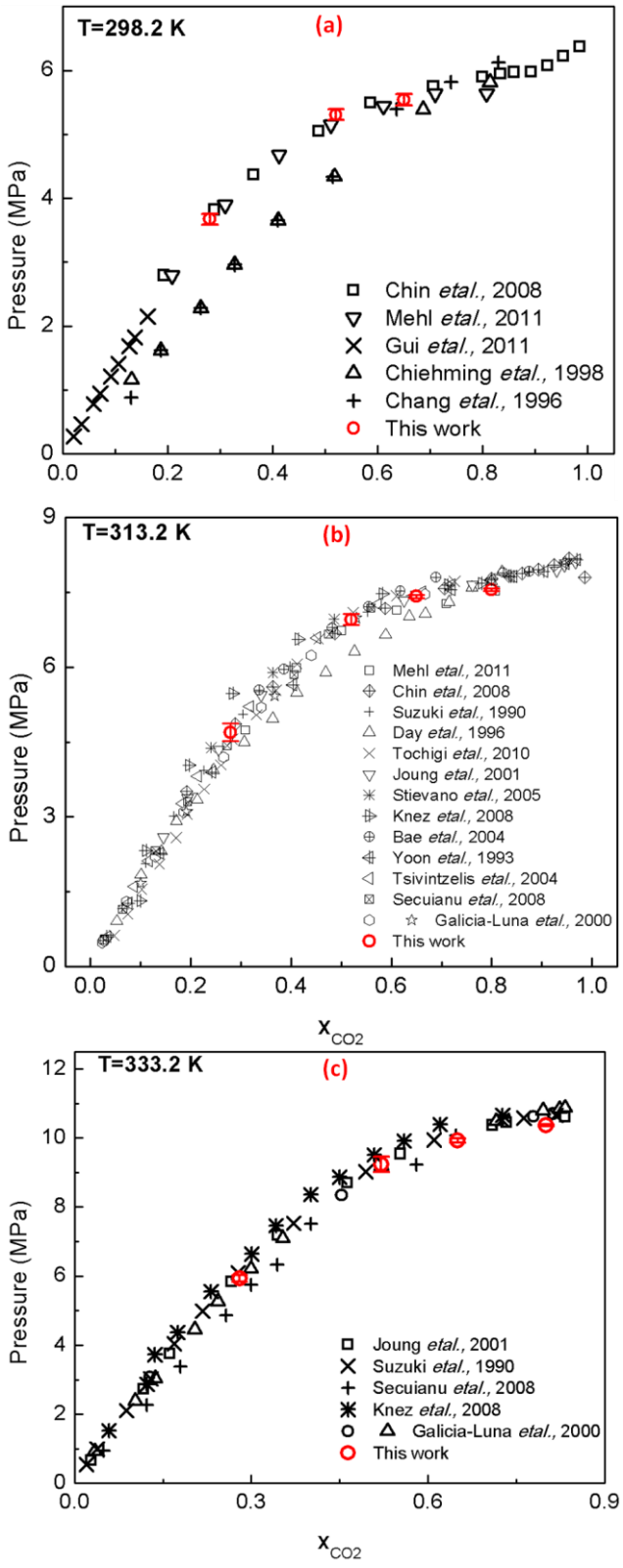

Figure 46 Comparison with literature values of bubble point pressures of C_2H_5OH-CO_2 binary mixture at (a) 298.2 K; (b) 313.2 K; (c) 333.2 K. The deviations in pressure for the data of the present work were represented as error bars.

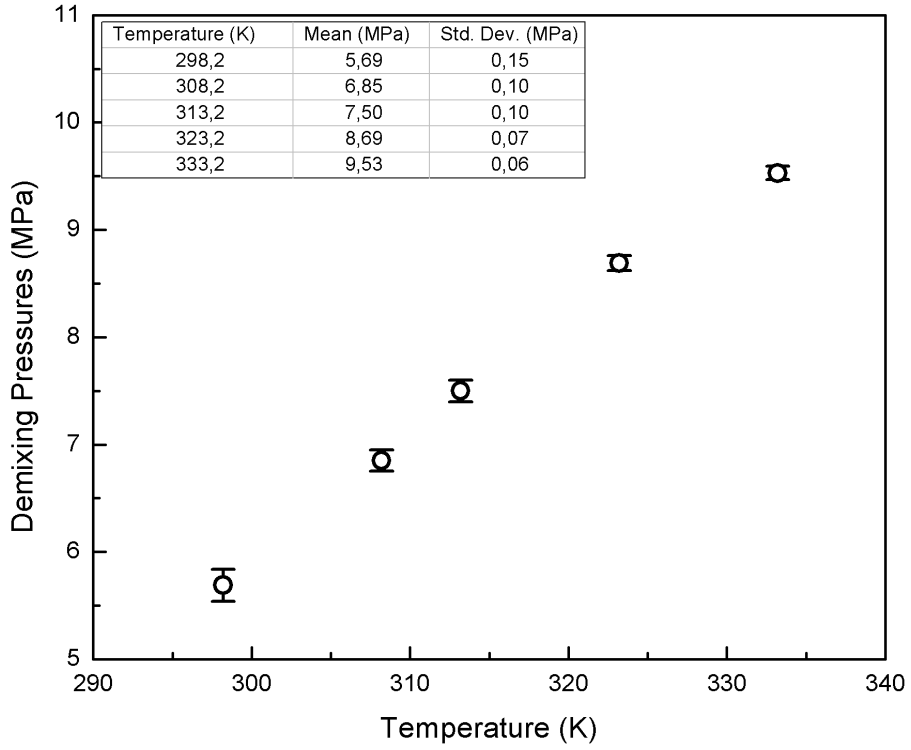

Figure 47 Reproducibility of bubble point pressure measurements of HMDS-CO_2 binary mixture at five temperatures (298.2 K, 308.2 K, 313.2 K, 323.2 K, 333.2 K) with CO_2 mass fraction of 0.83. The deviations in pressure were given as the error bars.

Figure 48 shows the bubble point pressures of the HMDS-CO_2 binary mixture at different CO_2 mole fractions and at five temperatures. The data are also listed in Table 18. For the highest two temperatures, namely 323.2 K and 333.2 K, and for CO_2 mole fractions greater than 0.94, the phase separations were observed to occur as dew points. The bubble point pressures at constant temperature increased with the increasing CO_2 mole fraction. This behavior was attributed to the low vapor pressure of HMDS (0.0042 MPa at 298.2 K) [129] that is well below the vapor pressure of CO_2 (6.401 MPa at 298.2 K) [102] which makes them the heavy and light components of the mixture, respectively. In addition, with the increasing temperature the bubble point pressures also increased at a fixed composition, which is typical for systems that show LCST behavior [130-131]. On the other hand, a decrease in dew point pressures was observed for increasing CO_2 mole fractions.

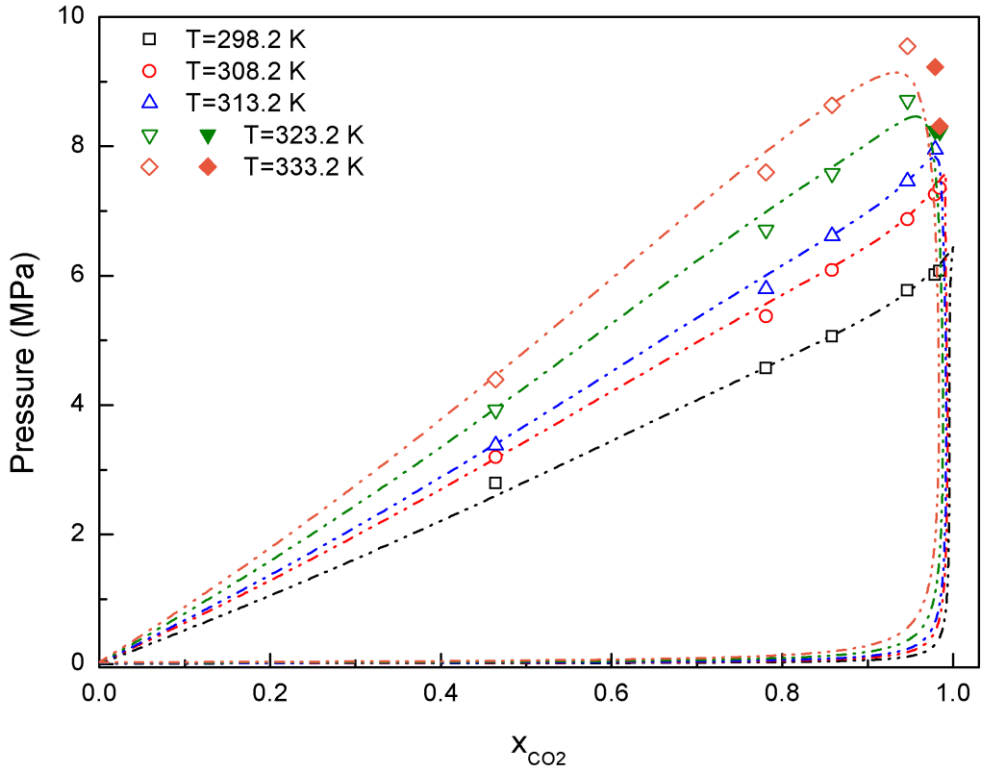

Figure 48 Bubble point and dew point pressures of HMDS-CO_2 binary mixture at different temperatures. The color filled symbols represents the dew points for the respective temperatures. The dashed lines represent the PRSVEoS model predictions for respective temperatures.

Table 18 Experimental bubble point pressures for HMDS-CO_2 binary mixture at various mole fractions of CO_2 and temperatures.

T = 298.2 K		**T = 308.2 K**		**T = 313.2 K**	
x_{CO2}	*P (MPa)*	x_{CO2}	*P (MPa)*	x_{CO2}	*P (MPa)*
0.98	6.1	0.98	7.4	0.97	8.0
0.97	6.0	0.97	7.3	0.95	7.5
0.95	5.8	0.95	6.9	0.86	6.6
0.86	5.1	0.86	6.1	0.78	5.8
0.78	4.6	0.78	5.4	0.46	3.4
0.46	2.8	0.46	3.2		

T =323.2 K		**T =333.2 K**	
x_{CO2}	*P (MPa)*	x_{CO2}	*P (MPa)*
0.98	8.2 (DP)	0.98	8.3 (DP)
0.97	8.2 (DP)	0.97	9.2 (DP)
0.95	8.7	0.95	9.6

0.86	7.6	0.86	8.6
0.78	6.7	0.78	7.6
0.46	3.9	0.46	4.4

DP: Dew point

4.4.1.2. Modeling Results

For modeling the phase behavior of HMDS-CO_2 binary mixture, κ_{1i} for HMDS and CO_2 were computed by fitting the vapor pressure data of each species and are summarized in Table 19 together with the pure component critical properties and acentric factors [129-130]. The absolute average errors for optimizing κ_{1i} values were 1.28% for CO_2 and 0.4% for HMDS. With the obtained κ_{1i} values, the binary interaction parameters, k_{ij}, were computed for each experimental temperature by fitting the experimental bubble point pressure data using the PRSVEoS as explained previously in section 2.4. [106].

The regression results for the computation of k_{ij} values are listed in Table 20 together with the average absolute error values (AAE %). The k_{ij} values were found to increase almost linearly with increasing temperature as shown in Figure 49. The computed k_{ij} values were able to predict the experimental data with errors smaller than 2% for each temperature. The maximum average absolute error was 1.49 % at 333.2 K whereas the minimum error was 0.58 % at 308.2 K.

Table 19 Thermodynamic parameters of HMDS and CO_2 together with the optimized κ1 values. The average absolute errors (AAE %) were computed from the experimental and calculated vapor pressure data.

Material	T_c (K)	P_c (MPa)	ω	κ_1	AAE (%)
CO_2	304.19	7.325	0.23	0.108	1.28
HDMS	518.7	1.925	0.42	0.0152	0.4

Table 20 Computed binary interaction parameters. AAE (%) values were calculated from the experimental and computed pressures.

T (K)	k_{ij}	AAE (%)
298.2	0.0568	0.69
308.2	0.0748	0.58
313.2	0.0764	0.92
323.2	0.0875	1.41

333.2	0.0947	1.49

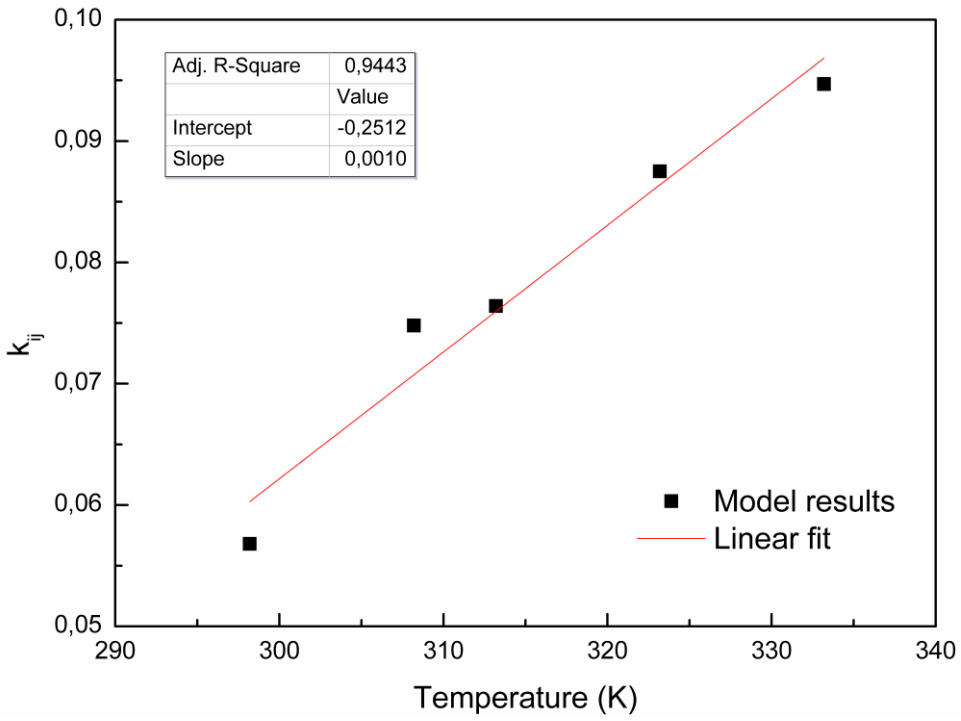

Figure 49 Variation of k_{ij} with temperature.

With the regressed k_{ij} values, single phase and two-phase P-x-T regions of the binary mixture were predicted for the entire composition range. The computed P-x-T regions along with the experimental data points are displayed in Figure 48 at each temperature. It is obvious from these figures that the predictions of the model agree very well with the experimental values with small deviations.

Additionally, the P-T projection of the critical locus of HMDS-CO_2 binary mixture was computed with PRSVEoS for each k_{ij} value by using GPEC software [131]. As shown in Figure 50, HMDS-CO_2 binary mixture was found to exhibit Type II phase behavior where, in addition to the continuous l=g curve, one can also observe a l_2=l_1 critical curve and a l_2l_1g three phase curve at low temperature values, intersecting at UCEP (Upper Critical End Point) ((l_2=l_1)+g). The l_2=l_1 critical curve runs steeply to high pressure values and represents upper critical solution temperatures. There is no experimental evidence about the existence of a l_2=l_1 critical curve and a l_2l_1g three phase curve since there is no previous study of this binary system. Thus, the critical locus displayed in Figure 6 should further be investigated experimentally to test the reliability of the model predictions. In P-T-x space, a two phase (l_2+l_1) region is observed at temperatures lower than the l_2=l_1 critical curve and pressures higher than the l_2l_1g three phase curve. The difference between k_{ij} values does not seem to

have a significant effect on the P-T projection since the only noticeable deviation was the shift of l_2=l_1 critical curve to higher temperatures with increasing k_{ij} values.

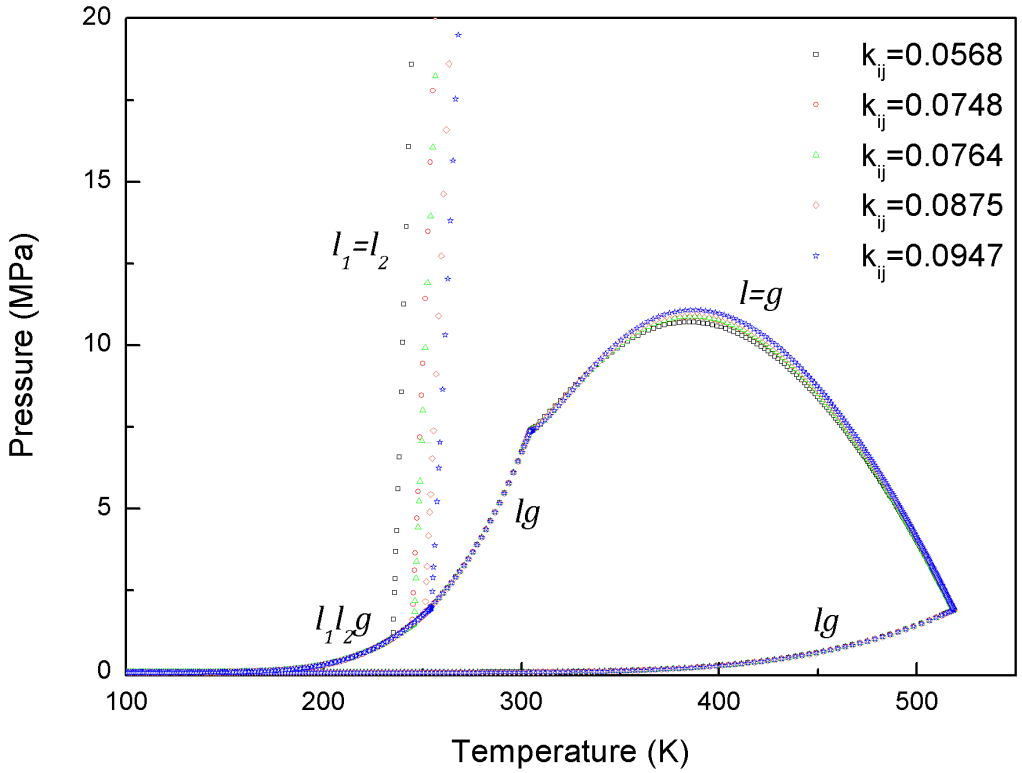

Figure 50 P-T projection of HMDS-CO_2 binary mixture computed for each k_{ij} value.

4.4.1.3. CO_2 Capture Capacity

Over the past few decades, a significant number of studies have focused on search of CO_2-philic molecules for a wide variety of applications involving supercritical carbon dioxide ($scCO_2$). These started with the pioneering study of Laintz et al. who discovered that the solubilities of fluorinated metal diethyldithiocarbamates in supercritical carbon dioxide ($scCO_2$) were about 1000 times more than their non-fluorinated analogs [132]. The hypothesis which formed the basis for this investigation emerged from realization that some of the fluorinated compounds which were being tested as blood-substitutes at the time had very high capacities to dissolve CO_2. The authors correctly hypothesized that the reverse, namely compounds having fluoroalkyl groups having high solubilities in $scCO_2$, may also be true. Subsequently, a number of reagents and polymers containing CO_2-philic moieties such as fluoroalkyl, fluoroether, phosphazene, siloxane and fluoroacrylate have been investigated or developed for applications involving $scCO_2$ [133].

On a similar note, Miller et al. recently hypothesized that oligomers and polymers that have high solubility in $scCO_2$ may have high CO_2 absorbing capacities and therefore may be good candidates as sorbents to remove CO_2 from gas streams [134]. The authors investigated CO_2 absorption capacity of various oligomers including polyethyleneglycol dimethylether, polypropyleneglycol dimethylether (PPGDME), polypropyleneglycol diacetate, polybutyleneglycol diacetate, polytetramethyleneetherglycol diacetate, glyceryl triacetate, polydimethylsiloxane (PDMS), and perfluorpolyether at two different temperatures. The demixing pressures of the binary mixtures of these compounds with CO_2 were compared with the values of the commercial CO_2 sorbent, Selexol. The demixing pressures of PDMS (M_n=550) were demonstrated to be comparable to Selexol indicating a similar CO_2 absorption capacity [134]. It was suggested that PDMS was more advantageous than Selexol since its lower kinematic viscosity (2 mm^2/sec) than Selexol (ν=5.73 mm^2/sec) would lead to lower pumping costs and mass transfer resistances. In addition, it was suggested that the immiscibility of PDMS with water brought an additional advantage in the CO_2-capture step at the downstream of water-gas shift reactor of the IGCC process since Selexol is completely miscible with water in all proportions.

PDMS is one of the few CO_2-philic polymers with a high solubility in $scCO_2$. Even though the exact reason behind this phenomenon is not known, it is most likely due to the ability of CO_2 molecules to mediate the attractive intra-chain forces responsible for the solvent-polymer demixing [135]. It was also demonstrated that this favorable interaction led to the viscosity reduction of PDMS using supercritical CO_2 [98, 136-137].

The chemical formula of PDMS is $(CH_3)_3Si\text{-}[O\text{-}Si(CH_3)_2]_n\text{-}O\text{-}Si(CH_3)_3$ where n is the number of siloxane repeating units. When n is equal to zero, the resulting compound is hexamethyldisiloxane (HMDS). It is a well-known phenomenon that the solubility of polymers in $scCO_2$ increases with the decreasing molecular mass of the polymer [138-139]. Therefore, being the smallest PDMS molecule, HMDS may have higher capacity for CO_2 compared to PDMS oligomers with larger molecular masses.

In light of the considerations given above, HMDS could be an even more advantageous sorbent for CO_2-capture since its kinematic viscosity (ν =0.65 mm^2/s) is much lower than PDMS and Selexol, and it is completely immiscible with water similar to PDMS. With regard to CO_2 uptake capacities, the bubble point pressures of HMDS-CO_2 mixture are compared with the demixing pressures of PDMS-CO_2 and Selexol-CO_2 binary mixtures in Figure 51(a)

and Figure 51(b). The data of PDMS-CO_2 and Selexol-CO_2 mixtures were taken from the study of Miller *et.al.* in which the measurements were performed at 298.2 K and 313.2 K. As shown in Figure 51(a) and Figure 51(b), at a fixed pressure the solvent mass fraction is appreciably lower for HMDS-CO_2 mixture compared to the two other binary mixtures which demonstrates that the amount of CO_2 which can be dissolved by HMDS is greater compared to PDMS and Selexol. Moreover, Selexol was previously reported to have a CO_2 capacity of 4.51 $mol_{CO2}/kg_{Selexol}$ at 40 bar and 313 K [140]. With the results displayed in Figure 51(b), the CO_2 absorption capacity of Selexol was computed to be 5.68 $mol_{CO2}/kg_{Selexol}$ whereas that of HMDS was found as 7.5 mol_{CO2}/kg_{HMDS} under the same conditions. The variation between the reported and calculated values of CO_2 solubility in Selexol probably originates from the difference in the molecular weights since Selexol is formed from a mixture of dimethyl ethers of polyethylene glycol and has a molecular weight range of 178-443 g/mol. Nevertheless, the CO_2 solubility in HMDS was almost two fold of that of Selexol which demonstrates the enhanced CO_2 capacity of HMDS compared to Selexol.

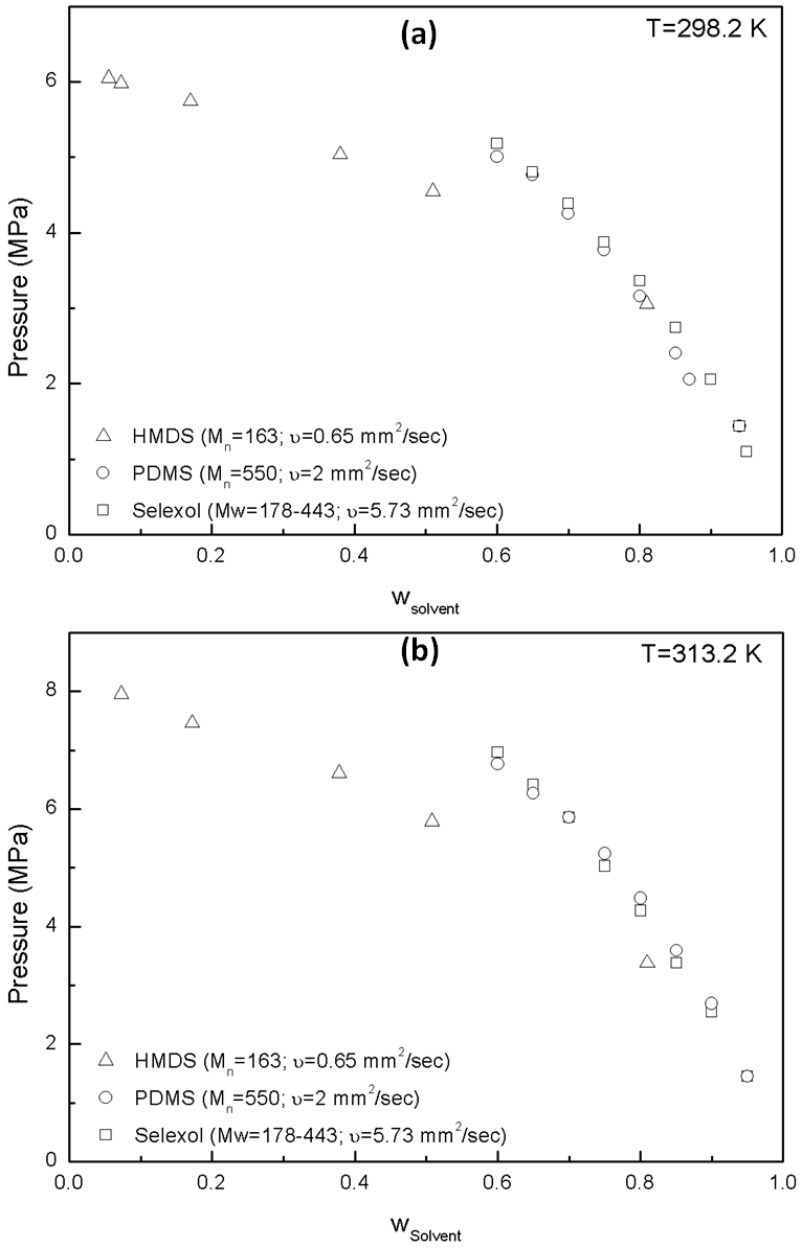

Figure 51 Demixing pressures of HMDS-CO_2, PDMS-CO_2 and Selexol-CO_2 binary mixtures at (a) 298.2 K and (b) 313.2 K.

Since CO_2 uptake at atmospheric pressure generally is of interest for determining the potential of a particular solvent for most of the CO_2 capture applications, the liquid and vapor phase mole fractions of HMDS-CO_2 binary mixture at atmospheric pressure were predicted from the model results to assess the viability of HMDS as CO_2 absorbent. The liquid and vapor phase mole fractions at 1 atm were computed with the regressed k_{ij} values. Table 21 lists the results of these predictions. Considering the liquid phase mole fractions, the CO_2 uptake capacity of HMDS at atmospheric pressure is around 1-2% and decreases with increasing temperature. However, the amount of HMDS in the vapor phase is rather high and increases at higher

temperatures, which may not be desirable for CO_2 capture applications. Therefore, a higher molecular mass oligomer of dimethylsiloxane unit may be more suitable as a CO_2 absorbent due to a lower vapor pressure value. For instance, the vapor pressure of HMDS (M_n=163 g/gmol; kinematic viscosity (ν) =0.65 mm^2/s) at 298.2 K is 0.0042 MPa whereas the vapor pressure of octamethyltrisiloxane with a repeating unit of 1 (M_n=237 g/gmol; kinematic viscosity (ν) =1 mm^2/s) is 0.00053 MPa and the vapor pressure of decamethyltetrasiloxane with repeating unit of 2 (M_n=310.7 g/gmol; kinematic viscosity (ν) =1.5 mm^2/s) is 0.000057 MPa at the same temperature. When compared to the vapor pressure of Selexol which is $9.3x10^{-8}$ MPa at 298 K, the vapor pressures of the abovementioned compounds still seems to be high. However, solvent losses in the vapor phase may be sufficiently small since the given values are quite low despite being higher than the vapor pressure of Selexol.

Table 21 Computed liquid and vapor phase mole fractions for HMDS-CO2 binary mixture at 1 atm.

T(K)	P(MPa)	x_{CO2}	x_{HMDS}	y_{CO2}	y_{HMDS}
298.2	0.10056	0.01880	0.9812	0.9403	0.05966
308.2	0.10023	0.01487	0.9851	0.9039	0.09614
313.2	0.10060	0.01369	0.9863	0.8802	0.1198
323.2	0.10080	0.01110	0.9889	0.8178	0.1822
333.2	0.10148	0.00898	0.9910	0.7322	0.2678

With these considerations, one can conclude that increasing the molecular mass of the oligomer leads to a reduction in CO_2 absorption capacity, as well as an increase in pumping costs due to increased viscosity. However, the vapor pressure of the sorbent decreases leading to lower fractions of the oligomer in the vapor phase. Hence, the most appropriate dimethylsiloxane based compound for CO_2 capture applications can be discovered by exploring the phase behavior of binary mixtures of CO_2 and dimethylsiloxane oligomers with different molecular masses. This investigation will be the concern of future studies.

4.4.1.4. P-T-ρ Measurements

Measurements at constant mixture densities were also conducted to determine the P-T behavior of single phase HMDS-CO_2 binary mixtures. Initially, P-T measurements with pure CO_2 were carried out at three different densities and the data were compared with the values obtained from NIST database [102] as well as the IUPAC equation of state (IUPAC EoS) with 52 parameters [141] in order to examine whether the technique is suitable for density

measurements. The results are given in Figure 52 shows that the measured P-T values are in very good agreement with the values obtained from NIST database and the IUPAC EoS for all three densities. In addition, successive P-T measurements were performed with the HMDS-CO_2 binary mixture for a mixture density of 812 kg/m^3 and CO_2 mole fraction of 0.95 to assess the reproducibility of the measurements for this mixture, as well. The pressures were obtained as 10.9±0.003 MPa at 303.2 K, 13.4±0.015 MPa at 308.2 K, 16.0 ±0.03 MPa at 313.2 K, 18.6±0.015 MPa at 318.2 K, 21.1±0.036 MPa at 323.2 K, 23.6±0.15 MPa at 328.2 K, and 26.0±0.19 MPa at 333.2 K. The small deviations in pressure indicate the excellent reproducibility of the data for HMDS-CO_2 binary mixture.

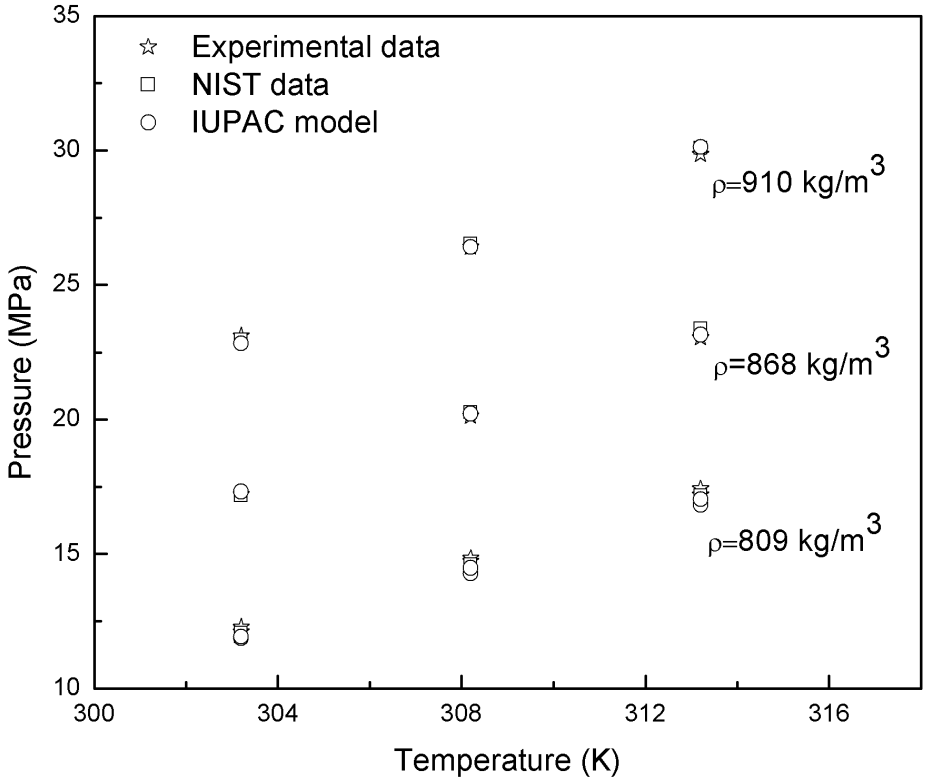

Figure 52 Variation of temperature with pressure for pure CO_2 with densities of 809 kg/m^3, 868 kg/m^3, and 910 kg/m^3.

P-T measurements of single phase HMDS-CO_2 binary mixture at various mixture densities and CO_2 mole fractions are given in Table 22. Figure 53(a) displays the P-T data for identical mixture densities but with two different CO_2 mole fractions. At a fixed temperature pressure was observed to shift to a higher value with increasing CO_2 fraction which originates from CO_2 being the lighter component in the HMDS-CO_2 mixture. In addition, the P-T data of two different mixture densities for the same CO_2 mole fraction are shown in Figure 53(b). The

increase in pressure with the increasing mixture density observed in Figure 53(b), was also reasonable by means of the thermodynamic relation between the density and pressure.

Table 22 Experimental P-T data and calculated excess volumes (V^{Excess}) of HMDS-CO_2 binary mixture at various mixture densities and CO_2 mole fractions.

		T=303.2 K		*T=308.2 K*		*T=313.2 K*	
x_{CO2}	ρ_{mix} (g/cm^3)	*P (MPa)*	V^{Excess} (cm^3/mol)	*P (MPa)*	V^{Excess} (cm^3/mol)	*P (MPa)*	V^{Excess} (cm^3/mol)
0.79	0.803	9.6	-5.77	12.4	-6.10	15.3	-6.43
0.81	0.848	14.8	-6.70	17.8	-7.00	20.8	-7.30
0.85	0.803	11.5	-2.43	14.3	-2.67	17.1	-2.90
0.87	0.884	13.5	-8.39	16.5	-8.60	19.5	-8.80
0.95	0.838	13.2	-3.56	15.9	-3.64	18.7	-3.72
0.95	0.812	10.9	-1.80	13.4	-1.88	16.0	-1.96

		T=318.2 K		*T=323.2 K*		*T=328.2 K*	
x_{CO2}	ρ_{mix} (g/cm^3)	*P (MPa)*	V^{Excess} (cm^3/mol)	*P (MPa)*	V^{Excess} (cm^3/mol)	*P (MPa)*	V^{Excess} (cm^3/mol)
0.79	0.803	18.2	-6.77	21.0	-7.11	23.8	-7.46
0.81	0.848	23.7	-7.61	26.4	-7.92	29.0	-8.23
0.85	0.803	19.9	-3.15	22.7	-3.39	25.5	-3.64
0.87	0.884	22.4	-9.01	25.3	-9.23	28.0	-9.44
0.95	0.838	21.5	-3.80	24.2	-3.88	26.7	-3.97
0.95	0.812	18.6	-2.04	21.1	-2.12	23.7	-2.20

		T=333.2 K	
x_{CO2}	ρ_{mix} (g/cm^3)	*P (MPa)*	V^{Excess} (cm^3/mol)
0.79	0.803	26.6	-7.82
0.81	0.848	31.6	-8.55
0.85	0.803	28.2	-3.89
0.87	0.884	30.9	-9.66
0.95	0.838	29.4	-4.05
0.95	0.812	26.2	-2.29

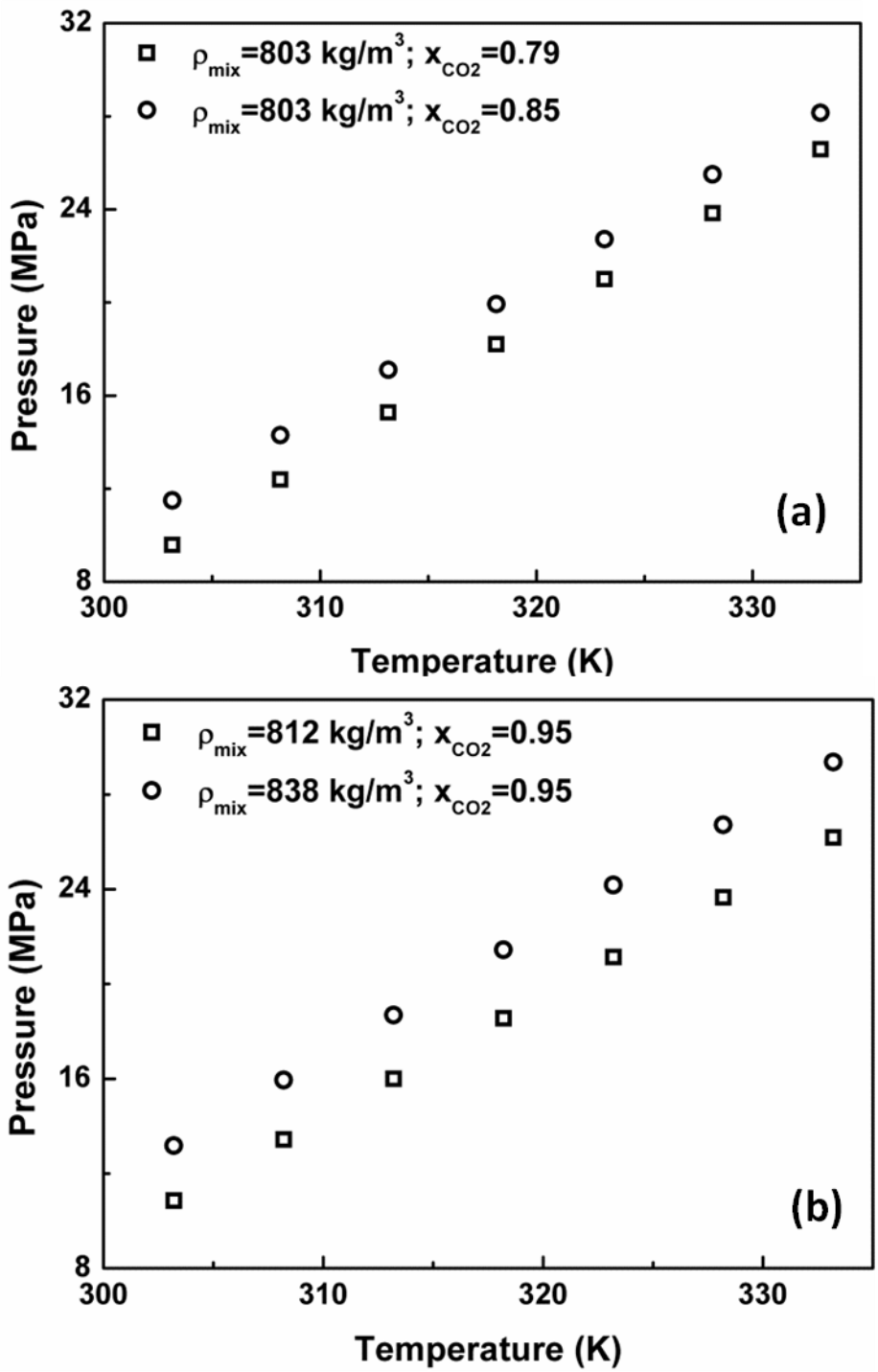

Figure 53 Variation of temperature with pressure for HMDS-CO_2 binary mixture at; (a) fixed ρmix=803 kg/m^3 and at two different CO_2 mole fractions; (b) fixed x_{CO2}=0.95 and at two different mixture densities.

4.4.1.5. Excess Volume Calculations

The excess molar volumes of HMDS-CO_2 binary mixture were computed at 298.2 K, the temperature at which the loading of the components to the vessel was performed. The following equation was utilized for the calculations.

$$V^{Excess} = \left[\frac{x_1 M_1 + x_2 M_2}{\rho_{mix}}\right] - \left[\left(\frac{x_1 M_1}{\rho_1}\right) + \left(\frac{x_2 M_2}{\rho_2}\right)\right] \quad (4.25)$$

where x_1 and x_2 are the mole fractions of CO_2 and HMDS, M_1 and M_2 are the molecular masses of CO_2 and HMDS, ρ_1 and ρ_2 are the pure component densities of CO_2 and HMDS, and ρ_{mix} is the mixture density. The pure component densities of CO_2 and HMDS at 298.2 K were taken from the literature [102, 142].

The calculated excess volumes are listed in Table 22 along with the P-T-ρ data. All of the excess volumes calculated for HMDS-CO_2 binary mixture were found to be negative. In principle, the excess volume indicates how much the two components of a mixture like each other. In the ideal case, when there is no intermolecular interaction between the molecules of the components of a mixture, the excess volume is equal to zero, that is, the volume of the mixture is equal to the sum of the volumes of the components. When two components of a mixture do not have a favorable interaction, then the molecules of the two components tend to be as far as possible from each other and as a result the volume of the mixture is greater than the sum of the volumes components, that is, the excess volume has a positive value. On the other hand, when the molecules of the components have attractive interactions they tend to have a close-packed molecular order in the mixture. As a result, the volume of the mixture is smaller than the sum of the volumes of the components and a negative excess volume is obtained for such mixtures. Ideality of a mixture can be judged considering how far or close the excess volumes to zero. Regarding HMDS-CO_2 binary mixtures, it is apparent that HMDS and CO_2 molecules form attractive intermolecular interactions with each other resulting in negative excess volumes. Figure 54 displays the variation of calculated values with CO_2 mole fraction at various temperatures. The excess volumes became more negative with increasing temperature. Therefore, it can be concluded that with increasing temperature the interactions become more favorable causing HMDS and CO_2 molecules to adopt a more closely-packed order. However, it is important to note that, the effect of temperature was more pronounced at low CO_2 fractions, such that at high CO_2 contents the excess volumes for different temperatures approach each other.

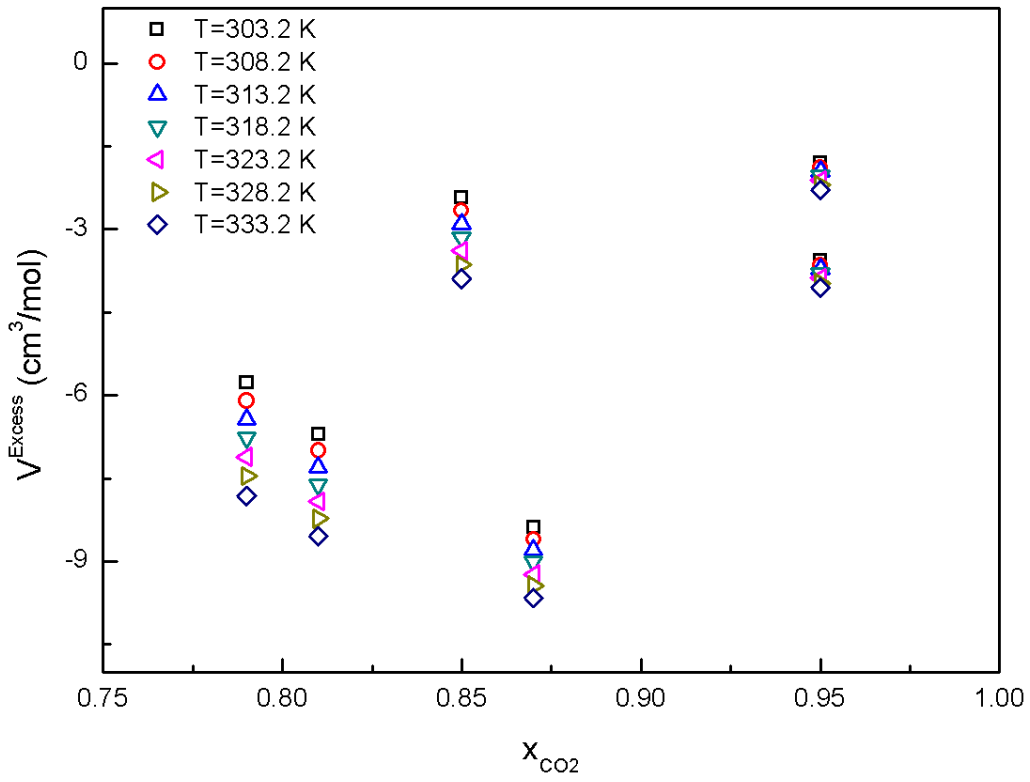

Figure 54 Excess volumes of HMDS-CO_2 binary mixtures at various temperatures and CO_2 mole fractions.

4.4.2. PDMS(OH)-CO_2 Binary Mixtures

4.4.2.1. The Demixing Pressures

The demixing pressures of PDMS(OH)–CO_2 binary mixtures were measured for an extensive composition range. The demixing pressures of PDMS(OH)–CO_2 mixture with the polymer with number–average molecular weight of 2750 g/mol are displayed in Figure 55 for various CO_2 weight fractions and at three different temperatures. Different types of behavior were observed at different composition intervals and represented with different markers in Figure 55. At high CO_2 weight fractions, namely, CO_2 fractions greater than 0.85, the appearance of the binary mixture was slowly transformed from transparent and homogenous to a white cloud. It is well–known that for the polymer mixtures the cloud point transitions occur over a pressure interval of around 5–7 bar [139]. Similar transition intervals were also observed for PDMS(OH)–CO_2 binary mixtures. However, the pressure where this transformation was first noticed was taken as the cloud point pressure.

At higher PDMS(OH) fractions, that is for CO_2 weight fractions up to 0.546, a small bubble of CO_2 was found to instantly form at the top of the vessel chamber and these pressures were

recorded as the bubble point pressures. Additionally, for CO_2 weight fractions between 0.706 and 0.794 the color of the mixtures were observed to change slowly first to yellow, then to brown and finally to black where all the light was absorbed and no visual observation was possible through the sapphire windows. During this color change, the mixtures were homogenous, clear and single–phase and no phase separation either as a cloud or bubble formation was observed. Kirby and McHugh stated that the critical point for CO_2–polymer mixtures is not observed at the maximum of the coexistence curve of a typical P–x diagram and shifts to higher polymer compositions and lower pressures when compared to the small molecule–supercritical fluid mixtures [139]. Therefore, the color change was attributed to being at a state close to the critical point of the mixture and the pressures where all the light was absorbed by the mixtures were noted as the mixture critical points.

As given in Figure 55, the demixing pressures were observed to decrease with the increasing polymer content at constant temperature. This trend was attributed to the much lower vapor pressure of PDMS(OH) than CO_2 which makes it the heavy component of the binary mixture. Figure 55 additionally shows that the demixing pressures increased with the increasing temperature at constant composition which is a typical LCST behavior. The LCST behavior was also observed by Kiran's group for PDMS(CH_3)–CO_2 binary mixtures for specific composition and temperature ranges [96-97].

Similarly, Figure 56 displays the demixing pressures of PDMS(OH)–CO_2 binary mixture with a polymer number–average molecular weight of 18000 g/mol for various compositions and at three temperatures. Similar behavior was also observed for these binary mixtures. Bubble points were observed up to a CO_2 weight fractions of 0.515, color change for w_{CO2} between 0.713 and 0.818, and cloud point for w_{CO2} greater than 0.9 [101]. Different markers in Figure 56 represent the respective type of the phase separation. The same LCST behavior was also observed for these binary mixtures up to CO_2 weight fraction of 0.95, that is, the demixing pressures decreased with the increasing PDMS(OH) fraction at constant temperature and increased with the increasing temperature at constant composition.

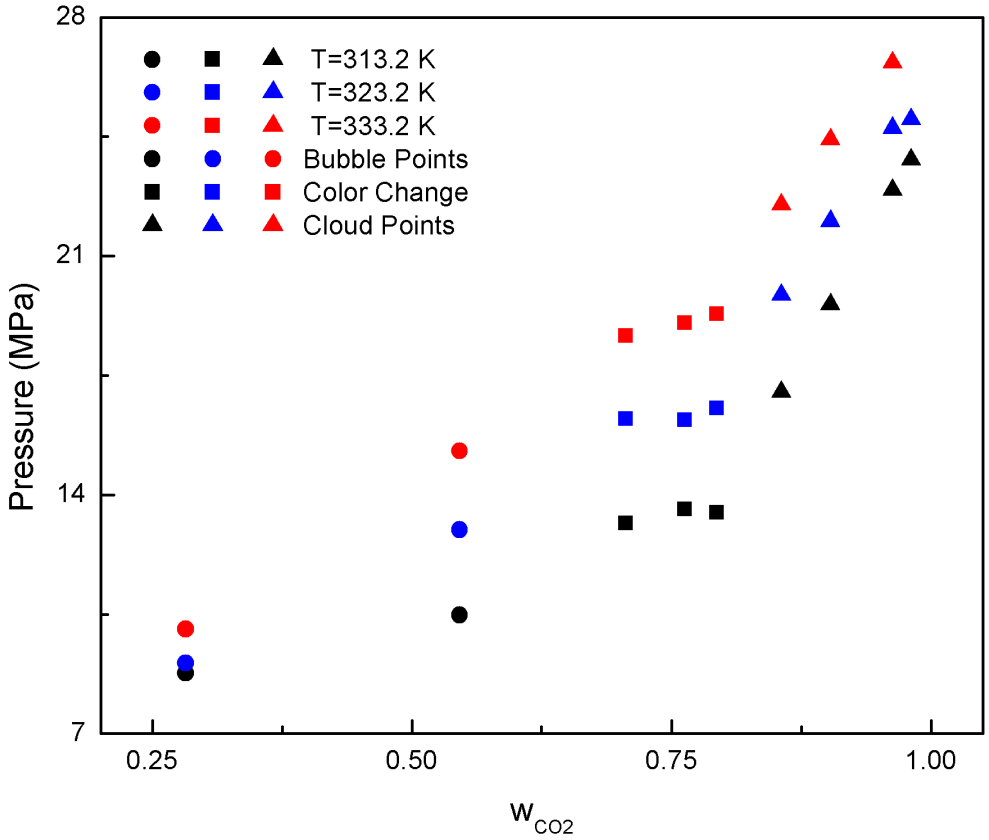

Figure 55 Demixing pressures of PDMS(OH) (Mn=2750 g/mol) – CO_2 binary mixture at 313.2 K, 323.2 K and 333.2 K [101].

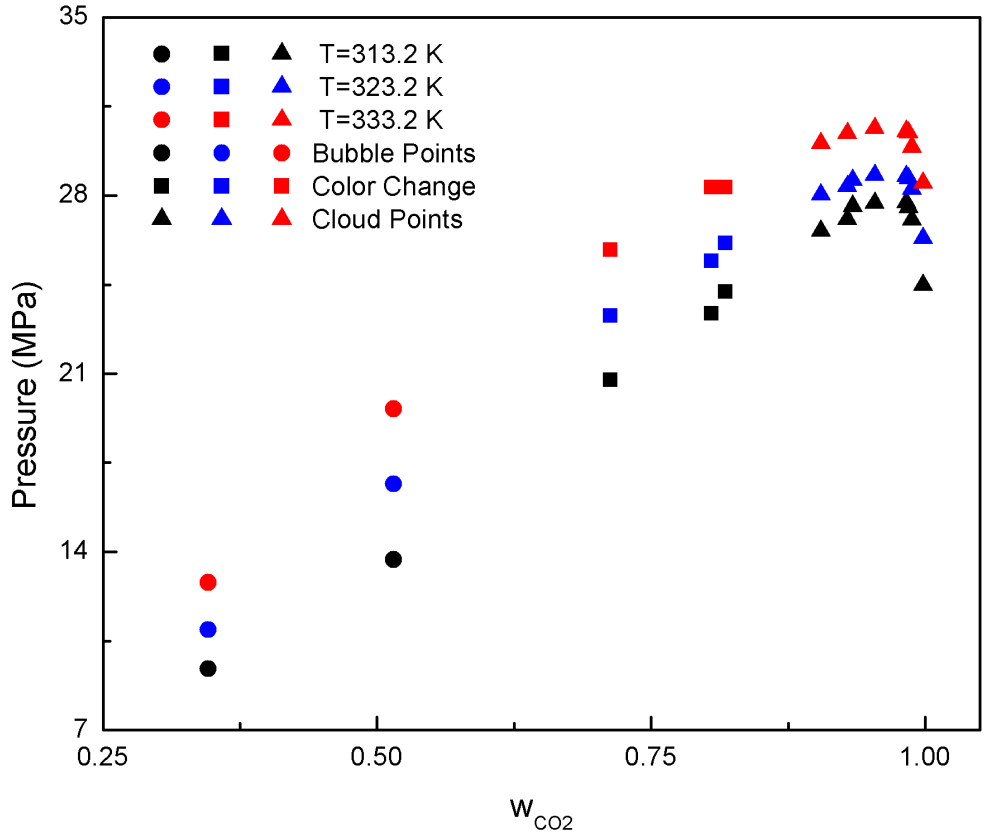

Figure 56 Demixing pressures of PDMS(OH) (Mn=18000 g/mol) – CO_2 binary mixture at 313.2 K, 323.2 K and 333.2 K [101].

The effect of polymer molecular weight on the demixing pressures of PDMS(OH) – CO_2 binary mixtures is displayed in Figure 57 at 323.2 K. The data obtained at other temperatures had the same trend, that is, the demixing pressures increased with increasing polymer molecular weight. Such a trend with molecular weight is typical for other polymer–CO_2 systems and was previously reported also for PDMS(CH_3) – CO_2 binary mixtures. For 5 wt.% of PDMS(CH_3) and at 323 K, the demixing pressures were determined as 27 MPa, 30 MPa, and 41 MPa for polymers with 13700, 31300, and 119500 (g/mol) number average molecular weights, respectively [96]. The demixing pressures of PDMS(OH) – CO_2 binary mixtures were obtained at the same composition as 23 MPa (extrapolated from the data points of 9.7 and 3.7 wt% of PDMS(OH)) and 28 MPa for polymers with 2750 and 18000 (g/mol) number average molecular weights, respectively. These data are plotted in Figure 58 and it is evident that the demixing pressures fall on a smooth line which suggests that the terminal groups of the polymer does not have a significant effect on the demixing pressures.

Quite a few studies were reported thus far on the phase behavior of PDMS(CH_3)–CO_2 binary mixtures. However, in most of these studies the measured data were in limited composition ranges. For example, in the study of Garg *et.al.* the solubility of CO_2 in PDMS(CH_3) was obtained up to 25 wt.% at 333.2 K. In 1995 and 1999, the demixing pressures of PDMS(CH_3)–CO_2 mixtures were studied by Kiran's group for PDMS(CH_3) weight fractions up to 0.10. In this study, the demixing pressures of PDMS(OH)–CO_2 binary mixtures could be determined up to 71.8 wt.% of polymer contents which makes these systems particularly interesting for studying phase behavior of polymer – CO_2 mixtures.

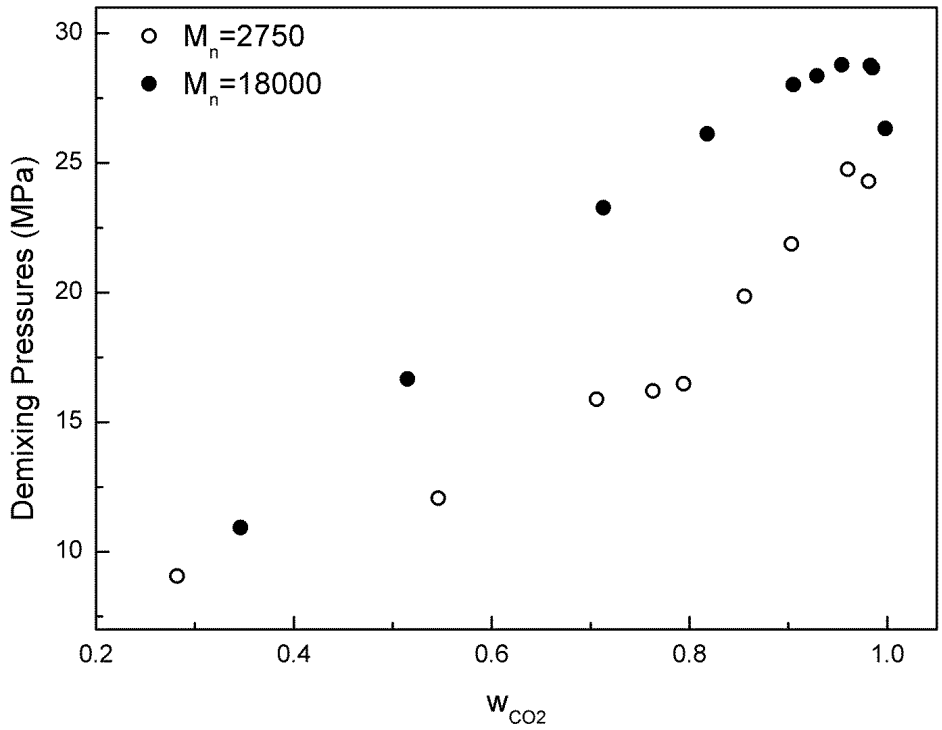

Figure 57 The effect of molecular weight on the demixing pressures of PDMS(OH) – CO_2 binary mixtures at 323.2 K.

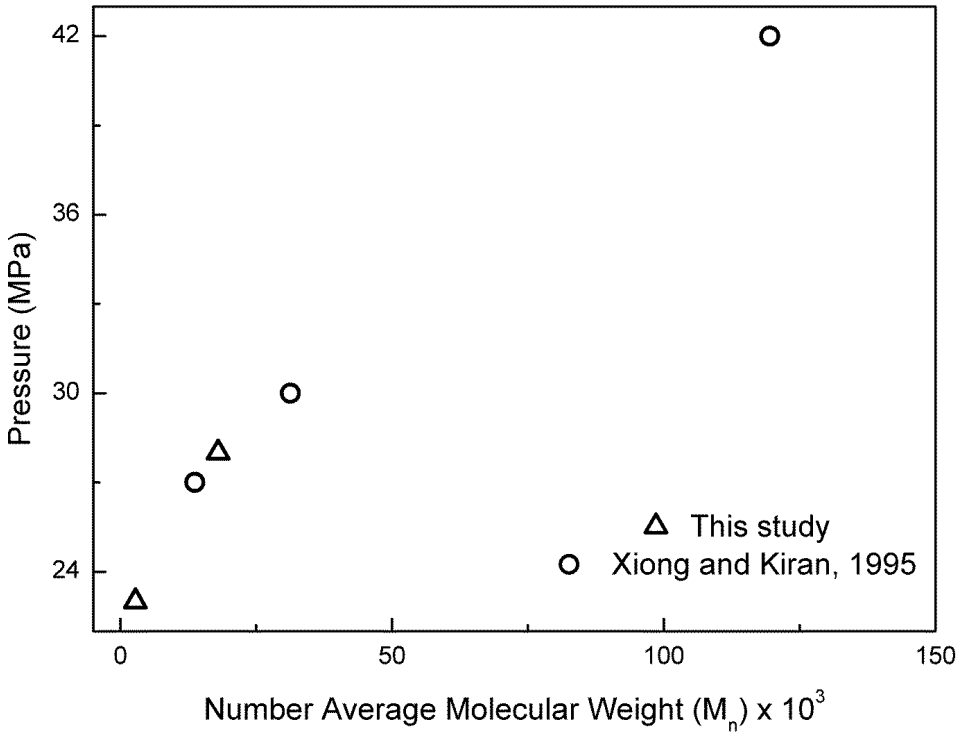

Figure 58 The effect of molecular weight on the demixing pressures of PDMS(OH) – CO_2 and PDMS(CH3) – CO_2 binary mixtures at 323.2 K for 5 wt.% of polymer composition.

4.4.2.2. Modeling Results

There is no published data on the thermophysical properties of PDMS(OH) which would enable the calculation of pure component characteristic parameters. The data for PDMS(OH)–CO_2 binary mixtures were modeled by using the pure component characteristic parameters of PDMS(CH_3) [98, 110]. Table 23 lists the pure component characteristic parameters that were employed in the modeling. This assumption can be justified by the observation that the demixing pressures of PDMS(CH_3)–CO_2 and PDMS(OH)–CO_2 binary mixtures fall on the same line as demonstrated in Figure 58 which indicated that the terminal groups can be considered to have a negligible effect on the demixing pressures.

Table 23 Pure component characteristic parameters.

Component	T* (K)	P* (MPa)	ρ^* (g/cm^3)
CO_2	305	567	1.51
PDMS(CH_3)	476	302	1.104

For a typical P–x loop of a binary mixture, the compositions of different phases that are in equilibrium with each other are determined by horizontal tie lines. However, this is not the case for the polymer mixtures; the compositions of the coexisting phases at constant pressure donot fall on a horizontal line in the P–x loop. The reason for this behaviour is that each phase contains different amounts of oligomers of varying molecular wieghts. Therefore, it is not possible to predict the composition of the cloud phase with model and the only way to determine these compositions is to perform measurements with the precitpitating phase at the cloud point [139]. Therefore, only the bubble point pressure data of PDMS(OH)–CO_2 binary mixtures were modeled by employing SLEoS. At the bubble point, the chemical potential of CO_2 in the polymer rich phase was equated to the chemical potential of CO_2 in the bubble phase as given by Eqn. 4.13. The bubble phase was assumed to be pure CO_2. The regressed binary interaction parameters at the studied temperatures are given in Table 24 together with the percent absolute errors (AE) in the compositions. It seems that one can predict the bubble point pressures with an average abolute error of 17.5 % and 13.4 %, for the low and high molecular weight polymer mixtures, respectively. As shown in Table 4.2, the AE% is higher for mixtures with the lower molecular weight polymer. Additionally, the variation of the binary interaction parameters with the temperature are displayed in Figure 59. The binary interaction parameter for both of the mixtures decreased with increasing temperature.

Even though there are some studies on the effects of inter–chain hydrogen bonding between silanol groups of some silicon containing polymers such as 4–vinylphenyldimethylsilanol (VPDMS) and 4–vinylphenylmethylphenylsilanol (VPMPS) [143-144], we could find only a single study on the effects of hydrogen bonding between the terminal silanol groups of hydroxy terminated PDMS. In this study, it was suggested that the surprising difference in the kinetics of crystallization between PDMS and PDMD(OH) could perhaps be attributed to the inter–chain hydrogen bonding between teminal OH groups [145]. Therefore, it is possible that the decrease of the binary interaction parameters with the increasing temperature may be due to the diminishing strength of the inter–chain hydrogen bonds between the terminal silanol gorups. Moreover, the binary interaction parameter of the low molecular weight polymer mixture was found to be more sensitive to temperature compared to high molecular wieght mixture. This is reasonable since the effects of hydrogen bonding for the low molecular weight polymer chains are expected to be higher than the chains with a higher moleular weight.

In theory, one can expect the δ_{ij} values to be the same for both low and high molecular weight polymer mixtures since the repeating units are the same and therefore the molecular interactions with CO_2 are also expected to be the same. However, the slight difference between binary interaction parameters for polymer mixtures of different molecular weights can also perhaps be attributed to the differences in the strength of inter–chain hydrogen bonds.

Table 24 Regressed binary interaction parameters for the polymer mixtures together with the predicted compositions and AE (%) [101].

PDMS(OH) (Mn=2750 g/mol)–CO_2				
T (K)	**δ_{ij}**	**w_{CO2} experimental**	**w_{CO2} calculated**	**AE (%)**
313.2	*0.061*	0.28	0.21	25.5
		0.55	0.53	2.9
323.2	*0.051*	0.28	0.19	32.6
		0.55	0.49	10.3
333.2	*0.048*	0.28	0.2	29.1
		0.55	0.52	4.8
PDMS(OH) (Mn=18000 g/mol)–CO_2				
313.2	*0.057*	0.35	0.412	19.1
		0.52	0.454	11.8

323.2	*0.056*	0.35	0.4	15.6
		0.52	0.467	9.3
333.2	*0.055*	0.35	0.391	13
		0.52	0.576	11.8

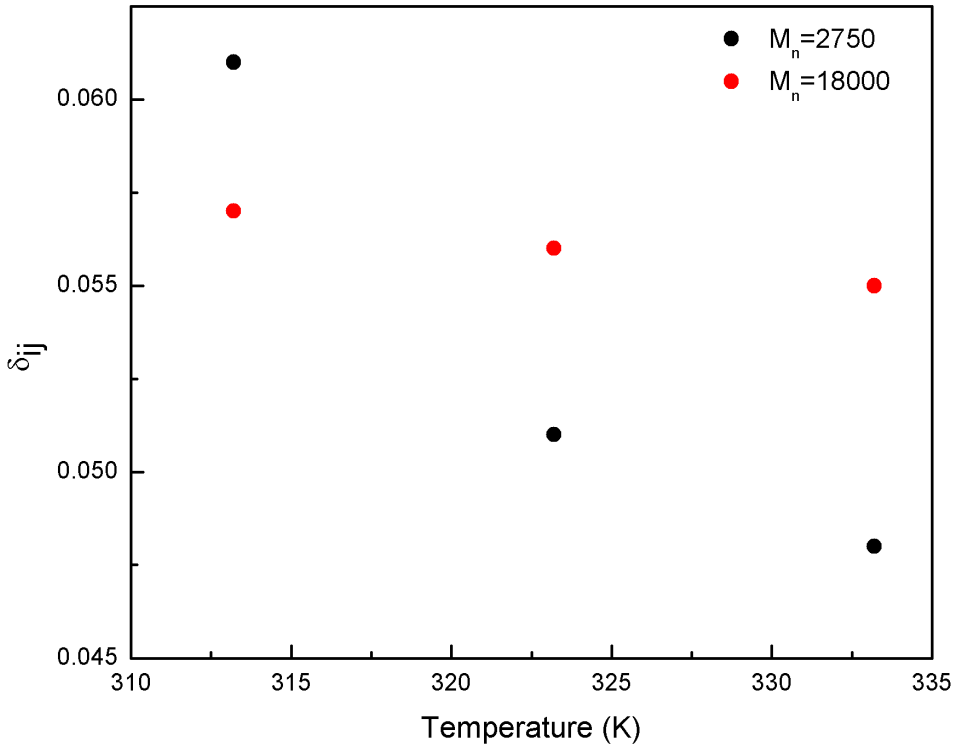

Figure 59 Temperature dependency of the regressed binary interaction parameters for low and high polymer molecular weight mixtures [101].

SLEoS was previously employed for modeling the phase behavior of mixtures of CO_2 and PDMS(CH_3) with higher molecular weights (50000 and 308000 g/mol) [98, 108]. In these studies, the composition ranges varied up to 0.2 and 0.4 CO_2 weight fractions. The binary interaction parameters were succesfully regressed with agreeable errors which indicated that the succesful predictions of the bubble points were perhaps due to narrower composition ranges compared to this study. As an example, the experimental data of Garg *et.al.* were modeled with SLEoS and the results are displayed in Figure 60. The binary interaction parameter was computed as 0.076 whereas it was originally reported to be 0.075 by Garg et.al. [98]. Small deviation between these two values probably originate from the slight differences in the characteristic parameters employed. It is interesting to see that the binary interacion parameters regressed for PDMS(OH)–CO_2 mixtures are close to that of PDMS(CH_3)–CO_2 mixtures. More importantly, it can be observed in Figure 60 that as the CO_2 fraction increased the deviations between the model predictions and the experimental data increased as well. In

that respect, the errors obtained with SLEoS predictions in this study may originate due to the measurement of bubble points at relatively higher CO_2 fractions.

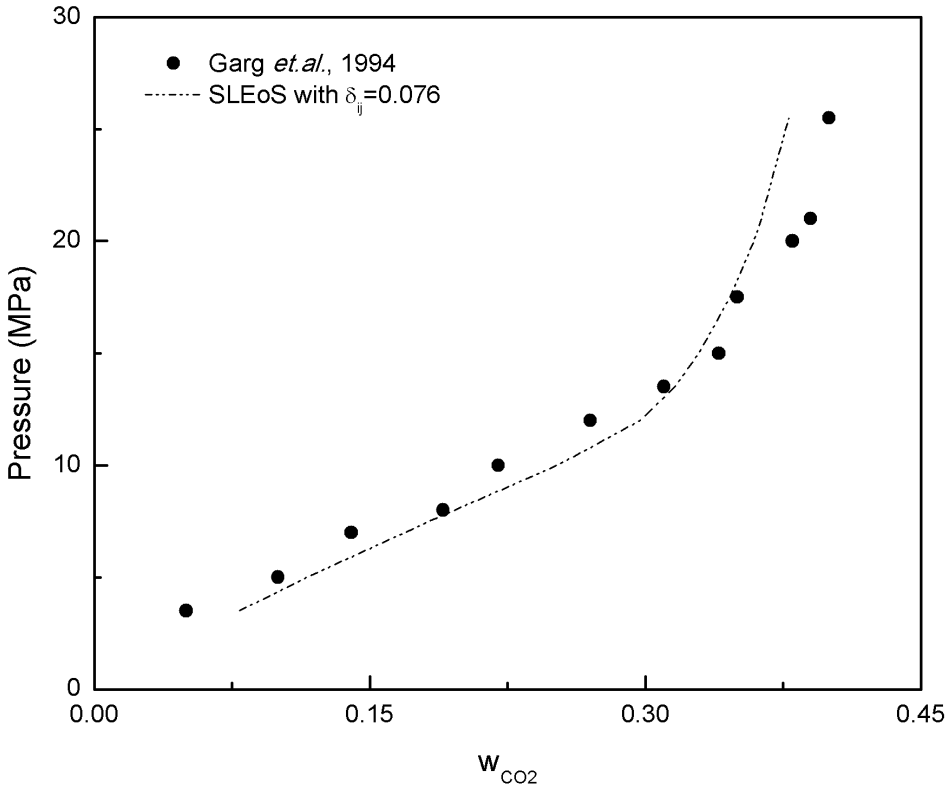

Figure 60 SLEoS model predictions of bubble point data for PDMS(CH3) (Mw=308000)–CO_2 binary mixture [79].

4.5. Summary and Conclusion

Initially, the bubble point pressures of HMDS-CO_2 binary mixture were determined at various temperatures and compositions and were found to increase with increasing temperature and CO_2 mole fraction. The modeling of the phase behavior of the mixture was carried out using the Peng-Robinson Stryjek–Vera equation of state (PRSVEoS). The binary interaction parameters, k_{ij}, regressed from experimental bubble point pressures were observed to have a linear dependency on temperature. The modeling results showed that the binary mixture exhibits a Type II phase behavior. P-T-ρ measurements and excess molar volume computations were also conducted. Comparison of the bubble point pressures show that HMDS can be considered as a better solvent than PDMS and Selexol with enhanced CO_2 uptake capacity. One drawback of utilizing HMDS in such absorption processes would be the rather high mole fraction of HMDS in the vapor phase which originates from the high vapor pressure of HMDS. However, this obstacle can perhaps be overcome by utilization of a higher molecular mass oligomer of dimethylsiloxane with a reduced vapor pressure.

In addition to HMDS-CO_2 binary mixtures, the phase behavior of PDMS(OH)–CO_2 mixtures with two different molecular weights of PDMS(OH), 2750 and 18000 g/mol were also investigated. The demixing pressures for PDMS(OH)–CO_2 mixtures were measured for the first time in an extensive composition interval and at three temperatures (313.2 K, 323.2 K and 333.2 K). The compositions were varied up to 0.718 polymer weight fraction which constitutes almost the entire composition range. Interestingly, due to the wide composition ranges studied, three different types of behavior were observed during depressurization depending on the composition of the mixture; bubble point, cloud point and a color change which was attributed to the mixture critical point. The demixing pressures were found to increase with the increasing polymer molecular weight. In addition, with increasing temperature the demixing pressures at constant composition increased as well, which is LCST type behavior. The bubble point pressures were modeled with SLEoS and the binary interaction parameters for each data set were regressed. It was found that the binary interaction parameters decreased with increasing temperature. The temperature sensitivity of the interaction parameter of the low molecular weight polymer mixtures was higher than the high molecular weight polymer mixtures. Both of these polymers were found to form miscible mixtures with CO_2 at all compositions at pressures lower than 31 MPa in the temperature range 313.2 – 333.2 K.

The mixtures of PDMS(OH) and CO_2 can be considered as intriguing solvents for surface modification applications due to the easily accessible single phase region which enables mild operating conditions and tunable properties. The thermodynamic data about these mixtures demonstrated in this study represent efficient guidelines for the surface modification studies which reveal the temperature, pressure and composition ranges of the miscibility regions for the PDMS(OH)–CO_2 binary mixtures as well as different phase separation characteristics. Future studies utilizing the thermodynamic information demonstrated here can reveal different application areas for these low viscosity solvent mixtures.

CHAPTER 5

PDMS(OH)–SILICA AEROGEL COMPOSITES BY REACTIVE SUPERCRITICAL DEPOSITION (RSCD)

5.1. Introduction

The desired transparency could not be achieved with the composites that were synthesized by the modification of the sol–gel process. Hence, a novel route was followed and composites of silica aerogels were synthesized by incorporating the polymer onto the silica aerogel surface by reactive supercritical deposition technique. The technique basically emerged from the idea of coating of the transparent aerogel surface with a transparent polymer so that the transparency can be retained within the composites. The technique was developed based on the information that PDMS(OH) and its derivatives have substantial solubility in $scCO_2$. Reactive supercritical deposition of PDMS(OH) on silica aerogels is a surface silylation technique and is conducted by accomplishing a few subsequent steps;

- Dissolution of the polymer in $scCO_2$ and obtaining a single phase polymer–CO_2 binary mixture,
- Exposure of dry silica aerogel sample to the single phase binary mixture of polymer and CO_2,
- Covalent attachment of polymer onto the silica aerogel surface,
- Extraction of unreacted polymer with pure $scCO_2$.

The deposition conditions such as pressure, temperature and the polymer concentration were determined according to the demixing pressure data that were obtained from phase behavior measurements, in such a way that the single phase binary mixture of PDMS(OH)–CO_2 is attained in the high pressure vessel throughout the deposition experiments. The depositions were conducted with the experimental setup that is depicted in Figure 61. A syringe pump was used for the transfer of CO_2 into the high pressure vessel. The pressure controller was utilized to set the pressure value to the desired pressure. The pressure and temperature in the high pressure vessel were monitored with a pressure transducer and a thermocouple, respectively. A heating circulator was used to keep the temperature at the desired value. A magnetic stirrer was used to stir the contents of the vessel during the course of the depositions.

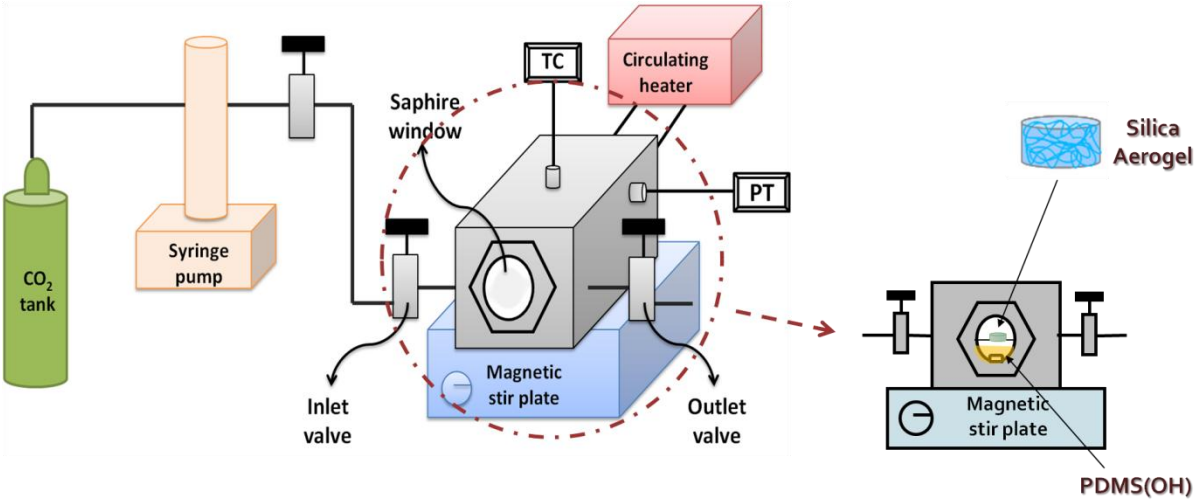

Figure 61 The experimental setup for the reactive supercritical deposition.

Initially, a certain amount of polymer was placed into the vessel together with the silica aerogel sample and the vessel was brought to the desired temperature. A wire mesh was used to separate the aerogel sample from the polymer in order to avoid the contact of the sample with the liquid polymer which would destroy the aerogel structure. With continuous stirring, CO_2 was pumped into the vessel and the dissolution of the polymer in CO_2 was achieved. When the desired pressure value was reached, a single phase binary mixture of PDMS(OH)–CO_2 was obtained in the vessel. The silica aerogel sample was exposed to this single phase mixture for varying durations. Typical volumes of the aerogel samples were around 1 mL. As the final step of the deposition, extraction with pure CO_2 was performed to remove the unreacted polymer which remained in the vessel. The volume of pure CO_2 needed for complete extraction of the unreacted PDMS(OH) from the vessel was determined in separate experiments by passing varying amounts of CO_2. The phase behavior measurements showed that even if small amounts of PDMS(OH) existed in the mixture ($< w_{PDMS(OH)}=0.01$), cloud points are observed during the depressurization of the vessel. It was found that 5–6 vessel volume (~300 mL) of CO_2 was sufficient to remove the entire unreacted polymer since no cloud points were observed during depressurization following the extraction. Furthermore, material balance calculations showed that the PDMS(OH) concentration in the fluid phase dropped to $1/200^{th}$ of its initial value after passing 6 vessel volumes of CO_2 at a flow rate of 100 mL/h. Following the depositions, the polymer uptakes of the deposited samples were determined gravimetrically.

Initially, trial deposition experiments were carried out to verify the validity of the technique for developing the composites of silica aerogels with PDMS(OH).

5.2. Trial Deposition Experiments

To test the efficiency of the reactive supercritical deposition of PDMS(OH) on silica aerogels, two trial experiments were conducted; deposition of PDMS(OH) with following $scCO_2$ extraction and without $scCO_2$ extraction. For both cases, a certain amount of PDMS(OH) (Mw=2750) was placed into the high pressure vessel together with the silica aerogel sample and liquid CO_2 was pumped into the vessel until a single phase mixture was obtained. The polymer weight fraction used in the depositions was $w_{PDMS(OH)} = 0.022$. The weights of the aerogel samples for the deposition experiments were measured as 0.185 g and 0.079 g, respectively. Both deposition experiments were performed at 313.2 K and 310 bar for 4 hours.

The first deposition experiment was conducted without $scCO_2$ extraction. After the treatment, the outlet valve was opened and the system was slowly depressurized. During the depressurization, PDMS(OH) was observed to liquefy in the vessel due to the decreased the solvation power of CO_2 with decreasing pressure which caused the single phase system to undergo a phase change. The liquefaction of PDMS(OH) resulted in the destruction of the solid network of silica aerogel since liquid PDMS(OH) condensed onto the aerogel sample. The resulting aerogel sample was observed to have two coaxial layers; the outer polymer rich layer was completely damaged and had a white opaque appearance, whereas the inner aerogel layer was intact with a highly translucent appearance.

Based on these results, $scCO_2$ extraction was performed following the deposition in order to prevent the liquefaction of the polymer and subsequent destruction of the silica aerogel structure. $ScCO_2$ extraction was carried out by passing 5 vessel volumes of pure CO_2. After the depressurization, a translucent and homogenous aerogel sample was obtained, as displayed in Figure 62. Table 25 displays the initial and final aerogel sample weights for both deposition experiments (without and with $scCO_2$ extraction), together with the calculated PDMS(OH) mass uptakes and appearances of the deposited samples. The higher polymer uptake observed without $scCO_2$ extraction obviously originated from the amount of polymer that is liquefied on the aerogel sample during the depressurization. The mass uptake decreased to 36.3 wt.% after $scCO_2$ extraction due to the removal of the liquefied and physically adsorbed PDMS(OH) molecules with $scCO_2$. Yet, high polymer uptake obtained after the $scCO_2$ extraction points out a possible chemical reaction between the polymer and the silica aerogel.

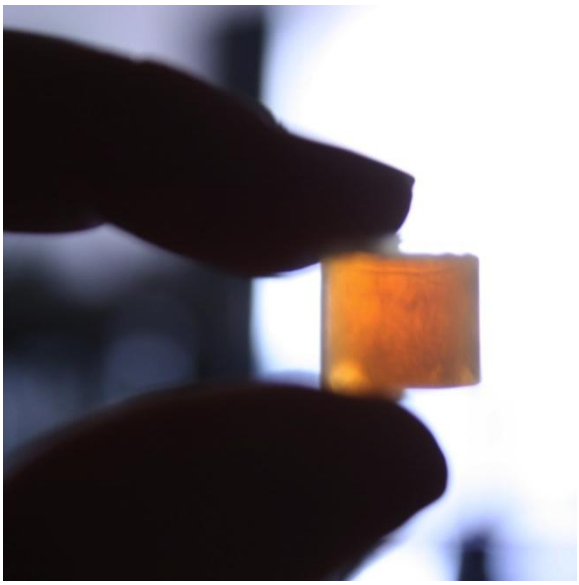

Figure 62 Silica aerogel after the deposition and $scCO_2$ extraction.

Table 25 Deposition results with and without $scCO_2$ extraction.

	Initial Aerogel Mass (g)	**Final Aerogel Mass (g)**	**Mass Uptake (wt.% of aerogel)**	**Appearance**
Without $scCO_2$ extraction	0.185	0.29	56.8	Opaque
With $scCO_2$ extraction	0.079	0.108	36.3	Translucent

In order to analyze the chemical composition ATR–FTIR analysis was performed with the deposited sample obtained with $scCO_2$ extraction. Figure 63 compares the spectra of the deposited aerogel sample obtained with $scCO_2$ extraction with that of native silica aerogel sample. According to Figure 63, the peaks at 850 cm^{-1} and 1267 cm^{-1} wavenumbers are characteristic markers of Si–C stretching vibrations, whereas the sharp peak at around 2963 cm^{-1} originates from the C–H stretching of the methyl groups. The aforementioned peaks did not appear in the spectrum of standard aerogel sample since pure silica aerogel does not contain any methyl groups. The appearance of Si–C and C–H vibrational peaks in verifies the presence of PDMS(OH) in the deposited aerogel sample.

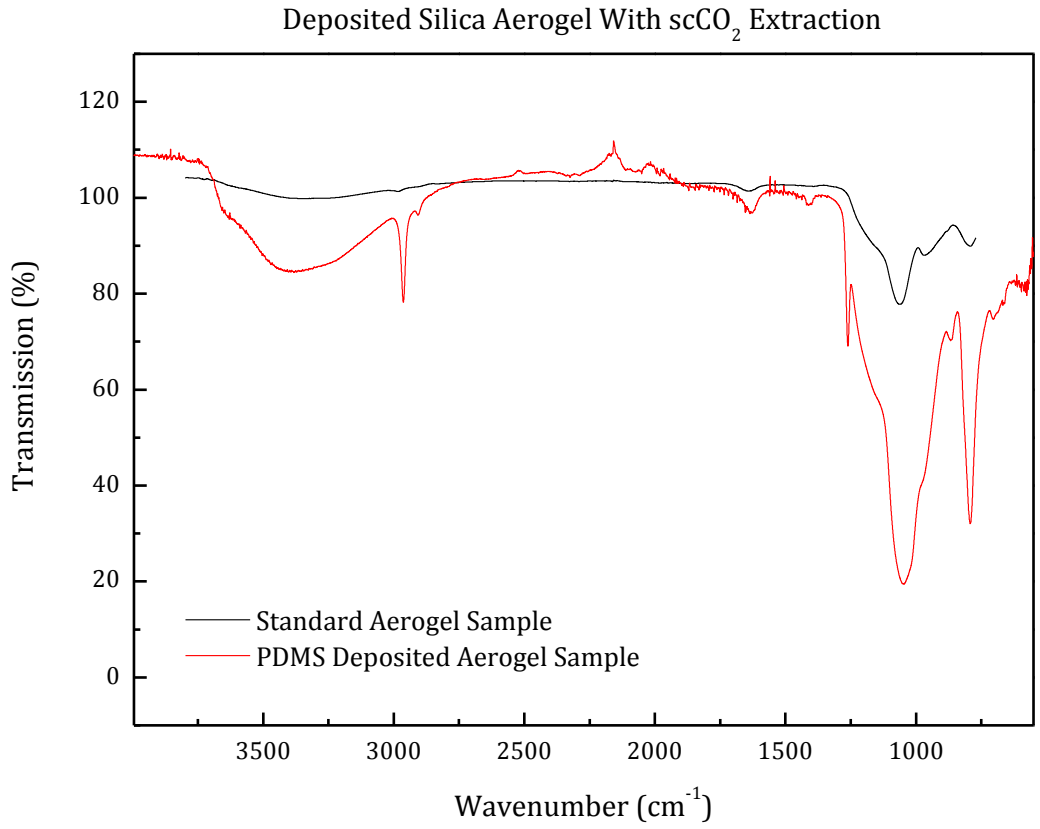

Figure 63 ATR–FTIR spectra of the deposited aerogel sample obtained with $scCO_2$ extraction and native silica aerogel.

Moreover, N_2 adsorption–desorption analysis was carried out with the aerogel sample obtained with $scCO_2$ extraction in order to examine the changes in the pore structure upon deposition. Table 26 displays the analysis results of the deposited sample in comparison to the values of native silica aerogel. According to the results, the BET surface area of the deposited sample had a three–fold decrease compared to the native silica aerogel which apparently originated from the deposition of the polymer molecules which resulted in coating of the silica aerogel surface. The decrease in total pore volume additionally supports the idea of coating of the silica aerogel surface by polymer molecules. Moreover, the increase in average pore radius can be explained by the filling of the small pores with polymer molecules.

Table 26 N_2 adsorption–desorption analysis results for the deposited aerogel sample compared to the native silica aerogel.

Sample	BET Surface Area (m^2/g)	Average Pore Radius (nm)	Total Pore Volume (cm^3/g)
Deposited silica aerogel with $scCO_2$ extraction	310.9	8.7	2.1

Native silica aerogel	926.4	5.9	2.8

Additionally, it was observed, although with simple hand–made tests, that the deposited aerogel samples had extreme mechanical durability compared to the native silica aerogel samples.

Based on the abovementioned results of the trial experiments, reactive supercritical deposition of PDMS(OH) from $scCO_2$ and following extraction with pure $scCO_2$ was concluded to be a novel and promising technique. It was observed that the composites synthesized with this route were monolithic and homogenous. Moreover, the composite with 36.6 wt.% polymer uptake was translucent which indicated that the transparent samples could be obtained by varying polymer content. The results also indicated that there may be a chemical reaction between the polymer molecules and silica aerogel surface. Thus, further experiments were performed to investigate this possible reaction between the polymer and the silica aerogel surface.

5.3. Reaction of PDMS(OH) with Silica Aerogel Surface

Since the reaction of the polymer with the silica aerogel necessitates the presence of the surface –OH groups, removal of these groups, such as in the case of a superhydrophobic silica aerogel, would prevent this reaction and thus no polymer would be deposited on such superhydrophobic aerogels. Therefore, in order to investigate whether the deposition takes place as chemisorption (with a chemical reaction) or physisorption (physical adsorption), simultaneous supercritical depositions were conducted with a native hydrophilic silica aerogel and a superhydrophobic aerogel.

A superhydrophobic silica aerogel reference sample was obtained by supercritical deposition of hexamethyldisilizane (HMDS) with CO_2 [92]. HMDS is a siloxane based compound which has been widely utilized for surface modification applications in order to render hydrophilic surfaces hydrophobic. HMDS has a high solubility in $scCO_2$ which allows for the treatment of surfaces of the porous materials with $scCO_2$. When silica aerogel surface is exposed to HMDS that is dissolved in $scCO_2$, the surface –OH groups are replaced with trimethylsilyl ($Si(CH_3)_3$) groups of HMDS resulting in a hydrophobic surface. The experimental setup that is displayed in Figure 61 was utilized for HMDS deposition and the deposition was conducted with an initial HMDS amount of 2 mL at 333.2 K and 13.8 MPa for 12 hours. Following the deposition, supercritical extraction was carried out with 300 mL of pure $scCO_2$ in order to

remove the un–reacted HMDS from the vessel. The mass uptake after HMDS deposition was 16.7 wt.%. The superhydrophobicity of the aerogel sample was confirmed with a water droplet test where a droplet of water was placed onto the silica aerogel sample. The water droplet was unable to stand on the surface of the aerogel and moved away from the surface which indicated that the sample was superhydrophobic.

Subsequently, simultaneous deposition of PDMS(OH) on hydrophilic and superhydrophobic silica aerogel samples were performed at 323.2 K and 31 MPa for 24 hours with PDMS(OH) weight fraction of $w_{PDMS(OH)} = 0.022$ followed by supercritical extraction with pure $scCO_2$. As given in Table 27, the mass uptake for the hydrophilic silica aerogel sample was 66.7 wt.% whereas the uptake for that of superhydrophobic silica aerogel sample was 4.4 wt.%. The drastic difference between the mass uptakes of the two aerogel samples constitutes evidence that the PDMS(OH) molecules chemically reacts with the –OH groups on the silica aerogel surface. In addition, the 4.4 wt.% mass uptake observed for the superhydrophobic aerogel may either occur due to the physical adsorption of the polymer molecules on the superhydrophobic surface or chemical reaction with the residual silanol (Si–OH) groups which remain on the surface after the HMDS deposition. Figure 64 displays the images of the hydrophilic and superhydrophobic aerogel samples after the PDMS(OH) deposition. The higher amount of polymer in the hydrophilic aerogel was observed to decrease the transparency significantly when compared to the superhydrophobic aerogel. The hydrophilic aerogel with 66.7 wt.% of polymer uptake had almost an opaque appearance compared to the superhydrophobic silica aerogel sample with 4.4 wt.% of polymer uptake which had a transparent appearance.

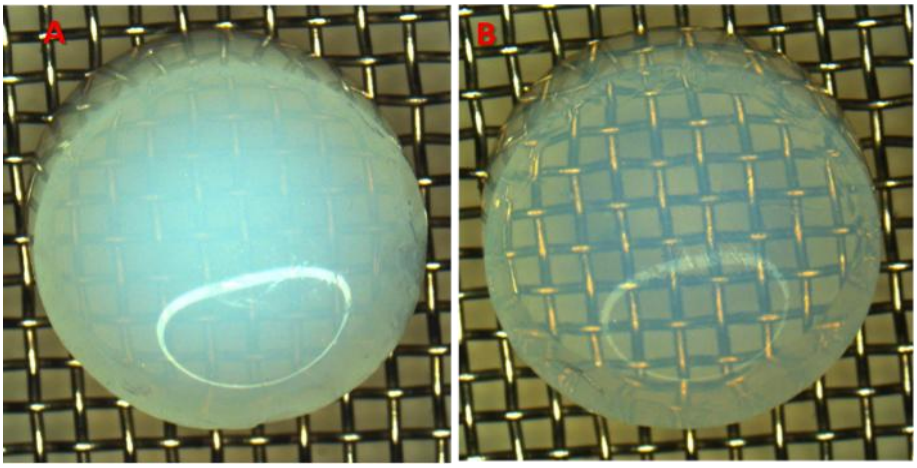

Figure 64 Images of A) hydrophilic and B) superhydrophobic aerogel samples after the deposition.

Table 27 Mass uptakes of the silica aerogel samples after the PDMS(OH) deposition.

Sample	$m_{Aerogel}$ Before Deposition (g)	$m_{Aerogel}$ After Deposition (g)	Mass Uptake (wt.% of aerogel)
Hydrophilic Aerogel	0.09	0.150	66.7
Superhydrophobic Aerogel	0.114	0.119	4.4

Moreover, the pore structures characteristics of the samples were analyzed with N_2 adsorption–desorption and the results are listed in Table 28. When the hydrophilic aerogel sample before and after the deposition are compared, a three–fold decrease in the BET surface area, and almost a two–fold decrease in pore volume are observed which originated due to 66.7 wt.% of polymer uptake. On the other hand, when the values for superhydrophobic aerogel sample are compared, it can clearly be observed that the total pore volume did not change upon PDMS(OH) deposition, while there was a slight decrease in BET surface area. Similar conclusions can be deduced from the pore size distributions of the aerogel samples that are given in Figure 65. The pore size distribution of the hydrophilic silica aerogel became broader upon deposition and the peak shifted to higher average pore sizes. Additionally, there was a remarkable difference between the maximum pore volumes that were obtained at the peak positions of the pore size distribution curves before and after the deposition which occurred due to deposition of the polymer on the pore surface. On the other hand, the change was slight for the superhydrophobic aerogel before and after the polymer deposition which can be explained by 4.4 wt.% of polymer uptake.

Table 28 N_2 adsorption–desorption analysis results of the silica aerogel samples before and after PDMS(OH) deposition.

Sample	BET Surface Area (m^2/g)	Average Pore Radius (nm)	Total Pore Volume (cm^3/g)
Hydrophilic Aerogel (Before Deposition)	1024.9	9.1	5.5
Hydrophilic Aerogel (After Deposition)	343.7	11.3	2.9
Hydrophobic Aerogel (Before Deposition)	675.3	9.6	3.9
Hydrophobic Aerogel (After Deposition)	595.5	10.1	3.9

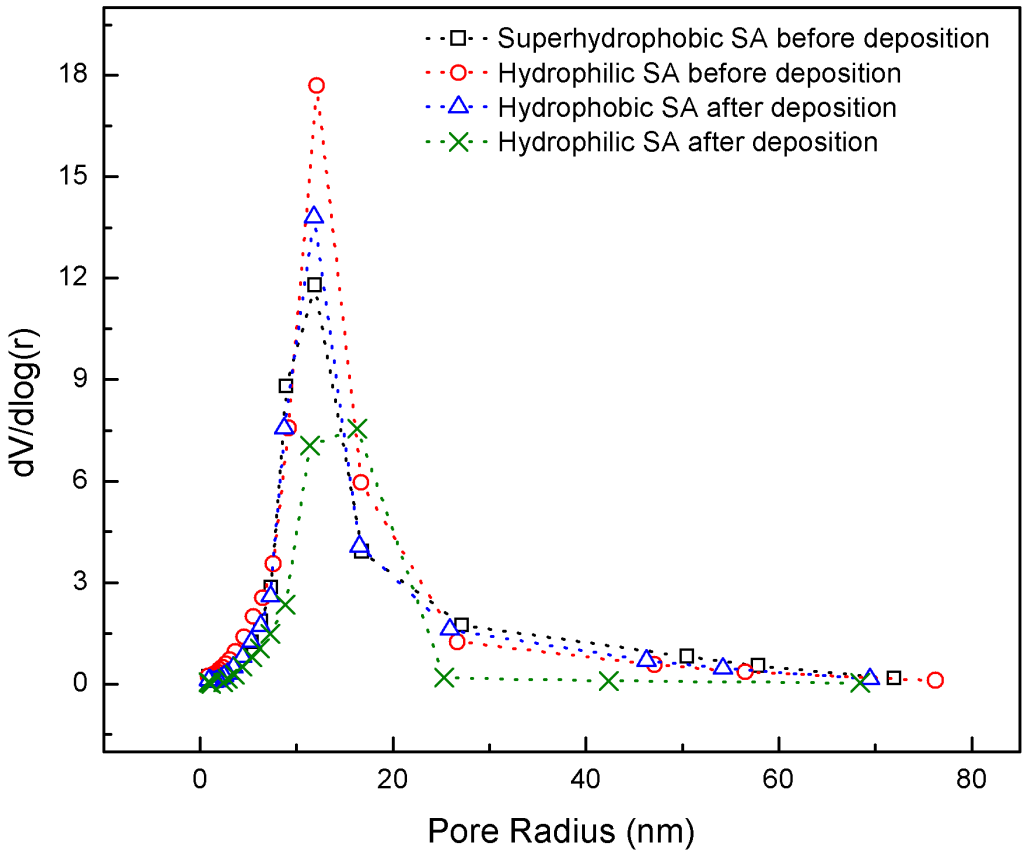

Figure 65 Pore size distribution of the aerogel samples.

Moreover, ATR–FTIR analysis was performed with the aerogel samples to analyze the chemical groups on the surface after the PDMS(OH) deposition. Figure 66 displays the ATR–FTIR spectra for the hydrophilic and superhydrophobic aerogel samples after the deposition along with the native silica aerogel spectrum. The intensity of the broad –OH band between 3000 and 3700 cm^{-1} wavenumbers for the superhydrophobic sample diminished compared to the native silica aerogel which confirms the hydrophobic character of the surface. Moreover, there are two peaks of special interest that can be analyzed for comparison of the structures: the peak at 2963 cm^{-1} wavenumber representing the C–H stretching vibrations and the peak at 1267 cm^{-1} wavenumber which stands for the Si–C stretching vibrations. In Figure 66 these peak positions are marked. The C–H stretching vibration peak in hydrophilic silica aerogel originated from the methyl side groups of PDMS(OH) that was bound on the surface whereas the same peak in the superhydrophobic sample mainly occurred due to the trimethylsilyl ($Si(CH_3)_3$) groups that were attached to the surface with HMDS deposition. The comparison of the Si–C stretching vibration peaks indicates the binding of PDMS(OH) to silica aerogel surface for the hydrophilic sample as well as the binding of $Si(CH_3)_3$ of HMDS for the superhydrophobic sample. However, the peak for superhydrophobic sample shifted from 1267

cm^{-1} to 1250 cm^{-1} which probably occurred due to the chemical nature of Si–C groups, that is, the silicon of the Si–C groups that occurred due to PDMS(OH) are bound to oxygen forming the $(SiO_2)_n$ backbone of the polymer whereas silicon of Si–C groups that occurred due to HMDS deposition are only bound to the surface of silica aerogel.

In conclusion, the mass uptake, N_2 adsorption–desorption and ATR–FTIR results that are explained in this subsection, confirms that the mechanism that governs the PDMS(OH) deposition process is the chemisorption, that is, the polymer molecules are covalently attached to the surface –OH groups of the silica aerogel from the terminal –OH groups. Therefore, the supercritical deposition process is confirmed to be a reactive supercritical deposition of PDMS(OH).

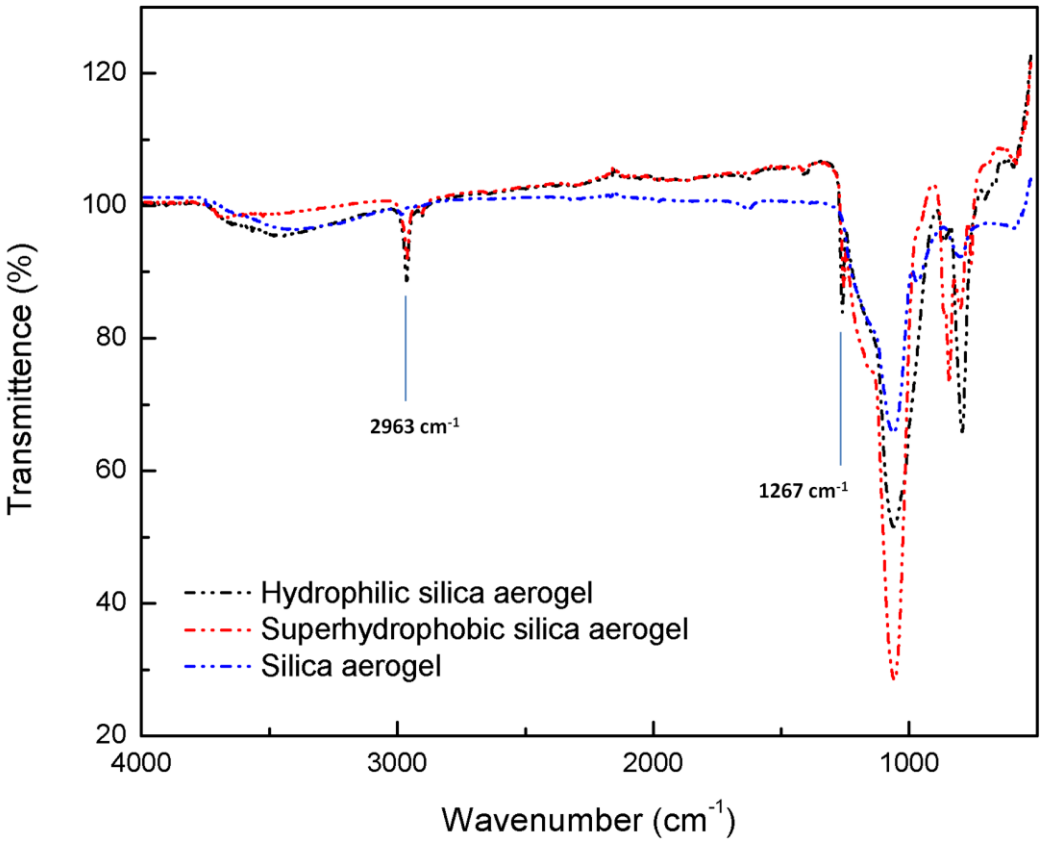

Figure 66 ATR–FTIR spectra of the silica aerogel samples.

Another way to distinguish chemisorption and physisorption is the extraction with pure $scCO_2$ since PDMS(OH) was determined to be highly soluble in $scCO_2$. If adsorption is physisorption, then the deposited polymer can be extracted with pure CO_2 due to the reversible nature of physical adsorption and also due to the substantial solubility of PDMS(OH) in $scCO_2$. However, in the case of chemisorption, since the molecules are

attached to the surface by chemical bonds, the polymer cannot be extracted with pure CO_2. Therefore, an aerogel composite was developed with 75.4 wt.% of polymer uptake and prolonged extraction of the sample was performed with pure $scCO_2$ at 323 K in an Applied Separations Spe–ed SFE extraction unit in two stages for a total of 32 hours. In the first stage supercritical extraction with CO_2 was performed at the deposition conditions for 12 hours and the weight loss of the sample corresponded to 3.3 % of the sample weight. The sample was then placed in the extractor and the extraction was continued for an additional 20 hours. The weight loss of the sample was measured to be 0.6 mg corresponding to only 0.3 wt.% of the sample weight. This weight loss is quite low compared to the initial mass uptake (75.4 wt.%) which demonstrates that loaded polymer cannot be desorbed with further extraction. With the prolonged extraction of 32 hours, a total of 6.6 mg of PDMS(OH) was extracted corresponding to 7.9 % of the initially loaded polymer amount which can perhaps be attributed to the extraction of physisorbed polymer molecules. These results indicate that the major type of adsorption is chemisorption and the PDMS(OH) molecules react with the surface –OH groups and become attached to the silica aerogel surface. This reaction generates water which is either adsorbed on the silica aerogel surface or partitions into the fluid phase. In all the experiments, the amount of water generated was considerably smaller than the amount which could be dissolved in CO_2 based on the solubility data of water in $scCO_2$ at the experimental conditions (0.008 mol H_2O per mole of CO_2) [146].

5.4. Reactive Supercritical Deposition of PDMS(OH)

5.4.1. Effect of Deposition Time and Polymer Concentration

The composites of silica aerogels with PDMS(OH) was developed with reactive supercritical deposition of the polymer from $scCO_2$ by utilizing PDMS(OH) with number average molecular weight of M_n=2750. Deposition experiments with different initial PDMS(OH) concentrations were conducted at 323.2 K and 31 MPa for 24 hours and the effects of the polymer concentration on uptake amount was investigated. All of the deposited samples were obtained as crack–free monoliths. Figure 67 displays the mass uptakes of the aerogel samples for different polymer weight fractions and shows that there is almost a linear increase in the mass uptake with increasing initial PDMS(OH) fraction. This increase in mass uptake was attributed to the higher concentration gradients between the bulk and the surface obtained with higher polymer weight fractions which resulted in enhanced rates of diffusion and/or reaction of the PDMS(OH) molecules. Polymer loading as high as 75.4 wt.% could be

obtained which is quite high compared with the values reported in the literature for composites of PDMS(OH) with silica gel obtained by other methods [46, 49].

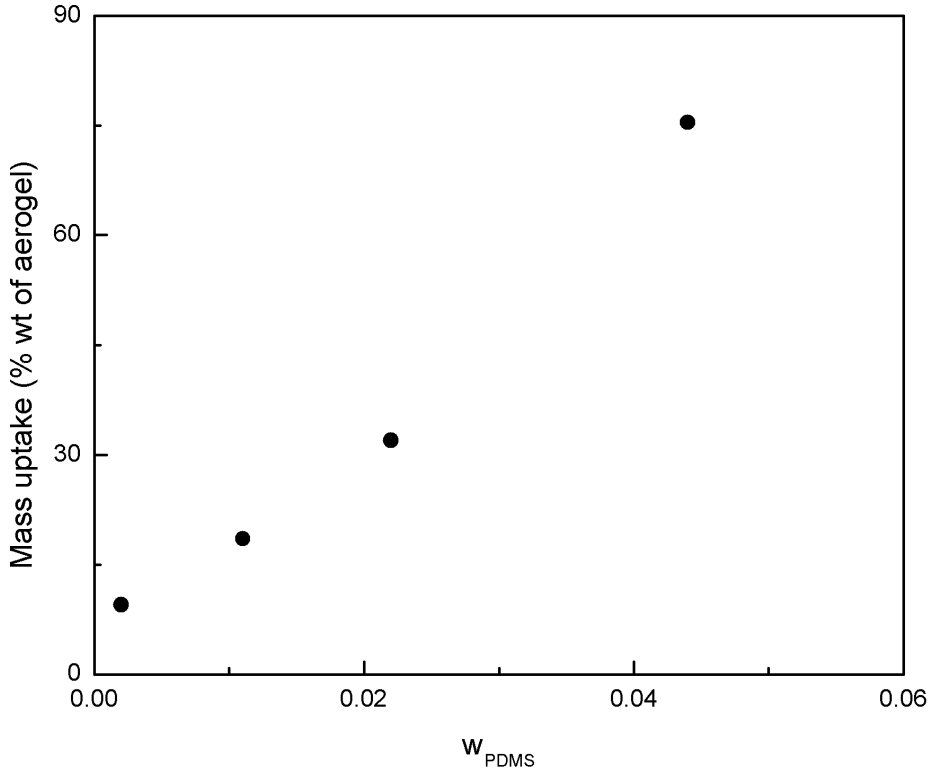

Figure 67 The mass uptakes for different initial PDMS(OH) compositions.

ATR–FTIR analysis further supports the covalent bonding of the polymer on the aerogel surface. Figure 68 compares the ATR–FTIR spectra of the deposited aerogel samples with the native silica aerogel. There are two intense peaks that are specific to the chemical groups of silica and therefore occur in both spectra since both the backbone of the polymer and the aerogel network is made from SiO_2. These peaks occur at 800 cm^{-1} and 1080 cm^{-1} and are characteristic to Si–O–Si bending and stretching vibrations, respectively [65]. After deposition, the intensity of the peak at 800 cm^{-1} increases due to additional Si–O–Si bending vibrations of the polymer backbone. The broad band which appears at 3400 cm^{-1} originates from hydrogen bonded Si–OH with the adsorbed molecular water which is observed to weaken after the deposition of the polymer. More importantly, there are three peaks indicative of the presence of the polymer in the aerogel sample. The peak at 2963 cm^{-1} represents the C–H stretching vibrations originating from the methyl side groups of PDMS(OH). The peak at 1267 cm^{-1} is due to the Si–C stretching vibrations that originate from methyl side groups attached to the polymer backbone. The peak appearing at 850 cm^{-1} for the deposited sample was attributed to ≡Si–O–Si$(CH_3)_2$–R bond that were formed due to the condensation reaction between the ≡Si–OH groups of the aerogel and OH–Si$(CH_3)_2$–R end groups of PDMS(OH)

[65]. The intensities of the C–H and Si–C stretching vibration peaks as well as the Si–O–Si peak that signifies the reaction between PDMS(OH) and surface –OH groups of the silica aerogel increased accordingly with the increasing polymer amount in the deposited samples. Furthermore, the peak at 960 cm^{-1} that was observed in native silica aerogel sample was attributed to stretching of Si–OH groups of the aerogel [65-66]. The disappearance of this peak upon deposition additionally indicates the reaction between PDMS(OH) and the surface Si–OH groups of the aerogel. The evolution of these specific peaks can be observed from the marked positions in Figure 68.

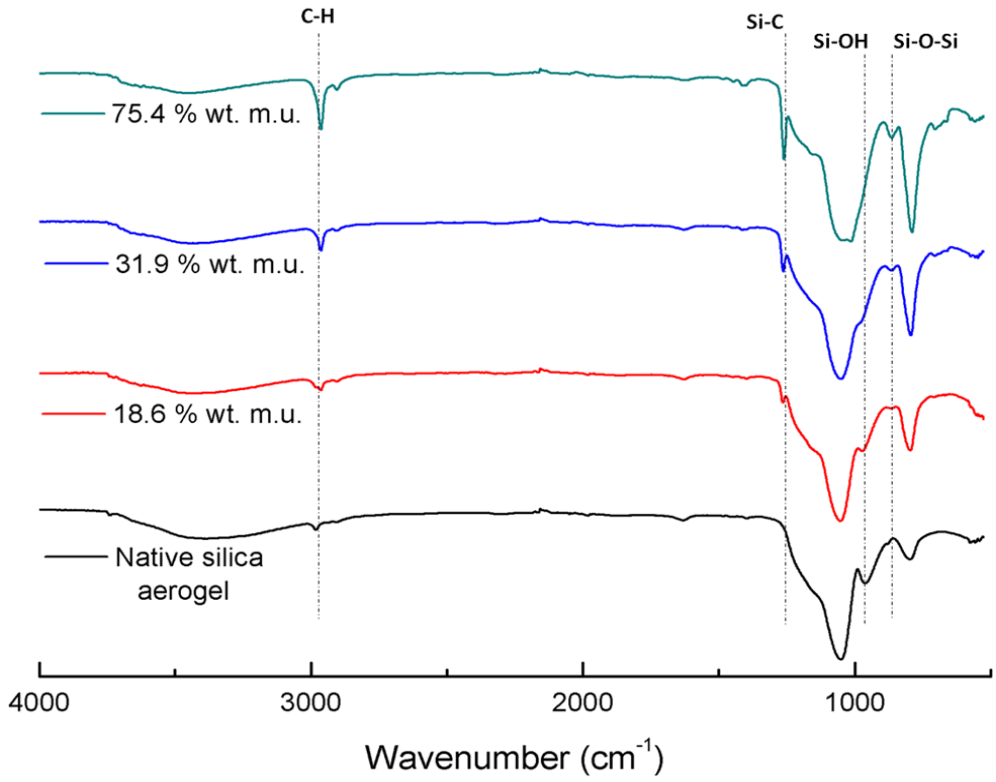

Figure 68 ATR–FTIR spectra showing the evolution of Si–C, C–H and Si–O–Si peaks upon deposition.

The effects of the deposition time on mass uptake were also investigated by conducting deposition experiments for various durations. The experiments were performed at 31 MPa and 323.2 K with $w_{PDMS(OH)}$ of 0.022. Subsequent supercritical extraction with 300 mL of pure $scCO_2$ was performed. Each deposition experiment was repeated three times. Figure 69 displays the mass uptakes for various deposition times with the standard deviations represented as the error bars for each data point. According to Figure 69, the mass uptakes increased with increasing deposition time. However, after 24 h the mass uptake seems to be reaching to an equilibrium point which indicates that with around 30 wt.% of polymer uptake

the aerogel surface becomes saturated with PDMS(OH) molecules and further elongation of the exposure time does not cause any significant increase in the uptake value. This observation can originate from two possible situations; either almost all of the –OH groups on the aerogel surface reacted with the PDMS(OH) molecules or some of the surface –OH groups become inaccessible because of the polymer chains attached on the surface. For an uptake amount of 36 wt.%, calculations indicated that approximately 8 PDMS(OH) molecules were present on 100 nm^2 of silica aerogel surface. Considering that there are approximately 500 –OH molecules per 100 nm^2 of native silica aerogel surface [7, 147-148], only a small fraction of surface –OH groups participated in reactions with PDMS(OH).

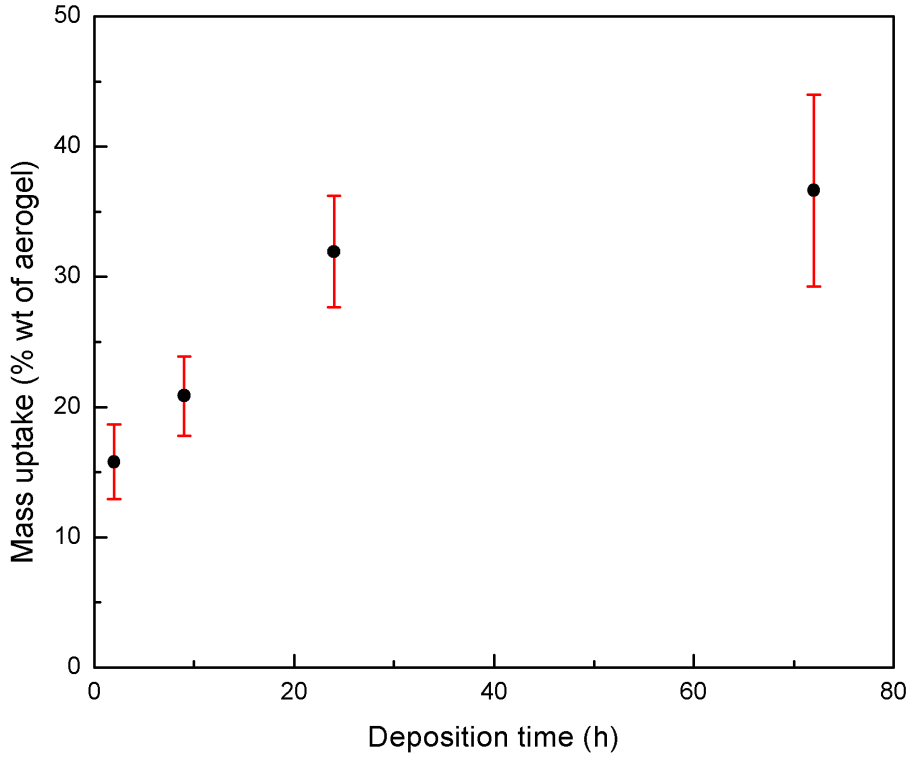

Figure 69 Mass uptake values for various deposition times.

The adsorption of polymers on inorganic surfaces is known to be quite a complicated process which is governed by different intermolecular interactions between the polymer and the surface [149]. The structure of polymer and surface, pH, temperature, the geometry of polymer, the topology of the surface, concentration and molecular weight of the polymer are some of the factors that govern the extent of adsorption and the structure of the adsorbed polymer phase [150]. When the polymer concentration on the surface is below the saturation point, the polymer chains adopt rather a flat conformation with enhanced number of interactions with the surface. With increased polymer concentration, the surface becomes

saturated with the polymer chains which results in the entangled chains on the surface. The loop and tail portions of the entangled chains repel free polymer chains away from the surface due to the steric hindrance [150].

There have been some studies investigating the adsorption of PDMS on silica surfaces and the structure of the adsorbed PDMS layer. In some of these studies the PDMS chains were demonstrated to be partially adsorbed on the surface, that is, some segments of the polymer chain interact with the surface while other segments are free and protrude from the surface. It was proposed that the segments that are not involved in the interactions with the surface can form loop like structures depending on the chain length of the polymer [151-153]. The adsorption of PDMS(OH) on silica surface was also investigated and it was proposed that the polymer chains can coat the silica surface forming a core–shell structure or can bind to each other forming bridges [66]. In any case, it is likely that a significant number of –OH groups on the silica surface are unavailable for new interactions either because they are involved in bonding with the polymer or are covered by the bound polymer chains [151].

Regarding these considerations, it is likely that the chemisorbed PDMS(OH) molecules cover the unreacted surface –OH groups on aerogel surface and prevent the access of other PDMS(OH) molecules to these sites and therefore hinders their reactions. Another issue is the steric hindrance due to the crowding of the polymer molecules on the aerogel surface that may occur with increasing polymer loading. All these possible interactions can cause the saturation of the surface with polymer molecules as observed in the mass uptake results.

Figure 70 shows the images of aerogel samples that were deposited for 2 h, 9 h and 72 h, with polymer contents of 15.8 wt.%, 20.9 wt.% and 36.6 wt.%, respectively. It is evident that with increasing deposition time and thus the polymer content of the samples, the transparency decreases. During the depressurization, there occurs a transition from a good solvent medium ($scCO_2$) to a weak one (gaseous CO_2) which affects the structure and morphology of the adsorbed polymer layer. It is known that polymers adopt a brush–like structure in the presence of a good solvent and a mushroom–like, more closely–packed structure in the presence of a weak solvent [154-156]. Therefore, it is possible for the reacted PDMS(OH) molecules to become entangled on the surface upon depressurization. One possible explanation for the decrease in transparency is that these entangled polymer molecules constitute additional scattering centers on the aerogel surface, which decreases the amount of light transmitted through the sample. Nonetheless, it is important to note that the transparency of the aerogels

can be adjusted with the amount of polymer loaded and it is possible to obtain transparent aerogel composites at low polymer loadings. One of the most promising applications of silica aerogels is their utilization as core materials in transparent vacuum insulation panels. Therefore, being able to retain the transparency of the samples after the deposition is an essential feature of this technique that needs to be emphasized.

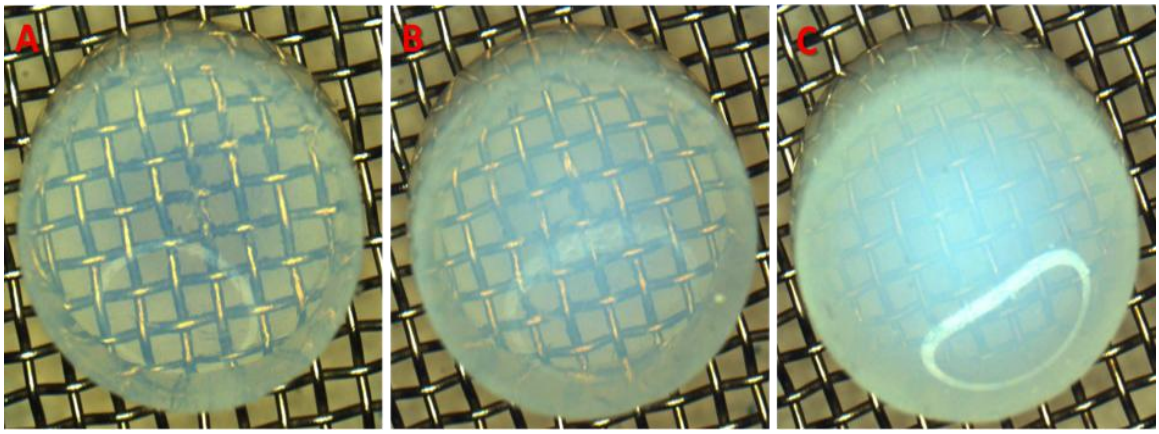

Figure 70 Images of aerogel samples with A) 15.8 wt.%; B) 20.9 wt.% and C) 36.6 wt.% mass uptakes.

The homogeneity of the deposited samples, that is, whether the polymer molecules were homogenously distributed throughout the entire volume of the cylindrical samples, was also investigated. The visual observation of the cylindrical samples broken into two pieces indicated no non–homogeneities in the appearance. Moreover, ATR–FTIR analyses were performed with the portions taken from the center and from the outer surface of the cylindrical sample. Figure 71 displays the spectra of the samples deposited for 72 h. It is evident that the spectra of the samples from the center and the outer surface overlap. The intensities of the specific peaks that are related to the polymer are identical indicating that the concentrations of the polymer molecules at the center and at the outer surface of the samples are similar. These results indicate that the polymer molecules penetrated to the center of the monoliths and were uniformly distributed.

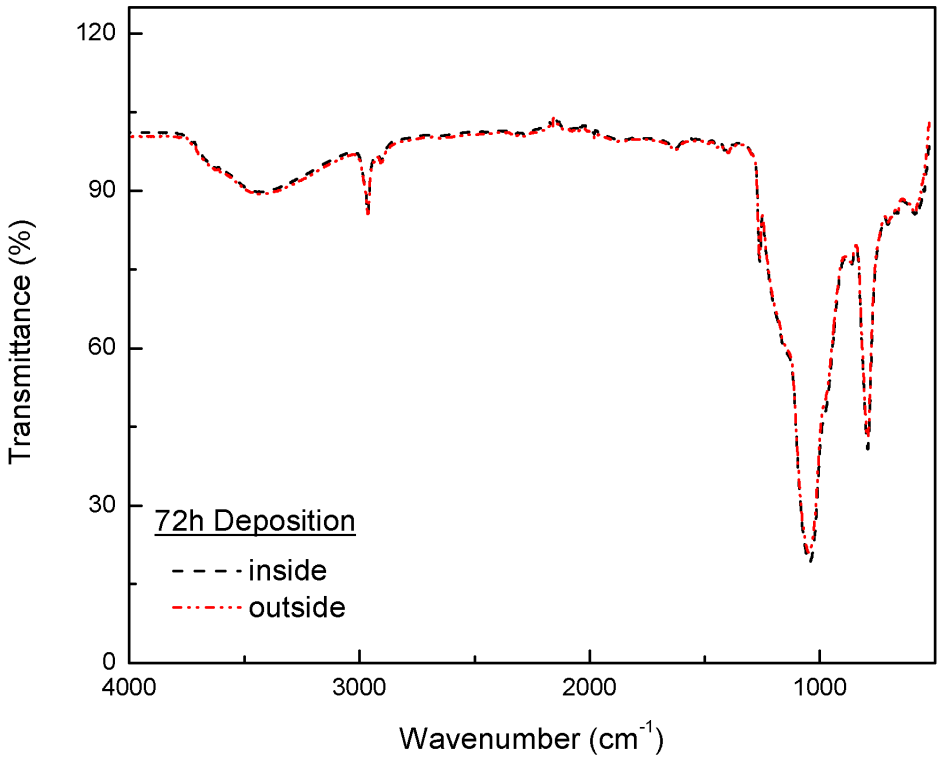

Figure 71 ATR–FTIR spectra of the samples from the center and outer surface of the monoliths deposited for 72 hours.

The effects of mass uptake on the pore characteristics of the samples such as surface area, pore volume and pore size distribution were investigated by analyzing the N_2 adsorption–desorption isotherms. The analysis results are summarized in Table 29 together with the mass uptakes and densities. It is obvious that with increasing mass uptake the densities of the samples increased whereas the surface areas and pore volumes decreased.

Furthermore, pore size distribution of the samples were obtained from the desorption branch of the isotherm by employing BJH method. The pore size distributions of the samples were compared with the native silica aerogel in Figure 72 which shows that the average pore radius changed very slightly upon deposition. For comparison, the N_2 adsorption–desorption isotherms of the native silica aerogel and deposited aerogel with 36.6 wt.% uptake were additionally given in Figure 72. It is clearly observed that the aerogel samples have Type IV isotherm with H1 type hysteresis loop with desorption branch reflecting equilibrium capillary evaporation. The isotherms for the other the samples were similar but omitted for clarity.

Table 29 Densities and pore characteristics of the deposited aerogels.

Mass Uptake (wt.% of aerogel)	Density (kg/m^3)	BET Surface Area (m^2/g)	Total Pore Volume (cm^3/g)	*C*
15.8	186	665	4.56	38.14

20.9	188	596	4.14	31.19
36.6	215	454	3.04	19.97
75.4	276	280	2.06	14.38

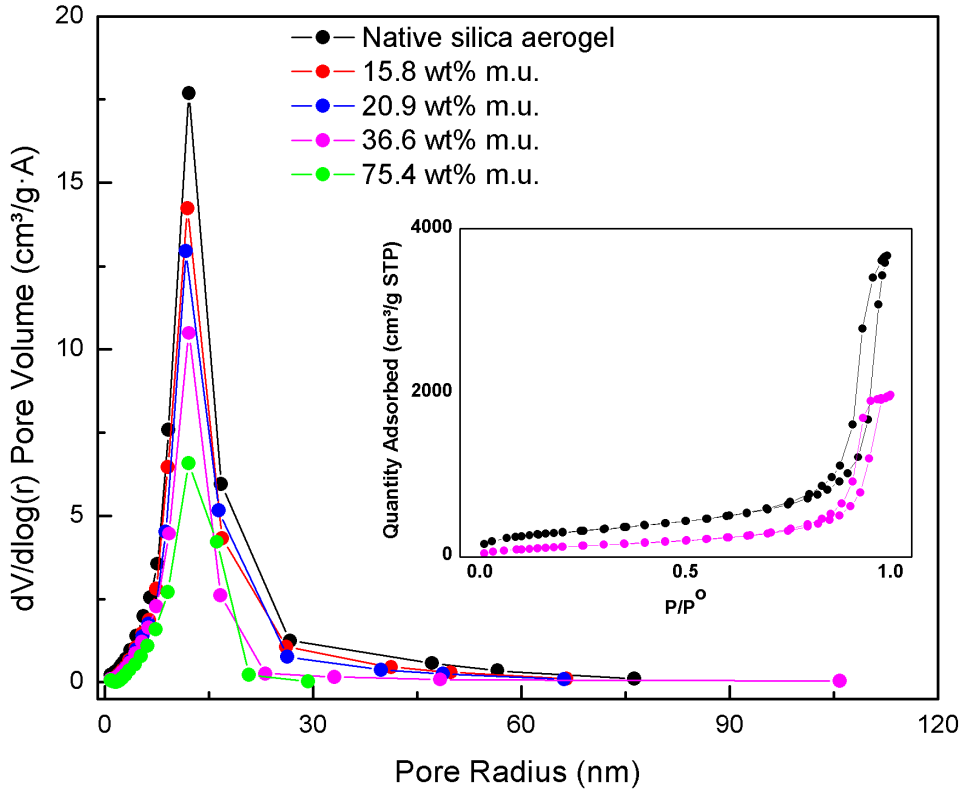

Figure 72 Pore size distribution and N_2 adsorption–desorption isotherms of the deposited samples (m.u.: mass uptake).

The volumes occupied by the polymer molecules in the pores were compared to the reductions in the pore volumes (the difference between the pore volumes of the native silica aerogel and the deposited samples as determined from N_2 adsorption–desorption isotherms by using BJH analysis). As shown in Figure 73, there is a very good match between those two volumes for all the samples. The slope of the best fit straight line through these points (the red dotted line) is 1.03 with an R–square value of 0.93. The closeness of the value of the slope to 1.0 shows that the volume of the PDMS(OH) molecules in the samples correspond to the reduction in the pore volumes which occurred upon deposition.

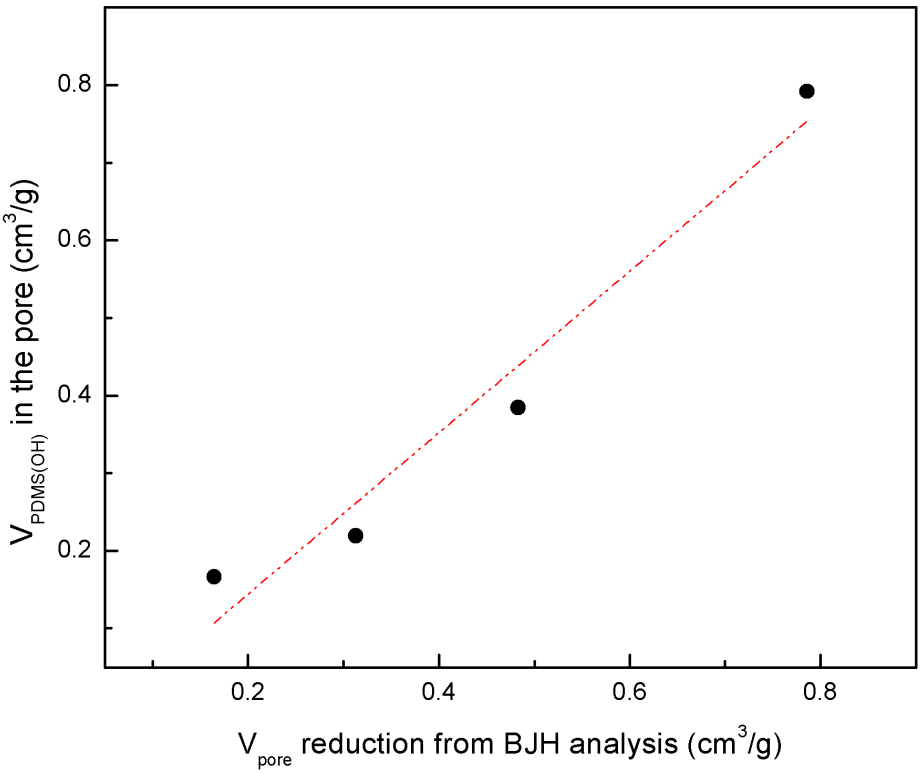

Figure 73 Correlation between volume of PDMS(OH) in the pores and pore volume reduction obtained from BJH analysis (red dotted line is the linear fit).

The analysis based on the pore size distribution revealed that there is a reduction in the pore volume for the entire pore size range and this volume reduction corresponds to the volume of the deposited polymer molecules. These observations suggest some sort of conformal coating of the aerogel surface with the polymer molecules. In order to investigate this coating hypothesis, the thickness of the coating layer was calculated for different pore sizes of each deposited sample by employing the BJH analysis results in the following manner. The thickness is calculated by dividing the polymer volume (volume corresponding to the difference between the pore volume of the deposited sample and the pore volume of the native silica aerogel) corresponding to a particular pore size range by the surface area of the native aerogel. Figure 74 displays the results obtained for each aerogel sample for the entire pore size range. The thickness of the polymer layer was found to be large (up to 14 nm) for the pores with radii larger than 26 nm. Moreover, the deviations in layer thicknesses of different polymer uptakes were calculated to be high for this pore size. However, the contribution of the amount of polymer in these pores to the total polymer uptake are negligible for all the samples since the pores in this range are only 1% of the entire pores of the mesoporous silica aerogels. For pores smaller than 26 nm, the thickness of the polymer layer fluctuates between 1 and 2 nm and seems to slightly increase with increasing mass uptake indicative of a

conformal coating of 1–2 nm on the silica aerogel surface. The polymer layer thicknesses around 1–2 nm additionally explains the insignificant decreases of the average pore sizes displayed in Figure 72. The thickness of the polymer layer was also calculated from the adsorption branch of the N_2 sorption isotherms by following the same procedure. The calculated thicknesses were around 1 nm for the mesopore range and increased for larger pores. The calculated polymer layer thicknesses were further employed to determine the surface areas of the samples after the deposition. Spherical pore geometry was assumed in the calculations for simplicity and the surface areas of polymer coated samples were determined per gram of the composites. The pore radii used in the calculations were obtained by subtracting the coating thicknesses from the pore radii of the native silica aerogel. The results were compared with the surface areas obtained from BJH analysis, since BJH analysis results were utilized for the calculations of layer thicknesses. The good agreement between the calculated values and the analysis results displayed in Figure 75 verifies the coating of the silica aerogel surface with polymer layer of the determined thicknesses. The deviations in Figure 75 most probably originate from the spherical pore geometry assumption which is a very crude assumption for the interconnected pore networks such as in the case of aerogels.

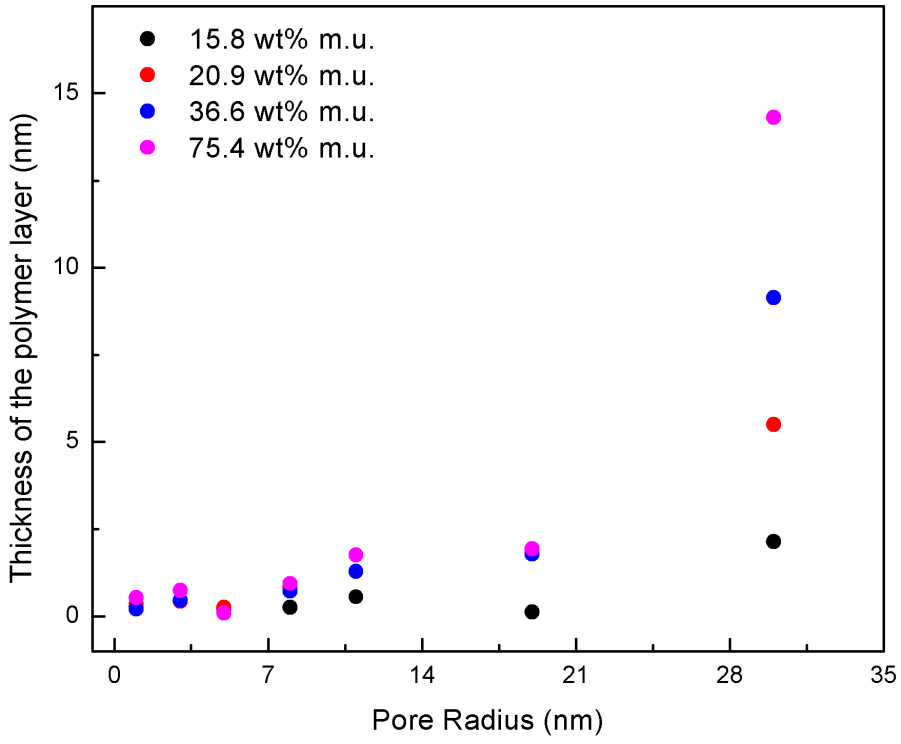

Figure 74 The thickness of the polymer layers for different pore sizes of the deposited samples.

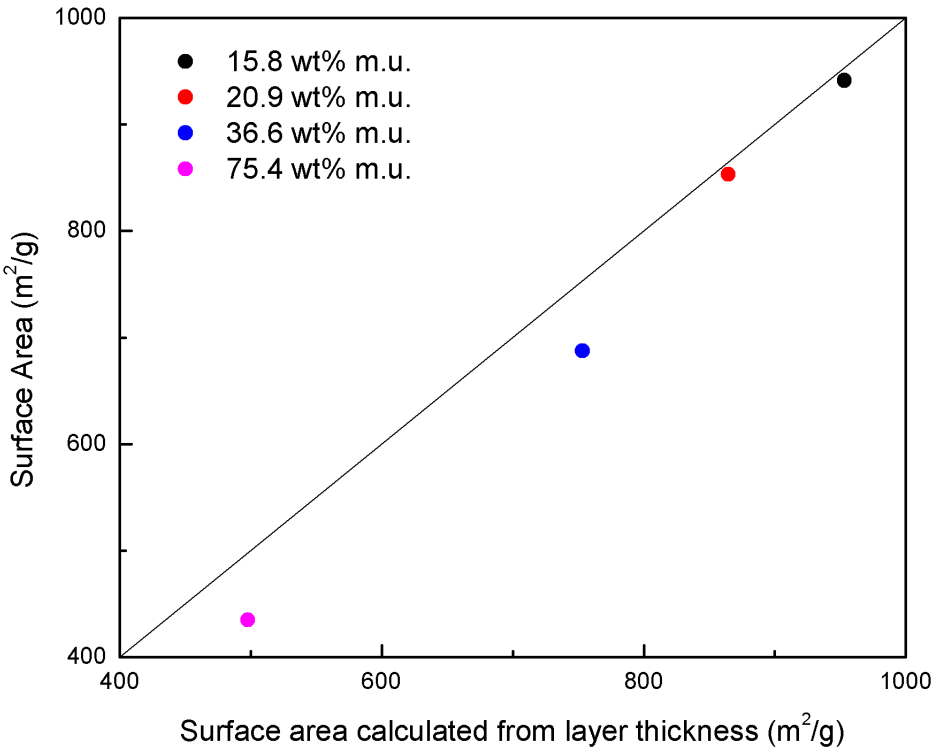

Figure 75 The surface areas of the samples obtained from BJH analysis and calculated from deposited layer thicknesses.

5.4.2. Effect of Polymer Molecular Weight and Deposition Temperature

The deposition experiments were additionally performed by utilizing PDMS(OH) with number average molecular weight of 18000 g/mol. The experimental pressure, temperature and composition were again determined according to the demixing pressure data such that a single phase binary mixture of PDMS(OH)–CO_2 was retained in the vessel throughout the experiments [101]. All of the depositions were conducted at 31 MPa. After the deposition the aerogel samples were extracted with 300 mL of pure CO_2 at the deposition conditions in order to remove the unreacted polymer. Each deposition experiment was repeated 3 times to evaluate the reproducibility.

In the previous section, PDMS(OH) (M_n=2750 g/mol) was demonstrated to react with the surface –OH groups of silica aerogels from the terminal –OH groups. As a result of this reaction the polymer molecules were found to form a thin coating layer on the aerogel surface [93]. As a continuation of that study, we investigated the effects of deposition temperature as well as the polymer molecular weight on the silica aerogel–PDMS(OH) nanocomposite materials. The deposition of low (M_n=2750 g/mol) and high (M_n=18000 g/mol) molecular weight PDMS(OH) was performed with 0.5 g of polymer amount which corresponded to 2.2

wt.% of polymer concentration in the vessel. The silica aerogel samples were exposed to PDMS(OH)–CO_2 binary mixtures for 24 h. The depositions were conducted at three different temperatures, namely, 313.2 K, 323.2 K and 333.2 K. Figure 76 displays the polymer uptakes of the aerogel samples. The deviations for each deposition were represented as error bars. It is apparent that the mass uptakes increased with increasing temperature which was attributed to the enhanced reaction rates at higher deposition temperatures. In addition, mass uptakes were higher for the higher molecular weight PDMS(OH) with larger deviations which indicated that the depositions performed with lower molecular weight PDMS(OH) were more reliable by means of reproducibility. The average grafting densities of PDMS(OH) were also calculated in terms of mmol polymer per gram of silica aerogel and the results are shown in Figure 77. Although higher polymer uptakes were obtained for high molecular weight PDMS(OH), the grafting densities were significantly lower compared to the low molecular weight PDMS(OH). Low molecular weight PDMS(OH) (M_n=2750 g/mol) has 37 repeating units whereas PDMS(OH) with 18000 g/mol molecular weight has 242 repeating units. The lower grafting densities obtained for high molecular weight PDMS(OH) were attributed to the large repeating unit number of the polymer. Reaction of one PDMS(OH) molecule with 242 repeating units probably shielded many adjacent surface –OH groups of aerogel and prevented further reactions of them with other polymer molecules.

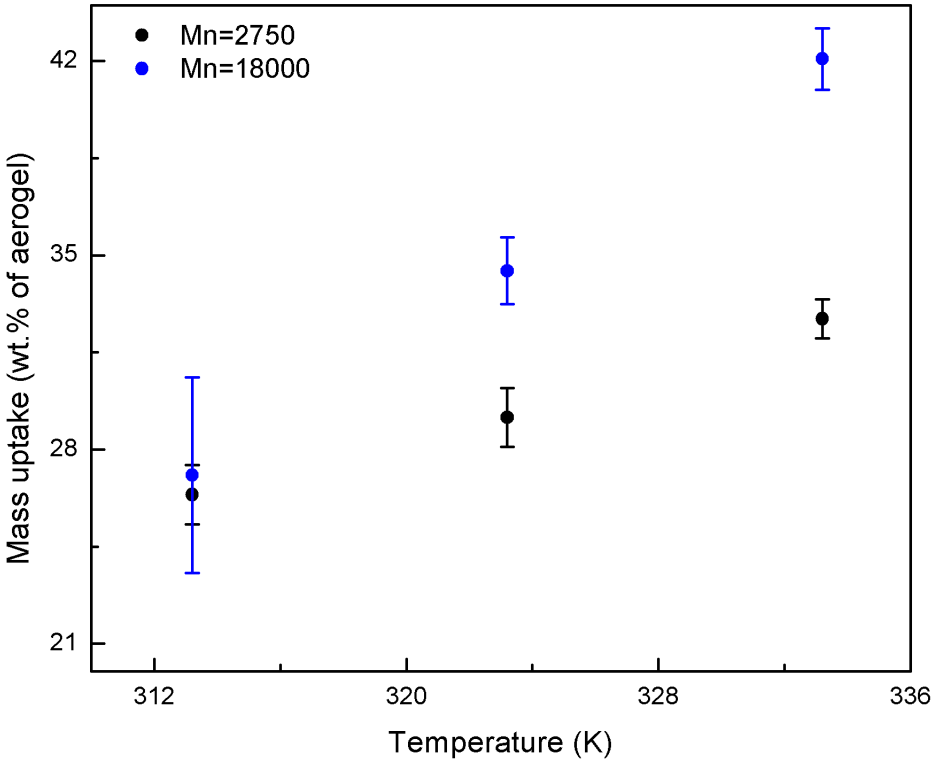

Figure 76 Mass uptakes of the aerogel samples at different temperatures.

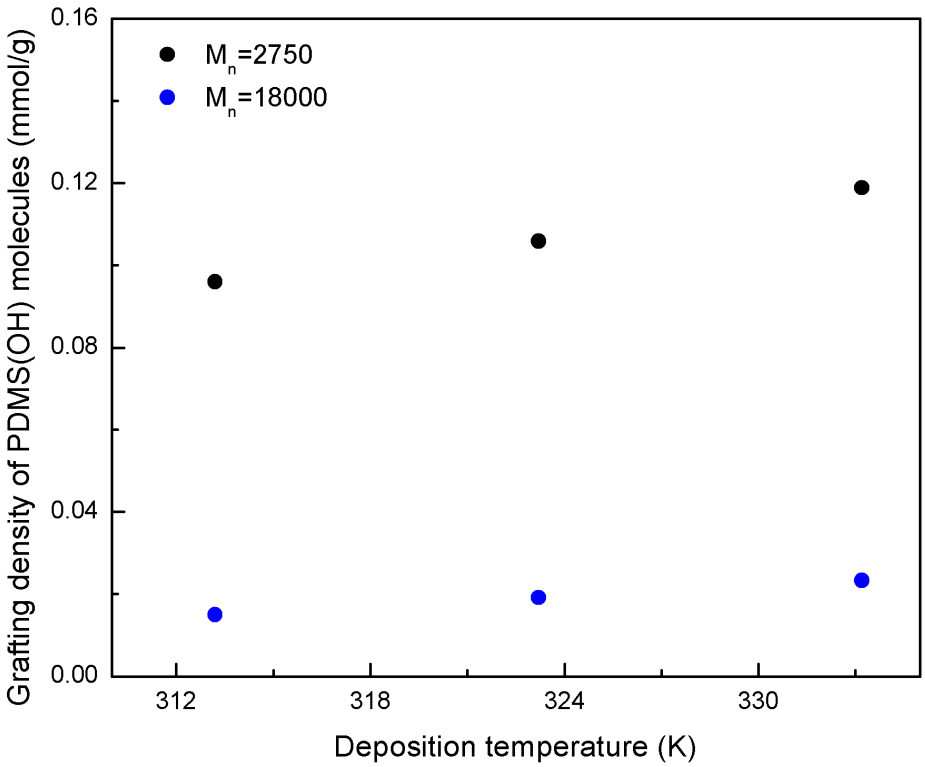

Figure 77 Grafting densities of PDMS(OH) on the deposited aerogel samples at different temperatures.

The ATR–FTIR analyses were performed with the deposited samples to confirm the binding of the polymer to the silica aerogel surface. Figure 78 compares IR spectra of the native silica aerogel and aerogel sample deposited with high molecular weight PDMS(OH). There are two intense peaks that are specific to the chemical structure of silica and therefore occur in both spectra since both the backbone of the polymer and the solid silica network of the aerogel is made from silica. These peaks occur at 800 cm^{-1} and 1080 cm^{-1} and are characteristic to Si–O–Si bending and stretching vibrations, respectively [65]. After deposition, the intensity of the peak at 800 cm^{-1} increases due to additional Si–O–Si bending vibrations of the polymer backbone. More importantly, there are three peaks indicative of the presence of the polymer in the aerogel sample. The peak at 2963 cm^{-1} represents the C–H stretching vibrations originating from the methyl side groups of PDMS(OH). The peak at 1267 cm^{-1} is due to the Si–C stretching vibrations that originate from methyl side groups attached to the polymer backbone. The peak appearing at 850 cm^{-1} for the deposited sample was attributed to ≡Si–O–$Si(CH_3)_2$–R bond that were formed due to the condensation reaction between the ≡Si–OH groups of the aerogel and OH–$Si(CH_3)_2$–R end groups of PDMS(OH) [65]. The C–H and Si–C stretching vibration peaks appeared upon polymer deposition while the intensity of Si–O–Si peak increased which signifies the reaction between PDMS(OH) and surface –OH groups of

the silica aerogel in the deposited nanocomposites. Furthermore, the peak at 960 cm^{-1} that was observed in native silica aerogel sample was attributed to stretching of Si–OH groups of the aerogel [65-66]. Upon deposition this peak was observed to shift to left and merge with Si–O–Si peak which was additionally attributed to the reaction between PDMS(OH) and the surface Si–OH groups of the aerogel. The aforementioned specific peaks can be observed from the marked positions in Figure 78.

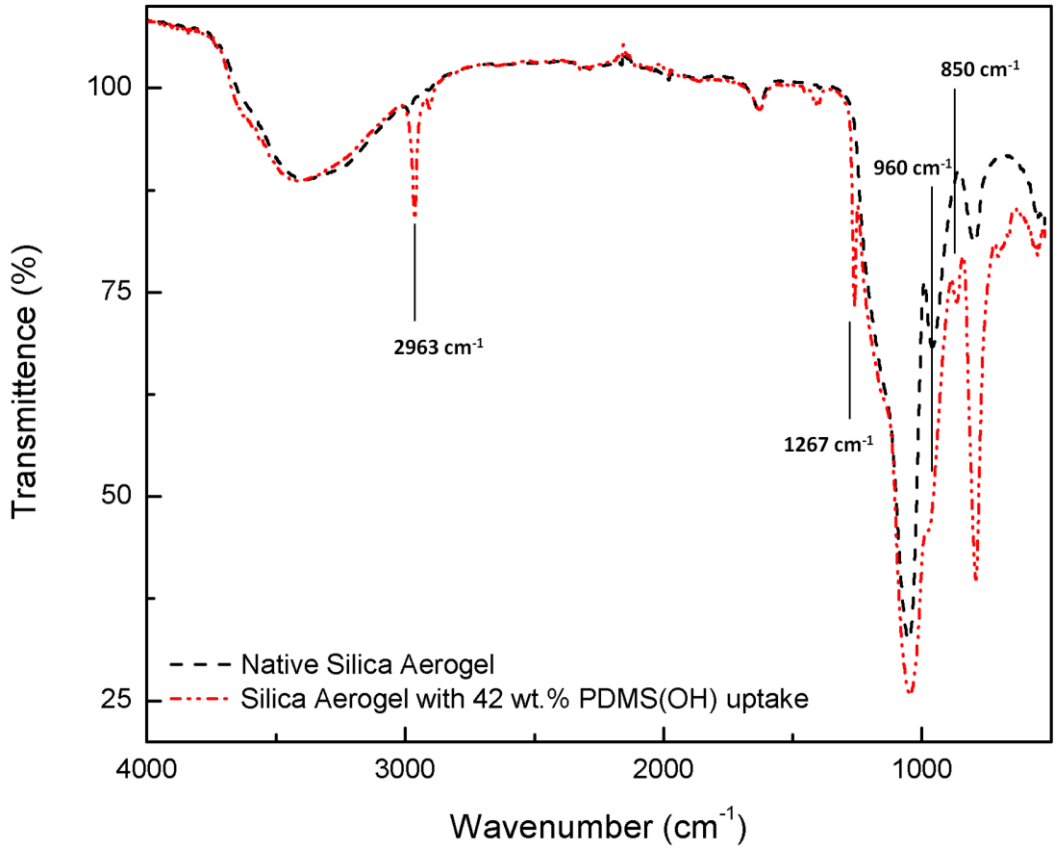

Figure 78 ATR–FTIR spectra of native silica aerogel sample and silica aerogel–PDMS(OH) nanocomposite.

High molecular weight of a polymer generally induces diffusion limitations, especially when the polymer molecules have to travel through a path of nano–size features that are compared to the size of the polymer. In order to investigate such possible diffusion limitations ATR–FTIR analyses of the deposited aerogel samples were performed with the portions taken from the outer surface and the center of the cylindrical samples. Figure 79 and Figure 80 displays the spectra obtained from the aerogel samples deposited with low and high molecular weight PDMS(OH), respectively. The spectra in Figure 79 clearly show that the peaks that are specific to PDMS(OH) coincide for the center and outer surface of the sample that was deposited with the low molecular weight PDMS(OH). This observation indicates that the

amount of polymer at the center and outer surface of the aerogel sample was the same and there were no diffusion limitations in the case of deposition of low molecular weight polymer. On the other hand, it is apparent from Figure 80 that there were significant differences in the intensities of the aforementioned peaks for the deposition of high molecular weight PDMS(OH), the intensities for the outer surface being significantly higher than the center. This means that the amount of polymer molecules deposited at the outer surface of the aerogel sample was higher than the amount deposited at the center which can be explained by diffusion limitations caused by the high molecular weight of the polymer. One possibility is that the bulky polymer molecules that were deposited at the outer surface of the aerogel sample at the initial contact perhaps blocked some pores which eventually prevented further diffusion of the polymer molecules to the center of the cylindrical sample. In addition, by employing Funazukuri's correlation [157-158], the binary diffusion coefficient of PDMS(OH) with 2750 g/mol molecular weight was estimated to be 2.56 times greater than that of PDMS(OH) with 18000 g/mol molecular weight in $scCO_2$. Slower diffusion of high molecular weight PDMS(OH) could be another factor that have caused the difference in the amount of deposited polymer molecules and hence the difference in peak intensities. The non–homogenous distribution of the polymer molecules throughout the silica aerogel can additionally be observed from the top views of the cylindrical samples given in Figure 81. It is obvious that the appearance of the deposited aerogel sample close to the outer perimeter of the cylinder is more opaque and white than the center. In addition, the effect of polymer deposition on the transparency of the aerogel can be noticed from Figure 81, as well.

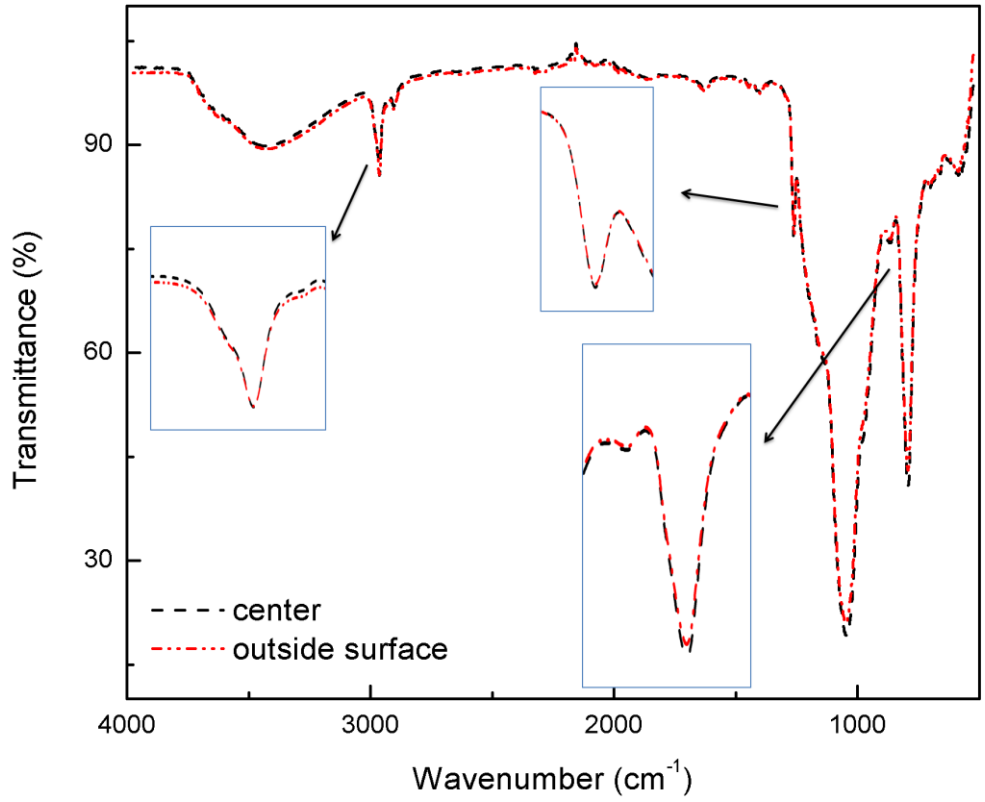

Figure 79 ATR–FTIR spectra of aerogel sample deposited with PDMS(OH) of molecular weight 2750 g/mol.

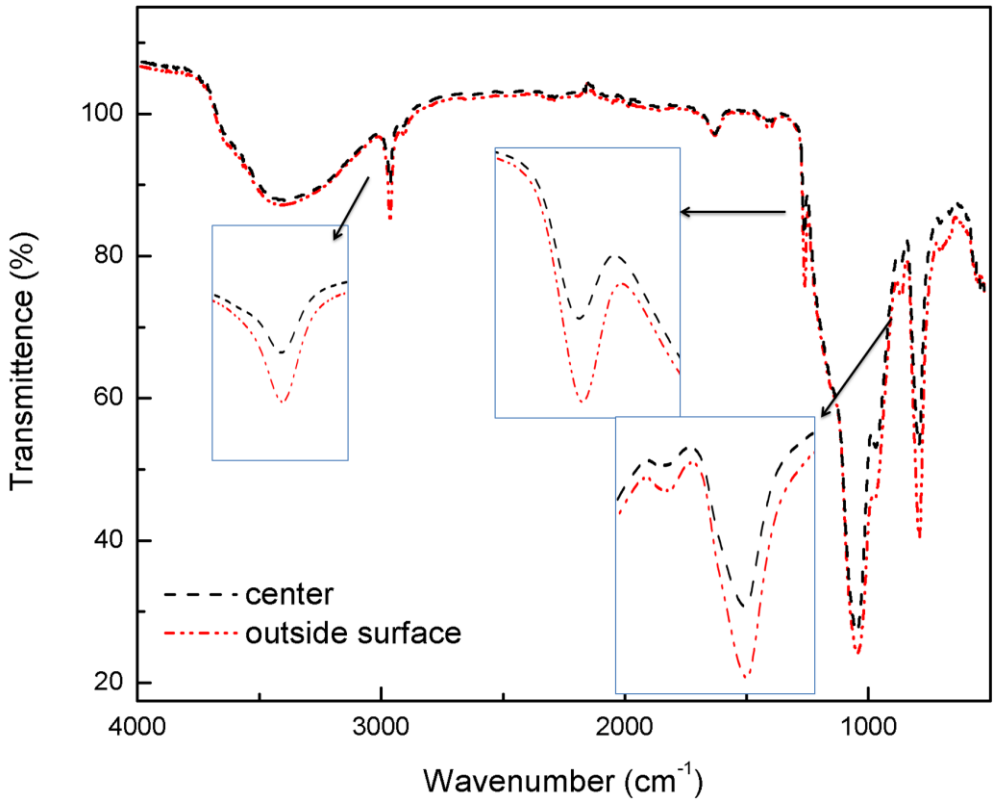

Figure 80 ATR–FTIR spectra of aerogel sample deposited with PDMS(OH) of molecular weight 18000 g/mol.

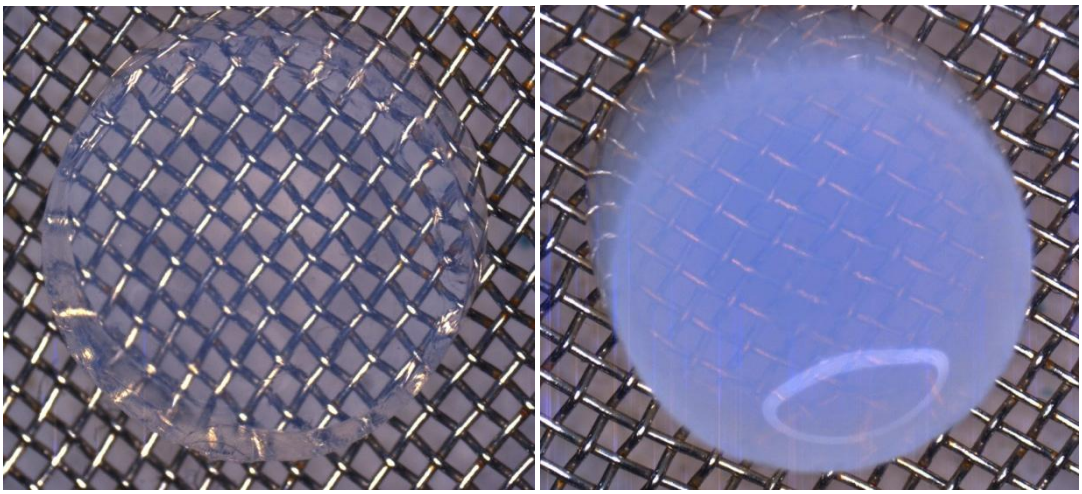

Figure 81 Images of native silica aerogel (left) and aerogel deposited with PDMS(OH) at 313.2 K (right).

It was previously demonstrated that PDMS(OH) with 2750 g/mol molecular weight form a thin coating layer on the silica aerogel surface without filling or blocking any pores. The homogenous distribution of polymer molecules throughout the samples was confirmed with ATR–FTIR analysis. On the other hand it was also understood from the ATR–FTIR measurements that the aerogel samples deposited with the high molecular weight polymer were non–homogenous with larger polymer amount at the outer surface and less polymer at the inner part. In order to clarify the structural outcomes of these observations N_2 sorption analyses were performed with the aerogels that were deposited with the high molecular weight PDMS(OH) and the pore structures of the nanocomposites were investigated. The pore size distributions of the deposited samples are shown in Figure 82. For comparison, the N_2 adsorption–desorption isotherms of the areogel sample deposited with PDMS(OH) at 333.2 K and native silica aerogel sample are also given in Figure 82. The isotherms for the other deposited samples were similar but omitted for clarity. The maximum pore volume obtained from the peak point of the pore size distribution curve decreased accordingly with the increasing deposition temperature which resulted in increasing amount of polymer in the nanocomposites. In addition, it is clearly observed from the N_2 sorption isotherms that the aerogel samples have Type IV isotherms with hysteresis loops which are specific to multi–layer adsorption on mesoporous materials with capillary condensation. The important feature that should be noted is that a shift from Type H1 hysteresis loop (native silica aerogel) to Type H2 hysteresis loop (deposited sample) was observed. H1 hysteresis loops are generally observed for materials with uniform pores and narrow pore size distributions whereas H2 hysteresis loops are associated with materials exhibiting more complex pore structures in

which pore network effects such as pore blocking are significant. Hence, the observed shift of the hysteresis loop from Type H1 to Type H2 upon deposition was attributed to the blocking of the pores by the deposited polymer molecules which was also confirmed by ATR–FTIR analysis. Summary of N_2 sorption analyses results are additionally listed in Table 30. It is apparent that the BET surface areas and pore volumes decreased with increasing polymer amount in the nanocomposites. Moreover, BJH adsorption average pore radius of the deposited samples decreased accordingly with increasing temperature and thus PDMS(OH) amount in the samples. *C* constants that are given in the last column of Table 30 are associated with the heat of adsorption between the adsorbate (N_2 molecules) and adsorbent (silica aerogel) and represent the interaction between the two. Higher *C* values indicate stronger interactions. From Table 30 it is obvious that there is a remarkable decrease of *C* values up on deposition compared to the native silica aerogel which indicates that the interaction of N_2 molecules with the surface of silica aerogel–PDMS(OH) nanocomposites was significantly weaker than that of with the native silica aerogel surface. In our previous study, the aerogel samples deposited with PDMS(OH) were shown to be hydrophobic due to the methyl side groups of the polymer backbone with contact angles up to 145^o [93]. Therefore, the significant decrease observed in *C* constants was attributed to the increasing hydrophobicity of the nanocomposites, and thus, weakening interaction of N_2 molecules with the surface. The hydrophobicity of the nanocomposites is also explained in detail in the next section.

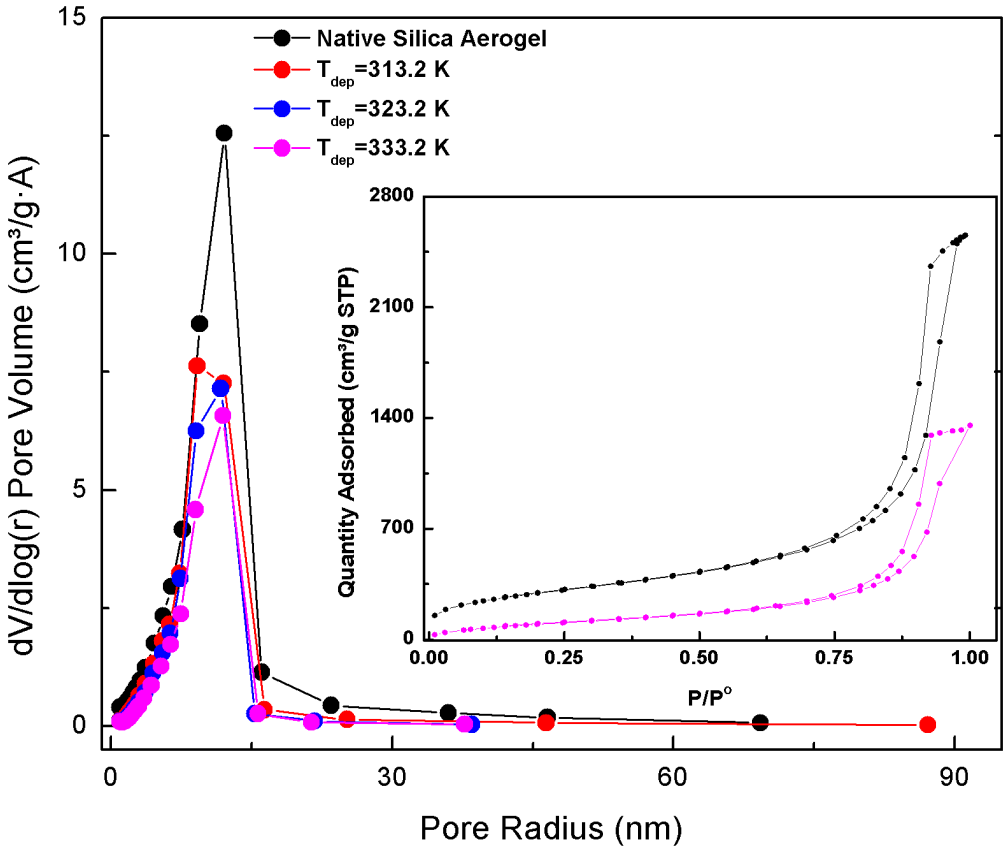

Figure 82 Pore size distributions and isotherms of native silica aerogel and aerogels deposited with PDMS(OH) of molecular weight 18000 g/mol.

Table 30 Summary of N_2 adsorption–desorption analyses results.

Deposition *T* (K)	BET Surface Area (m^2/g)	Pore Volume (cm^3/g)	BJH Adsorption Average Pore Radius (nm)	*C*
313.2	589.04	2.72	7.67	40.15
323.2	474.18	2.40	6.54	28.37
333.3	391.55	2.09	6.07	22.39
Native Silica Aerogel	1046.94	3.87	7.12	99.63

Furthermore, N_2 sorption data of the aerogel samples were analyzed with the non–local density functional theory (NLDFT) and the cumulative surface area and differential pore volume distributions for different pore widths were calculated. Figure 83 and Figure 84 compares the respective distributions of the deposited samples with that of the native silica aerogel. It can clearly be ascertained from both figures that the deposition of the polymer blocks the pores that are smaller than 7 nm. There was no contribution to the cumulative surface area nor to differential pore volume from these pore sizes for the deposited samples while native silica aerogel sample exhibited certain amount of pore volume and surface area

for pore widths smaller than 7 nm. There were also significant reductions in the pore volumes and surface areas at larger pore widths of the deposited samples compared to native silica aerogel as seen in the figures. Total area and volume in the pores were extracted from NLDFT analysis and the results were summarized in Table 31. As expected, the pore area and volume values decreased upon deposition due to the increasing polymer amount in the composites. In addition, the pore size distributions of the deposited samples were compared with native silica aerogel in Figure 85.

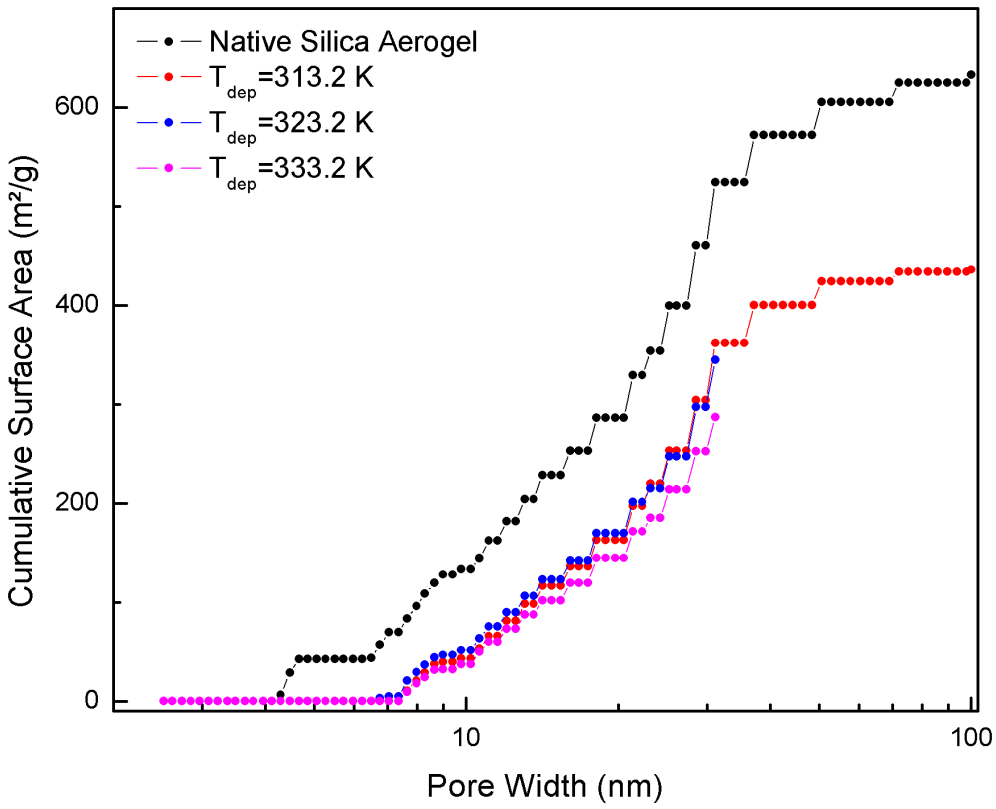

Figure 83 Cumulative surface areas of the aerogel samples for different pore widths obtained from NLDFT analyses.

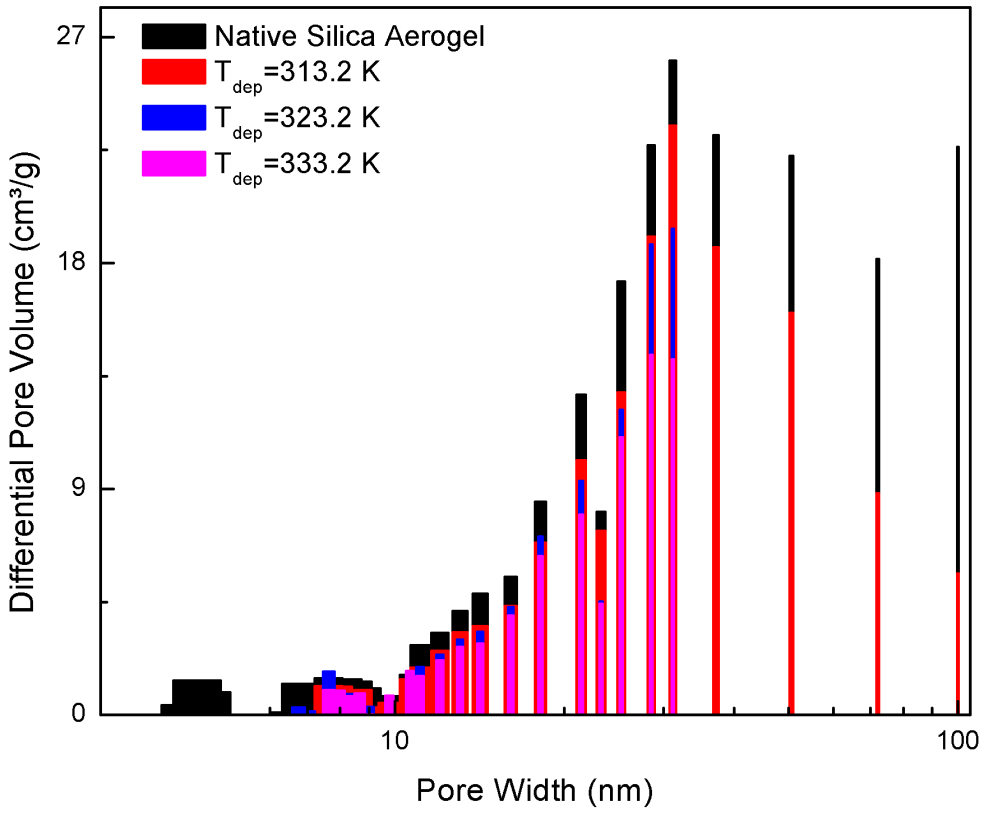

Figure 84 Differential pore volumes of the aerogel samples for different pore widths obtained from NLDFT analyses.

Table 31 NLDFT results from N_2 adsorption–desorption analyses.

Deposition *T* (K)	Total Area in Pores > 2.5 nm (m^2/g)	Total Volume in Pores <100 nm (cm^3/g)
313.2	436.2	2.74
323.2	344.92	1.71
333.3	287.32	1.41
Native Silica Aerogel	633.45	3.87

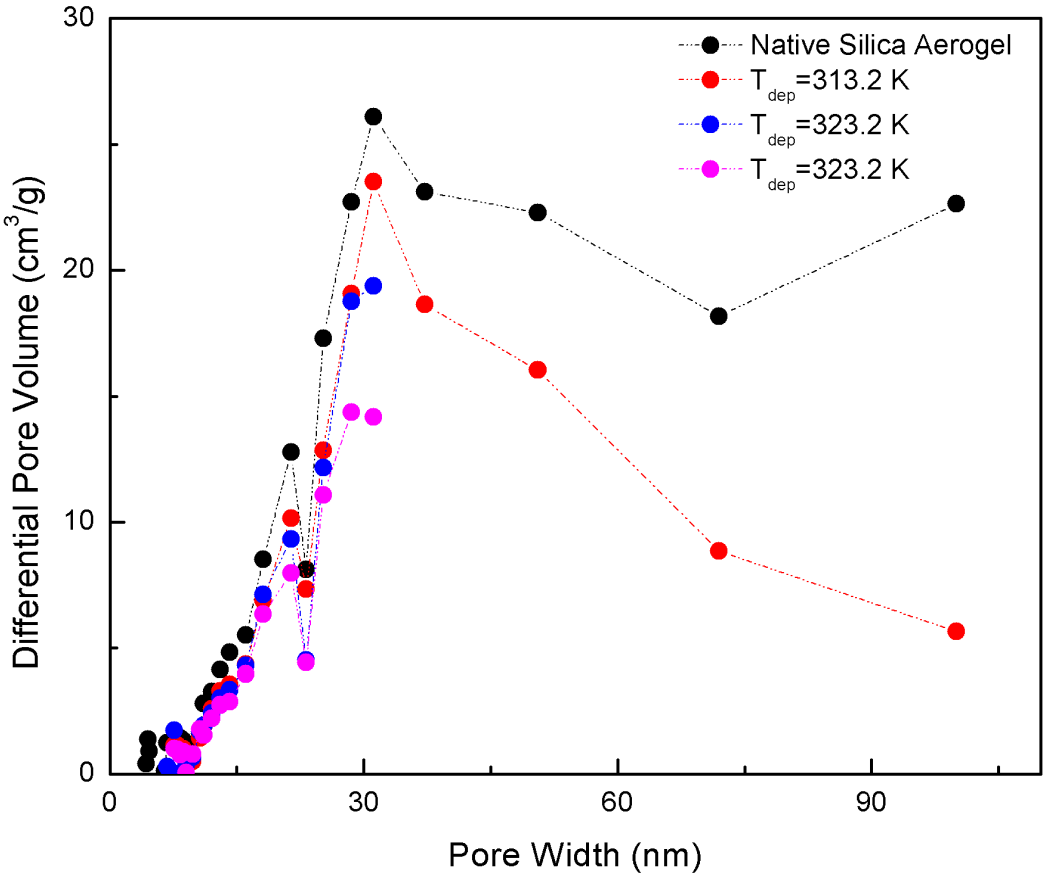

Figure 85 Differential pore volumes of the aerogel samples for different pore widths obtained from NLDFT analyses.

5.4.3. Hydrophobicity

Silica aerogels are inherently highly hydrophilic due to the vast amount of –OH groups present on their surface. On the other hand, PDMS(OH) is a hydrophobic polymer with methyl side groups attached to the silica backbone. Coating the surface of the silica aerogels with a PDMS(OH) layer should cause an increase in the hydrophobicity of the surface. The contact angles of the two deposited samples with mass uptakes of 36.6 wt.% and 75.4 wt.% were measured along with the native silica aerogel and the results are shown in Figure 86. The native silica aerogel was completely wetted upon water contact. However, the contact angles for the samples with 36.6 wt.% and 75.4 wt.% polymer were determined to be 108^{o} and 145.1^{o}, respectively. The increasing contact angles with increasing amount of polymer in the samples was expected and also in agreement with the C values listed in Table 29. Hydrophobicity is a key property for these materials which significantly increases the product life and hence, these observations are crucial when the utilization of aerogel composites in transparent VIPs is considered.

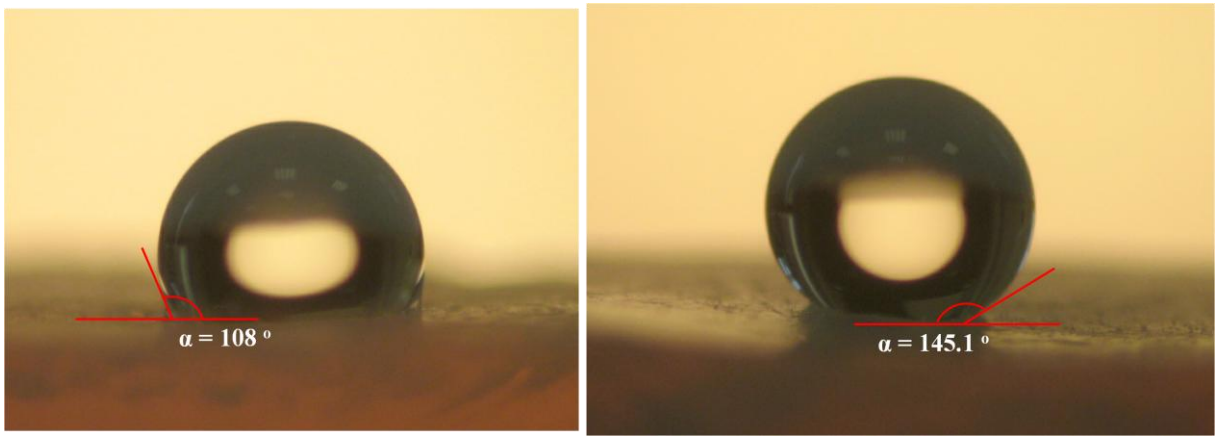

Figure 86 The water droplets on the deposited aerogels with 36.6 wt.% (left) and 75.4 wt.% (right) PDMS(OH).

5.4.4. Thermal Conductivity

Additionally, 6.5x6.5 cm^2 silica aerogel samples having different densities were synthesized for the thermal conductivity measurements. The thermal conductivity measurements were performed with the guarded hot plate at EMPA, Switzerland. Silica aerogel samples were synthesized with the standard two–step sol–gel procedure. In order to obtain aerogels with various densities the aging of the samples were performed in TEOS–water–ethanol solutions with different concentrations. One of the aerogel samples was additionally deposited with small amount of PDMS(OH).

Figure 87 displays the images of the 6.5x6.5 cm^2 silica aerogel samples synthesized for the thermal conductivity measurements. The deposited aerogel sample had a polymer uptake of 3 wt.% of aerogel. The thermal conductivity measurements were performed with a home–made guarded hot plate device at EMPA (Zurich, Switzerland), which can perform measurements of the samples of typical size of as low as 5x5 cm^2. The measurements of the aerogel samples were repeated twice to identify the reproducibility of the technique. Table 32 lists the thermal conductivity results for the aerogel samples together with their apparent densities.

It is apparent that the thermal conductivities listed above are slightly higher than the values reported in the literature. Therefore, the accuracy of the home-made guarded hot plate equipment was questioned. It is well-known that the most accurate and eligible measurement technique in determining the thermal conductivity of highly insulating materials such as aerogels is the guarded hot plate technique which requires 30x30 cm^2 sample sizes. Hence 30x30x1.2 cm^3 native silica aerogel panel was synthesized and the thermal conductivity was measured by commercial guarded hot plate equipment. The density of the silica aerogel panel

was measured to be 0.19 g/cm^3 which is a very close value to the low density silica aerogel that is listed in Table 32. However, the thermal conductivity of the silica aerogel panel was measured as 16 mW/mK which verified the speculated overestimation of the values obtained at EMPA. It was calculated that, the thermal conductivity measured at EMPA was 34% higher than the actual value that was obtained with the guarded hot plate. Regarding this percentage, the thermal conductivities that were measured at EMPA were corrected down and these values are also listed in Table 32.

Figure 87 6.5x6.5 cm^2 silica aerogel samples with densities; 0.183 g/cm3 (left) and 0.272 g/cm3 (right).

Table 32 The thermal conductivities and densities of 6.5x6.5 cm^2 silica aerogel samples.

Sample	**Density (cm^3/g)**	**Raw Thermal Conductivity (mW/mK)**	**Corrected Thermal Conductivity (mW/mK)**
Silica Aerogel–Low density	0.183	21.4	16
Silica Aerogel–High density	0.272	28.7	21.4
PDMS(OH)–Silica Aerogel Composite	0.244	21.9	16.3

Moreover, a model was established based on the formulations given in Chapter 2. The contributions of different mechanisms on total thermal conductivity was first estimated for a standard silica aerogel sample with 150 kg/m^3 density and 20 nm pore diameter. The model results are given in Figure 88. It is clear that the minimum total thermal conductivity can be obtained at densities around 100–130 kg/m^3 where the contributions from each mechanism sum up to a minimum. In addition, the effects of pore diameter on the total conductivity of aerogels were investigated and it can clearly be observed from Figure 89 that increasing pore sizes significantly increase the total thermal conductivity of aerogels.

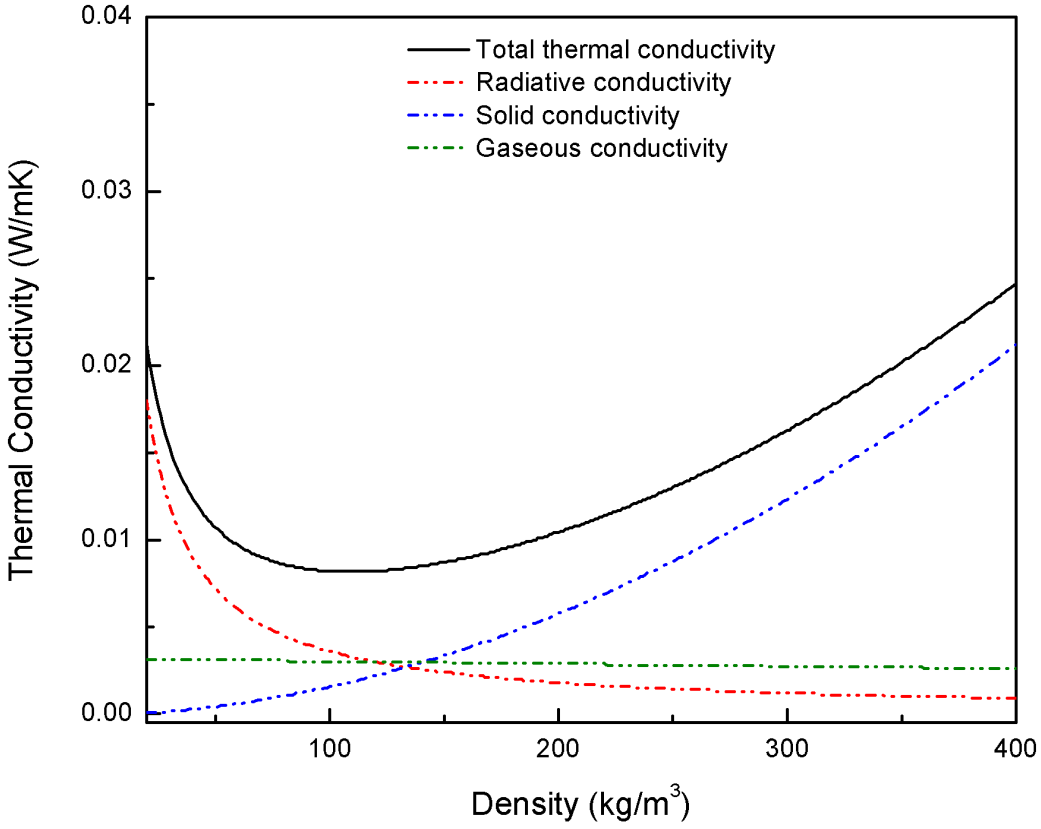

Figure 88 Contributions of different mechanisms on total thermal conductivity.

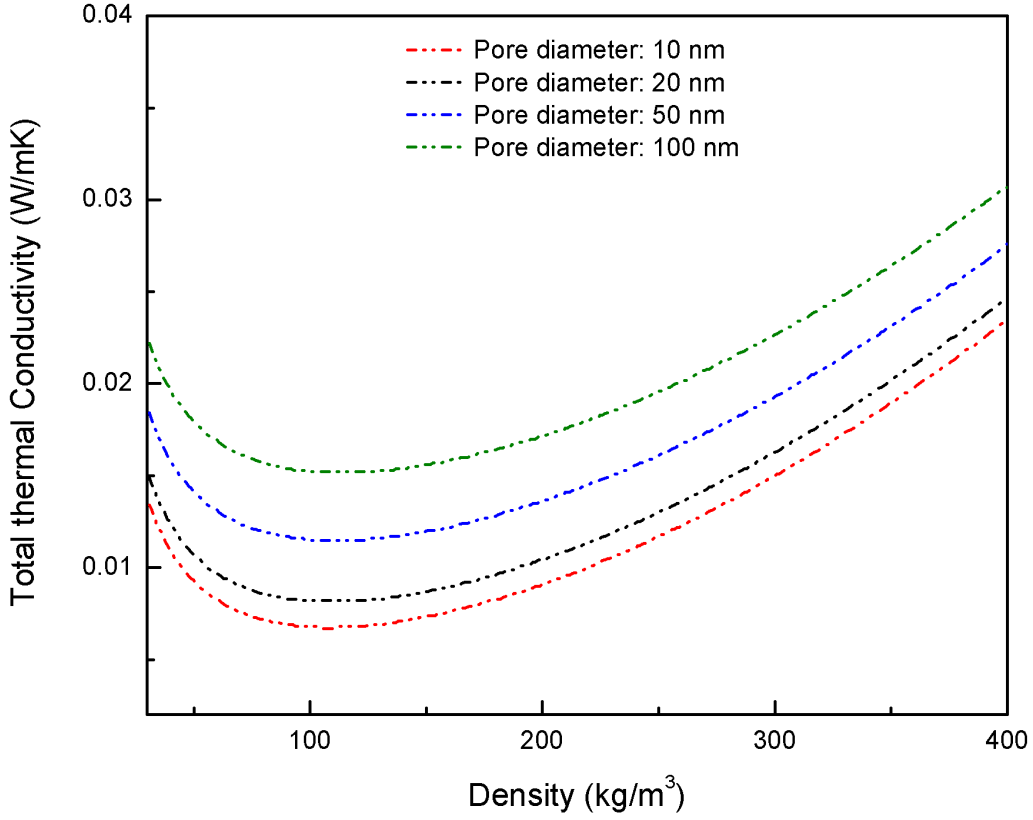

Figure 89 Effects of pore size on total thermal conductivity.

Moreover, the effects of the deposited polymer layer on the thermal conductivity of silica aerogels were further estimated. Figure 90 compares the total thermal conductivities of a native silica aerogel and a PDMS(OH)–silica aerogel composite with 30 wt.% of polymer uptake. It is observed that the deposition of the polymer decreased the thermal conductivity. However, the increase in density up on polymer deposition was not considered in Figure 90 which is displayed in Figure 91. Figure 91 shows the effects of different polymer uptakes on the density as well as the total thermal conductivity of silica aerogels. One important point that is observed in Figure 91 is that up to around 25 wt.% of polymer uptake there is a decrease in total thermal conductivity up on deposition, although the density is monotonically increased. These results indicate that the amount of polymer in PDMS(OH)–silica aerogel composites does not increase the total thermal conductivity when the polymer uptakes are kept up to around 25 wt.%.

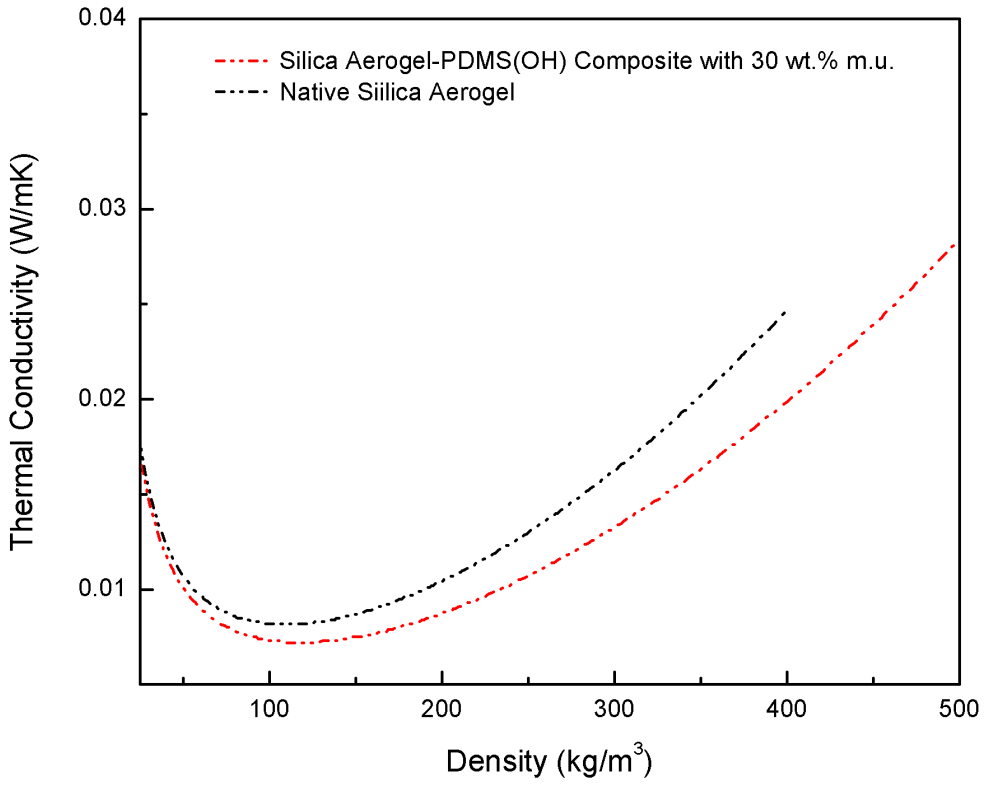

Figure 90 Effects of polymer deposition on total thermal conductivity.

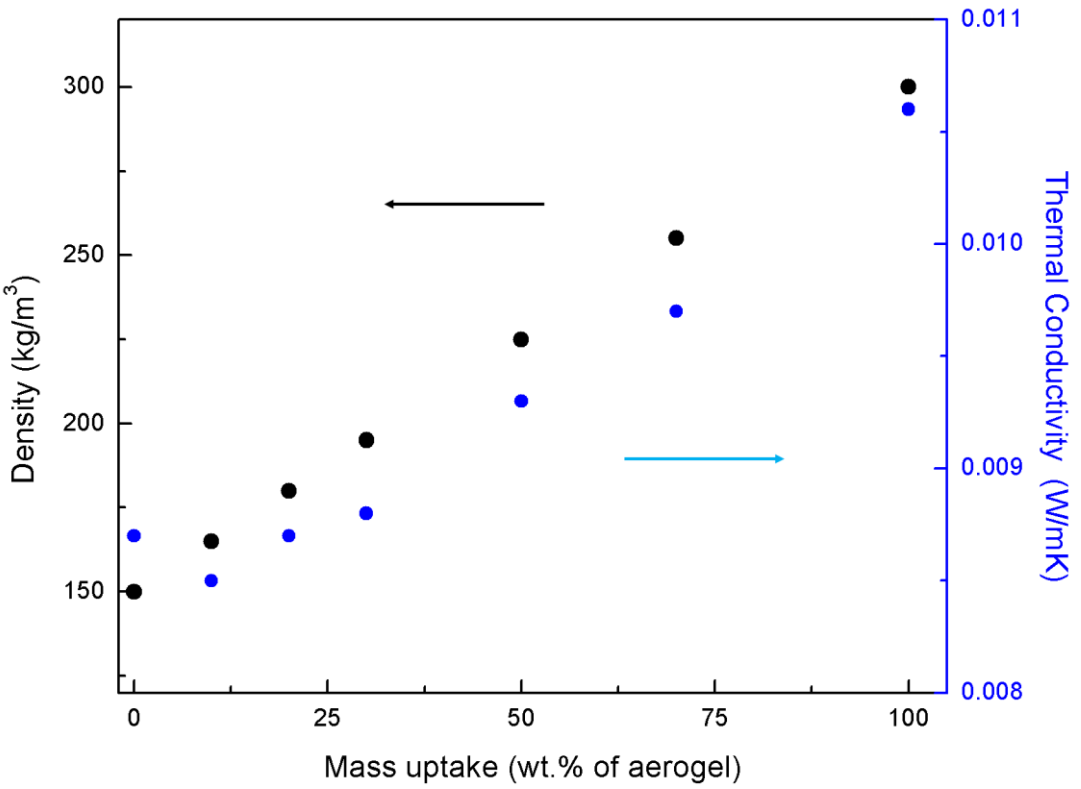

Figure 91 Effects of different mass uptakes on density and total thermal conductivity.

It is apparent that the values listed in Table 32 do not agree very well with the model results given above. However, it should be noted that the formulations used in the calculations are merely rough estimates and a more detailed model should be utilized along with accurately determined material parameters. The computations were carried out solely to give an idea about the effects of different parameters on the total thermal conductivity of aerogels.

5.4.5. Mechanical Properties

The mechanical properties of aerogels were quantified by compression tests and the results were evaluated. Figure 92 compares the stress–strain curve of the silica aerogel deposited with PDMS(OH) at 313.2 K with that of the native silica aerogel. As seen in the figure, compressive strength of PDMS(OH)–silica aerogel nanocomposite material was obtained to be greater than the native silica aerogel. In addition, no yield was observed for the materials. Compressive strength is defined as the capacity of a material to withstand the compressive forces, and thus it can be concluded from Figure 92 that there was a significant improvement in the mechanical strength of the silica aerogel upon deposition of PDMS(OH). Such improvement was attributed to the highly flexible and rubbery structure of PDMS(OH). It is believed that, upon deposition, PDMS(OH) molecules form a coating layer on the surface of

silica aerogel reinforcing the weak regions (i.e. necks between the secondary particles) of the native silica aerogel network structure. Therefore, at a constant stress, the displacement in aerogel composite was much less than native silica aerogel, meaning that native silica aerogel was more deformed under the effect of the same force. Moreover, compressive moduli of the materials were also calculated [64]. The values obtained as 0.113 MPa and 0.396 MPa for the native silica aerogel and the deposited sample, respectively. The compressive modulus of the silica aerogel–PDMS(OH) nanocomposite was more than three times higher than that of the native silica aerogel which confirms the anticipated improvement of the mechanical strength upon deposition.

In 2008, Paakko *etal.* employed the same technique to measure the compression strength and specific compression modulus of cellulose aerogel materials [159]. The cellulose aerogels reported in the study had very low densities, in the order of 0.02 – 0.03 g/cm^3, and the compression strength for these materials were measured as 0.2 – 0.24 MPa with specific compression moduli of 0.18 – 0.24 MPa. It is important to note that the maximum strain obtained for these materials was approximately 70%. In another study, the same measurement technique was utilized to determine the mechanical properties of polyacrylamide hydrogels [64]. The compressive strength up to 0.003 MPa was obtained whereas the specific compressive modulus varied between 0.0021 and 0.0043 MPa for different hydrogels. Apparently, it is not reasonable to compare such materials with the silica aerogel samples, however the results are explained to give an idea about the mechanical properties of materials with similar structures.

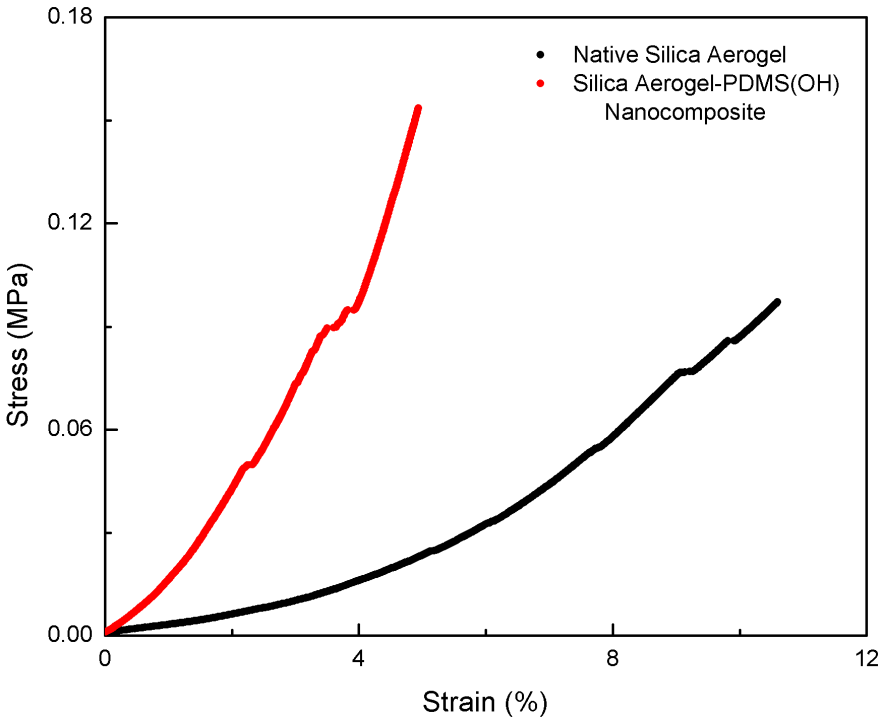

Figure 92 Strain–stress curves for native silica aerogel and deposited silica aergel sample obtained from compression tests.

5.4.6. CO_2 Uptake Capacities

Since PDMS(OH) is a highly CO_2–philic polymer, it was speculated that the PDMS(OH)–silica aerogel composites may have a high CO_2 sorption capacity. CO_2 uptakes of the composites were measured by utilizing a Micromeritics ASAP 2020 N_2 adsorption–desorption equipment. CO_2 was adsorbed on the samples at 298 K up to 1 bar of pressure. Figure 93 shows the CO_2 adsorption isotherms of PDMS(OH)–silica aerogel composites with different amount of polymer together with the native silica aerogel. The amount of CO_2 adsorbed by the samples was given as mmol/m^2 for consistency, since the surface areas are decreased upon polymer deposition. It is clearly observed that the amount of CO_2 adsorbed increased accordingly with the increasing polymer amount in the composites, although the increase is not significant when compared to native silica aerogel. In addition, it can be also observed from Figure 93 that the adsorption can be defined with a linear equation representative of physisorption.

It was previously reported that pure silica surfaces do not interact very strongly with CO_2 because the surface –OH groups cannot induce strong enough interactions with CO_2 [160]. CO_2 uptake capacity of raw silica gel materials was reported to be in the order of 0.05–0.1

mmol/g at 10 kPa [160] whereas the value was found to be 0.12 mmol/g for native silica aerogel in our experiments. Regarding these results, PDMS(OH)-silica aerogel composites can be considered as potential candidates also for CO_2 capture and storage applications and further studies can be carried out to improve the CO_2 uptake capacities of these materials.

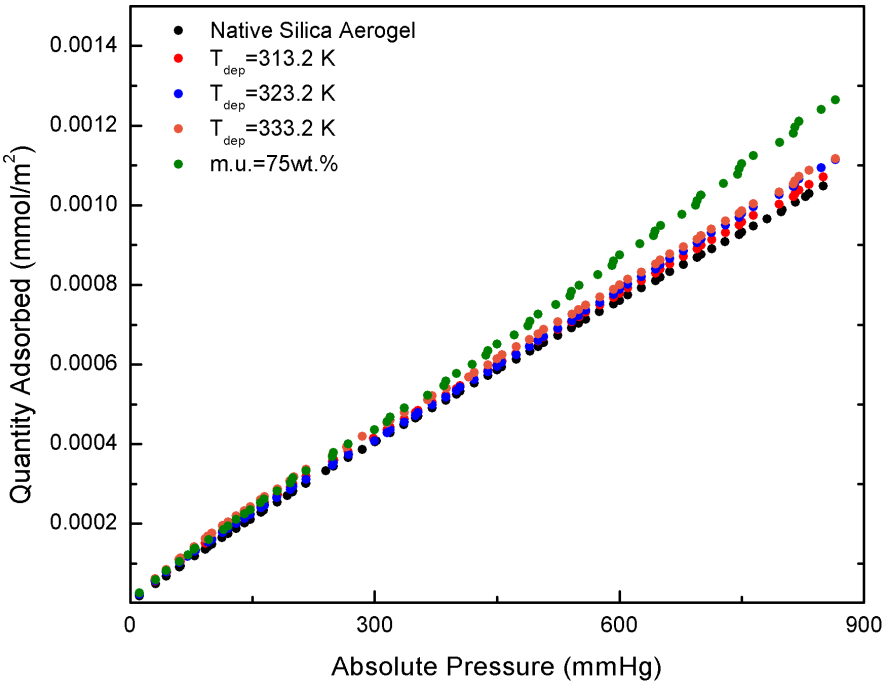

Figure 93 CO_2 uptakes of the native silica aerogel and deposited aerogel samples (m.u.=mass uptake).

5.5. Summary and Conclusion

PDMS(OH)-silica aerogel composites were developed by employing a reactive supercritical deposition technique. The technique is composed of two basic stages; first stage is the dissolution of PDMS(OH) in CO_2 that results in a single phase binary mixture of PDMS(OH)–CO_2 in the vessel and the second stage is the exposure of the silica aerogel samples to the single phase binary mixture. Throughout the experiments the deposition conditions were determined according to the demixing pressure data of PDMS(OH)-CO_2 binary mixtures. The polymer molecules were demonstrated to react with the surface –OH groups of the aerogel samples. The polymer concentration, the deposition time and temperature were found to increase the polymer uptake of the aerogels. It was shown that polymer uptakes as high as 75.4% wt of aerogel could be attained depending on the composition of the initial binary mixture. The deposited samples retained their monolithic structure and the transparency of the aerogels could be preserved up to polymer loadings of around 20 wt.%. Furthermore, the polymer molecules were determined to be homogenously

distributed throughout the aerogel when the low molecular weight PDMS(OH) is used. On the other hand, the aerogel samples deposited with high molecular weight PDMS(OH) had more polymer on the outer surface than the center of the aerogel. This non-homogeneity was attributed to the diffusion limitations originated from the high molecular weight and bulky chain of the polymer. According to the analysis results obtained from N_2 adsorption–desorption isotherms, the specific surface area and the pore volume of the deposited samples decreased with increasing polymer content. From the BJH analysis results the thickness of the polymer layer was calculated and it was found that PDMS(OH) molecules form a coating layer of ~1nm thickness on the silica aerogel surface. The deposited samples were also demonstrated to be hydrophobic and hydrophobicity increased with increasing polymer content. When compared to native silica aerogel, a threefold improvement was also observed for the PDMS(OH)-silica aerogel composites which fulfill the objectives of the NanoInsulate project. An additional outcome was the CO_2 uptake capacities of the developed composites which make them potential candidates to be used as membranes in CO_2 capture and storage applications.

CHAPTER 6

CONCLUSION

Composites of silica aerogels were developed within the context of NanoInsulate project which aimed to develop durable, robust, cost-effective, opaque and transparent vacuum insulation panels incorporating new nanotechnology-based core materials (such as aerogels and aerogel composites) and high-barrier films, that are up to six times more energy efficient than current solutions.

Silica aerogel composites with PDMS(OH) were develop in order to obtain monolithic, crack-free, transparent and mechanically durable composite materials to be used in transparent VIPs. Two different routes were followed for this purpose.

Initially, PDMS(OH)-silica aerogel and PDMS(bisalkyl-OH)-silica aerogel composites were derived by modifying the standard two-step sol-gel process. The effects of various processing parameters such as polymer addition step, polymer-to-precursor ratio and type of co-solvent on the properties of the composites were investigated. Some of the composites were obtained as monolithic whereas others were broken during the supercritical drying step. In addition, when THF and/or toluene were used as the co-solvent, the volumetric shrinkage of the composites was very high. All of the composites had opaque or highly translucent appearances which makes their usage in transparent VIPs impossible. However, the derived composites had improved mechanical properties compared to native silica aerogel and therefore they are suitable to be used as opaque core materials in VIPs.

Reactive supercritical deposition technique was employed as the second route and composites of silica aerogels with PDMS(OH) were developed by deposition of the polymer from supercritical CO_2. The deposition experiments were performed from single phase binary mixtures of PDMS(OH)-CO_2 therefore prior to the deposition experiment phase behavior studies were performed to reveal the phase boundaries of PDMS(OH)-CO_2 binary mixtures. The demixing pressures of the binary mixtures were determined at three different temperatures, namely 313.2 K, 323.2 K and 333.2 K, and up to 31 MPa pressure. Three different type of phase separation was observed for the binary mixtures depending on the composition; bubble point, cloud point and color change which was attributed to the mixture

critical point. The demixing pressures increased with decreasing polymer concentration and increasing temperature. The bubble point data were modeled with Sanchez-Lacombe equation of state and the binary interaction parameters were regressed. The demixing pressure data were further exploited in the deposition experiments to determine the experimental conditions. PDMS(OH) with two different molecular weight, namely 2750 g/mol and 18000 g/mol, were employed in the deposition experiments. Various parameters such as polymer concentration, deposition time, polymer molecular weight and deposition temperature were investigated and the effects of such parameters on the properties of aerogel composites were evaluated. It was found that the polymer uptakes increased with increasing polymer concentration, deposition time and deposition temperature. In addition, PDMS(OH) molecules were demonstrated to form a thin coating layer of ~1 nm on the silica aerogel surface. It was revealed that the transparency of the composites can be retained up to ~20 wt.% of polymer uptakes. Moreover, homogenous composites were obtained with low molecular weight PDMS(OH), whereas the composites were non-homogenous when the high molecular weight polymer was used. The composites were also revealed to be hydrophobic which is a crucial property in terms of the stability of the monolithic structure. More importantly, it was demonstrated that the deposition of the polymer resulted in a threefold improvement in the mechanical properties of the native silica aerogels.

In conclusion, the studies that were performed within the scope of this Ph.D. thesis fulfilled the demands of the NanoInsulate project. The PDMS(OH)-silica aerogel composite materials having monolithic form, high-to-moderate transparency and improved mechanical durability were demonstrated to be the most potential and suitable candidates to be used as core materials in transparent VIPs.

BIBLIOGRAPHY

1. Baetens, R., et al., *Vacuum insulation panels for building applications: A review and beyond.* Energy and Buildings, 2010. **42**(2): p. 147-172.
2. Binz, A., et al., *Vacuum Insulation in the Building Sector, in: Systems and Applications (Subtask B), Final Report for the IEA/ECBCS Annex 39 HiPTI-Project*, in *High Performance Thermal Insulation for Buildings and Building Systems*. 2005.
3. Simmler, H., et al., *Vacuum Insulation Panels, Study on VIP-components and Panels for Service Life Prediction in Building Applications (Subtask A), Final Report for the IEA/ECBCS Annex 39 HiPTI-project*, in *High Performance Thermal Insulation for Buildings and Building Systems*. 2005.
4. Leventis, N., et al., *Nanoengineering Strong Silica Aerogels.* Nano Letters, 2002. **2**(9): p. 957-960.
5. Capadona, L.A., et al., *Flexible, low-density polymer crosslinked silica aerogels.* Polymer, 2006. **47**(16): p. 5754-5761.
6. Cai, J., et al., *Cellulose–Silica Nanocomposite Aerogels by In Situ Formation of Silica in Cellulose Gel.* Angewandte Chemie International Edition, 2012. **51**(9): p. 2076-2079.
7. Brinker, C.J. and G.W. Scherer, *Sol-Gel Science*. 1990, San Diego (CA): Academic Press.
8. Soleimani Dorcheh, A. and M.H. Abbasi, *Silica aerogel; synthesis, properties and characterization.* Journal of Materials Processing Technology, 2008. **199**(1-3): p. 10-26.
9. Hüsing, N. and U. Schubert, *Aerogels*, in *Ullmann's Encyclopedia of Industrial Chemistry*. 2000, Wiley-VCH Verlag GmbH & Co. KGaA.
10. Gerona, M.M.i., *Silica Aerogels: Synthesis and Characterization*. 2002, University of Barcelona. p. 273.
11. Al-Ajlan, S.A., *Measurements of thermal properties of insulation materials by using transient plane source technique.* Applied Thermal Engineering, 2006. **26**(17–18): p. 2184-2191.
12. Bouquerel, M., et al., *Heat transfer modeling in vacuum insulation panels containing nanoporous silicas—A review.* Energy and Buildings, 2012. **54**(0): p. 320-336.
13. Lee, O.-J., et al., *Determination of mesopore size of aerogels from thermal conductivity measurements.* Journal of Non-Crystalline Solids, 2002. **298**(2–3): p. 287-292.
14. Caps, R., et al., *Thermal conductivity of polyimide foams.* International Journal of Heat and Mass Transfer, 1997. **40**(2): p. 269-280.
15. Fricke, J., et al., *Optimization of monolithic silica aerogel insulants.* International Journal of Heat and Mass Transfer, 1992. **35**(9): p. 2305-2309.
16. Hrubesh, L.W. and R.W. Pekala, *Thermal properties of organic and inorganic aerogels.* Journal of Materials Research, 1994. **9**(03): p. 731-738.
17. Yoldas, B.E., M.J. Annen, and J. Bostaph, *Chemical Engineering of Aerogel Morphology Formed under Nonsupercritical Conditions for Thermal Insulation.* Chemistry of Materials, 2000. **12**(8): p. 2475-2484.
18. Lu, X., et al., *Correlation between structure and thermal conductivity of organic aerogels.* Journal of Non-Crystalline Solids, 1995. **188**(3): p. 226-234.
19. Lu, X., et al., *Thermal conductivity of monolithic organic aerogels.* Science., 1992. **255**(5047): p. 971-2.

20. Clyne, T.W., et al., *Porous materials for thermal management under extreme conditions.* Philos Trans A Math Phys Eng Sci., 2006. **364**(1838): p. 125-46. doi: 10.1098/rsta.2005.1682.
21. Zeng, S.Q., A. Hunt, and R. Greif, *Theoretical modeling of carbon content to minimize heat transfer in silica aerogel.* Journal of Non-Crystalline Solids, 1995. **186**(0): p. 271-277.
22. Rettelbach, R., et al., *THERMAL-CONDUCTIVITY OF IR-OPACIFIED SILICA AEROGEL POWDERS BETWEEN 10 K AND 275 K.* Journal of Physics D-Applied Physics, 1995. **28**(3): p. 581-587.
23. Lu, X., et al., *THERMAL-CONDUCTIVITY OF MONOLITHIC ORGANIC AEROGELS.* Science, 1992. **255**(5047): p. 971-972.
24. Wang, J., J. Kuhn, and X. Lu, *Monolithic silica aerogel insulation doped with TiO2 powder and ceramic fibers.* Journal of Non-Crystalline Solids, 1995. **186**(0): p. 296-300.
25. Hummer, E., et al., *HEAT-TRANSFER IN OPACIFIED AEROGEL POWDERS.* Journal of Non-Crystalline Solids, 1992. **145**(1-3): p. 211-216.
26. Reim, M., et al., *Silica aerogel granulate material for thermal insulation and daylighting.* Solar Energy, 2005. **79**(2): p. 131-139.
27. Lu, G., et al., *Effects of non-ideal structures and high temperatures on the insulation properties of aerogel-based composite materials.* Journal of Non-Crystalline Solids, 2011. **357**(22–23): p. 3822-3829.
28. Novak, B.M., D. Auerbach, and C. Verrier, *Low-Density, Mutually Interpenetrating Organic-Inorganic Composite Materials via Supercritical Drying Techniques.* Chemistry of Materials, 1994. **6**(3): p. 282-286.
29. Wang, X. and S.C. Jana, *Synergistic Hybrid Organic–Inorganic Aerogels.* Acs Applied Materials & Interfaces, 2013. **5**: p. 6423-6429.
30. Martin, J., et al., *Mechanical and acoustical properties as a function of PEG concentration in macroporous silica gels.* Journal of Non-Crystalline Solids, 2001. **285**(1-3): p. 222-229.
31. Nguyen, B.N., et al., *Elastic Behavior of Methyltrimethoxysilane Based Aerogels Reinforced with Tri-Isocyanate.* Acs Applied Materials & Interfaces, 2010. **2**(5): p. 1430-1443.
32. Meador, M.A.B., et al., *Cross-linking amine-modified silica aerogels with epoxies: Mechanically strong lightweight porous materials.* Chemistry of Materials, 2005. **17**(5): p. 1085-1098.
33. Meador, M.A.B., et al., *Structure-Property Relationships in Porous 3D Nanostructures: Epoxy-Cross-Linked Silica Aerogels Produced Using Ethanol as the Solvent.* Acs Applied Materials & Interfaces, 2009. **1**(4): p. 894-906.
34. Ilhan, U.F., et al., *Hydrophobic monolithic aerogels by nanocasting polystyrene on amine-modified silica.* Journal of Materials Chemistry, 2006. **16**(29): p. 3046-3054.
35. Katti, A., et al., *Chemical, Physical, and Mechanical Characterization of Isocyanate Cross-linked Amine-Modified Silica Aerogels.* Chemistry of Materials, 2005. **18**(2): p. 285-296.
36. Zhang, G.H., et al., *Isocyanate-crosslinked silica aerogel monoliths: preparation and characterization.* Journal of Non-Crystalline Solids, 2004. **350**: p. 152-164.
37. Ge, D.T., et al., *Hydrophobic and thermal insulation properties of silica aerogel/epoxy composite.* Journal of Non-Crystalline Solids, 2009. **355**(52-54): p. 2610-2615.
38. Boday, D.J., et al., *Formation of polycyanoacrylate - Silica nanocomposites by chemical vapor deposition of cyanoacrylates on aerogels.* Chemistry of Materials, 2008. **20**(9): p. 2845-2847.

39. Boday, D.J., et al., *Strong, Low-Density Nanocomposites by Chemical Vapor Deposition and Polymerization of Cyanoacrylates on Aminated Silica Aerogels.* Acs Applied Materials & Interfaces, 2009. **1**(7): p. 1364-1369.
40. Boday, D.J., et al., *Strong, low density, hexylene- and phenylene-bridged polysilsesquioxane aerogel-polycyanoacrylate composites.* Journal of Materials Science, 2011. **46**(19): p. 6371-6377.
41. Nguyen, B.N., et al., *Tailoring Elastic Properties of Silica Aerogels Cross-Linked with Polystyrene.* Acs Applied Materials & Interfaces, 2009. **1**(3): p. 621-630.
42. DeFriend, K.A., B. Espinoza, and B. Patterson, *Templating silica aerogel with polystyrene to improve their mechnical properties.* Fusion Science and Technology, 2007. **51**(4): p. 693-700.
43. Mulik, S., et al., *Cross-linking 3D assemblies of nanoparticles into mechanically strong aerogels by surface-initiated free-radical polymerization.* Chemistry of Materials, 2008. **20**(15): p. 5035-5046.
44. Fidalgo, A., et al., *Hybrid silica/polymer aerogels dried at ambient pressure.* Chemistry of Materials, 2007. **19**(10): p. 2603-2609.
45. Liu, Y., et al., *Preparation and characterization of porous silica films by a modified base-catalyzed sol-gel process containing PVA: I. The precursor solution synthesis.* Journal of Sol-Gel Science and Technology, 2002. **25**(2): p. 95-101.
46. Kramer, S.J., F. RubioAlonso, and J.D. MacKenzie, *Organically modified silicate aerogels, "aeromosils"*, in *Better Ceramics through Chemistry Vii: Organic/Inorganic Hybrid Materials*, B.K. Coltrain, et al., Editors. 1996, Materials Research Soc: Pittsburgh. p. 295-300.
47. Dong, W., et al., *Acoustic Properties of Organic/Inorganic Composite Aerogels.* MRS Online Proceedings Library, 2009. **1188**.
48. Almeida, R.M., ed. *Handbook of Sol–Gel Science and Technology: Processing, Characterization and Applications*. ed. S. Sakka. Vol. Volume II: CHARACTERIZATION and PROPERTIES of SOL–GEL MATERIALS and PRODUCTS 2005, Kluwer Academic Publishers: New York.
49. Jespersen, H.T., et al., *Supercritical fluids applied to the sol-gel process for preparation of AEROMOSILS/palladium particle nanocomposite catalyst.* Journal of Supercritical Fluids, 2008. **46**(2): p. 178-184.
50. Miller, M.B., D.R. Luebke, and R.M. Enick, *CO2-philic Oligomers as Novel Solvents for CO2 Absorption.* Energy & Fuels, 2010. **24**: p. 6214-6219.
51. Garcia-Gonzalez, C.A., et al., *Measurements and Correlation of Octyltriethoxysilane Solubility in Supercritical CO2 and Assembly of Functional Silane Monolayers on the Surface of Nanometric Particles.* Industrial & Engineering Chemistry Research, 2009. **48**(22): p. 9952-9960.
52. Cao, C.T., A.Y. Fadeev, and T.J. McCarthy, *Reactions of organosilanes with silica surfaces in carbon dioxide.* Langmuir, 2001. **17**(3): p. 757-761.
53. Miller, M.B., et al., *Solubility of CO2 in CO2-philic oligomers; COSMOtherm predictions and experimental results.* Fluid Phase Equilibria, 2009. **287**(1): p. 26-32.
54. Dzielawa, J.A., et al., *Carbon dioxide solubility enhancement through silicone functionalization: "CO2-philic" oligo(dimethylsiloxane)-substituted diphosphonates.* Separation Science and Technology, 2008. **43**(9-10): p. 2520-2536.
55. Shin-Etsu Chemical Co Ltd., *Silane Coupling Agents*. 2014: Japan.
56. Tripp, C.P. and M.L. Hair, *Reaction of chloromethylsilanes with silica: a low-frequency infrared study.* Langmuir, 1991. **7**(5): p. 923-927.
57. Tripp, C.P. and M.L. Hair, *Reaction of alkylchlorosilanes with silica at the solid/gas and solid/liquid interface.* Langmuir, 1992. **8**(8): p. 1961-1967.

58. Tripp, C.P. and M.L. Hair, *An infrared study of the reaction of octadecyltrichlorosilane with silica.* Langmuir, 1992. **8**(4): p. 1120-1126.
59. Combes, J.R., L.D. White, and C.P. Tripp, *Chemical Modification of Metal Oxide Surfaces in Supercritical CO2: In Situ Infrared Studies of the Adsorption and Reaction of Organosilanes on Silica.* Langmuir, 1999. **15**(22): p. 7870-7875.
60. Gelest Inc., *Silane Coupling Agents: Connecting Across Boundaries*. 2006: Morrisville, PA.
61. Kartal, A.M. and C. Erkey, *Surface modification of silica aerogels by hexamethyldisilazane–carbon dioxide mixtures and their phase behavior.* The Journal of Supercritical Fluids, 2010. **53**(1–3): p. 115-120.
62. Sanz-Moral, L.M., et al., *Gradual hydrophobic surface functionalization of dry silica aerogels by reaction with silane precursors dissolved in supercritical carbon dioxide.* The Journal of Supercritical Fluids, 2013. **84**(0): p. 74-79.
63. Lowell, S., Shields, J. E., *Powder Surface Area and Porosity* 3rd ed. Particle Technology Series. Vol. 2. 1991: Springer. 268
64. Lester, C.L., et al., *Physical Properties of Hydrogels Synthesized from Lyotropic Liquid Crystalline Templates.* Chemistry of Materials, 2003. **15**(17): p. 3376-3384.
65. Mosquera, M.J., D.M. de los Santos, and T. Rivas, *Surfactant-Synthesized Ormosils with Application to Stone Restoration.* Langmuir, 2010. **26**(9): p. 6737-6745.
66. Zhang, X.X., et al., *One-step sol-gel preparation of PDMS-silica ORMOSILs as environment-resistant and crack-free thick antireflective coatings.* Journal of Materials Chemistry, 2012. **22**(26): p. 13132-13140.
67. Bozbag, S.E., D. Sanli, and C. Erkey, *Synthesis of nanostructured materials using supercritical CO2: Part II. Chemical transformations.* Journal of Materials Science, 2012. **47**(8): p. 3469-3492.
68. Stojanovic, D., et al., *Preparation of MEMO silane-coated SiO2 nanoparticles under high pressure of carbon dioxide and ethanol.* The Journal of Supercritical Fluids, 2010. **52**(3): p. 276-284.
69. Roy, C., et al., *Assessment of scCO2 techniques for surface modification of micro- and nanoparticles: Process design methodology based on solubility.* The Journal of Supercritical Fluids, 2010. **54**(3): p. 362-368.
70. Loste, E., et al., *Anhydrous Supercritical Carbon Dioxide Method for the Controlled Silanization of Inorganic Nanoparticles.* Advanced Materials, 2004. **16**(8): p. 739-744.
71. Domingo, C., E. Loste, and J. Fraile, *Grafting of trialkoxysilane on the surface of nanoparticles by conventional wet alcoholic and supercritical carbon dioxide deposition methods.* The Journal of Supercritical Fluids, 2006. **37**(1): p. 72-86.
72. Gu, W. and C.P. Tripp, *Reaction of Silanes in Supercritical CO2 with TiO2 and Al2O3.* Langmuir, 2006. **22**(13): p. 5748-5752.
73. García-González, C.A., et al., *Preparation of silane-coated TiO2 nanoparticles in supercritical CO2.* Journal of Colloid and Interface Science, 2009. **338**(2): p. 491-499.
74. García-González, C.A., et al., *Preparation and Characterization of Surface Silanized TiO2 Nanoparticles under Compressed CO2: Reaction Kinetics.* The Journal of Physical Chemistry C, 2009. **113**(31): p. 13780-13786.
75. Yarita, T., et al., *Endcapping of Octadecylsilyl-Silica Gels Using Supercritical Fluid as Reaction Medium.* Analytical Sciences, 1999. **15**(4): p. 377-380.
76. Yarita, T., A. Nomura, and Y. Horimoto, *In situ silylation of silica-based packings using supercritical fluid as reaction medium.* Journal of Chromatography A, 1996. **724**(1–2): p. 373-377.

77. Jespersen, H.T., et al., *Supercritical fluids applied to the sol–gel process for preparation of AEROMOSILS/palladium particle nanocomposite catalyst.* The Journal of Supercritical Fluids, 2008. **46**(2): p. 178-184.
78. O'Neil, A. and J.J. Watkins, *Fabrication of Device Nanostructures Using Supercritical Fluids.* MRS Bulletin, 2005. **30**(12): p. 967-975.
79. Pham, V.Q., et al., *Positive-Tone Photoresist Process for Supercritical Carbon Dioxide Development.* Chemistry of Materials, 2003. **15**(26): p. 4893-4895.
80. Sha, J. and C.K. Ober, *Fluorine- and siloxane-containing polymers for supercritical carbon dioxide lithography.* Polymer International, 2009. **58**(3): p. 302-306.
81. Cao, C., A.Y. Fadeev, and T.J. McCarthy, *Reactions of Organosilanes with Silica Surfaces in Carbon Dioxide.* Langmuir, 2001. **17**(3): p. 757-761.
82. Jia, X. and T.J. McCarthy, *Buried Interface Modification Using Supercritical Carbon Dioxide.* Langmuir, 2002. **18**(3): p. 683-687.
83. Efimenko, K., et al., *Formation of Self-Assembled Monolayers of Semifluorinated and Hydrocarbon Chlorosilane Precursors on Silica Surfaces from Liquid Carbon Dioxide.* Langmuir, 2002. **18**(16): p. 6170-6179.
84. Rébiscoul, D., et al., *Alkoxysilane layers deposited by SC CO2 process on silicon oxide for microelectronics applications.* The Journal of Supercritical Fluids, 2009. **51**(2): p. 287-294.
85. Kim, J.Y., et al., *Preparation of Self-Assembled Monolayers in scCO2 and Their Application to Fabrication and Patterning of Polymer Thin Films.* Journal of Industrial and Engineering Chemistry, 2007. **13**(6): p. 1023-1028.
86. Zemanian, T.S., et al., *Deposition of Self-Assembled Monolayers in Mesoporous Silica from Supercritical Fluids.* Langmuir, 2001. **17**(26): p. 8172-8177.
87. Keagy, J.A., et al., *CO2 promotes penetration and removal of aqueous hydrocarbon surfactant cleaning solutions and silylation in low-k dielectrics with 3 nm pores.* The Journal of Supercritical Fluids, 2007. **42**(3): p. 398-409.
88. Xie, B. and A.J. Muscat, *Silylation of porous methylsilsesquioxane films in supercritical carbon dioxide.* Microelectronic Engineering, 2004. **76**(1–4): p. 52-59.
89. Xie, B. and A.J. Muscat, *The restoration of porous methylsilsesquioxane (p-MSQ) films using trimethylhalosilanes dissolved in supercritical carbon dioxide.* Microelectronic Engineering, 2005. **82**(3–4): p. 434-440.
90. Xie, B., L. Choate, and A.J. Muscat, *Repair and capping of porous MSQ films using chlorosilanes and supercritical CO2.* Microelectron. Eng., 2005. **80**: p. 349-352.
91. Vyhmeister, E., et al., *Surface Modification of Porous Silicon-Based Films Using Dichlorosilanes Dissolved in Supercritical Carbon Dioxide.* Industrial & Engineering Chemistry Research, 2013. **52**(13): p. 4762-4771.
92. Kartal, A.M. and C. Erkey, *Surface modification of silica aerogels by hexamethyldisilazane-carbon dioxide mixtures and their phase behavior.* Journal of Supercritical Fluids, 2010. **53**(1-3): p. 115-120.
93. Sanli, D. and C. Erkey, *Monolithic Composites of Silica Aerogels by Reactive Supercritical Deposition of Hydroxy-Terminated Poly(Dimethylsiloxane).* ACS Applied Materials & Interfaces, 2013. **5**(22): p. 11708-11717.
94. Vyhmeister, E., et al., *High-pressure phase equilibria for chlorosilane + carbon dioxide mixtures.* Fluid Phase Equilibria, 2008. **270**(1–2): p. 121-128.
95. García-González, C.A., et al., *Measurements and Correlation of Octyltriethoxysilane Solubility in Supercritical CO2 and Assembly of Functional Silane Monolayers on the Surface of Nanometric Particles.* Industrial & Engineering Chemistry Research, 2009. **48**(22): p. 9952-9960.

96. Xiong, Y. and E. Kiran, *Miscibility, Density and Viscosity of Poly(dimethylsiloxane) in Supercritical Carbon Dioxide.* Polymer, 1995. **36**(25): p. 4817-4826.
97. Bayraktar, Z. and E. Kiran, *Miscibility, phase separation, and volumetric properties in solutions of poly(dimethylsiloxane) in supercritical carbon dioxide.* Journal of Applied Polymer Science, 2000. **75**(11): p. 1397-1403.
98. Garg, A., E. Gulari, and C.W. Manke, *Thermodynamics of Polymer Melts Swollen with Supercritical Gases.* Macromolecules, 1994. **27**(20): p. 5643-5653.
99. Enick, R.M., et al., *Hydrophobic Polymeric Solvents for the Selective Absorption of CO2 from Warm Gas Streams that also Contain H2 and H2O.* Energy & Fuels, 2013. **27**(11): p. 6913-6920.
100. Dindar, C. and E. Kiran, *High-pressure viscosity and density of polymer solutions at the critical polymer concentration in near-critical and supercritical fluids.* Industrial & Engineering Chemistry Research, 2002. **41**(25): p. 6354-6362.
101. Sanli, D. and C. Erkey, *Demixing pressures of hydroxy-terminated poly(dimethylsiloxane)–carbon dioxide binary mixtures at 313.2 K, 323.2 K and 333.2 K.* The Journal of Supercritical Fluids, 2014. **92**(0): p. 264-271.
102. Linstrom, P.J. and W.G. Mallard, National Institute of Standards and Technology (NIST).
103. Linstrom, P.J. and W.G. Mallard, *National Institute of Standards and Technology (NIST).*
104. Dilek, C., *Supercritical carbon dioxide-soluble polyhedral oligomeric silsesquioxane (POSS) nanocages and polymer surface modification.* The Journal of Supercritical Fluids, 2013. **73**(0): p. 171-177.
105. Stryjek, R. and J.H. Vera, *Prsv - an Improved Peng-Robinson Equation of State with New Mixing Rules for Strongly Nonideal Mixtures.* Canadian Journal of Chemical Engineering, 1986. **64**(2): p. 334-340.
106. Orbey, H. and S.I. Sandler, *Modelling Vapor-Liquid Equilibria Cubic Equations of State and Their Mixing Rules*. 1998, New York: Cambridge University Press.
107. Walker, T.A., et al., *Thermodynamics of poly(dimethylsiloxane)/poly(ethylmethylsiloxane) (PDMS/PEMS) blends in the presence of high-pressure CO2.* Macromolecules, 2004. **37**(7): p. 2588-2595.
108. Kiszka, M.B., M.A. Meilchen, and M.A. McHugh, *Modeling High-Pressure Gas Polymer Mixtures Using the Sanchez-Lacombe Equation of State.* Journal of Applied Polymer Science, 1988. **36**(3): p. 583-597.
109. Gerhardt, L.J., et al., *Concentration-dependent viscoelastic scaling models for polydimethysiloxane melts with dissolved carbon dioxide.* Journal of Polymer Science Part B-Polymer Physics, 1998. **36**(11): p. 1911-1918.
110. Sanchez, I.C. and R.H. Lacombe, *Statistical Thermodynamics of Polymer Solutions.* Macromolecules, 1978. **11**(6): p. 1145-1156.
111. Panayiotou, C. and I.C. Sanchez, *Statistical Thermodynamics of Associated Polymer-Solutions.* Macromolecules, 1991. **24**(23): p. 6231-6237.
112. Chang, C.M.J., K.L. Chiu, and C.Y. Day, *A new apparatus for the determination of P-x-y diagrams and Henry's constants in high pressure alcohols with critical carbon dioxide.* J. Supercritical Fluids, 1998. **12**(3): p. 223-237.
113. Mehl, A., et al., *Vapor-Liquid Equilibrium of Carbon Dioxide+Ethanol: Experimental Measurements with Acoustic Method and Thermodynamic Modeling.* J. Thermodynamics, 2011. **Article ID 251075**: p. 11.
114. Chin, H.Y., M.J. Lee, and H.M. Lin, *Vapor-Liquid Phase Boundaries of Binary Mixtures of Carbon Dioxide with Ethanol and Acetone.* J. Chemical and Engineering Data, 2008. **53**(10): p. 2393-2402.

115. Chang, C.J., et al., *Densities and P-x-y diagrams for carbon dioxide dissolution in methanol, ethanol, and acetone mixtures.* Fluid Phase Equilibria, 1997. **131**(1-2): p. 243-258.
116. Gui, X., Z.G. Tang, and W.Y. Fei, *Solubility of CO2 in Alcohols, Glycols, Ethers, and Ketones at High Pressures from (288.15 to 318.15) K.* J. Chemical and Engineering Data, 2011. **56**(5): p. 2420-2429.
117. Gui, X., Z.G. Tang, and W.Y. Fei, *CO(2) Capture with Physical Solvent Dimethyl Carbonate at High Pressures.* J. Chemical and Engineering Data, 2010. **55**(9): p. 3736-3741.
118. Day, C.Y., C.J. Chang, and C.Y. Chen, *Phase equilibrium of ethanol plus CO2 and acetone plus CO2 at elevated pressures.* J. Chemical and Engineering Data, 1996. **41**(4): p. 839-843.
119. Suzuki, K. and H. Sue, *Isothermal Vapor-Liquid Equilibrium Data for Binary Systems at High Pressures - Carbon Dioxide-Methanol, Carbon Dioxide-Ethanol, Carbon Dioxide-1-Propanol, Methane-Ethanol, Methane-1-Propanol, Ethane-Ethanol, and Ethane-1-Propanol Systems.* J. Chemical and Engineering Data, 1990. **35**(1): p. 63-66.
120. Tochigi, K., et al., *Measurement and prediction of high-pressure vapor-liquid equilibria for binary mixtures of carbon dioxide plus n-octane, methanol, ethanol, and perfluorohexane.* J. Supercritical Fluids, 2010. **55**(2): p. 682-689.
121. Joung, S.N., et al., *Measurements and correlation of high-pressure VLE of binary CO2–alcohol systems (methanol, ethanol, 2-methoxyethanol and 2-ethoxyethanol).* Fluid Phase Equilibria, 2001. **185**: p. 219-230.
122. Stievano, M. and N. Elvassore, *High-pressure density and vapor-liquid equilibrium for the binary systems carbon dioxide-ethanol, carbon dioxide-acetone and carbon dioxide-dichloromethane.* J. Supercritical Fluids, 2005. **33**(1): p. 7-14.
123. Knez, Z., et al., *Vapor-liquid equilibrium of binary CO2-organic solvent systems (ethanol, tetrahydrofuran, ortho-xylene, meta-xylene, para-xylene).* J. Supercritical Fluids, 2008. **43**(3): p. 383-389.
124. Bae, W., et al., *Phase behavior of the poly(vinyl pyrrolidone) plus N-vinyl-2-pyrrolidone plus carbon dioxide system.* J. Supercritical Fluids, 2004. **30**(2): p. 127-137.
125. Yoon, J.H., H.S. Lee, and H. Lee, *High Pressure Vapor-Liquid Equilibria for Carbon Dioxide + Methanol, Carbon Dioxide + Ethanol, and Carbon Dioxide + Methanol + Ethanol.* J. Chemical and Engineering Data, 1993. **38**(1): p. 53-55.
126. Tsivintzelis, I., et al., *Phase compositions and saturated densities for the binary systems of carbon dioxide with ethanol and dichloromethane.* Fluid Phase Equilibria, 2004. **224**(1): p. 89-96.
127. Secuianu, C., V. Feroiu, and D. Geana, *Phase behavior for carbon dioxide plus ethanol system: Experimental measurements and modeling with a cubic equation of state.* J. Supercritical Fluids, 2008. **47**(2): p. 109-116.
128. Galicia-Luna, L.A., A. Ortega-Rodriguez, and D. Richon, *New apparatus for the fast determination of high-pressure vapor-liquid equilibria of mixtures and of accurate critical pressures.* J. Chemical and Engineering Data, 2000. **45**(2): p. 265-271.
129. Homann, J., *Experimental thermodynamic and physical properties of mixtures and pure substances from a total of 24,000 compounds*. 2012, FIZ CHEMIE Berlin.
130. Yaws, C.L., *Handbook of Thermodynamic Diagrams*. Inorganic Compounds and Elements. Vol. 4. 1996, Houston, Texas: Gulf Publishing Company.
131. (PLAPIQUI), G.o.P.T.G.o.P.P.d.I.Q. and U.N.d.S. (UNS), *GPEC (Global Phase Equilibria Calculation)*. 2007.

132. Laintz, K.E., et al., *Solubility of Fluorinated Metal Diethyldithiocarbamates in Supercritical Carbon Dioxide.* J. Supercritical Fluids, 1991. **4**: p. 194-198.
133. Erkey, C., *Supercritical Fluids and Organometallic Compounds: From Recovery of Trace Metals to Synthesis of Nanostructured Materials,* ed. E. Kiran. 2011, Amsterdam, The Netherlands: Elsevier
134. Miller, M.B., D.R. Luebke, and R.M. Enick, *CO(2)-philic Oligomers as Novel Solvents for CO(2) Absorption.* Energy & Fuels, 2010. **24**: p. 6214-6219.
135. Melnichenko, Y.B., et al., *Pressure- and temperature-induced transitions in solutions of poly(dimethylsiloxane) in supercritical carbon dioxide.* Macromolecules, 1999. **32**(16): p. 5344-5347.
136. Mertsch, R. and B.A. Wolf, *Solutions of Poly(Dimethylsiloxane) in Supercritical Co2 - Viscometric and Volumetric Behavior.* Macromolecules, 1994. **27**(12): p. 3289-3294.
137. Gerhard, L.J., et al. *Supercritical fluids as polymer processing aids*. in *3rd International Symposium on Supercritical Fluids*. 1994. Strasbourg, France.
138. Kemmere, M.F. and T. Meyer, eds. *Supercritical Carbon Dioxide in Polymer Reaction Engineering*. 2005, WILEY-VCH Verlag GmbH & Co. KGaA: Weinheim, Germany.
139. Kirby, C.F. and M.A. McHugh, *Phase Behavior of Polymers in Supercritical Fluid Solvents.* Chemical Reviews, 1999. **99**(2): p. 565-602.
140. Revelli, A.L., F. Mutelet, and J.N. Jaubert, *High Carbon Dioxide Solubilities in lmidazolium-Based Ionic Liquids and in Poly(ethylene glycol) Dimethyl Ether.* J. Physical Chemistry B, 2010. **114**(40): p. 12908-12913.
141. Angus, S., B. Armstrong, and K.M. de Reuck, eds. *International Thermodynamic Tables of the Fluid State: Carbon Dioxide*. 1976, Pergamon Press: New York.
142. McLure, I.A., A.J. Pretty, and P.A. Sadler, *Specific volumes, thermal pressure coefficients, and derived quantities of five dimethylsiloxane oligomers from 25 to 140 C.* J. Chemical Engineering Data, 1977. **22**: p. 372-376.
143. Lu, S., E.M. Pearce, and T.K. Kwei, *Synthesis and characterization of novel 4-vinylphenylmethylphenylsilanol polymer and its styrene copolymers.* Journal of Polymer Science Part A: Polymer Chemistry, 1994. **32**(13): p. 2597-2601.
144. Pearce, E.M., T.K. Kwei, and S. Lu, *Hydrogen Bond Interactions and Self-Condensation of Silanol-Containing Polymers in Polymer Blends and Organic-Inorganic Polymeric Hybrids,* in *Silicones and Silicone-Modified Materials*. 2000, American Chemical Society. p. 419–432.
145. Singh, S., *Studies of the Crystallization and Morphology of Ploy(dimethylsiloxane),* in *Department of Chemistry*. 2001, McGill University: Montreal, Quebec, Canada.
146. Wiebe, R., *The Binary System Carbon Dioxide-Water under Pressure.* Chemical Reviews, 1941. **29**(3): p. 475-481.
147. Kulkarni, M.M., et al., *Microstructural and mechanical properties of silica-PEPEG polymer composite xerogels.* Acta Materialia, 2006. **54**(19): p. 5231-5240.
148. Aegerter, M.A., N. Leventis, and M. Koebel, eds. *Aerogel Handbook.* Advances in Sol-Gel Derived Materials
and Technologies, ed. M.A. Aegerter and M. Prassas. 2011, Springer Science+Business Media: New York.
149. Al Akoum, R., et al., *How Silanization of Silica Particles Affects the Adsorption of PDMS Chains on Its Surface.* Journal of Polymer Science Part B-Polymer Physics, 2010. **48**(22): p. 2371-2378.
150. Parida, S.K., et al., *Adsorption of organic molecules on silica surface.* Advances in Colloid and Interface Science, 2006. **121**(1-3): p. 77-110.
151. Levresse, P., D.L. Feke, and I. Manas-Zloczower, *Analysis of the formation of bound poly(dimethylsiloxane) on silica.* Polymer, 1998. **39**(17): p. 3919-3924.

152. Litvinov, V.M., H. Barthel, and J. Weis, *Structure of a PDMS layer grafted onto a silica surface studied by means of DSC and solid-state NMR.* Macromolecules, 2002. **35**(11): p. 4356-4364.
153. Panja, D., G.T. Barkema, and A.B. Kolomeisky, *Non-equilibrium dynamics of single polymer adsorption to solid surfaces.* Journal of Physics-Condensed Matter, 2009. **21**(24): p. 242101.
154. Hsu, H.P., W. Paul, and K. Binder, *Structure of Bottle Brush Polymers on Surfaces: Weak versus Strong Adsorption.* Journal of Physical Chemistry B, 2011. **115**(48): p. 14116-14126.
155. Auroy, P., L. Auvray, and L. Leger, *Building of a Grafted Layer.1. Roleof the Cencentration of Free Polymers in the Reaction Bath.* Macromolecules, 1991. **24**(18): p. 5158-5166.
156. Karim, A., et al., *Self-Organization of Polymer Brush Layers in a Poor Solvent.* Journal De Physique Ii, 1995. **5**(10): p. 1441-1456.
157. Funazukuri, T., C.Y. Kong, and S. Kagei, *Binary diffusion coefficients in supercritical fluids: Recent progress in measurements and correlations for binary diffusion coefficients.* The Journal of Supercritical Fluids, 2006. **38**(2): p. 201-210.
158. Kong, C.Y., et al., *Measurements of binary diffusion coefficients and retention factors for dibenzo-24-crown-8 and 15-crown-5 in supercritical carbon dioxide by chromatographic impulse response technique.* Fluid Phase Equilibria, 2007. **257**(2): p. 223-227.
159. Paakko, M., et al., *Long and entangled native cellulose I nanofibers allow flexible aerogels and hierarchically porous templates for functionalities.* Soft Matter, 2008. **4**(12): p. 2492-2499.
160. López-Aranguren, P., et al., *Regenerable solid CO2 sorbents prepared by supercritical grafting of aminoalkoxysilane into low-cost mesoporous silica.* The Journal of Supercritical Fluids, 2014. **85**(0): p. 68-80.

APPENDIX

A.1. Global Phase Equilibria Calculations (GPEC)

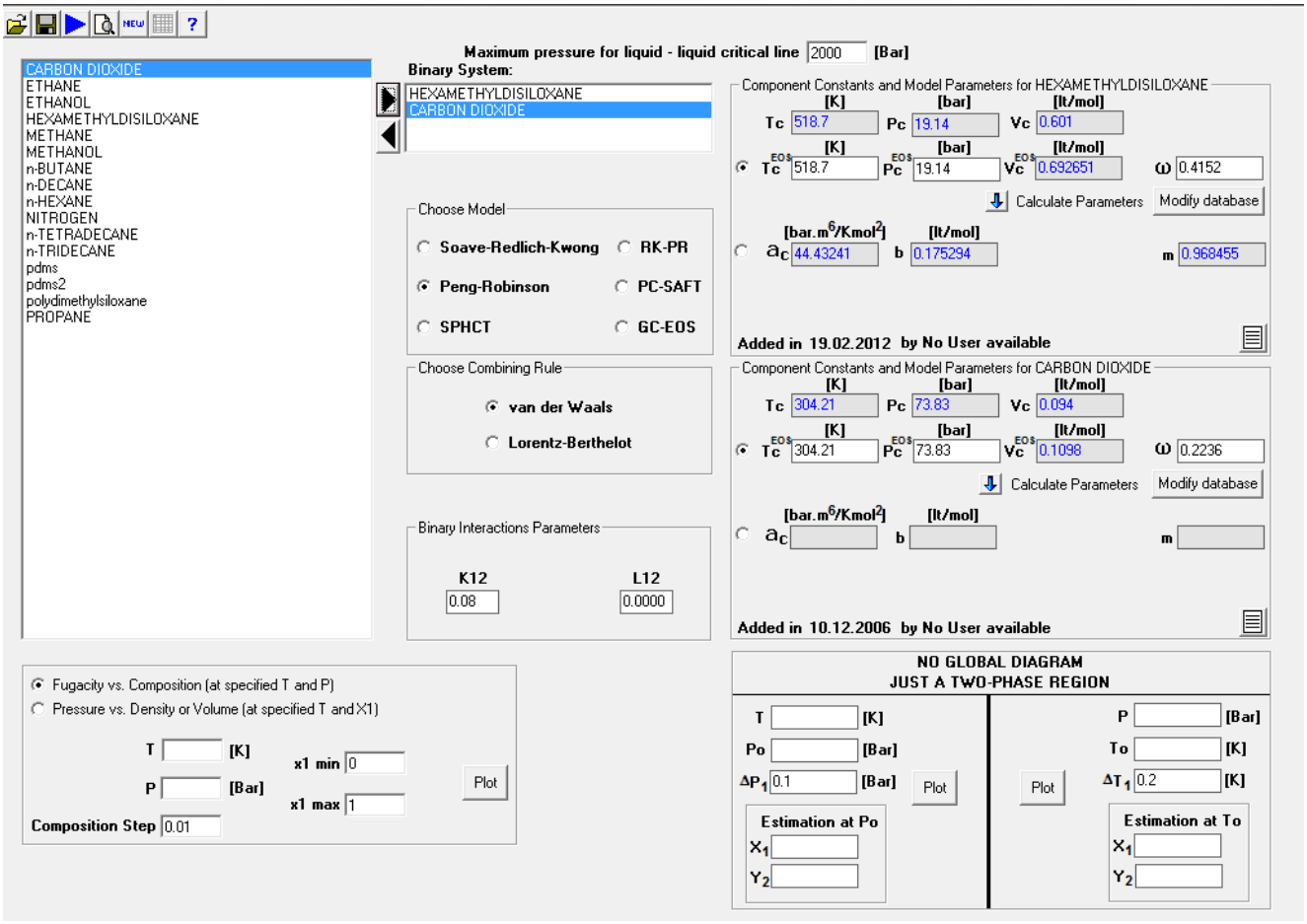

Figure A.1.1. Program input window for computations of CO_2-HMDS binary mixture

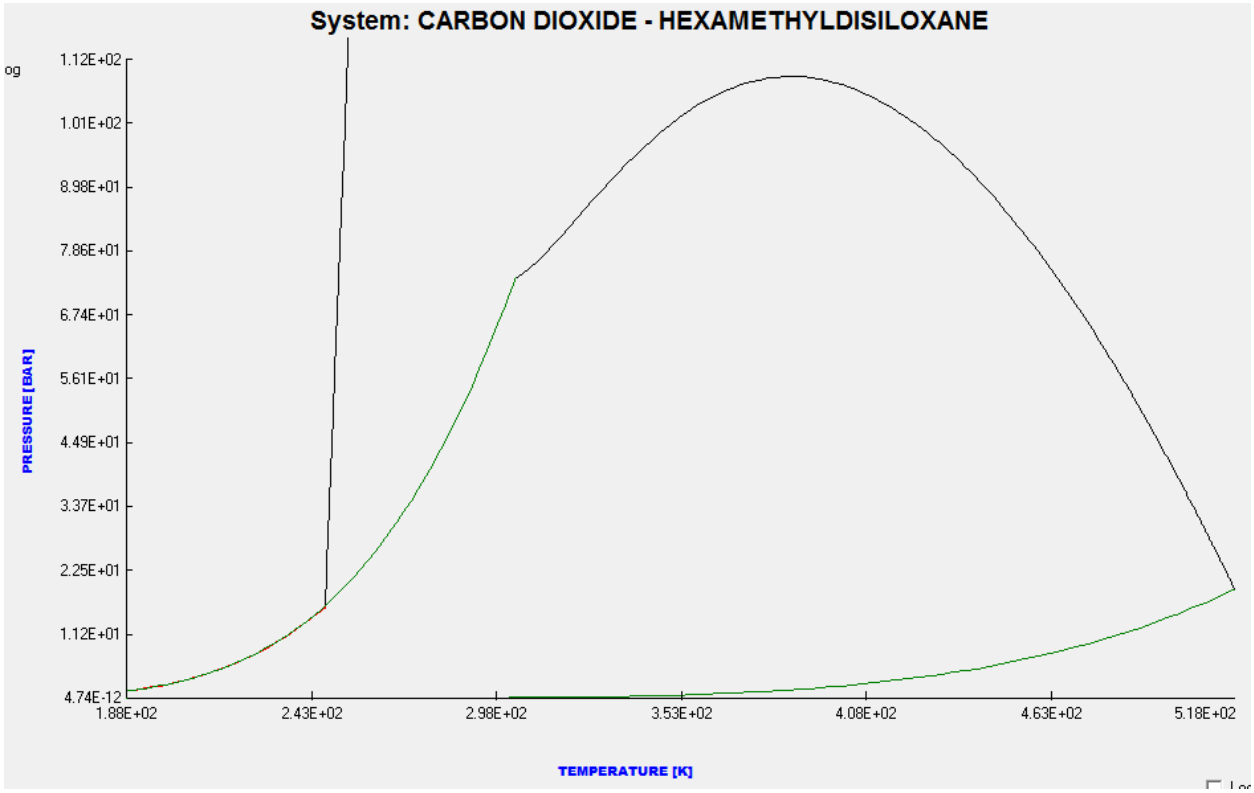

Figure A.1.2. P-T diagram of CO_2-HMDS binary mixture obtained from GPEC

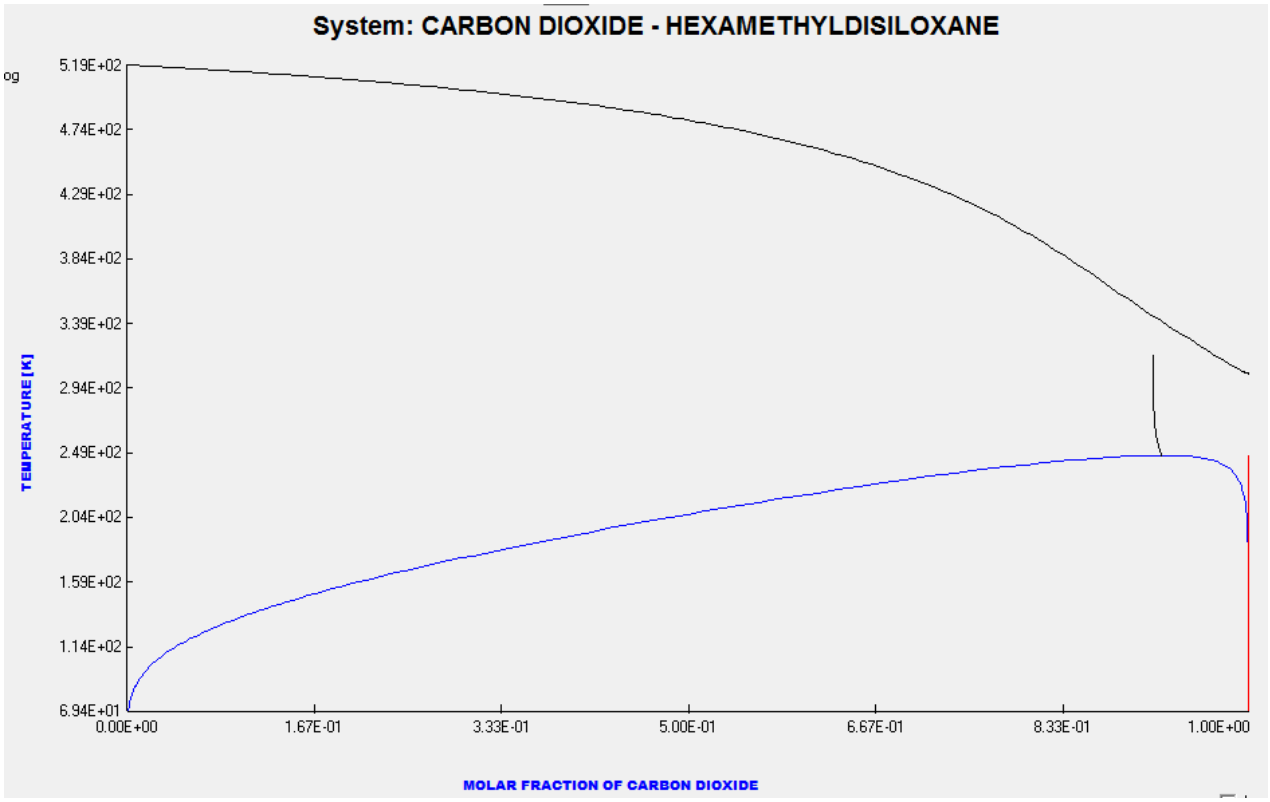

Figure A.1.3. T-x diagram of CO_2-HMDS binary mixture obtained from GPEC

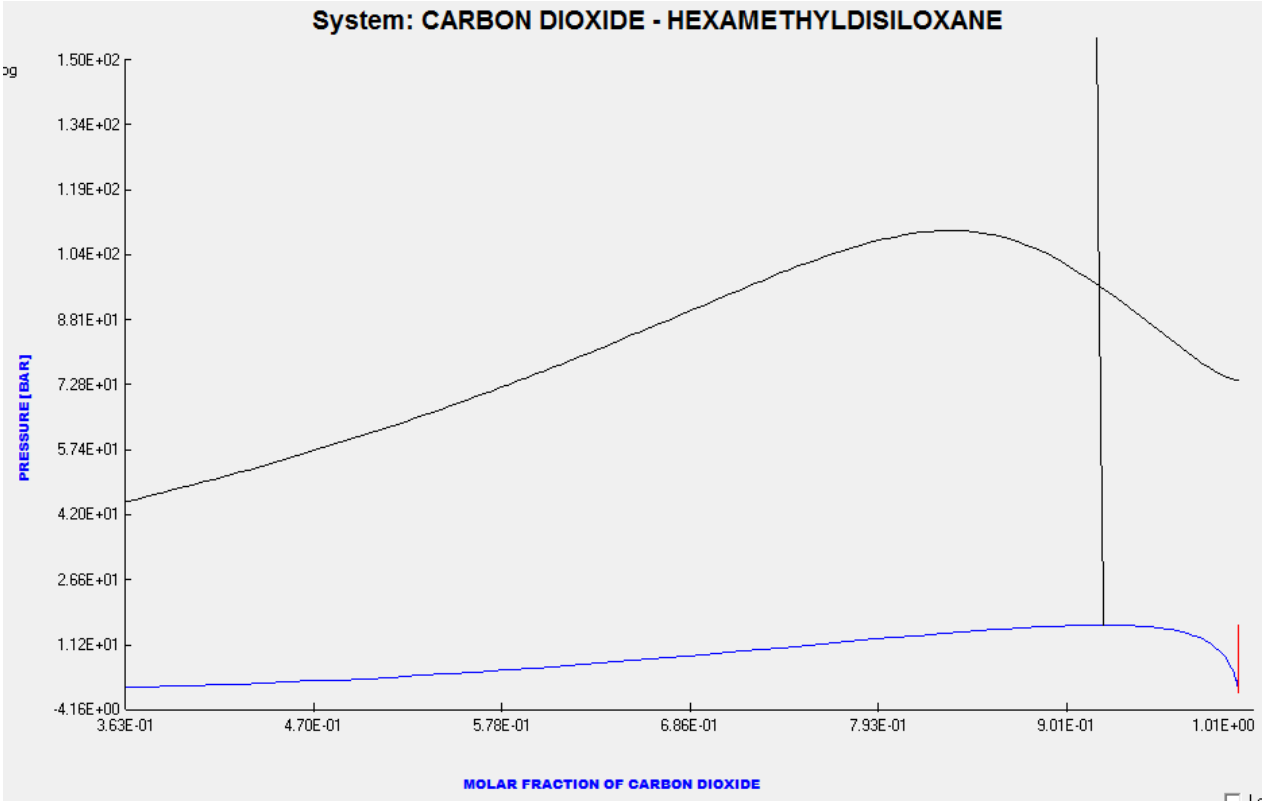

Figure A.1.4. P-x diagram of CO_2-HMDS binary mixture obtained from GPEC

A.2. Kappa 1 Optimization

A.2.1. Kappa 1 Optimization for Peng-Robinson equation of state for HMDS

```
PROGRAM :KOPT: KAPPA-1 OPTIMIZATION FOR THE PRSV EQUATION
 c:hmds

 hexamethyldisiloxane

 KAPPA-1=  .0153
```

T(K)	PEXP(BAR)	PCAL	AAD	VL(CM3/MOL)	VV
309.9910	.0990	.0994	.3696	207.4842	256966.9
320.0170	.1540	.1540	.0100	210.0657	170504.1
330.0160	.2320	.2309	.4633	212.8538	116647.6
340.0270	.3380	.3368	.3642	215.8858	81879.6
350.0310	.4810	.4786	.4987	219.1882	58835.5
359.9690	.6690	.6633	.8552	222.7762	43237.1
369.9820	.9090	.9025	.7117	226.7470	32277.7
380.0230	1.2160	1.2061	.8167	231.1440	24464.9
389.9910	1.5870	1.5812	.3670	235.9890	18840.1
400.0100	2.0500	2.0439	.2967	241.4272	14665.3

```
 PERCENT AAD (OVERALL), SUM(ABS(PEXP-PCAL)/PEXP)*100/NP:     .475
```

A.2.2. Kappa 1 Optimization for Peng-Robinson equation of state for CO_2

```
PROGRAM :KOPT: KAPPA-1 OPTIMIZATION FOR THE PRSV EQUATION (different initial guess)
 c:co2

 carbon dioxide
```

```
 KAPPA-1=  .0481

      T(K)       PEXP(BAR)     PCAL        AAD      VL(CM3/MOL)      VV
   243.1500     14.2970     14.1692       .0089     39.7205        1201.7
   248.1500     16.8400     16.7250       .0068     40.7374        1013.4
   253.1500     19.7200     19.6071       .0057     41.8766         857.7
   258.1500     22.9200     22.8403       .0035     43.1637         727.9
   263.1500     26.5100     26.4496       .0023     44.6329         618.9
   268.3000     30.5600     30.5881       .0009     46.3858         524.0
   273.1500     34.8700     34.9016       .0009     48.3237         447.8
   283.1500     44.9800     45.1785       .0044     53.6475         320.9
   288.1500     50.8600     51.0716       .0042     57.4055         268.9
   293.1500     57.2600     57.5087       .0043     62.5207         222.1
   298.1500     64.3300     64.5190       .0029     70.3552         178.1

 PERCENT AAD (OVERALL), SUM(ABS(PEXP-PCAL)/PEXP)*100/NP:     .408
```

A.3. Peng-Robinson Stryjek Vera Equation of State Results

A.3.1. k_{ij} at 298 K

```
PROGRAM: VDW - VAN DER WAALS MODEL(S), 1-PARAMETER (CONVENTIONAL, 1PDW) OR
 2-PARAMETER, 2PDW
 d1
 co2-hmds 298

 K12=  .0568 T(K)=  298.15

  PHASE VOLUMES ARE IN CC/MOL, PRESSURE IS IN UNITS OF THE DATA.

   X-EXP      P-EXP      P-CAL       Y-EXP     Y-CAL     VL-CAL   VV-CAL
   .4641      27.920     25.937     .99000    .99565     137.23    803.1
   .7809      45.710     45.720     .99000    .99585      93.34    372.4
   .8584      50.610     50.613     .99000    .99589      83.65    313.1
   .9465      57.710     57.240     .99000    .99656      74.32    244.1
   .9791      60.120     60.888     .99000    .99775      71.95    209.2
   .9844      60.740     61.631     .99000    .99813      71.67    202.2

 AAD-Y=      .671
 AAD-P=     1.781

 AAD=SUM[ABS(EXP-CAL)/EXP]*100/(NO. OF DATA POINTS)
```

A.3.2. k_{ij} at 308 K

```
PROGRAM: VDW - VAN DER WAALS MODEL(S), 1-PARAMETER (CONVENTIONAL, 1PDW) OR
 2-PARAMETER, 2PDW
 d2
 co2-hmds 308

 K12=  .0748 T(K)=  308.15

  PHASE VOLUMES ARE IN CC/MOL, PRESSURE IS IN UNITS OF THE DATA.

   X-EXP      P-EXP      P-CAL       Y-EXP     Y-CAL     VL-CAL   VV-CAL
   .4641      31.990     31.617     .99000    .99336     140.04    665.2
   .7809      53.710     55.313     .99000    .99226      97.79    299.1
   .8584      60.880     60.889     .99000    .99163      89.52    248.6
   .9465      68.740     68.585     .99000    .99107      85.53    184.5
   .9791      72.600     73.254     .99000    .99135      92.75    141.7
   .9844      73.570     74.240     .99000    .99121      97.11    128.9

 AAD-Y=      .183
```

```
 AAD-P=     1.033

 AAD=SUM[ABS(EXP-CAL)/EXP]*100/(NO. OF DATA POINTS)
```

A.3.3. k_{ij} at 313 K

```
PROGRAM: VDW - VAN DER WAALS MODEL(S), 1-PARAMETER (CONVENTIONAL, 1PDW) OR
 2-PARAMETER, 2PDW
 d3
 co2-hmds 313

 K12=  .0764 T(K)=  313.15

  PHASE VOLUMES ARE IN CC/MOL, PRESSURE IS IN UNITS OF THE DATA.


   X-EXP      P-EXP      P-CAL       Y-EXP     Y-CAL     VL-CAL   VV-CAL
   .4641      33.780     33.775     .99000    .99192     141.47    629.6
   .7809      57.920     59.541     .99000    .98998      99.94    276.8
   .8584      66.120     65.673     .99000    .98873      92.40    227.2
   .9465      74.600     73.969     .99000    .98620      92.07    162.7
   .9791      79.500     77.599     .99000    .98229     114.98    123.8

 AAD-Y=      .297
 AAD-P=     1.346

 AAD=SUM[ABS(EXP-CAL)/EXP]*100/(NO. OF DATA POINTS)
```

A.3.4. k_{ij} at 323 K

```
PROGRAM: VDW - VAN DER WAALS MODEL(S), 1-PARAMETER (CONVENTIONAL, 1PDW) OR
 2-PARAMETER, 2PDW
 d4
 co2-hmds 323

 K12=  .0875 T(K)=  323.15

  PHASE VOLUMES ARE IN CC/MOL, PRESSURE IS IN UNITS OF THE DATA.


   X-EXP      P-EXP      P-CAL       Y-EXP     Y-CAL     VL-CAL   VV-CAL
   .4641      39.230     39.091     .99000    .98826     144.55    552.8
   .7809      67.090     68.981     .99000    .98309     104.84    234.8
   .8584      75.770     75.769     .99000    .97928      99.21    189.6
   .9465      87.080     83.467     .99000    .95975     109.60    122.2
   .9791      ... single phase obtained for this data point..
   .9844      ... single phase obtained for this data point..

 AAD-Y=     1.106
 AAD-P=     2.698

 AAD=SUM[ABS(EXP-CAL)/EXP]*100/(NO. OF DATA POINTS)
```

A.3.5. k_{ij} at 333 K

```
PROGRAM: VDW - VAN DER WAALS MODEL(S), 1-PARAMETER (CONVENTIONAL, 1PDW) OR
 2-PARAMETER, 2PDW
 d5
 co2-hmds 333

 K12=  .0947 T(K)=  333.15

  PHASE VOLUMES ARE IN CC/MOL, PRESSURE IS IN UNITS OF THE DATA.


   X-EXP      P-EXP      P-CAL       Y-EXP     Y-CAL     VL-CAL   VV-CAL
   .4641      43.920     43.916     .99000    .98333     147.83    502.3
```

.7809	75.980	77.766	.99000	.97319	110.15	207.5
.8584	86.320	85.074	.99000	.96439	106.69	165.2
.9465	95.490	92.556	.99000	.94836	123.99	125.5
.9791	... single phase obtained for this data point..					
.9844	... single phase obtained for this data point..					

AAD-Y= 1.803
AAD-P= 4.097

AAD=SUM[ABS(EXP-CAL)/EXP]*100/(NO. OF DATA POINTS)

A.4. Mathcad Algorithm for Regression of Binary Parameter from Sanchez-Lacombe Equation of State

SL-EOS for the binary mixture of CO_2-PDMS

The units for this section are MPA pressure, K for temperature, g/cm3 for density and (MPa*cm3)/(molK) for the gas constant. indices are; 1: CO2, 2: PDMS

Characteristic Parameters for CO_2

$P1star := 464.2$

$T1star := 328.1$

$\rho 1star := 1.426$

$M1 := 44.01$

Characteristic Parameters for PEG200

$P2star := 302$

$T2star := 476$

$\rho 2star := 1.104$

$M2 := 308000$

Gas Constant $R := 8.314$

$T := 333.2$

$$r10 := \frac{P1star \cdot M1}{R \cdot T1star \cdot \rho 1star} \qquad r20 := \frac{P2star \cdot M2}{R \cdot T2star \cdot \rho 2star}$$

$$v1star := T1star \cdot \frac{R}{P1star} \qquad v2star := T2star \cdot \frac{R}{P2star}$$

Function $\rho rd(P, T, w1, \delta)$ calculates the reduced density of a mixture given the pressure (bar), Temperature (K), weight fraction of CO_2 dissolved in the polymer phase, and the binary interaction parameter.

$$\rho rd(P, w1, \delta) :=$$

$v2star \leftarrow T2star \cdot \frac{R}{P2star}$

$\phi 1 \leftarrow \frac{\frac{w1}{\rho 1star}}{\left(\frac{w1}{\rho 1star}\right) + \left[\frac{(1 - w1)}{\rho 2star}\right]}$

$\phi 10 \leftarrow \frac{\left(\frac{w1}{\rho 1star \cdot v1star}\right)}{\left(\frac{w1}{\rho 1star \cdot v1star}\right) + \left[\frac{(1 - w1)}{\rho 2star \cdot v2star}\right]}$

$\phi 2 \leftarrow 1 - \phi 1$

$\phi 20 \leftarrow 1 - \phi 10$

$vstar \leftarrow \phi 10 \cdot v1star + \phi 20 \cdot v2star$

$P12star \leftarrow \sqrt{P1star \cdot P2star} \cdot (1 - \delta)$

$Pstar \leftarrow P1star \cdot \phi 1^{2} + P2star \cdot \phi 2^{2} + 2 \cdot \phi 1 \cdot \phi 2 \cdot \sqrt{P1star \cdot P2star} \cdot (1 - \delta)$

$T1rd \leftarrow \frac{T}{T1star}$

$T2rd \leftarrow \frac{T}{T2star}$

$Tstar \leftarrow T \cdot \left[\frac{\left[\left[\left(\frac{\phi 1}{T1rd}\right) + \left(\frac{v1star}{v2star}\right) \cdot \left(\frac{\phi 2}{T2rd}\right)\right]\right]}{\left[\phi 1 + \left(\frac{v1star}{v2star}\right) \cdot \phi 2\right]} - \phi 1 \cdot \phi 2 \cdot \frac{[(P1star + P2star - 2 \cdot P12star) \cdot vstar]}{R \cdot T}\right]$

$Prd \leftarrow \frac{P}{Pstar}$

$Trd \leftarrow \frac{T}{Tstar}$

$x1 \leftarrow \frac{\left(\frac{w1}{M1}\right)}{\left(\frac{w1}{M1}\right) + \left[\frac{(1 - w1)}{M2}\right]}$

$x2 \leftarrow 1 - x1$

$r \leftarrow \frac{(r10 \cdot x1 \cdot v1star + r20 \cdot x2 \cdot v2star)}{vstar}$

$f(\rho rd) \leftarrow \rho rd^{2} + Prd + Trd \cdot ln(1 - \rho rd) + Trd \cdot \rho rd - Trd \cdot \frac{\rho rd}{r}$

$root(f(\rho rd), \rho rd, 0.001, 0.999)$

Calculation of chemical potential of pure CO_2 phase

$$\mu pureCO2(P) :=$$

$\rho 1rd \leftarrow \rho rd(P, 1, 1)$

$P1rd \leftarrow \frac{P}{P1star}$

$T1rd \leftarrow \frac{T}{T1star}$

$v1rd \leftarrow \frac{1}{\rho 1rd}$

$r10 \cdot \left[P1rd \cdot \frac{v1rd}{T1rd} - \frac{\rho 1rd}{T1rd} + v1rd \cdot (1 - \rho 1rd) \cdot ln(1 - \rho 1rd) + \frac{ln(\rho 1rd)}{r10}\right]$

Calculation of chemical potential of polymer rich phase

$$\mu PCO2(P, w1, \delta) := \left|\begin{array}{l} \phi 1 \leftarrow \dfrac{\dfrac{w1}{\rho 1star}}{\left(\dfrac{w1}{\rho 1star}\right)+\left[\dfrac{(1-w1)}{\rho 2star}\right]} \\ \phi 2 \leftarrow 1-\phi 1 \\ \phi 10 \leftarrow \dfrac{\left(\dfrac{w1}{\rho 1star\cdot v1star}\right)}{\left(\dfrac{w1}{\rho 1star\cdot v1star}\right)+\left[\dfrac{(1-w1)}{\rho 2star\cdot v2star}\right]} \\ \phi 20 \leftarrow 1-\phi 10 \\ vstar \leftarrow \phi 10\cdot v1star+\phi 20\cdot v2star \\ \chi \leftarrow \left[P1star+P2star-2\cdot\sqrt{P1star\cdot P2star}\cdot(1-\delta)\right]\cdot\dfrac{v1star}{R\cdot T} \\ \rho rd \leftarrow \rho rd(P, w1, \delta) \\ T1rd \leftarrow \dfrac{T}{T1star} \\ P1rd \leftarrow \dfrac{P}{P1star} \\ r1 \leftarrow r10\cdot v1star\cdot\rho rd \\ r2 \leftarrow r20\cdot v2star\cdot\rho rd \\ \left[ln(\phi 1)+\phi 2-\phi 2\cdot\dfrac{r1}{r2}+r10\cdot\rho rd\cdot\chi\cdot\phi 2^{2}+r10\cdot\left[\dfrac{-\rho rd}{T1rd}+\dfrac{P1rd}{T1rd\cdot\rho rd}+(1-\rho rd)\cdot\dfrac{ln(1-\rho rd)}{\rho rd}+\dfrac{ln(\rho rd)}{r10}\right]\right] \end{array}\right.$$

Regression of CO2 weight fraction at equilibrium of two phases

$$\Delta\mu(P, w1, \delta) := T\cdot R\cdot(\mu pureCO2(P)-\mu PCO2(P, w1, \delta))$$

$$wCO2(P, \delta) := root(\Delta\mu(P, w1, \delta), w1, 0.01, 0.999)$$

$$w1cal(P, \delta) := \left|\begin{array}{l} j \leftarrow 0 \\ \text{for } i \in 0..rows(P)-1 \\ \quad \left|\begin{array}{l} w_{j,0} \leftarrow P_i \\ w_{j,1} \leftarrow wCO2(P_i, \delta) \\ j \leftarrow j+1 \end{array}\right. \\ w \end{array}\right.$$

$$P := \begin{pmatrix} 3.5 \\ 5 \\ 7 \\ 8 \\ 10 \\ 12 \\ 13.5 \\ 15 \\ 17.5 \\ 20 \\ 21 \\ 25.5 \end{pmatrix} \qquad w1exp := \begin{pmatrix} 0.05 \\ 0.1 \\ 0.14 \\ 0.19 \\ 0.22 \\ 0.27 \\ 0.31 \\ 0.34 \\ 0.35 \\ 0.38 \\ 0.39 \\ 0.4 \end{pmatrix}$$

$\delta := 0.076$

$RAAD(\delta) := \left(w1exp - w1cal(P, \delta)^{\langle 1 \rangle}\right)^2$

Given

$RAAD(\delta) = 0$

$\delta := Minerr(\delta)$

$\delta = 0.076$

$ERR = 1.983 \times 10^{-3}$

A.5. Calculation of Thermal Conductivity for Porous Materials

A.5.1. m-file for Calculation of Mean Free Path and Knudsen Number

```
function meanfreepath(L)

kb=1.38*10^(-23); %m2kg/s2K
dg=3.54*10^(-10); % m (for air)

Ti=298.15; %ambient temperature (K)
Pi=101325; %ambient pressure (Pa)(Pa=N/m2=kg/ms2)


LP=(kb*Ti*10^9)./(sqrt(2)*pi*dg^2*Pi)

pd=[1:1:100]; %pore diameter range (nm)

Kn=LP./pd; %Knudsen number for different pore sizes

plot(pd,Kn)

end
```

A.5.2. m-file for Calculation of Total Thermal Conductivity for Various Aerogel Densities andPore Sizes

```
function conductivity2(Vg,d)

ro=2200; %kg/m3 for bulk silica
rop=190; %kg/m3 for silica aerogel
cv=80; %J/kgK for bulk silica
l=40; %mean free path of phonons in silicon at RT
Lso=1.34; %pure SiO2 thermal conductivity

roaero=[10:1:400];%vector specifying different aerogel densities (kg/m3) from 100
kg/m3 to 200 kg/m3

Vg=1-(roaero/ro); %porosity calculated from densities given in the above vector
```

```
d=[1:1:1000]; %vector specifying different average pore diameters (nm) ranging from
1 nm to 1000 nm

Lg=zeros(length(Vg),length(d));  %formation of the matrix that will collect gaseous
cond. every row specifies gaseous conductivities at a fixed porosity for varying
pore diameter, every column specifies gaseous cond. at a fixed pore diameter for
varying porosity
Lt=zeros(length(Vg),length(d));  %formation of the matrix that will collect total
cond. every row specifies gaseous conductivities at a fixed porosity for varying
pore diameter, every column specifies gaseous cond. at a fixed pore diameter for
varying porosity

for i=1:1:length(Vg)
    Ls(i)=Lso*0.39*(1-Vg(i))^1.88;
    Lr(i)=(16*5.67*10^(-8)*300^3)/(3*22.7*roaero(i));
    for j=1:1:length(d)

        Lg(i,j)=(2.534*10^(-2)*Vg(i))/(1+(140/d(j)));

        Lt(i,j)=Lg(i,j)+transpose(Ls(i))+transpose(Lr(i));
    end
end

% PLOTS %
plot(roaero,Lt(:,20),'black') %total conductivity: black line
hold on
plot(roaero,Lr,'green') %radiative conductivity: green line
hold on
plot(roaero,Lg(:,20),'blue') %gaseous conductivity: blue line
hold on
plot(roaero,Ls,'red') %solid conductivity: red line

% SAVING DATA TO FILES %
fid = fopen('LT_20nm.txt','w');
fprintf(fid,'%6.4f\n',Lt(:,20));
status = fclose(fid);

fid = fopen('LT_10nm.txt','w');
fprintf(fid,'%6.4f\n',Lt(:,10));
status = fclose(fid);

fid = fopen('LT_50nm.txt','w');
fprintf(fid,'%6.4f\n',Lt(:,50));
status = fclose(fid);

fid = fopen('LT_100nm.txt','w');
fprintf(fid,'%6.4f\n',Lt(:,100));
status = fclose(fid);

fid = fopen('Lr.txt','w');
fprintf(fid,'%6.4f\n',Lr);
status = fclose(fid);

fid = fopen('Ls.txt','w');
fprintf(fid,'%6.4f\n',Ls);
status = fclose(fid);

fid = fopen('Lg_20nm.txt','w');
fprintf(fid,'%6.4f\n',Lg(:,20));
status = fclose(fid);

fid = fopen('roaero.txt','w');
fprintf(fid,'%6.4f\n',roaero);
status = fclose(fid);

end
```

A.5.3. m-file for Calculation of Effect of Polymer Deposition on Thermal Conductivity for 30 wt.% of Polymer Uptake

```
function condpolym(Vg,d)

ro=2200; %kg/m3 for bulk silica
rop=190; %kg/m3 for silica aerogel
cv=80; %J/kgK for bulk silica
l=40; %mean free path of phonons in silicon at RT
Lss=1.34; %pure SiO2 thermal conductivity
Lsp=0.1511;

ro1=[10:1:400];
roaero=1.3*ro1; %vector specifying different aerogel densities (kg/m3) from 100
kg/m3 to 200 kg/m3

Vg=1-(roaero/ro); %porosity calculated from densities given in the above vector

di=[1:1:1000]; %vector specifying different average pore diameters (nm) ranging
from 1 nm to 1000 nm
d=di-2;

Lg=zeros(length(Vg),length(d));  %formation of the matrix that will collect gaseous
cond. every row specifies gaseous conductivities at a fixed porosity for varying
pore diameter, every column specifies gaseous cond. at a fixed pore diameter for
varying porosity
Lt=zeros(length(Vg),length(d));  %formation of the matrix that will collect total
cond. every row specifies gaseous conductivities at a fixed porosity for varying
pore diameter, every column specifies gaseous cond. at a fixed pore diameter for
varying porosity

for i=1:1:length(Vg)
    Ls(i)=(Lss*0.77+Lsp*0.23)*0.39*(1-Vg(i))^1.88;
    Lr(i)=(16*5.67*10^(-8)*300^3)/(3*22.7*roaero(i));
    for j=1:1:length(d)

        Lg(i,j)=(2.534*10^(-2)*Vg(i))/(1+(140/d(j)));

        Lt(i,j)=Lg(i,j)+transpose(Ls(i))+transpose(Lr(i));
    end
end

% SAVING DATA TO FILES %
fid = fopen('LTrop.txt','w');
fprintf(fid,'%6.4f\n',Lt(:,18));
status = fclose(fid);

fid = fopen('rop.txt','w');
fprintf(fid,'%6.4f\n',roaero(:));
status = fclose(fid);

end
```